2-17-2016

Dynamic Simulation, Optimization, and Control of Flexible Chemical-Looping Combustion Processes

Lu Han
University of Connecticut - Storrs, lu.han@uconn.edu

Dynamic Simulation, Optimization, and Control of Flexible Chemical-Looping Combustion Processes

Lu Han, Ph.D.

University of Connecticut, 2016

Combustion of hydrocarbon fuels using the concept of chemical-looping combustion (CLC) is a novel approach projected to have higher energy efficiency than conventional CO_2 capture technologies. For CLC technologies to become commercially relevant, it is important to optimize the design of CLC reactor systems for high efficiencies for CO_2 capture and power generation. From an engineering point of view, CLC is a complex system with a large number of candidate materials and reactor configurations that need to be considered for process improvement. In this work, a model-based methodology was proposed as a formal framework to guide in developing novel technologies, using CLC as an exemplary case study. This framework deals with the development and validation of process models, optimization of a cyclic controls strategy for batch systems, and elimination process bottlenecks through the intensification of chemical reactors. As a first step, modelling and simulation was integrated with bench-scale CLC experiments to understand the phenomenological changes inside the CLC reactor and identify sources of model uncertainty. Optimal experimental design techniques were used to determine statistically-rich kinetic networks and parameters, in order to obtain kinetic models that are valid for prediction and extrapolation to large-scale systems. Optimization problems

were formulated to maximize the efficiency of the CLC reactors with respect the cycle operation, to seamlessly integrate CLC into advanced power cycles. It was found that the process efficiency of conventional CLC reactor configurations was limited by an upper bound due to restrictions originating from poor gas/solid contact and low bed utilization. To improve upon the existing reactor designs, a novel reverse-flow reactor was proposed as a process intensification option for CLC. From a theoretical analysis, the reverse-flow process is shown to be a potentially disruptive technology, which offers the ability to reach higher plant efficiencies, while minimizing the process footprint. The feasibility of this structured methodology is demonstrated, as a means to enable faster deployment of novel technologies.

Dynamic Simulation, Optimization, and Control of Flexible Chemical-Looping Combustion Processes

Lu Han

B.Sc., University of Connecticut, 2011

A Dissertation

Submitted in Partial Fulfillment of the

Requirements for the Degree of

Doctor of Philosophy

at the

University of Connecticut

2016

APPROVAL PAGE

Doctor of Philosophy Dissertation

Dynamic Simulation, Optimization, and Control of Flexible Chemical-Looping Combustion Processes

Presented by

Lu Han, B.Sc.

Major Advisor _____

Dr. George M. Bollas

Associate Advisor _____

Dr. Ranjan Srivastava

Associate Advisor _____

Dr. Brian Willis

Associate Advisor _____

Dr. Leslie Shor

Associate Advisor _____

Dr. Steven Suib

University of Connecticut

2016

Dedicated to my family for always believing in me...

and to my beloved Fenway, for being my beacon of light ...

ACKNOWLEDGMENTS

This research would not be possible without the support of many people. I would like to thank my parents for their encouragement to pursue a PhD in Chemical Engineering. I would also like thank my boyfriend, Shayan, for his support and patience through this arduous journey. I would like to extend my sincere gratitude to Prof. Bollas, who had the role of scientific supervision and mentorship of this work. His contributions have profoundly enriched this thesis. I would like to extend my acknowledgement and recognition to the distinguished thesis committee members: Prof. Brian Willis, Prof. Ranjan Srivastava, Prof. Steven L. Suib, and Prof. Leslie Shor. Their comments and suggestions have been a great contribution to this dissertation. I owe my sincere thanks to the past and current members of this research group, Dr. Zhiquan Zhou, Dr. Shoucheng Du, Chen Chen, Chunxiang Zhu, Brian Baillie, Kyle Palmer, and William Hale, as well as the undergraduate assistants whom I mentored, Clarke Palmer and Kyle Such.

This material is based upon work supported by the National Science Foundation under Grant No. 1054718. Part of the work was supported by the National Science Foundation Graduate STEM fellowship in K-12 Education (NSF GK-12). Part of this work was sponsored by the UTC Institute for Advanced Systems Engineering (UTC-IASE) of the University of Connecticut and the United Technologies Corporation. Any opinions expressed herein are those of the authors and do not represent those of the sponsor. Support by W.R. Grace & Co. by providing the Al_2O_3/SiO_2 matrices is gratefully acknowledged.

Table of Contents

List of Tables

List of Figures

Chapter 1 INTRODUCTION

Growing global concern over unabated CO_2 emissions puts demand on conventional fossil fueled power systems to seek out new technologies that mitigate anthropogenic carbon emissions. In this context, carbon capture and storage (CCS) technology is regarded as a feasible near-term option that permits the continued usage of fossil fuels without emitting CO_2 into the atmosphere. CCS can be implemented in three steps of CO_2 separation and compression, CO_2 transportation, and CO_2 storage in stable geological reservoirs. A large portion of the total CCS cost is associated with the CO_2 separation step, due to the high energy penalties imposed by the current industrial separation technologies. Chemical-looping combustion (CLC) is an effective and versatile process that can convert a gaseous hydrocarbon fuel into electricity, while providing CO_2 capture at a low cost. For CLC to be commericalized, its path forward is dependent on the knowledge of the design and operation of the reactor and the optimal oxygen carrier performance. Though considerable research on the CLC technology has been reported, most studies focus on the oxygen carrier synthesis and development, and those related to the reactor system operation and integrated large scale process development are scarce. This chapter provides the motivation for CO_2 mitigation, description of the current CO_2 capture technologies from power plants, and a brief overview of the chemical-looping technology.

1.1. Motivation for CO_2 mitigation

The accumulation of greenhouse gases in the earth atmosphere accelerates the natural greenhouse gas effect and is the cause for global warming. Carbon dioxide (CO_2) from the conversion of fossil sources (gas, oil, and coal) accounts for 57% of the global greenhouse gas emissions [1]. As can be seen in **Figure 1.1**, the global carbon emissions from fossil fuels have increased by over 16 times between 1900 and 2008 and by about 1.5 times between 1900 and 2008 [2]. The global atmospheric concentration of CO_2 increased from a pre-industrial value of about 280ppm to 399 ppm in 2015 [3]. To prevent significant changes in the earth global climate, the CO_2 concentration must not exceed 450 ppm. Therefore, it is

generally accepted that a reduction in global greenhouse gas emissions is necessary in the foreseeable future.

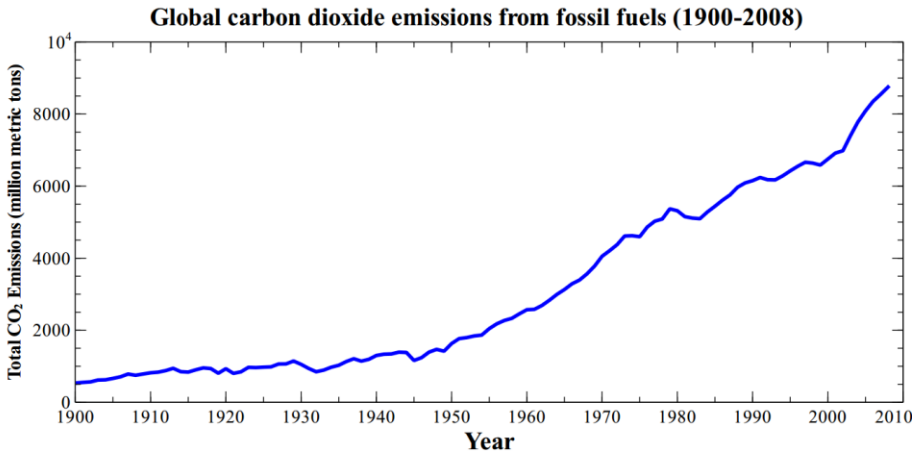

Figure 1.1: Trends in global CO_2 emissions [2].

The technological options for reducing net CO_2 emissions into the atmosphere include [4]: (a) reducing energy consumption by increasing efficiency of the energy conversion and/or utilization; (b) switching to less carbon intensive fuels; (c) increasing the use of renewable energy sources (biofuel, wind, solar, etc.) or nuclear energy; (d) sequestrating CO_2 by enhancing biological absorption capacity in forest and solids. The renewable energy sources have the intrinsic advantage of not generating CO_2 or contributing to zero net CO_2 emissions. However, in their current status of development and/or availability, alternative energy technologies cannot fully replace the fossil fuels as the energy source. Thus, Carbon Capture and Storage (CCS) technology in conjunction with the other mentioned technologies appears as an additional option to achieve the necessary reduction in CO_2 emissions. The CCS process involves CO_2 separation (from either stack gas or other intermediate gas streams), followed by pressurization, transportation, and sequestration. According to IEA's roadmap, 20% of the total CO_2 emissions should be removed by CCS by 2050 [5]. A majority of the current research endeavors is focused on CO_2 removal from stationary power plants for

many reasons. First, stationary power plants are by far the most dominant contributors of CO_2 emissions, accounting for 47% of the total anthropogenic CO_2 emissions [4]. In addition, they share similarities with existing processes, where CO_2 capture has been used for many decades. Hence, technologies for capture CO_2 from stationary power plants are more mature than those for capture from mobile sources, such as in the transportation sector. Finally, it is more practical to capture the CO_2 from large point sources, such as fossil fuel power plants, and take advantage of economies of scale.

1.2. CO_2 capture in power generation

The CO_2 capture step is the most expensive part of CCS. The cost for CO_2 capture is estimated at \$15-\$75 per ton of CO_2 processed, whereas the costs for transportation and geological storage are estimated at \$1-\$8 and \$0.5-\$8 per ton of CO_2 [4]. Thus, developing a cost-effective carbon capture technology is the key to affordable CO_2 emissions control in fossil fuel based power plants. Several options exist for implementing carbon capture and they vary according to the type of power plant (fuel source, thermal cycle, combustion type, etc.). They are generally categorized into post-combustion, pre-combustion, oxy-fuel capture, and chemical-looping combustion (CLC), shown in **Figure 1.2**. Current status of these options can be found in several review papers [6–10].

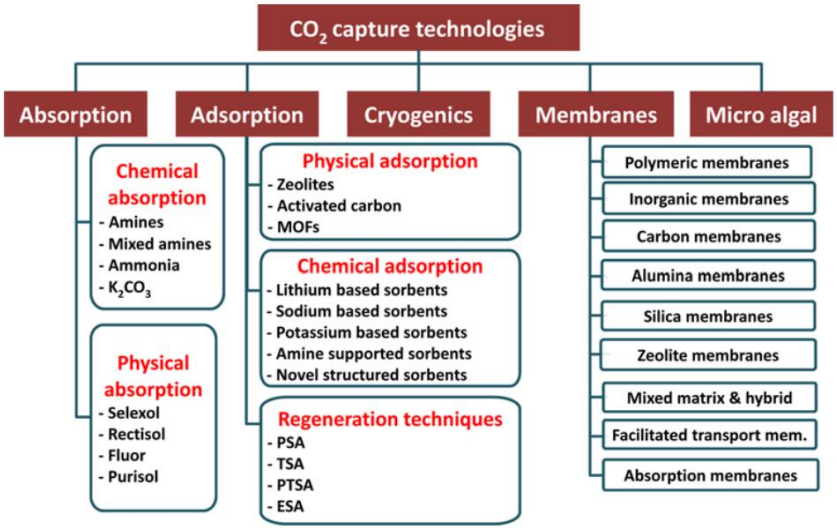

Figure 1.2: Overview of CO_2 capture technologies from Zaman and Lee [6].

1.2.1. Post-combustion capture

Post-combustion capture involves separation of CO_2 from flue gas after the power generation step. The separation of CO_2 from nitrogen and small quantities of oxygen and water vapor can be performed by following processes: absorption using solvents or solid sorbents, pressure and temperature swing adsorption using various solid sorbents, cryogenic distillation and membranes [11]. The concentration of CO_2 in the flue gas is in the range of 12-15 vol.% in coal-fired power plants and less than 8 vol.% in natural gas-fired power plants [12]. Due to the low partial pressures of CO_2, chemical absorption, especially using monoethanolamide (MEA), is preferred over physical absorption. The anticipated drop in the net efficiency of the power plant with post-combustion capture is about 10-14% points [13]. The efficiency decrease attributed to post-combustion capture is due to low concentrations of CO_2 in the flue gas, large volumes of the flue gas that needs to be treated, high compression demand to reach storage pressure, and high energy expenditure for cooling the CO_2 before it is captured [6]. The advantage of post-combustion capture is that all existing power plants can be retrofitted without any significant changes since the capture unit can be incorporated downstream of the boiler without any significant

changes to the original plant [14]. Furthermore, the energy demand of the power plant can be controlled by adjusting the CO_2 capture level, even bypassing the CO_2 capture step during peak loads. Post-combustion CO_2 capture can be used in pulverized coal (PC), oil-fired or gas-fired power plants, and can be applied to combined cycle power plants. **Figure 1.3** shows an example of post-combustion capture applied to a natural gas fired combined cycle (NGCC) plant.

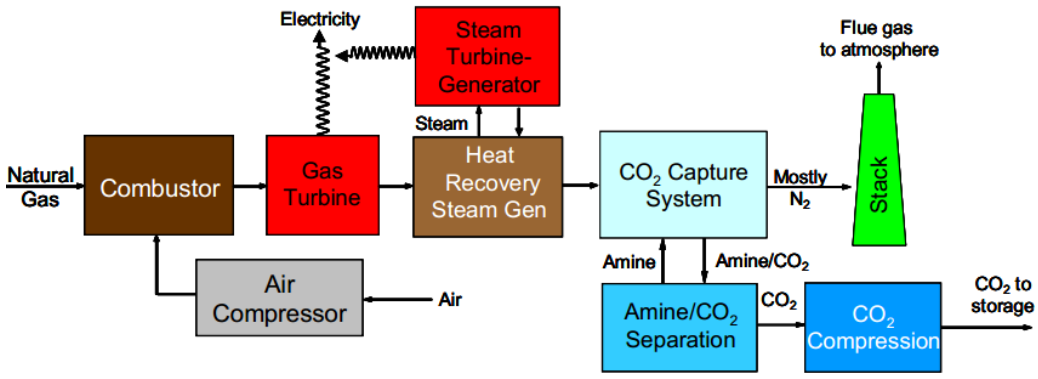

Figure 1.3: Schematic of an amine-based post-combustion CO_2 capture system applied to a coal-fired or natural gas-fired combined cycle from Folger [15].

1.2.2. Pre-combustion capture

Pre-combustion capture refers to the process of decarbonisation of a hydrocarbon fuel before combustion. It is achieved through partial oxidation of fuel followed by a shift reaction and CO_2 capture step prior to combustion in air. An example of a pre-combustion process is the integrated gasification combined cycle (IGCC). In the IGCC process, coal is gasified with oxygen and steam at high temperatures and pressures to produce syngas (mixture of CO and H_2). Afterwards, the syngas reacts with steam in a water gas shift reactor, to produce a mixture of mainly CO_2 and H_2. CO_2 is captured from this fuel gas, leaving just H_2 from power generation. This type of power plant is shown in **Figure 1.4**. Pre-combustion capture can also be applied to natural gas fired power plants, wherein natural gas is first converted to syngas *via*

reforming. This process is more costly than post-combustion capture for natural gas fired plants [16]. Technno-economic evaluations of IGCC reveal that the major hurdles for this process are the high capital costs and complicated nature of the process [13,17,18].

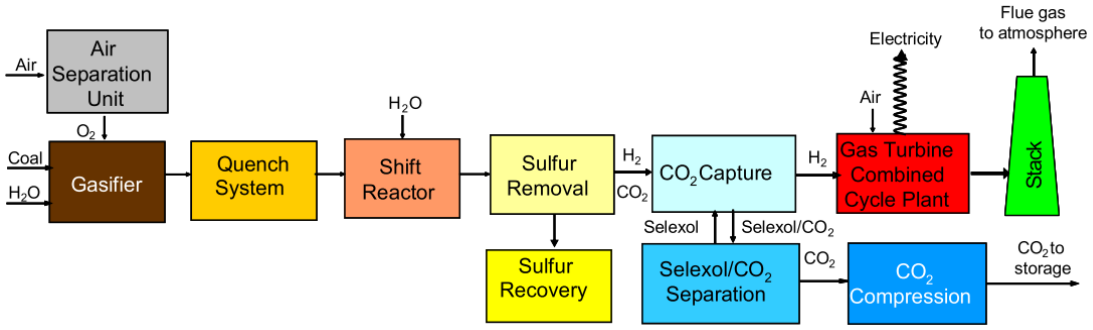

Figure 1.4: Schematic of an integrated gasification combined cycle (IGCC) coal power plant with pre-combustion from Rubin et al. [16].

1.2.3. Oxy-fuel combustion capture

Oxy-fuel combustion capture, shown in **Figure 1.5**, is an adaption of post-combustion capture for coal-fired power plants. Pure oxygen rather than air is used for combustion. Therefore, the exhaust gases contain only CO_2 and steam, without N_2 dilution, and condensation of the water vapor is needed to obtain a high purity steam of CO_2. A major advantage of oxy-fuel combustion is the lower cost of CO_2 capture. However, the separation of pure O_2 from air can be costly for a large scale power plant. Another challenge is that the temperatures in oxy-fuel combustion are much higher than in air combustion due to the use of pure O_2 at reduced gas flows. This problem is overcome by recycling the flue gas back into the boiler to keep the temperatures under control and makeup the volume of the missing N_2. An additional advantage of this process is that the NO_x emissions are substantially reduced [19]. However, major improvements are needed in the development of cost-effective oxygen production technologies. It is reported that the air separation unit accounts for 60% of the power consumption for carbon capture and

reduces the overall plant efficiency by 7-9% points [13].

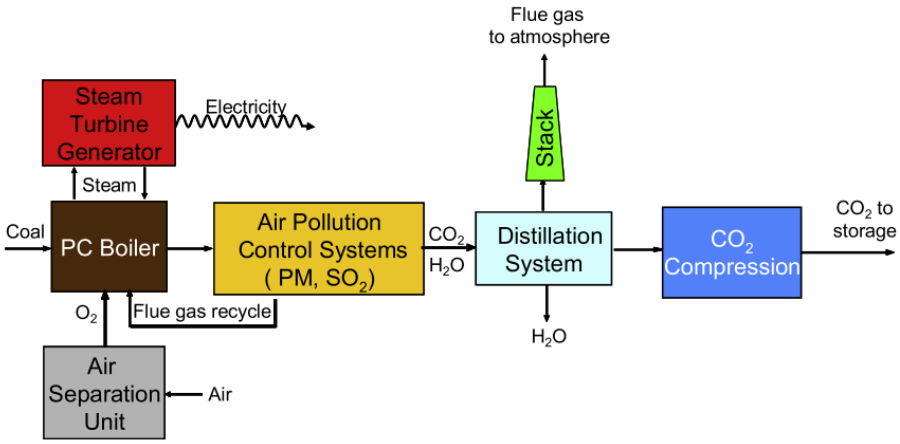

Figure 1.5: Schematic of an oxy-fuel coal-fired power plant from Rubin et al. [16].

1.3. Concept of chemical-looping combustion

The CO_2 capture options based on post-combustion, oxy-fuel combustion, and pre-combustion have undergone a great deal of development during the past decades and some of them are available at commercial scale [16]. The main obstacle to the wide adoption of CCS is the high cost of CO_2 capture, which reduces the energy efficiency and increases the price of electricity. In 2000, the CO_2 Capture Project (CCP) was formed as a collaborative effort between governments, industry, universities, and environmental interest groups to search for the most promising technologies that had the potential to deliver performance and efficiency improvements resulting in close to a 50% reduction in the cost of CO_2 [20]. Chemical-looping combustion (CLC) was suggested as among the best alternative technologies to reduce the cost of CO_2 capture [21]. CLC was mentioned by the Intergovernmental Panel on Climate Change (IPCC) in their special report on Carbon Dioxide Capture and Storage [4] and by the EU under their project "Enhanced Capture of CO2 "(ENCAP), both of which included CLC as an efficient and one of the cheapest CO_2 capture technologies [22]. The estimated cost was \$7-\$15 per ton of CO_2 avoided for

CLC, $20-$41 for pre-combustion, and $15-$33 for oxy-fuel combustion [23]. The main drawback of CLC is the low technological readiness level, as a consequence of the lack of maturity of the technology (**Figure 1.6**). At the present, CLC must be considered as an emerging technology. However in the past decade, there has a tremendous progress in the areas of research and development, contributing to the growing popularity of this technology.

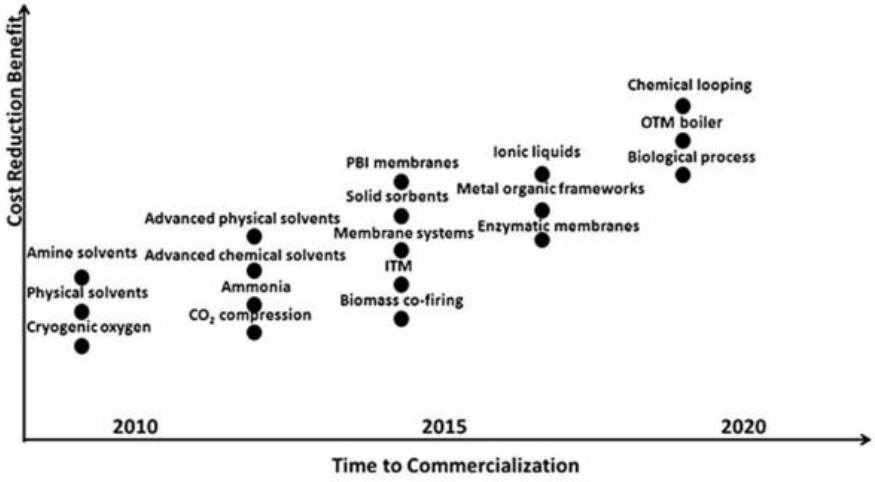

Figure 1.6: U.S. DOE roadmap for current and emerging CO_2 capture technologies in terms of cost reduction potential and time to commercialization [24].

CLC is a novel combustion concept for the purpose of power generation with inherent CO_2 capture. The term "inherent" implies that CO_2 is readily available in a concentrated form by virtue of the process itself. Early work on the CLC dates back to 1983 by Richter and Knoche [25], who suggested a fuel oxidation reaction scheme involving two intermediary reactions with a metal oxide as an oxygen carrier. Other pioneers to the field include Ishida et al. [26], who termed the process "chemical-looping combustion." The novelty of CLC as compared to conventional combustion is that the air and fuel remain in separate environments with no direct contact. CLC can be regarded as as un-mixed combustion.

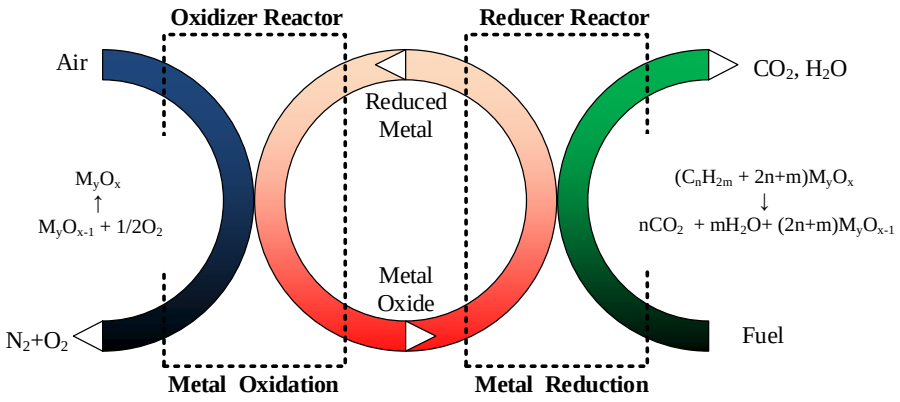

Figure 1.7: Diagram of the chemical-looping combustion (CLC) process.

Figure 1.7 depicts the principle of CLC. Fuel conversion is accomplished by a reduction-oxidation scheme using an intermediate metal/metal oxide oxygen carrier. The terminology for the Oxidizer and Reducer are with respect to metal and metal oxide. The oxygen carrier transfers the oxygen from the air to combust the fuel, generating CO_2 and steam. By eliminating contact between the air and fuel streams, the combustion products are not diluted with N_2, allowing for a high purity stream of CO_2 to be obtained after water condensation. The energy balance inside the reactors depends on the oxygen carrier and the fuel. The oxidation reaction is always strongly endothermic, while the reduction reaction can be endothermic or exothermic. The net energy change of CLC is the same as ordinary combustion. An additional benefit of CLC compared to conventional combustion is that no NO_x is formed, since regeneration of the oxygen carrier takes place without flame at moderate temperatures.

In principle, CLC can be used with gaseous, liquid, or solid fuels. A process using gaseous fuels, such as natural gas, refinery gas, or synthesis gas, would be the easiest to implement. There is also considerable interest in developing CLC for solid fuels, such as coal and biomass. In the case of solid fuels, the char is first gasified in the presence of steam, producing CO and H_2, which can then react with the oxygen carrier in the Reducer Reactor. An alternative to CLC for solid fuels using the gasification of the car is chemical-looping with oxygen uncoupling (CLOU), in which the char reacts directly with gaseous oxygen

spontaneously released from the oxygen carrier [27]. Chemical-looping can also be used for hydrogen production, wherein the regeneration of the oxygen carrier can be done using air or steam. When air is used for regeneration, it can be differentiated: the Steam Reforming process integrated with CLC (SR-CLC), where CLC is used to provide the energy required for catalytic steam reforming; and the Chemical-Looping Reforming process (CLR), where a mixture of fuel and steam is sent to the Reducer to produce H_2 and CO [23]. Other processes use the reduced form of the oxygen carriers to convert steam into hydrogen production, also known "water-splitting." The Syngas Chemical-Looping Process (SCL) and the Coal Direct Chemical-Looping (CDCL) process are in this category [23]. This thesis is focused the status of development of the Chemical-Looping Combustion processes. In the next Chapter, major topics of research are discussed, focusing on the major progress made in material selection, reactor design and prototype testing, and conceptual process design integrated with thermal cycles.

Chapter 2 LITERATURE REVIEW

This chapter provides a comprehensive literature review of the major research topics on CLC. First, the development of suitable oxygen carrier materials for CLC is discussed. Most of these oxygen carriers are synthetic materials, where the active metal oxides are dispersed over inert supports. Next, the various reactor configurations for CLC are introduced. Their potential advantages and issues associated with the design, operation, and scale-up are discussed. Third, modeling studies for CLC are reviewed, following the sequence of reaction kinetics, reactor simulation, and process design.

2.1. Oxygen carriers for CLC

Most of the technical literature on CLC has been focused on the development of suitable oxygen carrier materials. Some of the most active research institutes for CLC are Chalmers University of Technology, Instituto de Carboquímica of the Spanish National Research Council (ICB-CSIC), Tokyo Institute of Technology, and Korean Institute of Energy Research. A suitable oxygen carrier material should exhibit the following characteristics [28,29]:

- High thermal resistance
- Resistance to agglomeration or attrition
- High reactivity and stability during reduction and oxidation cycles
- High oxygen carrying capacity
- Environmentally benign and economically feasible

Most of the reported work on CLC has been accomplished using oxygen carrier particles where the active component is combined with an inert material [29,30], while there are some studies with iron ore [31] and ilmenite [32]. Transition metal oxides, such as nickel, cobalt, iron, and manganese are good candidates given their favorable reductive and oxidative behavior. From thermodynamic analysis, Mattisson and Lyngfelt [33] and Jerndal et al. [34] proposed the following metal oxides as suitable materials for gaseous

CLC: Mn_2O_3/Mn_3O_4, CuO/Cu_2O, Fe_2O_3/Fe_3O_4, NiO/Ni. To increase their reactivity, durability, and fluidizability, oxygen carriers are prepared by deposition the active metal oxides over an inert support, such as SiO_2, TiO_2, ZrO_2, Al_2O_3, YSZ, and bentonite. Methods for oxygen carrier preparation include freeze-granulation [35,36], spay-drying [37–39], impregnation [40–42], co-precipitation [43–45], spin-flash drying [46], sol-gel and dissolution [47]. In general, the resulting oxygen carrier has a porous structure with a high surface area.

Table 2.1: Summary of the experience time (in hours) on CLC and CLR in continuous units from Adanez et al. [23]. Abbreviations: CLC, chemical-looping combustion, CLCs, solid-fueled chemical-looping combustion, CLR, chemical-looping reforming.

	CLC	**CLCs**	**CLR**	**Total**
Nickel	2114	160	284	2558
Copper	391	--	--	391
Iron	97	30	--	127
Manganese	70	--	--	70
Cobalt	25	--	--	25
Mixed oxides	82	--	--	82
Low cost materials	111	88	--	199
Total	2890	278	284	3452

Among the candidate oxygen carrier particles, the most reactive material follows the order: $NiO>CuO>Mn_2O_3>Fe_2O_3$ [48]. Mixed oxide oxygen carriers have also been investigated, prepared by mixing different active metal oxides onto the same particle support. Studies have shown that the mixed oxides display better reactivity and suitability as compared to their monometallic counterparts [49–53]. An important aspect of the oxygen carrier is the longevity in continuous CLC operation during long periods of time. However, the number of materials tested in these units is limited. For a compilation of the specific operation time of each material, the readers are suggested to see the work of Adanez et al. [23]. In short, **Table 2.1** shows a summary of the operation hours in continuous plant for the various oxygen

carriers, up to the end of 2010. In this thesis, two of the most heavily investigated oxygen carriers (**Table 2.1**) are considered: (1) a Ni-based oxygen carrier supported on Al_2O_3; (2) a Cu-based oxygen carrier supported on SiO_2. In the following sections, these two oxygen carriers are further discussed on the basis for their reactivity, chemical stability, and suitability for large-scale CLC applications.

2.1.1. Nickel-based materials

Nickel-based oxygen carriers have been extensively studied in the CLC literature. They demonstrate very high reactivity in the reduction and oxidation environments and good stability at high working temperatures (900-1000°C). The melting point of is metallic Ni is 1453°C and that of NiO is 1990°C. Other nickel oxides (such as Ni_2O_3 and NiO_2 do not exist during CLC conditions), so only NiO has to be considered, in conjunction with Ni. Furthermore, Ni is a well-known reforming catalyst [54,55], which allows for the process to operate at near complete CH_4 conversions. However, carbon formation reactions catalyzed by Ni are disadvantageous to the CL process, by lowering the CO_2 capture efficiency [56] and also block pores [57,58].

Among the available supports for NiO/Ni materials, Al_2O_3 has received considerable attention due to its favorable fluidization properties and thermal stability [56,57,59–69]. There is possible interaction between free NiO with the Al_2O_3 support to form nickel aluminate spinel ($NiAl_2O_4$) as a result of calcination at temperatures above 1000°C [70,71]. The spinel is significantly less reactive than NiO [66], and as a result, the reactivity of the material can depart over time from that of the fresh materials [72]. To reduce the metal/support interaction, some authors suggested using excess nickel to compensate for the loss of Ni to the $NiAl_2O_4$ [56,63], or use of $NiAl_2O_4$ as the support in lieu of Al_2O_3, which has shown to improve oxygen carrier stability and decrease carbon deposition [60,62,65,66,73–76]. The addition of MgO and CaO to the Al_2O_3 support has been shown to reduce interaction between NiO and Al_2O_3 and stabilize the carrier by forming a protective layer of $MgAl_2O_4$ and $CaAl_2O_4$ spinel [70,77–80]. Also, Co can promote the performance of Co-Ni/Al_2O_3 oxygen carriers by reducing metal-support interactions [81].

2.1.2. Copper-based materials

Copper-based oxygen carriers, like Ni, have high reactivity in both reduction and oxidation cycles and high oxygen transfer capacity. Thermodynamic analysis shows that methane and synthesis gas fuels can be converted almost completely to H_2O and CO_2 using CuO as the oxygen carrier. Unlike Ni, the reduction and oxidation reactions with Cu-based oxygen carriers are exothermic, which reduces the preheating demands for the Reducer. Other advantages of Cu over Ni include the cheaper cost and non-toxicity. However, the main disadvantage of using CuO for CLC applications is its low melting point and high tendency for agglomeration. The operating temperatures of CuO-based CLC are limited to below 1085°C, which is the melting point of Cu. Several contributions address the reactivity of CuO in CLC and showed that at 950°C, the Cu-based oxygen carrier displayed high reactivity in the redox cycles, but after a few cycles, the reactivity was significantly reduced due to particle agglomeration [82,83].

Supported Cu-based oxygen carriers are typically favored over pure CuO. CuO/Al_2O_3 is commonly used in the literature [63,66,74,82,84–90], however the solid-solid reaction between CuO and Al_2O_3 starts above 850°C. Thus, the formation of $CuAl_2O_4$ can occur in the CLC system and lower the oxygen carrier reactivity. CuO/Al_2O_3 prepared by impregnation showed a high tendency for agglomeration if the CuO loading on the oxygen carrier was above 20 wt.% and no tendency if the loading was below 10 wt.% [88]. Chuang et al. [90] analyzed the influence of different preparation methods on the CuO/Al_2O_3 performance and found that oxygen carriers made by mechanical mixing and wet impregnation had a poor dispersion of CuO throughout Al_2O_3, resulting in agglomeration. However, co-precipitated oxygen carriers did not agglomerate and showed a high carrying capacity [90]. SiO_2 was identified by several researchers as a good binder for Cu [82,84,86,91–94] for its physical and chemical stability. CuO supported on SiO_2 displays high reactivity, albiet lower than Ni-based oxygen carriers. Still, the CuO/SiO_2 oxygen carrier is another good candidate for CLC.

2.2. Reactor design and operation

The reactor CLC should to achieve high conversion of the gas and solids, while maintaining a high CO_2 capture efficiency. Wolf [28] reported some of the essential features for an efficient CLC system:

- Sufficient particle circulation between Oxidzer and Reducer to achieve complete fuel combustion
- Adequate contact time between the fuel/air and the solid oxygen carrier to achieve maximum conversion of the gas and solid
- High temperature to maximize gas turbine efficiency (for the integrated combined cycle with CLC)
- High pressure operation to provide higher overall efficiency of the power generation
- Limited CO_2 leakage from the fuel and the air reactor

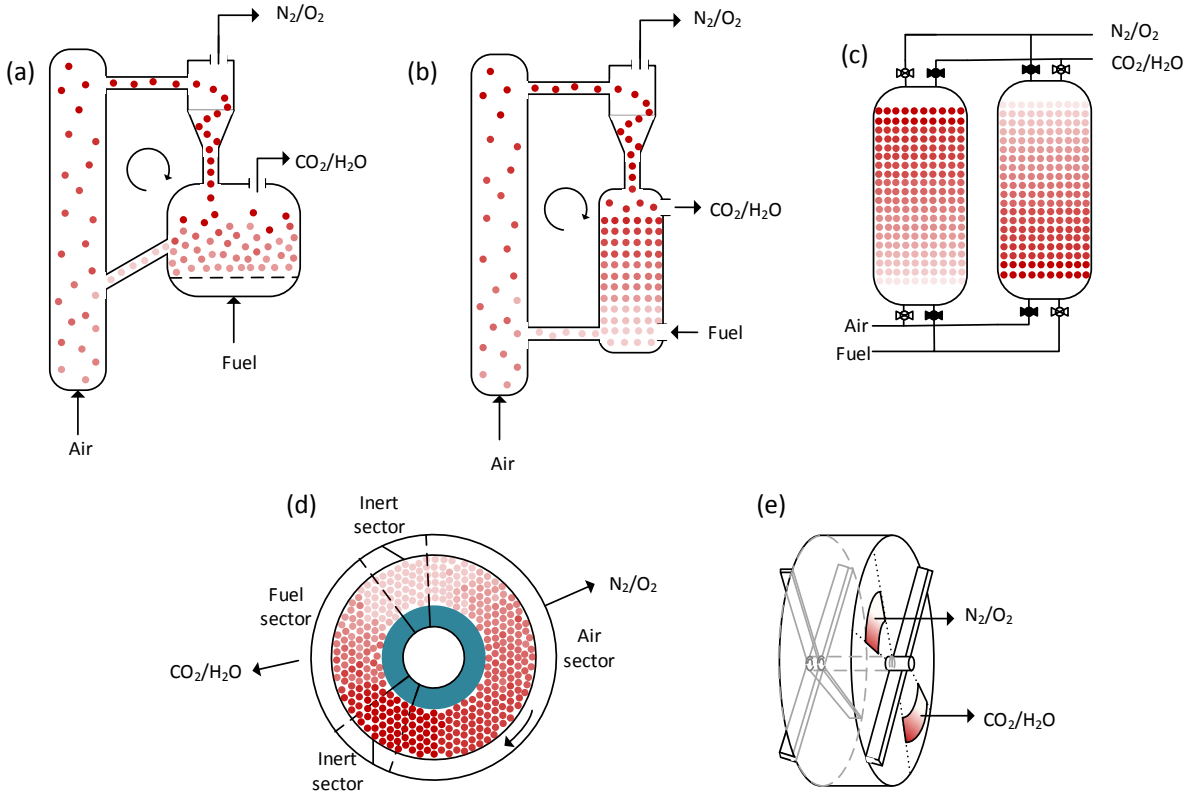

Figure 2.1: Reactor configurations for CLC: (a) interconnected fluidized bed reactor system [23], (b) moving bed reactor [95], (c) fixed bed reactor [96], (d) rotating reactor [97], (e) rotary bed reactor

[98,99].

To meet those criteria, various reactor configurations have been proposed in the literature, shown in **Figure 2.1**. In the following section, a brief description of the reactor units of **Figure 2.1** is given.

2.2.1. Interconnected fluidized bed reactor system

The interconnected fluidized bed reactor system (**Figure 2.1(a)**) has several appealing attributes for CLC, making it the most widely favored arrangement in the literature. The early designs were developed for combustion of gaseous fuels at atmospheric pressure, based on the circulating fluidized bed principle [100]. The solids exhibit a 'fluid-like' behavior due to the fluidization regime, which provides a good gas/solid contact, temperature and pressure uniformity, and stable reactor operation. There are several versions of the interconnected fluidized bed reactor design [101–103], operated by several research groups at Chalmers University of Technology, Vienna University of Technology, CSIC-ECB, Tokyo Institute of Technology, Korean Institute of Energy Research, and Southeast University of China.

Basically, a high-velocity riser and a low-velocity bubbling fluidized bed are considered as the Oxidizer and Reducer, respectively. The solid particles leaving the riser (Oxidizer) are recovered by a cyclone and sent to the Reducer. In the Reducer, the oxygen carriers react with the fuel and then are transported back to the riser. Particle loop-seals are located between the Oxidizer and Reducer in order to accommodate the pressure differences between the two reactors and avoid mixing of the flue gases. A longer residence time is often required for the Reducer because of the different reactivities of the oxygen carriers under reduction and oxidation environments [104,105].

A major difficulty of the fluidized bed reactor design deals with the transport of large amounts of solids, which becomes more problematic at elevated pressures. Efficient cyclones are necessary to separate the solids from the flue gas. This will lead to unavoidable particle attrition and release of fines into the atmosphere. For CLC process operating with expensive and/or toxic oxygen carrier materials, the attrition issue is a major bottleneck that can render the process economics unfavorable. Effective loop-seals are needed to achieve a pressure balance between the reactors and minimize gas leakage. A gas leakage from

the Reducer to the Oxidizer dilutes the flue gas stream with N_2, which lowers the CO_2 capture efficiency of the process. Therefore, it is essential to minimize the gas leakage as much as possible. It was reported that gas leakage could be reduced by incorporating two loop seals between the two reactor units [46].

2.2.2. Moving bed reactor

A moving bed concept (**Figure 2.1(b)**) was proposed by Fan and Li [106] for the Reducer. This concept was applied to the Syngas Chemical-Looping (SCL) process using FeO oxygen carriers and syngas fuels [107] at Ohio State University. Contrary to the fluidized bed reactor, a moving bed reactor has poor axial mixing of the gas and solids. The moving bed Reducer utilizes counter-current gas/solid flows to take advantge of the multiple oxidation states of iron oxide. A fresh fuel (syngas) reacts with iron at lower oxidation states, and meanwhile, the partially converted syngas will react with iron at higher oxidation states. Results of thermodynamic analysis show that the solid conversion in the moving bed is nearly 5 times higher than in the fluidized bed, resulting in significantly reduced solid circulation rate and reactor volume for the moving bed reactor [106]. However, the operational experience of this concept is limited to iron-based oxygen carriers. Issues related to the particle circulation and particle attrition are still existent in the moving bed design. Large particles are needed in order for the particles to resist fluidization, which can decrease the reactivity of the oxygen carriers due to intraparticle diffusion limitations. Gas leakage may occur if there is a pressure difference between the fluidized and moving bed reactors.

2.2.3. Fixed bed reactor

The main advantage of the fixed bed reactor (**Figure 2.1(c)**) is that the separation of gas and solids is intrinsic to the process, allowing for the reactor to be compact, without necessitating complicated equipment such as loop seals and cyclones [96]. Also, operation at high-pressures is easier to achieve with the fixed bed reactor due to the simplicity of the reactor. In the fixed bed CLC, the main process steps include: (i) oxidation and heat generation, (ii) heat removal, and (iii) reduction. These steps occur in succession in a single reactor, whereas in the fluidized bed and moving bed designs, the reduction and

oxidation/heat removal steps take place in separate reactors. Due to the cyclic nature of the operation, the fixed bed reactor is an inherent batch process that is dictated by the oxygen carrier material, fuel, and heat management strategy [108,109]. To achieve a continuous operation, several fixed bed reactors working in parallel are needed [110,111]. The disadvantages of this process include the need for high-temperature valves, high pressure drop across the bed, high temperature fluctuations between the reduction and oxidation steps, and possibly poor contact between the fuel and solids.

2.2.4. Rotating reactor

In the rotating reactor design (**Figure 2.1(d)**), the oxygen carrier is contained in a doughnut-shaped reactor that rotates between gas streams flowing radially outward through the bed [97,112,113]. Between the two reacting streams, one inert gas is introduced to avoid mixing of the two reacting gases. A radially directed gas flow was theorized to give the best flow performance since volume expansion from molar and temperature changes during reaction will be compensated by the radial reactor volume increase [97]. Early–phase testing found that internal gas mixing is unavoidable, but a CO_2 purity of 85% is obtainable. Further improvement to the process, construction, and operating conditions can lead to dramatic improvements in the future.

2.2.5. Rotary bed reactor

The rotary bed reactor (**Figure 2.1(e)**) is similar to the rotating reactor, wherein a solid matrix wheel rotates between reducing and oxidizing environments [98,99]. The oxygen carrier is coated or impregnated on the surface of the spinning wheel matrix. As the reactor rotates, oxygen is absorbed while the channels pass through the air section and then released to oxidize the fuel. During the cyclic operation, the solid wheel behaves like a heat exchanger to transfer the heat of reaction to the flowing gas. Effecting sealing systems can be used to avoid mixing. The drawbacks to the rotary bed design include temperature fluctuation, differential thermal distortion, and carbon deposition.

2.3. Modeling and simulation

Mathematical modeling of the reduction and oxidation reactions inside CLC reactors is helpful for design, optimization, and scale-up endeavors. A number of works can be found in the literature for the modeling of CLC systems. This section briefly addresses three major topics of CLC modeling: heterogeneous kinetic modeling, reactor modeling, and process simulation.

2.3.1. Chemical reactions of CLC

To develop an accurate kinetic model suitable for representation of the CLC system, the reaction kinetics and their mechanisms need to be estimated from experimental data. Typically, thermo-gravimetric analyzers [32,35,42,114–117] and bench-scale fixed bed reactors [58,118–120] are used to estimate kinetic parameters and compare solid-state reaction models. In most cases, the oxidation reaction can be represented by one reaction:

$$2Me_xO_{y-1} + O_2 \rightarrow 2Me_xO_y \quad \text{(R1)}$$

where Me_xO_y is the oxidized form and Me_xO_{y-1} is the reduced form.

The overall reduction reactions of metal oxide with CH_4, CO, and H_2, which are main compounds present in natural gas and syngas, are described by the following reactions,

$$4Me_xO_y + CH_4 \rightarrow 4Me_xO_{y-1} + CO_2 + H_2O \quad \text{(R2)}$$

$$Me_xO_y + CH_4 \rightarrow 4Me_xO_{y-1} + CO + 2H_2 \quad \text{(R3)}$$

$$Me_xO_y + CO \rightarrow Me_xO_{y-1} + CO_2 \quad \text{(R4)}$$

$$Me_xO_y + H_2 \rightarrow Me_xO_{y-1} + H_2O \quad \text{(R5)}$$

Other reactions that take place simultaneously with R2-R5 in the Reducer are gas phase reactions and heterogeneous reactions catalyzed by the reduced metal. For Ni-based oxygen carriers, the methane reforming reactions (R6-R8) play a significant role in the conversion of CH_4 [40,73,121]. The water gas shift reaction (R9) is also considered to take place in the presence of CO_2, H_2O, CO and H_2 [122,123]. Carbon formation reactions can also occur, in the presence of CH_4 (R10) or CO (R11). The solid carbon

can be removed *via* gasification with H_2O or CO_2 [124] or the lattice oxygen reaction (R13) [125]. If R11-R13 are faster than carbon generation, then carbon deposition is not observed.

$CH_4 + H_2O \leftrightarrow CO + 3H_2$ (R6)

$CH_4 + 2H_2O \leftrightarrow CO_2 + 4H_2$ (R7)

$CH_4 + CO_2 \leftrightarrow 2CO + 2H_2$ (R8)

$CO + H_2O \leftrightarrow CO_2 + H_2$ (R9)

$CH_4 \leftrightarrow C + 2H_2$ (R10)

$2CO \leftrightarrow C + CO_2$ (R11)

$C + H_2O \leftrightarrow CO + H_2$ (R12)

$Me_xO_y + C \leftrightarrow Me_xO_{y-1} + CO$ (R13)

Thus, various reaction pathways exist for the reduction of the oxygen carrier by CH_4 fuel, to generate a mixture of CO_2, H_2O, CO, H_2, and C. Most studies do not consider all of the aforementioned reduction reactions in their analysis, by neglecting certain reactions whose products are not observed. The kinetics of the metal oxide reduction reactions can differ widely, depending on the reducing fuel and metal oxide, preparation method, and conditions and duration of testing [42,49,57,114,115,126–128].

Reaction schemes had been proposed to take into account the metal-support interaction. Dueso et al. [114] proposed the following reaction scheme for the reduction of $NiAl_2O_4$ spinel:

$CH_4 + 4NiAl_2O_4 \rightarrow CO_2 + 2H_2O + 4Ni + 4Al_2O_3$ (R14)

$H_2 + NiAl_2O_4 \rightarrow H_2O + Ni + Al_2O_3$ (R15)

$CO + NiAl_2O_4 \rightarrow CO_2 + Ni + Al_2O_3$ (R16)

It was postulated that the formation of $NiAl_2O_4$ spinel occurred through the oxidation of metallic Ni to NiO, which then reacts with the Al_2O_3 support to form $NiAl_2O_4$:

$Ni + ½O_2 \rightarrow NiO$ (R17)

$NiO + Al_2O_3 \rightarrow NiAl_2O_4$ (R18)

Corbella et al. [86,87] proposed the following reaction scheme for the reduction and oxidation of $NiTiO_3$:

$4NiOTiO_3 + 3/2\ CH_4 \rightarrow 4\ Ni + 2Ti_2O_3 + 3/2\ CO_2 + 3H_2O$ (R19)

$Ni + ½\ Ti_2O_3 + 3/2\ O_2 \rightarrow NiTiO_2$ (R20)

The importance of the metal-support reaction rates on the overall reduction behavior depends on the relative amounts of the spinel and free metal oxide present in the oxygen carrier. In the study of Corbella et al. [87], the contribution by the $NiTiO_3$ to the reduction behavior was significant, due to the minor presence of the NiO phase. However, Dueso et al. [114] found that the effect of the $NiAl_2O_4$ phase was minor for the α-Al_2O_3-supported oxygen carriers and significant for the γ-Al_2O_3-supported oxygen carriers.

2.3.2. Reaction models

The solid conversion is often described as:

$$\frac{dX}{dt} = k(T) f(X) g(C_i) \ , \tag{2.1}$$

where X is the oxygen carrier conversion, $f(X)$ represents the structural changes as a function of the solid conversion, C_i is the gas concentration of the reacting species, g captures the effect of the gas concentration on reactivity, and k is the kinetic rate constant represented by the Arrhenius equation, as shown below:

$$k = k_0 e^{-E_a/RT} \ , \tag{2.2}$$

where k_0 is the pre-exponential factor, T is the temperature, R is the ideal gas law constant, and E_a is the activation energy.

There is no general consensus within the CLC literature to a single reaction mechanism that governs the CLC reduction and oxidation reactions for all the oxygen carriers. Thus, various forms of $f(X)$ were developed and used to predict the conversion profiles for the studied oxygen carriers. The most frequently used kinetic models for the non-catalytic reactions are: the reaction order model (Eq.(2.3)), the shrinking core model (Eq.(2.4)), and the nucleation model (Eq.(2.5)):

$$f(X) = (1 - X)^n , \tag{2.3}$$

$$f(X) = 3(1 - X)^{2/3} \ , \tag{2.4}$$

$$f(X) = n(1-X)[-\ln(1-X)]^{(n-1)/n}, \tag{2.5}$$

where *n* denotes the exponential terms of the respective mechanistic models. The reaction order-based models, including the volumetric model, assume a homogeneous reaction taking place within the particle. The shrinking core model is characterized by a clearly defined interphase of reaction in the grain [129]. The nucleation model, or also called Avrami-Erofe'ev model, assumes that the gas-solid reactions proceed by nucleation (nuclei formation) and subsequent nuclei growth. Before nucleation, there is an induction period for the activation of the solid phase to form nuclei [52,130,131]. The induction time primarily depends on the gas-solid system and reaction temperature, affecting the value of the *n* parameter of Eq.(2.5). As the reaction continues, nucleation growth causes overlapping of nuclei and ingestion of nucleation sites. Detailed discussion on these mechanistic models and their applications are provided in Adanez. et al. [23], Hossain et al. [29] and Zhou et al. [132].

2.3.3. Reactor simulation

The gas-solid reactive flows in the CLC reactor are generally complex and coupled to the reaction kinetics, hydrodynamics, and inter-phase interaction. Models for the circulating CLC processes, such as the fluidized bed reactor and moving bed reactor, are complex, because of the need to consider the flow and distribution of the solid particles and the gas species in the reactor. To address the modeling intricacies for fluidized bed reactors, computational fluid dynamics (CFD) and macroscopic fluid dynamics approaches are commonly used. CFD models are based on the first principles of momentum, heat and mass transfer, and can be heavily computationally expensive when tasked to simulate full-scale fluidized bed reactors. In recent papers, CFD models were used to simulate bubbling or circulating fluidized bed reactors, and the authors reported that the fuel conversion can be hindered by large and fast bubbles passing through the reactor and the system is highly sensitive to the bubble phase [133–136]. Cold-flow models were developed using CFD codes to consider the fluid dynamics for the complete CLC system [137,138]. However, there are limited works using CFD to simulate the large-scale CLC units in the range of 10-150 kW_{th}.

Macroscopic models, on the other hand, are more suitable for reactor design purposes because of their lower computational demands, and thus are more practical for design and optimization studies. The macroscopic models rely on empirical equations to describe the distribution of the gas flow among the bubble and emulsion phases as well as the distribution of the solids concentration in the bed. Models based on the two-phase theory for bubbling fluidized bed beds have been successfully used to predict CLC experimental data [139,140]. Zhou et al. [141,142] developed a three-phase hydrodynamic model with mass, energy, and momentum balances and showed accurate predictions against experimental data, for various oxygen carriers and operating conditions reported in the literature. In the work of Zhou et al. [141], the effects of bubble size, mass transfer between bubble and emulsion phases, and entrainment in the freeboard region were all found to be significant to fuel combustion efficiency. To summarize, macroscopic models are promising alternatives to the CFD models, to assist in the design, scale-up and optimization of the CLC technology.

2.4. Process integration

To determine the potential efficiency of a CLC-based power plant, a number of literature studies proposed preliminary system designs using CLC and compared its efficiencies against the conventional CO_2 capture methods (described in Section 1.2). One of the most common designs is a combined cycle (CC) power plant with CLC, wherein CLC replaces the gas combustor. A simplified layout of the CLC-CC plant is shown in **Figure 2.2**. Entering air and fuel (natural gas) are pressurized to 10-20 bar and sent to the Reducer and Oxidizer, respectively. The flue gas from the Air Reactor is used to drive the gas turbine. The gas turbine exhaust is sent to a bottoming steam cycle for additional electrical generation. The flue gas from the Reducer can be utilized to preheat the fuel or sent to a secondary CO_2/steam gas turbine for energy recovery. Several variations of the CC design with CLC have been investigated; for example, some authors proposed the use the flue gas from the Reducer to drive the steam cycle [143,144] or linked with a recuperator to preheat the compressed air [145]. Naqvi compared the theoretical net plant

efficiencies for several CLC combined cycles against a reference CC plant without CO_2 capture and with post-combustion [12]. From their design analyses, the CC with CO_2 gas turbine and steam turbine offers the highest efficiency, while the performance of the other two (CC with recuperation and CC with Fuel Reactor flue gas to drive the steam cycle) are comparable. It is important to note that all the studied CLC cycles achieved higher net efficiencies than the conventional natural-gas fired CC with post combustion CO_2 capture by means of chemical absorption [12].

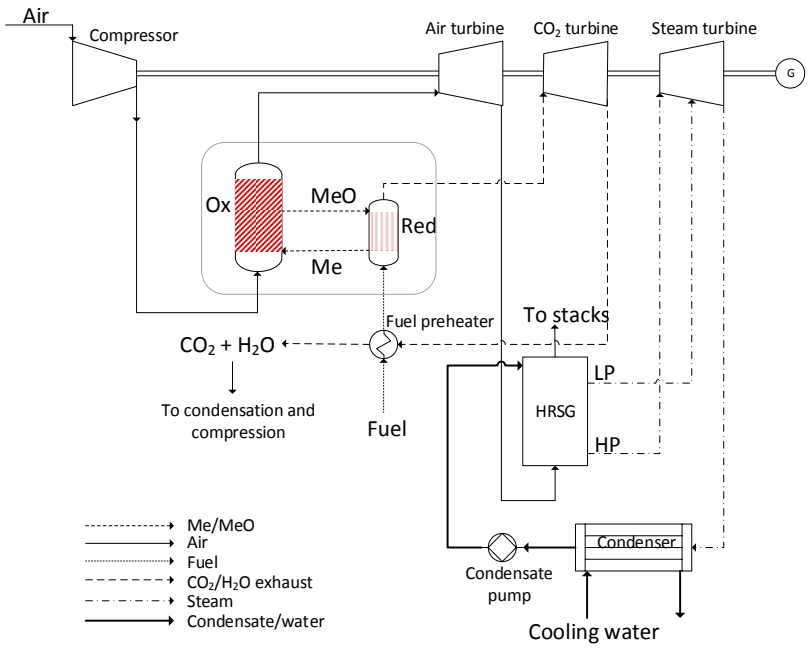

Figure 2.2: Diagram of a natural gas CLC-combined cycle (CLC-CLC) with a CO_2 turbine from Naqvi [12].

The efficiency of CLC-CC processes can be higher if the CLC reactor can operate at higher oxidation temperatures, to order to increase the efficiency of the downstream gas turbine. Modern day gas turbines can operate at turbine inlet temperatures of 1400°C or above, due to advancements in thermal barrier coatings, cooling technologies, and design configurations. For temperatures about 1000°C, the electrical efficiency of natural gas fired CLC plants is in the range of 47-53% [145,146]. It was estimated that for

every 100°C increase of the turbine inlet temperature (*TIT*), the net electrical efficiency increases by 2% points [145,146]. However, higher oxidation temperatures will increase the risk of agglomeration and reactivity loss for the oxygen carrier and also put demand on the reactor material to be stable at higher temperatures and pressures. Continuing research on novel oxygen carriers may broaden the operational window for CLC, and at the same time, specially designed reactors equipped with high-temperature resistant ceramics can be a feasible solution to increase the thermal stability of the reactor.

Options to increase the plant efficiency without increasing the oxidation temperature were proposed in several works. One alternative is to introduce reheat into the gas turbine by employing multiple CLC reactors [145]. Naqvi et al. [145] showed that a single reheat CLC-CC cycle with an oxidation temperature of 1000°C can achieve almost the same efficiency as the base-case CLC-CC plant with an oxidation temperature of 1200°C. Consonni et al. [144] proposed a post-firing step, to use a supplementary combustor placed between the exit of the Oxidizer and the gas turbine. The supplementary combustor takes a fraction of the fuel to combust the O_2 in the oxidation exhaust, in order to increase the inlet temperature of the gas turbine. The advantage of the firing step is that it allows the gas turbine to operate at higher efficiencies without affecting the CLC unit, but the disadvantage is the lower CO_2 capture efficiency. Lozza et al. [147] proposed a three-reactor concept, to exploit an intermediate oxidation state of FeO for H_2 production. The generated H_2 is used to raise the temperature of the gas stream out of the Oxidizer to values preferred by modern gas turbine technology (~1350°C), to achieve an electrical efficiency of 50.2-51.3%. This CLC layout was also proposed for hydrogen production in the work of Chiesa et al. [148].

To use coal as a primary fuel, the integrated gasification combined cycle (IGCC) with CLC was studied by Erlach et al. [149]. Their work considered pressurized reactors (20 bar) and assessed two different configurations for CO_2-rich stream cooling (expansion followed by steam generation and steam generation only). The analysis found that the net electrical efficiency increased by 1% point after increasing the oxidation temperature of the Oxidizer from 1200°C to 1300°C under optimized steam cycle

pressures. Rezvani et al. [150] proposed a dual-reactor configuration, where two CLC reactors, operated at 20 bar and at 7 bar, were able to achieve an efficiency of 36.1%, which is 1.6-1.9% points higher than the single reactor configuration (20 bar). Spallina et al. [151] performed a preliminary comparison of combined cycle and ultra-supercritical steam cycle for syngas-fed CLC. Their study found that the combined cycle plant achieves higher electrical efficiency (40% vs. 36.9%) for a maximum reactor temperature of 1200°C. Sorgenfrei and Tsatsaronis [152] proposed an IGCC power plant with iron-based syngas CLC and reported electrical efficiencies in the range of 39.7-44.8%. In summary, CLC has been revealed as a promising technology to decrease the cost of CO_2 capture in power generation.

2.5. Research objective

The objective of this thesis is to propose a novel process that delivers high efficiencies for CO_2 capture and power generation in a compact and scale-able reactor, utilizing highly reactive materials. Chemical-looping combustion (CLC) technology is explored due to its high potential for CO_2 remediation. Due to the novelty of CLC and the complexity of the multi-phase interactions, there is no general approach for reactor and/or process design from the current literature. Instead, common approaches are dictated from experimental observations or intuition and the results of the design analyses are heavily dependent on the oxygen carrier material and fuel. Furthermore, a lack of fundamental understanding of the intrinsic kinetics of the oxygen carrier materials and possible sub-optimal operating conditions hinder the deployment of CLC processes.

This thesis employs a structured methodology incorporating many facets of process systems engineering, in an effort to accelerate the technological development process. In the first step, modelling and simulation was integrated with bench-scale CLC experiments to understand the phenomenological changes inside the CLC reactor and identify sources of model uncertainty. Optimal experimental design techniques were used to determine statistically-rich kinetic networks and parameters. Large-scale CLC systems are simulated using the augmented process models with Maxwell-Stefan diffusion equations.

Emphasis is placed on optimizing the CLC plant performance, with respect to the CLC operation and reactor configuration. A dynamic optimization program was formulated to determine a set of control parameters that maximize the thermal efficiency of a large-scale CLC unit. After identifying the process bottlenecks, a novel reverse-flow reactor was proposed and proven theoretically and experimentally to improve the CO_2 capture-ability for any oxygen carrier and fuel-type. The reverse-flow reactor is an innovative method to provide efficient gas-solid contact with no particle attrition or gas/solid separations issues. A simulated moving bed reactor concept was proposed as an advanced version of the reverse-flow reactor. The reverse-flow and simulated moving bed reactors can be disruptive to future CLC research, by shifting attention to highly reactive oxygen carriers and more compact, scale-able reactor designs. These novelties produced and the conclusions drawn from this thesis were the result of applying process systems engineering principles to guide process design and optimization of CLC systems. The feasibility of this structured methodology is demonstrated, as a means to enable faster deployment of novel technologies.

Chapter 3 BENCH-SCALE EXPERIMENTATION

This chapter presents the experimental methods for oxygen carrier preparation, characterization, and reactivity studies conducted in a thermogravimetric analyzer and a bench-scale fixed bed reactor. The experimental results are simulated using different process models described in Chapters 4-5. The bench-scale experimental setup constitutes to the design space used to derive reduction kinetics in the model-based design of experiments section of Chapter 5.

3.1. Oxygen carrier preparation

NiO/Al_2O_3-SiO_2 oxygen carriers were prepared using the incipient wetness impregnation method. Commercial γ-Al_2O_3/SiO_2 particles (W.R. Grace & Co.) sieved to 50-150 μm in size, with a surface area of 157.8 m^2/g and mean pore size of 112.77 Å, were used as support. Aqueous $Ni(NO_3)_2$ was added to the γ-Al_2O_3/SiO_2 particles and the mixture was stirred at room temperature followed by drying at 120°C for 12 h and calcination in air at 800°C for 5 h. The apparent density of the particles was 1190 kg/m^3. The particle porosity was measured to be 0.45. The active (non-spinel) NiO loading in the oxygen carrier is measured to be 18 wt%, by oxidation in a thermogravimetric analyzer (TGA) after long-period reduction in H_2. The resulting oxygen carrier is then sieved to particle size of 50 – 150 μm, with BET surface area of 93 m^2/g for the fresh sample and ~68 m^2/g after TGA reduction/oxidation.

3.2. Characterization techniques

Identification of crystallite chemical species and crystallite size change was performed with *in-situ* hot-stage X-ray diffraction measurements, in a Bruker D8 Advance power XRD, equipped with a LynxEye-super speed detector and a high temperature Anton Paar HTK1200 heating stage. The experiments on the thermal evolution of the structure were carried out in the temperature range of 300 – 950 °C in air environment with constant flow rate of 50 sccm. The heating rate between target temperatures was

30 °C/min. The test starts at 300 °C with a step of 50 °C and 10-min holds before recording the X-ray patterns. The effect of calcination time was determined by taking two measurements of the same sample calcined at 950 ˚C for 10 min and 4 h, respectively. The recorded X-ray patterns were processed with standard background subtraction, peak match procedures and crystallite size calculation that are incorporated in the DIFFRAC.EVA program.

The pore properties and specific surface area of the oxygen carriers were determined in a Micrometitics ASAP 2020 Accelerated Surface Area and Porosimetry System. The pore size distribution was determined from adsorption/desorption of N_2 at 77 K with the Brunauer-Emmett-Teller (BET) method. All the samples were degassed at 250 °C for 12 h before analysis. Focused ion beam (FIB) scanning transmission microscopy electron microcopy (STEM) was used to identify the Ni distribution inside the particle of the fresh and used oxygen carriers.

3.3. Thermogravimetric analyzer (TGA) method

The reactivity of the oxygen carrier was measured in a NETZSCH STA 449 F3 Jupiter TGA. The sample (15 mg) was placed in the alumina crucible (3.8 mm in height and 5.95 mm in diameter) and heated at 10 °C/min up to the operating temperature in N_2 gas at atmospheric pressure. A thermocouple was continuously measuring the temperature of the gas phase directly adjacent to the crucible. The gas flow rate was kept constant at 240 sccm for the oxidation, reduction, and purge cycles. The Reynolds number of the flow across the crucible was 110. After the temperature reaches 950 °C, the flow was switched from N_2 gas to oxidizing and reducing gas. The reducing gas was composed of 4 vol.% H_2 (balance Ar) and the oxidizing gas was air. The TGA was purged with N_2 in between each oxidation and reduction cycles. In all isothermal experiments, temperature fluctuations of less than 2℃ were measured. The degree of conversion for reduction was calculated as:

$$X_{red} = \frac{m_{ox} - m}{m_{ox} - m_{red}} \tag{3.1}$$

where m is the instantaneous mass of the sample, m_{ox} is the mass of the fully oxidized sample, and m_{red} is the mass of the fully reduced sample.

3.4. Fixed bed reactor setup

Figure 3.1 shows the fixed bed experimental setup. In its designed operation, fuel (CH_4 or CO/H_2) and air (O_2/Ar) are sequentially fed to the reactor to simulate chemical-looping reduction and oxidation cycles. Inert gas (Ar) is fed between the cycles to isolate reduction and oxidation steps. The reactor temperature is controlled by a furnace and reaction products are measured with an online Agilent 5975C mass selective detector. The fixed bed is housed in a stainless steel tube (9.9 mm ID and 250 mm length), with a variable solid loading of 0.8-2.2 g. It is housed inside an electrical furnace capable of operating up to 1300°C, and can tolerate pressures up to 15 bars. Gas flow (Ar, CH_4, air) is controlled by mass flow controllers (MFC) and the reactor pressure is regulated by a back pressure regulator. At the start of the experiment, Ar flows through the reactor while the furnace reaches set-point. To initiate reduction, the gas flow is switched to a mixture of Ar and CH_4 (0-30 vol.% CH_4). After the reduction completes, Ar is used to purge the reactor for 5 minutes. The purge is followed by an oxidation period of 4 minutes, where gas flow is switched to air. After the oxidation step, the reactor is purged with Ar and the loop reinitiates. The experiment is repeated for multiple number of cycles to analyze the stability of the oxygen carrier. The gas flow rate is kept at 100 ml/min during the reduction, oxidation and purge periods. Typical reduction temperatures are in the range of 700-900°C. The sequential gas flow switch (CH_4/Ar → Ar → Air → Ar), is controlled automatically by the MFCs. In this configuration, 15 cycles are performed to ensure stability of the oxygen carrier reactivity. After stabilization, the experimental data from 3 consecutive cycles were used to calculate experimental variances and estimate kinetic parameters. For each experiment design, at least two independent experiments were performed, necessitating the experimental procedure to be repeated from a batch of newly synthesized oxygen carrier. The same batch of newly synthesized oxygen carriers was used for the reactivity tests. Thus, in summary every experimental measurement reported

here is the average of 6 repetitions with error bars in each plot showing the experimental standard deviation.

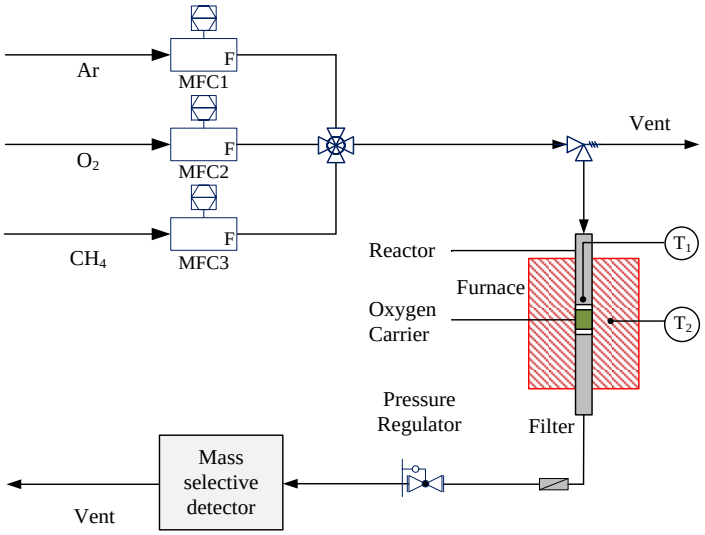

Figure 3.1: Fixed bed reactor experimental setup.

Chapter 4 HETEROGENEOUS MODELING OF CHEMICAL-LOOPING COMBUSTION: PART 1: REACTOR MODEL

Heterogeneous modeling is used to investigate the significance of intraparticle diffusion, temperature fluctuations, and dispersion on predicting fixed bed chemical-looping combustion (CLC) reactors. The model is validated against chemical-looping reduction experiments in the literature that utilize methane as fuel and a Ni-based oxygen carrier. The effect of particle size on CLC reduction reactions is studied by examination of the Weisz-Prater and Mears criteria for internal and external mass transfer limitations. Homogeneous and heterogeneous models are applied for two particle sizes and it is shown that diffusion limitations are significant for the larger particle. Furthermore, non-ideal flow patterns are evaluated where superior predictions are obtained by considering the effects of dispersion and convection processes. Radial dispersion in each experiment is analyzed in detail and the predicted temperature fluctuations inside the reactor and particle are presented. Lastly, the heterogeneous model is applied to design a particle that maximizes chemical-looping efficiency, measured as fuel conversion and product selectivity. Enhancements to the overall reaction rate and temperature profile are observed for the optimal particle size as a result of reducing the intraparticle resistance.

4.1. Introduction

Different mathematical models have been developed to simulate CLC systems. Ishida et al. [47] applied the un-reacted shrinking core model to interpret the experimental results on kinetics of the NiO mixed with yttria-stabilized zirconia (YSZ) particle. Comparison of model prediction with experimental results indicated that the reduction reaction was controlled by chemical reaction, while oxidation was controlled by both chemical reaction and ash-layer diffusion. Iliuta et al. [58] used an isothermal dynamic plug-flow model to estimate kinetic parameters that best fit their fixed bed micro-reactor. The gas-solid reaction parameters were then incorporated into a detailed hydrodynamic model to successfully model their fluidized-bed reactor. Sahir et al. [153] used the law of additive reaction times to approximate the gas-

solid reactions for analyzing the copper oxidation process. Ortiz et al. [118] studied the catalytic kinetics of steam methane reforming and water-gas-shift for NiO/α-Al_2O_3 and NiO/γ-Al_2O_3, and found that the activity increased with reduction of the oxygen carrier. Recently, Zhou et al. et al. [119] conducted a detailed kinetic analysis for the relevant oxygen carrier reduction reactions of NiO by CH_4 and Ni catalyzed reactions and validated the proposed kinetic scheme with different experimental results from literature.

Temperature variations inside the particle and reactor have been considered in numerical models [96,154–156]. Noorman et al. [154] proposed a detailed particle model which incorporated the effects of reaction kinetics, internal and external mass and heat transfer to study the reduction and oxidation characteristics of oxygen carriers. Modelling of the CuO/Cu system showed that internal mass transfer by was hindered by Knudsen diffusion for a range of pore sizes and instances where relatively large temperature differences can exist between the particle and the bulk gas [154]. A more accurate description of diffusion processes was obtained by applying Maxwell-Stefan diffusion, however Fickian diffusion can be reasonably applied in cases with simple dilute mixtures. Garcia-Labiano et al. [156] analyzed the reduction and oxidation characteristics of the major oxygen carriers based on Cu, Co, Fe, Mn, and Ni using a non-isothermal changing grain size particle model. The temperature changes inside the particle during the exothermic oxidation reactions depended on the particle size, overall reaction time, and the resistance to heat transfer in the external gas film, with the highest temperature variation corresponding to Ni for 1 mm particles [156].

Heterogeneous modelling can be applied to CLC processes to investigate the competing effects of fluid transport and chemical reactions occurring within a fixed-bed reactor. Oxygen carriers with particle size ranging from 0.08 to 2 mm have been used in the literature [157]. Larger particle sizes are advantageous in minimizing pressure drop across the reactor, but the effects of intraphase mass and heat transfer limitations can be significant. Noorman et al. [154] found that particles larger than 0.3 mm are severely diffusion-limited, which if neglected, models can lead to unreliable kinetic parameters. The role of

heterogeneous modeling can identify where the improvements to oxygen carrier performance are feasible in the regime of kinetic control or mass transfer control, thereby aiding oxygen carrier and reactor design. This work proposes a heterogeneous model that takes into account the effects of reaction kinetics in association with mass and heat transport in the particle phase, and convection, dispersion, and pressure drop in the bulk fluid phase. The effects of reaction and transport limitations on chemical-looping systems operating in fixed-bed reactors are analyzed based on published experimental results from three bench-scale fixed-bed reactors.

4.2. Model description

Flow in fixed bed reactors can be modelled by the motion of gaseous bulk fluid through the gaps between and within the oxygen carriers that constitute the solid phase [158]. Heat and mass transfer resistances can occur within the solid phase (intraparticle resistance) or between the solid and the bulk fluid (interfacial or interparticle resistance). Intraparticle resistance is related to the pore size and can be controlled by the dimensions of the oxygen carrier. Interfacial resistance is proportional to the thickness of the boundary layer at the gas-solid interface. The boundary layer can exhibit pronounced temperature gradients in cases of high heats of reaction that drive rapid changes in surface temperatures and concentrations. Though, this boundary layer effect can be damped by introducing higher gas flow rates and smaller packing sizes to induce mixing. According to the classification widely accepted in the chemical engineering society, the continuum models can be categorized into: pseudo-homogeneous and heterogeneous models [159]. In pseudo-homogeneous models, the catalyst surface is assumed to be completely exposed to the bulk fluid conditions, such that any fluid-to-particle heat and mass transfer resistances can be neglected. In contrast, heterogeneous models account for transport resistances of heat and mass from bulk fluid phase to the particle phase and within the particle. In this section, one- and two-dimensional pseudo-homogeneous and heterogeneous models are presented. The models are general and can be applied to any chemical looping process for any oxygen carrier. In the simulations, the gas species considered are CH_4, CO, CO_2, H_2, H_2O,

and an inert (usually Ar) and the solid species considered are NiO, Ni, deposited carbon, and an inert (Al_2O_3). Sections 4.2.1 – 4.2.2 detail the continuum models and Section 4.2.3 the momentum balance equation. The following Sections (4.2.4-4.2.5) summarize the transport correlations, physical properties, and kinetic scheme chosen for this work.

4.2.1. Homogeneous model design equations

4.2.1.1. One-dimensional

The one-dimensional pseudo-homogeneous model describes the axial profiles of the bulk fluid concentration and temperature. The dynamic axially dispersed plug flow reactor model is:

$$\varepsilon_b \frac{\partial C_i}{\partial t} + \frac{\partial F_i}{\partial V} = \varepsilon_b \frac{\partial}{\partial z}\left(D_{ax,i} \frac{\partial C_i}{\partial z} \right) + \rho_b \sum R_i \ , \tag{4.1}$$

$$\varepsilon_b C_{p,f} C_T \frac{\partial T}{\partial t} + C_{p,f} F_T \frac{\partial T}{\partial V} = \varepsilon_b \frac{\partial}{\partial z}\left(\lambda_{ax} \frac{\partial T}{\partial z} \right) + \rho_b \sum \left(-\Delta H_i\right)(R_i) - 4\frac{U}{d_t}\left(T - T_w\right), \tag{4.2}$$

with Danckwerts boundary conditions, expressing continuity of fluxes at steady state:

$$\varepsilon_b D_{ax,i} \left.\frac{\partial C_i}{\partial z}\right|_{z=0} = \left(F_i\big|_{z=0} - y_{i,feed} F_{in} \right) / A_c, \tag{4.3}$$

$$\varepsilon_b \lambda_{ax} \left.\frac{\partial T}{\partial z}\right|_{z=0} = \left(T\big|_{z=0} - T_{in} \right) C_{p,f} F_T / A_c, \tag{4.4}$$

$$\left.\frac{\partial C_i}{\partial z}\right|_{z=L} = \left.\frac{\partial T}{\partial z}\right|_{z=L} = 0. \tag{4.5}$$

4.2.1.2. Two-dimensional

Advancing in complexity, the two-dimensional model takes into account radial diffusion of bulk fluid and temperature. Reaction rates along the reactor diameter can be affected by effective thermal diffusivity and conductive heat transfer at the wall, which are determined by flow characteristics. The two-dimensional pseudo-homogeneous model is:

$$\varepsilon_b \frac{\partial C_i}{\partial t} + \frac{\partial F_i}{\partial V} = \varepsilon_b \frac{\partial}{\partial z}\left(D_{ax,i} \frac{\partial C_i}{\partial z} \right) + \frac{\varepsilon_b}{r}\left(r D_{rad,i} \frac{\partial C_i}{\partial r} \right) + \rho_b \sum R_i, \tag{4.6}$$

$$\varepsilon_b C_{p,f} C_T \frac{\partial T}{\partial t} + C_{p,f} F_T \frac{\partial T}{\partial V} = \varepsilon_b \frac{\partial}{\partial z}\left(\lambda_{ax} \frac{\partial T}{\partial z}\right) + \frac{\varepsilon_b}{r}\left(r \lambda_{rad} \frac{\partial C_i}{\partial r}\right) + \rho_b \sum\left(-\Delta H_i\right)(R_i)\,, \qquad (4.7)$$

with boundary conditions at r = R and r = 0:

$$\left.\frac{\partial C_i}{\partial r}\right|_{r=0} = \left.\frac{\partial T}{\partial r}\right|_{r=0} = \left.\frac{\partial C_i}{\partial r}\right|_{r=R} = 0\,, \qquad (4.8)$$

$$\varepsilon_b \lambda_{rad} \left.\frac{\partial T}{\partial r}\right|_{r=R} = -h_w\left(T\big|_{r=R} - T_w\right), \qquad (4.9)$$

and at $z = L$ and $z = 0$ are consistent with Eqs.(4.3)-(4.5).

4.2.2. Heterogeneous model design equations

The presented pseudo-homogenous model is applicable supposing there is negligible difference between solid and fluid conditions and mild radial temperature and concentration profiles. In the event that interparticle differences are important, a heterogeneous model should be used in place of the pseudo-homogenous model. Furthermore, intraparticle resistance is considered because limitations to diffusive transport inside the pores can significantly limit the reaction rates inside large particles. The most important assumptions made are: (i) spherical or cylindrical oxygen carrier, (ii) constant volume of the particle, (iii) macroscopically uniform particle structure that is not affected by reaction, and (iv) uniform Ni distribution within the particle. Local variations in structure or composition are not taken into the account due to the absence of experimental data. The gas concentrations and temperature inside the pores of the particle are functions of oxygen carrier radial direction, r_c, and/or axial direction, z_c. It is also assumed that the gas at any position inside the particle is at the same temperature as the solid, and that the thermal conductivity of the gas phase is negligible compared to that of the solid. Below, the conservation equations corresponding to a spherical oxygen carrier are discussed. For cylindrical oxygen carriers, the particle phase equations are summarized in the **Appendix**. Note that the transport of fluid phase is unspecific to particle geometry.

4.2.2.1. One-dimensional

The one-dimensional heterogeneous model for the fluid phase is:

$$\varepsilon_b \frac{\partial C_i}{\partial t} + \frac{\partial F_i}{\partial V} = \varepsilon_b \frac{\partial}{\partial z}\left(D_{ax,i} \frac{\partial C_i}{\partial z} \right) + k_{c,i} a_v \left(C_{c,i}\,|_{R_p} - C_i \right), \tag{4.10}$$

$$\varepsilon_b C_{p,f} C_T \frac{\partial T}{\partial t} + C_{p,f} F_T \frac{\partial T}{\partial V} = \varepsilon_b \frac{\partial}{\partial z}\left(\lambda_{ax} \frac{\partial T}{\partial z} \right) + h_f a_v \left(T_c\,|_{R_p} - T \right), \tag{4.11}$$

and for the particle phase is:

$$\varepsilon_c \frac{\partial C_{c,i}}{\partial t} = \frac{1}{r_c^{\,2}} \frac{\partial}{\partial r_c}\left(D_{e,i} r_c^{\,2} \frac{\partial C_{c,i}}{\partial r_c} \right) + \rho_s \sum R_i \,, \tag{4.12}$$

$$\left(\left(1-\varepsilon_c\right) \rho_s C_{p,s} + \varepsilon_c C_{p,c} C_{T,c} \right) \frac{\partial T_c}{\partial t} = \frac{\lambda_s}{r_c^{\,2}} \frac{\partial}{\partial r}\left(r_c^{\,2} \frac{\partial T_c}{\partial r_c} \right) + \rho_s \sum \left(-\Delta H_i\right)\left(R_i\right). \tag{4.13}$$

The boundary conditions for the particle phase are:

$$\left. \frac{\partial C_{c,i}}{\partial r_c} \right|_{r_c=0} = \left. \frac{\partial T_c}{\partial r_c} \right|_{r_c=0} = 0 \,, \tag{4.14}$$

$$-D_{e,i} \left(\frac{\partial C_{s,i}}{\partial r} \right)\Bigg|_{r_c=R_p} = k_{c,i} \left(C_{c,i}\Big|_{r_c=R_p} - C_i \right), \tag{4.15}$$

$$-\lambda_s \left(\frac{\partial T_s}{\partial r} \right)\Bigg|_{r_c=R_p} = h_f \left(T_s\Big|_{r_c=R_p} - T \right), \tag{4.16}$$

and for the fluid phase the boundary conditions are equivalent to the one-dimensional homogeneous model, Eqs.(4.3)-(4.5).

4.2.2.2. Two-dimensional

The two-dimensional heterogeneous model includes radial dispersion in the fluid phase. The design equations for the fluid phase are:

$$\varepsilon_b \frac{\partial C_i}{\partial t} + \frac{\partial F_i}{\partial V} = \varepsilon_b \frac{\partial}{\partial z}\left(D_{ax,i} \frac{\partial C_i}{\partial z} \right) + \frac{\varepsilon_b}{r}\left(r D_{rad,i} \frac{\partial C_i}{\partial r} \right) + k_{c,i} a_v \left(C_{c,i}\,|_{R_p} - C_i \right), \tag{4.17}$$

$$\varepsilon_b C_{p,f} C_T \frac{\partial T}{\partial t} + C_{p,f} F_T \frac{\partial T}{\partial V} = \varepsilon_b \frac{\partial}{\partial z}\left(\lambda_{ax} \frac{\partial T}{\partial z} \right) + \frac{\varepsilon_b}{r}\left(r \lambda_{rad} \frac{\partial C_i}{\partial r} \right) + h_f a_v \left(T_c\,|_{R_p} - T \right), \tag{4.18}$$

and for the particle phase are:

$$\varepsilon_c \frac{\partial C_{c,i}}{\partial t} = \frac{1}{r_c^2} \frac{\partial}{\partial r_c} \left(D_{e,i} r_c^2 \frac{\partial C_{c,i}}{\partial r_c} \right) + \rho_s \sum R_i \ , \tag{4.19}$$

$$\left(\left(1-\varepsilon_c\right) \rho_s C_{p,s} + \varepsilon_c C_{p,c} C_{T,c} \right) \frac{\partial T_c}{\partial t} = \frac{\lambda_s}{r_c^2} \frac{\partial}{\partial r} \left(r_c^2 \frac{\partial T_c}{\partial r_c} \right) + \rho_s \sum \left(-\Delta H_i\right)(R_i) \ , \tag{4.20}$$

with Eqs.(4.14)-(4.16) as boundary conditions for the solid phase and Eqs.(4.8)-(4.9) and Eqs.(4.3)-(4.5) for the bulk phase.

4.2.3. Momentum balance

The momentum balance assumes pseudo-steady state and is dominated by the friction factor. The pressure drop correlation using the Ergun friction factor for gas flow through a packed tubular reactor is written as [160]:

$$\frac{dP}{dz} = -\left(\frac{1-\varepsilon_b}{\varepsilon_b^3} \right) \left(\frac{\rho u_0^2}{D_p} \right) \left(\frac{150}{Re_p} + 1.75 \right), \tag{4.21}$$

where P is the total pressure in the bed and Re_p is the particle Reynolds number, defined as:

$$Re_p = \frac{\rho u_0 d_p}{\left(1-\varepsilon_b\right)\mu} \ . \tag{4.22}$$

The boundary condition at the bed exit is applied to maintain the effluent stream leaving the reactor at atmospheric conditions:

$$P\big|_{z=L} = P_{out} . \tag{4.23}$$

4.2.4. Heat and mass transfer correlations

The effective axial coefficient can be estimated by [159]:

$$\frac{1}{Pe_a} = \frac{\varepsilon_b}{\tau Re_p Sc} + \frac{0.45}{\left(1 + \frac{7.3}{Re_p Sc} \right)}, \tag{4.24}$$

and the effective radial dispersion coefficient can be estimated by [161]:

$$\frac{1}{Pe_r} = \frac{0.38}{\left(Re_i Sc\right)^{0.80}} + \frac{0.08}{\left(1 + \frac{11.1}{Re_i Sc}\right)}. \tag{4.25}$$

In general, for gases with $Re_p > 1$, $Pe_r \approx 10$ and $Pe_a \approx 1$, and for gases with $Re_p < 1$, $Pe_r \approx Pe_a$ which approach 0.7 [162]. Dispersion is usually more dominant in the radial direction, and consequently very small radial variations of concentration can be expected in the reactor. However a high dependency of reaction rates on temperature can lead to pronounced differences between the one-dimensional and two-dimensional models.

The effective radial and axial thermal conductivity can be estimated by Eq.(4.26) and Eq.(4.27), respectively by Yagi and Wakao [163] and Yagi et al. for metal spheres [164]. The static contribution, λ_e^0, is assumed to be 0.01 W/m-K.

$$\frac{\lambda_{rad}}{\lambda_m} = 13 + 0.11 Pr\, Re_p, \tag{4.26}$$

$$\frac{\lambda_{ax}}{\lambda_m} = \frac{\lambda_e^0}{\lambda_m} + 0.7 Pr\, Re_p. \tag{4.27}$$

The wall heat transfer coefficient is calculated from [165]:

$$Nu = 2 + 1.1 Pr^{1/3} Re_p^{\,0.6}\ . \tag{4.28}$$

The bed heat transfer coefficient is calculated by [166]:

$$h_{bed} = \frac{4\lambda_{er}}{D/2}. \tag{4.29}$$

The resistances to the radial heat transfer in the bed and at the wall can be combined to define the overall heat transfer coefficient to be used in the one-dimensional models:

$$\frac{1}{U} = \frac{1}{h_{bed}} + \frac{1}{h_w}. \tag{4.30}$$

The mass and heat transfer coefficients are estimated as [167]:

$$k_{c,i} = 0.357 Re^{-0359} Sc^{-2/3} \left(\frac{G}{\rho \varepsilon_b} \right), \tag{4.31}$$

$$h_f = 1.37 \left(\frac{0.357}{\varepsilon_b} \right) \left(C_{p,f} G \right) Re^{-0359} Sc^{-2/3} \ . \tag{4.32}$$

The bed porosity for a spherical catalyst and surface area per unit volume are calculated by Eq.(4.33) [168] and Eq.(4.34) [169]:

$$\varepsilon_b = \frac{1.0}{\left(D_t / D_p \right)^2} + 0.375 \ , \tag{4.33}$$

$$a_v = 6 \left(1 - \varepsilon_b \right) / D_p \ . \tag{4.34}$$

The pore diameter of a cylindrical pore can be calculated by [167]:

$$r_p = \frac{\varepsilon_c}{S_g \rho_s}. \tag{4.35}$$

4.2.5. Kinetic scheme

The main reduction reactions in CLC of NiO with CH_4 fuel are shown in

Table 4.1 based on the work of Zhou et al. [119]. The reducing gases that are active in the oxygen carrier reduction reactions (R1-R4) comprise of CH_4, H_2, and CO. In the work by Zhou et al. [119] and Iliuta et al. [58], non-catalytic gas solid reactions have been analyzed using the shrinking core model and a modified volumetric model. Because the modified volumetric model has been found to improve the model predictions, the kinetics based on the modified volumetric model is used in this work. The kinetic expressions for the four NiO reduction reactions are shown below, where a_0 is the initial oxygen carrier surface area, X is the oxygen carrier conversion, k_{s1}-k_{s4} are the Arrhenius rate constant, and C denotes the concentration of the gas species and solid weight fraction of NiO and Ni.

Table 4.1: Reduction reactions using NiO oxygen carrier selected by Zhou et al. [119].

Oxygen carrier reduction reactions	Partial CH_4 oxidation	$CH_4+2NiO \rightarrow 2Ni+CO_2+2H_2$	(R1)
	H_2 oxidation	$H_2+NiO \rightarrow Ni+H_2O$	(R2)
	CO oxidation	$CO+NiO \rightarrow Ni+CO_2$	(R3)
	Partial CH_4 oxidation	$CH_4+NiO \rightarrow Ni+2H_2+CO$	(R4)
Reduction reactions catalyzed by Ni	Steam methane reforming	$CH_4+H_2O \leftrightarrow 3H_2+CO$	(R5)
	Water gas shift	$CO+H_2O \leftrightarrow H_2+CO_2$	(R6)
	Dry reforming	$CH_4+CO_2 \leftrightarrow 2CO+2H_2$	(R7)
	Methane decomposition	$CH_4 \leftrightarrow 2H_2+C$	(R8)
	Carbon gasification by steam	$C+H_2O \leftrightarrow CO+H_2$	(R9)
	Carbon gasification by CO_2	$C+CO_2 \leftrightarrow 2CO$	(R10)

$$r_1 = a_0 (1-X) k_1 C_{CH4} C_{NiO} C_{Ni}, \tag{4.36}$$

$$r_2 = a_0 (1-X) k_2 C_{H2} C_{NiO}, \tag{4.37}$$

$$r_3 = a_0 (1-X) k_3 C_{CO} C_{NiO}, \tag{4.38}$$

$$r_4 = a_0 (1-X) k_4 C_{CH4} C_{NiO} C_{Ni}. \tag{4.39}$$

The conversion rate for the oxygen carrier is written as,

$$dX / dt = (2r_1 + r_2 + r_3 + r_4) / C'_{NiO}, \tag{4.40}$$

The mass balance for Ni and NiO is (assuming no migration of the Ni particles):

$$dC_{NiO} / dt = C'_{NiO} (1-X) M_{NiO}, \tag{4.41}$$

$$dC_{Ni} / dt = C'_{NiO} (X). \tag{4.42}$$

For the Ni-based system, the catalytic gas-solid reactions are steam methane reforming (R5), water gas shift (R6), dry reforming (R7), methane decomposition (R8), and carbon gasification by steam (R9) and CO_2 (R10). Normally, the rates of NiO reduction reactions (R1-R4) are dominant initially when NiO is in excess, while the catalytic reactions become increasingly important as Ni is formed. The rate expressions chosen by Zhou et al. [119] are:

$$r_5 = \frac{k_5}{P_{H_2}^{2.5}} \left(P_{CH_4} P_{H_2O} - \frac{P_{H_2}^3 P_{CO}}{K_5} \right) / \left(1 + K_{CO,5} P_{CO} + K_{H_2,5} P_{H_2} + K_{CH_4,5} P_{CH_4} + K_{H_2O,5} P_{H_2O} / P_{H_2} \right)^2, \tag{4.43}$$

$$r_6 = \frac{k_6}{P_{H_2}}\left(P_{CO}P_{H_2O} - \frac{P_{H_2}P_{CO_2}}{K_6} \right) / \left(1 + K_{CO,5}P_{CO} + K_{H_2,5}P_{H_2} + K_{CH_4,5}P_{CH_4} + K_{H_2O,5}P_{H_2O}/P_{H_2}\right)^2, \quad (4.44)$$

$$r_7 = k_7 K_{CH_4,dr}\left(P_{CH_4}P_{CO_2} - \frac{P_{CO}^2 P_{H_2}^2}{K_7} \right) / \left(1 + K_{CH_4,7}P_{CH_4}\right), \quad (4.45)$$

$$r_8 = k_8 K_{CH_4,8}\left(P_{CH_4} - \frac{P_{H_2}^2}{K_8} \right) / \left(1 + \frac{P_{H_2}^{3/2}}{K_{H_2,8}} + K_{CH_4,8}P_{CH_4} \right)^2, \quad (4.46)$$

$$r_9 = \frac{k_9}{K_{H_2O,9}}\left(\frac{P_{H_2O}}{P_{H_2}} - \frac{P_{CO}}{K_9} \right) / \left(1 + K_{CH4,9}P_{CH_4} + \frac{P_{H_2O}}{P_{H_2}K_{H_2O,9}} + \frac{P_{H_2}^{3/2}}{K_{H_2,9}} \right)^2, \quad (4.47)$$

$$r_{10} = \frac{k_{10}}{K_{CO,10}K_{CO_2,10}}\left(\frac{P_{CO_2}}{P_{CO}} - \frac{P_{CO}}{K_{10}} \right) / \left(1 + K_{CO,10}P_{CO} + \frac{P_{CO_2}}{P_{CO}K_{CO,10}K_{CO_2,10}} \right)^2. \quad (4.48)$$

4.2.6. Integration strategy

The dynamic model was implemented and solved in the equation-based process modeling platform gPROMS 3.6.0 [170]. Finite difference method is used for the discretization of partial differential equations along the fixed-bed axial (N_z nodes) and radial (N_r nodes) direction, and along the solid radial and/or axial directions (N_{rc} and N_{zc} nodes). The number of species is denoted as N_s. A summary of independent variables can be found in **Tables 4.2-4.3.** In the proceeding sections, the results are presented and discussed.

Table 4.2: Summary of independent variables in the 1-D model for a spherical oxygen carrier.

Variable	*Unit*	*Description*	*Dimension*
C(z,i)	mol/m^3	Gas phase concentration of species *i*	N_z x N_s
F(z,i)	mol/s	Gas phase molar flow rate of species *i*	N_z x N_s
T(z)	K	Gas phase temperature	N_z
P(z)	bar	Gas phase pressure	N_z
C_c(z,r_c,i)	mol/m^3	Concentration of *i* in the gas inside the catalyst pores at *z*	N_z x N_{rc} x N_s
T_c(z,r_c)	K	Temperature of the catalyst at z	N_z x N_{rc}

Table 4.3: Summary of independent variables in the 2-D model for a spherical oxygen carrier.

Variable	*Unit*	*Description*	*Dimension*
C(z,r,i)	mol/m^3	Gas phase concentration of species *i*	N_z x N_r x N_s
F(z,r,i)	mol/s	Gas phase molar flow rate of species *i*	N_z x N_r x N_s
T(z,r)	K	Gas phase temperature	N_z x N_r
P(z,r)	bar	Gas phase pressure	N_z
C_c(z,r,r_c,i)	mol/m^3	Concentration of *i* in the gas inside the catalyst pores at *z*	N_z x N_r x N_{rc} x N_s
T_c(z,r,r_c)	K	Temperature of the catalyst at z	N_z x N_r x N_{rc}

4.3. Results and discussion

The developed pseudo-homogeneous and heterogeneous models are applied to published chemical-looping fixed-bed experiments. In Section 4.3.1, the model predictions are shown against the experimental data, where the differences in estimated kinetic parameters will be discussed based on the importance of various transport effects and the assumptions associated with the model. The effect of dispersion and radial temperature variations is analyzed for each discussed experiment in Sections 4.3.2-4.3.3. A detailed analysis for the effect of internal and external diffusion resistance on individual reaction rates is conducted in Section 4.3.4 using the Wesiz-Prater and Mears numbers. Lastly, in Section 4.3.5 the oxygen carrier properties are treated as variables in an optimization scheme to select an optimal oxygen carrier for CLR that maximizes CH_4 conversion and H_2 selectivity.

Table 4.4: Oxygen carrier physical properties and experimental conditions of chemical-looping fixed-bed units studied in this work.

	Iliuta et al. [58]	*Jin and Ishida* [171]	*Rydén, et al.* [172]
OC properties	NiO/Al_2O_3 (15 Ni wt.%) D_p = 140E-3 mm a_0=102 m^2/g e_b = 0.37 ρ_b = 1040 kg/m^3	$NiO/NiAl_2O_4$ (60 Ni wt.%) D_p = 4.0 mm; L_p = 1.5 mm a_0=10 m^2/g* e_b = 0.487 ρ_b = 995 kg/m^3	$NiO/MgAl_2O_4$ (60 Ni wt.%) D_p = 120E-3 mm a_0=2 m^2/g** ρ_b = 1000 kg/m^3
L_{bed} [mm]	7.65	250	5.659
$D_{reactor}$ [mm]	4	16	15
Q (ml/min)	100 (10 % CH_4 in Ar)	900 (H_2O/CH_4 = 2)	60 (25% CH_4 in Ar)
U [W/(m^{2}K)]	480 – 880	30 – 110	240 – 800
ρ [kg/m^3]	0.35 – 0.46	0.2 – 0.6	0.3 – 0.4

μ [1e5×Pa s]	5.8 – 6.2	2.9 – 5.1	5.3 – 6.2
Cp_f [J/(kg K)]	20 – 27	20 – 50	20 – 35
λ_m, λ_{ax}, λ_{rad} [1E2×W/(m K)]	4.9 – 9.1; 1.0 – 1.1; 63 – 118	4 – 17; 1.5 – 1.8; 52 – 200	5 – 16; 1.0; 63 – 210
D_{ax}, D_{rad}, D_e [1E5×m^2/s]	1 – 10; 8.0 – 64; 0.028 – 0.13	32 – 63; 15 – 50; 0.58 – 2.4	1.0 – 10; 3 – 20; 0.42 – 3.0
Re	0.42 – 0.52	6 – 10	0.018 – 0.021
Sc	0.17 – 1.8	0.2 – 2.3	0.2 – 3.2
Pe_a, Pe_r	0.63 – 5.4; 0.38 – 2.4	3 – 5; 8 – 12	0.02 – 0.4; 0.03 – 0.2
Pr [x1E2]	1.6 – 2.7	0.74 – 0.27	0.94 – 2.65
Sh	0.35 – 0.76	1.6 – 3.8	0.41 – 1.0

* Estimated from Table 3.17 from [173]; ** Estimated from [126]

The proposed models are applied to predict experimental results from Iliuta et al. [58], Jin and Ishida [171], and Rydén et al. [172], whose fixed-bed reactor designs and operating conditions are summarized in **Table 4.4**. These experiments utilize methane as the fuel and a Ni-based oxygen carrier supported over alumina, which is within the scope of the kinetic scheme. In general, the fixed-bed reactors are housed in an electrical furnace and operated at atmospheric conditions, although Jin and Ishida [171] also conducted high pressure experiments for Co-Ni/YSZ oxygen carriers. Iliuta et al. [58] and Rydén et al. [172] operated in chemical-looping combustion conditions at 900°C, while Jin and Ishida [171] operated in chemical-looping reforming conditions at 600°C.

Table 4.5: Estimated kinetic rate constants for the CLC data of Iliuta et al. [58] at 900°C.

Frequency factors	*1D homogeneous model*	*1D heterogeneous model*
k_1	1.63E-05	8.16E-06
k_2	2.29E-05	2.26E-05
k_3	1.42E-05	1.32E-05
k_4	2.29E-05	2.13E-05
k_5	3.54E-03	5.44E-03
k_6	1.64E-05	1.68E-05
k_7	5.41E-05	9.37E-05
k_8*	5.10E-05	6.07E-05
k_9	5.40E-07	5.40E-07
k_{10}	1.35E-04	1.07E-04

*$k_{CH4,8}$ is estimated in lieu of k_8.

The oxygen carrier properties varied in size, preparation, support material, surface area, and pore size. Surface area measurements for the oxygen carriers used by Jin and Ishida [171], and Rydén et al. [172] were unavailable so they were estimated from Fan [173] and Mendiara et al. [126], accordingly. In the experiment by Rydén et al. [172], ε_b was estimated from Eq.(4.33) to be approximately 0.4 and ρ_b was assumed to be 1000 kg/m^3. The porosity of all of the studied oxygen carriers (ε_c) was assumed to be 0.37. To match experimental data, dynamic parameter estimation is performed to fit the frequency factor of the kinetic rate constant of all the reactions. The model assumes a constant wall temperature (of the reported furnace setting), atmospheric pressure at the reactor outlet, uniform distribution of oxygen carrier particles inside the bed, and homogeneity of the oxygen carrier properties (including particle size, pore size, and surface area). Initially, inert gas is present inside the reactor, and then following $t = 0^+$, the reactant gas flows into the reactor to commence the chemical looping reduction reactions. The simulation is run until complete reduction of the oxygen carrier is achieved. By applying the models to various experiments, a wide range of space times and particle sizes was studied and various contributing effects of transport limitations and dispersion were analyzed. The estimated kinetic parameters are presented in **Tables 4.5-4.7**.

. **Table 4.6:** Estimated kinetic rate constants for the CLR data of Jin and Ishida [171] at 600°C.

Frequency factors	*2D homogeneous model*	*2D heterogeneous model*
k_1	1.46E-05	5.84E-06
k_2	4.38E-07	1.26E-07
k_3	2.05E-07	6.41E-07
k_4	1.61E-08	8.50E-08
k_5	4.70E-07	1.82E-06
k_6	8.56E-04	3.10E-02
k_7	7.35E-09	7.34E-06
k_8*	0.00E+00	1.62E-03
k_9	1.06E-08	8.71E-04
k_{10}	2.38E-04	1.96E-04

*$k_{CH4,8}$ is estimated in lieu of k_8.

Table 4.7: Estimated kinetic rate constants for the CLC data of Rydén et al. [172] at 900°C.

Rate constants	*1D homogeneous model*	*2D homogeneous model*
k_1	3.65E-04	3.39E-04
k_2	2.93E-05	2.89E-05
k_3	2.20E-05	3.21E-05
k_4	3.49E-06	3.60E-06
k_5	6.30E-04	5.58E-04
k_6	2.41E+01	2.41E+01
k_7	1.59E-04	1.59E-04
k_8*	1.14E-02	1.37E-02
k_9	5.56E-06	5.65E-06
k_{10}	1.92E-02	2.38E-02

*$k_{CH4,8}$ is estimated in lieu of k_8.

4.3.1. Effect of particle size on diffusion limitation

The importance of mass and transport resistance to inside the particle can be evaluated based on the particle size. Since nearly all of the active sites are located within the pore network, the diffusion of molecules plays a crucial role in the observed rate of reaction. Molecular diffusion cannot capture the internal transport alone because the mean-free path of the gases often exceeds the pore length of the typical solid catalyst. Noorman et al. [154] found Knudsen diffusion to be very relevant for chemical-looping oxygen carriers with micro- and meso-porosity. As a guideline, diffusional limitations can be neglected for particles below 0.2 mm in diameter [156]. For larger particles (D_p > 0.2 mm), there is an influence of both chemical reaction kinetics and internal diffusion that can be captured with detailed heterogeneous modeling. Two case studies are presented to analyze the effect of particle size on overall transport resistance and determination of kinetic parameters.

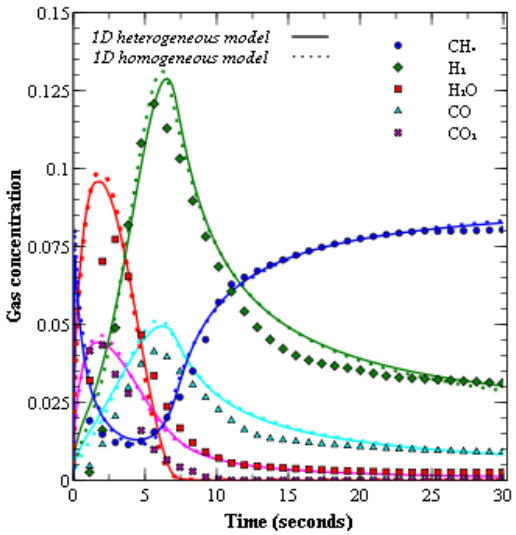

Figure 4.1: 1D model predictions of the experimental data reported by Iliuta et al. [58] at 900°C, 1 bar, and 10% CH_4 in Ar. CLC. Sum of squared errors for 1D homogeneous model is 9.7E-3 and for 1D heterogeneous model is 9.6E-3.

In the fixed bed experiment conducted by Iliuta et al. [58], the particle size was approximately 140 μm and thus, intraparticle and interfacial effects were neglected in their modeling approach. Here, the one-dimensional homogeneous and heterogeneous models are used to predict the exit concentrations from experiment. There is not a significant improvement from using a two-dimensional model to characterize this reactor because radial dispersion effects are minimal (discussed in Section 4.3.2). It can be seen in **Figure 4.1** that both models are capable of predicting the experimental data and hardly any differences can be observed between the two models. Thus, the quality of fit, expressed as the sum of squared errors, is relatively unchanged. The current modeling predictions are superior to the original fit published by Iliuta et al. [58] for the 900 °C fixed bed experiment (not shown here) because of the inclusion of energy balance, momentum balance, axial dispersion, and molar expansion in the design equations. The error in the H_2O prediction and experimental result, which is evident in the original fit and in **Figure 4.1**, can be explained by the calibration difficulty of H_2O on the mass spectrometer and the condensation of H_2O prior to the mass spectrometer [58].

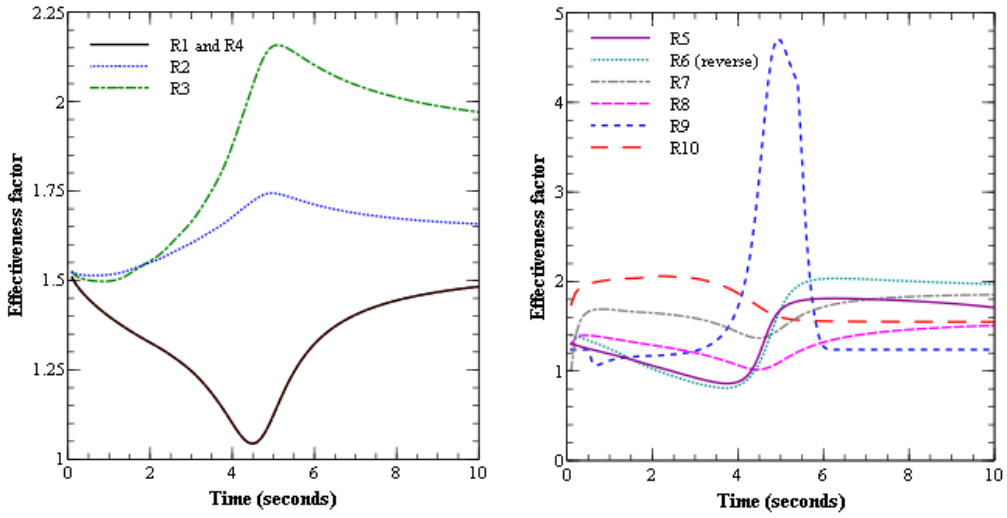

Figure 4.2: Effectiveness factors for R1-R10 from the 1D heterogeneous model for the fixed bed reactor reported by Iliuta et al. [58].

The effect of diffusional resistance on individual reaction rates is analyzed using the heterogeneous model. By virtue of the effectiveness factor, a quantitative measure can be obtained for the importance of diffusion to reaction limitations. Reactions that are limited by kinetics exhibit an internal effectiveness factor η approaching 1 and diffusion-limited cases observe $\eta \ll 1$. In non-isothermal conditions, values of η can be greater than 1 because the external surface temperature is less than the internal temperature of the solid where an exothermic reaction is taking place. **Figure 4.2** shows the variation of the effectiveness factor η with time in the reduction cycle. As expected from the small particle size, the reaction rates are essentially unaffected by diffusional limitations. R2 is the least diffusion-limited reaction among the NiO reduction reactions because of the high effective diffusivity of H_2. The effectiveness factors of R1 and R4 decrease to a minimum at t=4 seconds, while that of R2 and R3 see a maximum. This is attributed to the sensitivity of the reaction rates to the temperature drop inside the reactor (and particle), since R2 and R3 are exothermic and R1 and R4 are endothermic. The Ni-catalyzed reactions are kinetically-controlled because the calculated effectiveness factors are one or higher. The negligible effect of diffusional limitations inside the small particle supports the close agreement between

the homogeneous and heterogeneous simulations in terms of exit concentration profiles (**Figure 4.1**) and estimated kinetic parameters (**Table 4.5**).

In comparison, resistance to mass and heat transfer is important for large particles (D_p > 0.2 mm), where the local concentration and temperature inside the particle deviate from the surface. The model needs to distinguish between the fluid and solid phase to adequately account for the internal and external diffusion into the particle. The CLR fixed bed experiment conducted by Jin and Ishida [171], who prepared cylindrical-shaped oxygen carriers of 4.0 mm diameter and 1.5 mm length, is modeled using the developed heterogeneous and homogeneous models. Radial variations within the structure of the fixed-bed are accounted for in the two-dimensional models, described in Section 4.2.1.2 and 4.2.2.1. The bed of oxygen carriers is assumed to be uniform cylindrical pellets situated vertically and stacked in rotating layers to avoid gas by-pass. While the homogeneous model does not explicitly account the presence of the oxygen carrier, the heterogeneous particle model considers film resistance at the surface and internal diffusion along the axial and radial directions of the particle.

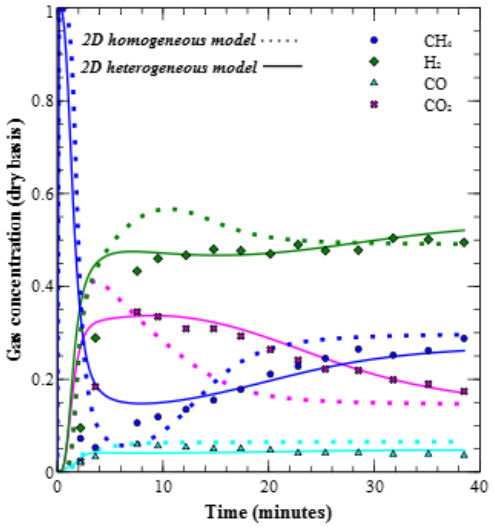

Figure 4.3: 2D model predictions of the experimental data reported by Jin and Ishida [171] at 600°C, 1 bar, and 33% CH_4 in H_2O. Sum of squared errors for 2D homogeneous model is 0.4082 and for 2D heterogeneous model is 0.2784.

Figure 4.3 shows the necessity of accounting for intraparticle and interfacial limitations to achieve accurate simulations and predictions. Compared to the homogeneous model, the heterogeneous model achieves over 30% improvement in quality of fit in terms of sum of squared errors, and noticeable improvements are seen in the CH_4, CO_2, and H_2 profiles. Large model-experimental deviations observed for the first two minutes can be explained by possible dilution of the exiting gas between the reactor exit and gas chromatographic-mass spectrometer (GC-MS), which is not included in the fixed-bed reactor model. The homogeneous model over-predicts the oxygen carrier conversion, which leads to higher-than-experimental H_2 and CO_2 concentrations.

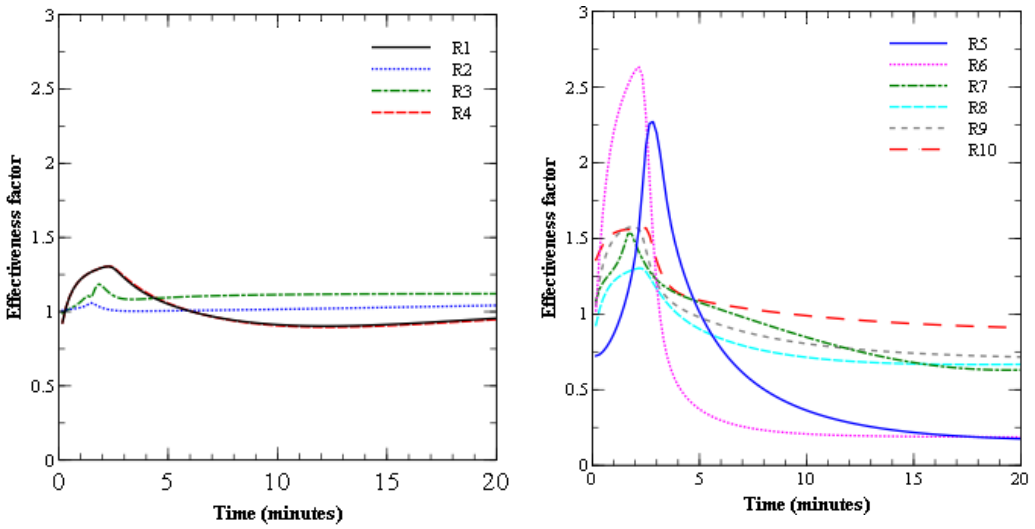

Figure 4.4: Effectiveness factor for R1-R10 from the heterogeneous model for the fixed bed reactor reported by Jin and Ishida [171].

The variation of effectiveness factor for all reactions with reduction time is shown in **Figure 4.4**. In the first five minutes, the rates are low due to methane activation, so transport within the particle is not the limiting factor and high effectiveness factors are observed. Beyond t=5 min, reaction rates are developed and conversion of the oxygen carrier begins. Effectiveness factors of the NiO reduction reactions remain relatively at one, indicating a high driving force for NiO reduction. However, diffusional limitations are

observed for the catalytic reactions for which effectiveness factors reach values less than one. This is related to the conversion of the solid NiO material to metallic Ni, which initiates at the external surface of the particle, and progresses toward the interior of the particle. Catalytic reaction rates are thus affected by the Ni concentration and tend to be highest on the surface, decreasing progressively along the interior. Local gas concentrations inside the particle are non-uniform and tend to approach equilibrium values moving away from the surface. When the reactions are close to equilibrium, the rates are sensitive to changes in local concentration gradients, and reverse reactions can be become favored. A likely cause for the rate reversal of R6 and R7 is attributed to the accumulation of combustion and reforming products (H_2, CO, CO_2) due to R1-R4 inside the particle that is re-directing the position of equilibrium reactions. Because of the strong particle effects, estimated rate constants vary significantly depending on the model, as shown in **Table 4.6.** The homogeneous model generally estimates lower kinetic rate constants because the model compensates for internal transport resistance by lowering the rates. This demonstrates that diffusion resistance cannot be neglected and a heterogeneous model is more realistic at predicting the experimental results.

4.3.2. Effect of particle dispersion

The presented models are developed to describe cases of non-ideal plug flow, whereby components are transported by bulk flow and convective diffusion (or dispersion). The CLC experiment performed by Rydén et al. [172] is representative of a system where there is significant contribution to transport by dispersion. The low Péclet number and even lower Reynolds number, shown in **Table 4.4**, point towards a mixed reactor. The importance of axial dispersion can be analyzed by noticeable differences in concentration profiles from the dispersive and non-dispersive models **(Figure 4.5)**. Dispersion serves to broaden concentration and temperature gradients and is important to characterize in the direction of bulk flow. In addition to its strongly dispersive flow, particle effects are negligible, owing to the small particle size (D_p = 120 μm) and large pore size. As shown in **Figure 4.5**, the homogeneous model has been able to adequately predict the experimental data. The heterogeneous model predictions are also satisfactory, but

the model does not bring added benefit in terms of quality of fit and thus need not be applied for estimation of kinetics.

The radial mass dispersion is very fast, so although the reactor diameter is comparably large, changes to the reaction rate due to temperature fluctuations across the radial direction are quickly recovered. Therefore, the two-dimensional model predictions do not deviate significantly from the one-dimensional model. The radial dispersion on reaction rates can be evaluated based on the estimated kinetic rates. As shown in

Table 4.7, the similarities between the two models further indicate that radial concentration gradients are not significant in this system. One note to mention is that the estimated value for k_6 is large, when compared to literature values. This may be caused by inaccuracy of the H_2O calculation by Rydén et al. [172] because only complete combustion of CH_4 was considered relevant in the beginning of the reduction cycle. However, this is not the case because NiO reduction proceeds through partial oxidation of CH_4 into CO and H_2 and inaccuracies in H_2O calculations largely impact the estimated kinetics of R6.

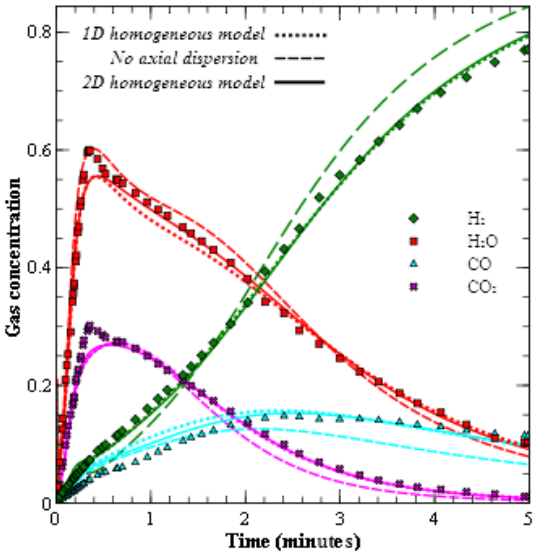

Figure 4.5: Homogeneous model predictions of the experimental data reported by Rydén et al. [172] at 900°C, 1 bar, and 25% CH_4 in Ar. Sum of squared errors for 1D homogeneous model is 0.2264 and for

2D homogeneous model is 0.2127.

4.3.3. Radial temperature variations

Detailed modeling of the temperature and conversion patterns in the fixed-bed necessitates inclusion of the resistance to heat and mass transfer in the radial direction of the fluid phase. Radial temperature gradients that arise from inadequate heat transfer can effectively alter reaction rates. In the experiment by Rydén et al. [172], temperature variations of around 40°C can be expected, in which the largest temperature decrease is exhibited at r=0. The solid phase temperature is equivalent to the bulk fluid, and from **Figure 4.6**, does not change inside the particle. Interfacial heat and mass exchange is much higher compared to the reaction rate because particle effects are not important in this system.

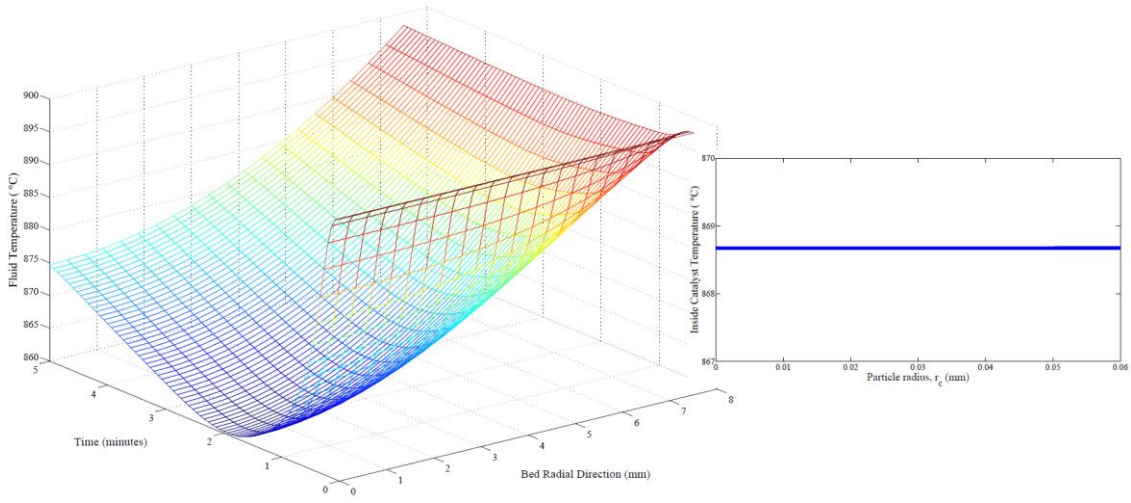

Figure 4.6: Radial fluid and solid temperature profile predicted by the 2D heterogeneous model for the experiment conducted by Rydén et al. [172]. Fluid temperature modeled at z=L/2, and solid temperature at z=L/2, r=R/2, t= 100 s. Chemical-looping combustion reduction at 900°C, 1 bar, and 25% CH_4 in Ar.

In the other previously discussed CL experiments by Jin and Ishida [171] and Iliuta et al. [58], the presence of dispersion in axial and radial directions is less significant. However, it is interesting to

explore if radial gradients occur. **Figure 4.7** shows the fluid and solid temperature profile prediction for the experiment conducted by Iliuta et al. [58]. The temperature drop inside the reactor reaches up to 45°C, while the radial temperature variation is at most 30°C. The reaction rates are not noticeably affected by the thermal gradients because of the small temperature fluctuation and small reactor diameter. Therefore, a one-dimensional model is suited to model this experiment. **Figure 4.7** also shows that the temperature inside the particle does not vary along the radius of the oxygen carrier, due to the high thermal conductivity of the solid. The difference between the temperature in the solid phase and the bulk fluid temperature is 3°C, which points to a negligible resistance for external heat transfer.

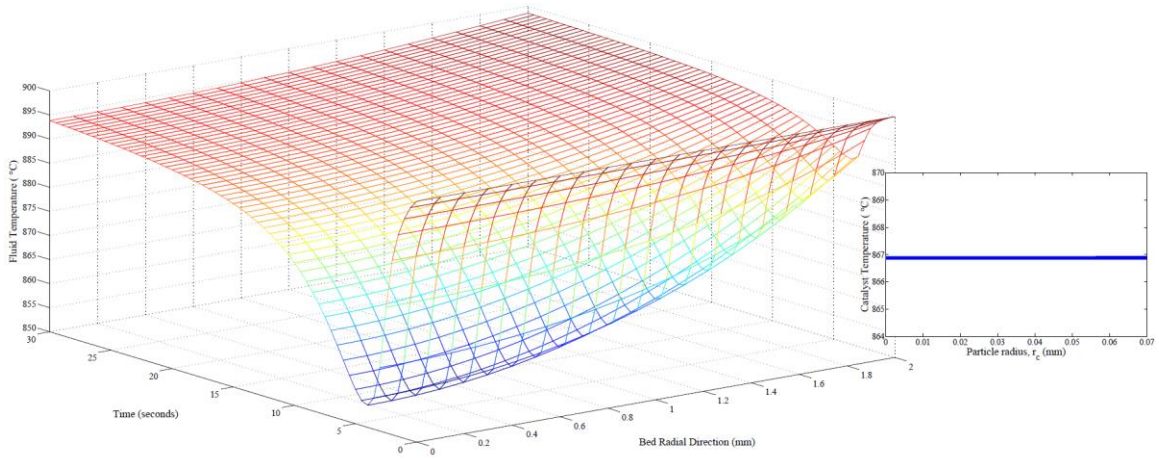

Figure 4.7: Radial fluid and solid temperature profile predicted by the 2D heterogeneous model for the experiment conducted by Iliuta et al. [58]. Fluid temperature modeled at z=L/2, and solid temperature at z=L/2, r=R/2, t=6 s. Chemical-looping combustion reduction at 900°C, 1 bar, and 10% CH_4 in Ar.

The radial temperature profile for the CLR experiment conducted by Jin and Ishida [171] is shown in **Figure 4.8** and predicts a temperature drop of 58°C in the reactor and 20°C along the radial direction of the bed due to insufficient heat transfer rate with the wall. The temperature inside the particle remains constant; however, the particle temperature can be 15°C colder than the bulk. This temperature difference

results from the interfacial heat transfer resistance which causes a lower temperature in the particle. Due to moderate thermal gradients and strong dependency of the reaction rates on temperature, model-model discrepancy between the one- and two-dimensional models is observed. Radial mass dispersion limitations arise in the Jin and Ishida [171] experiment because, even though the reactor diameters chosen by Jin and Ishida [171] and Rydén et al. [172] are comparable, the radial Péclet number is much larger than that observed for Rydén et al. [172] and contribute to a smaller dispersion rate, and thus lower heat transfer.

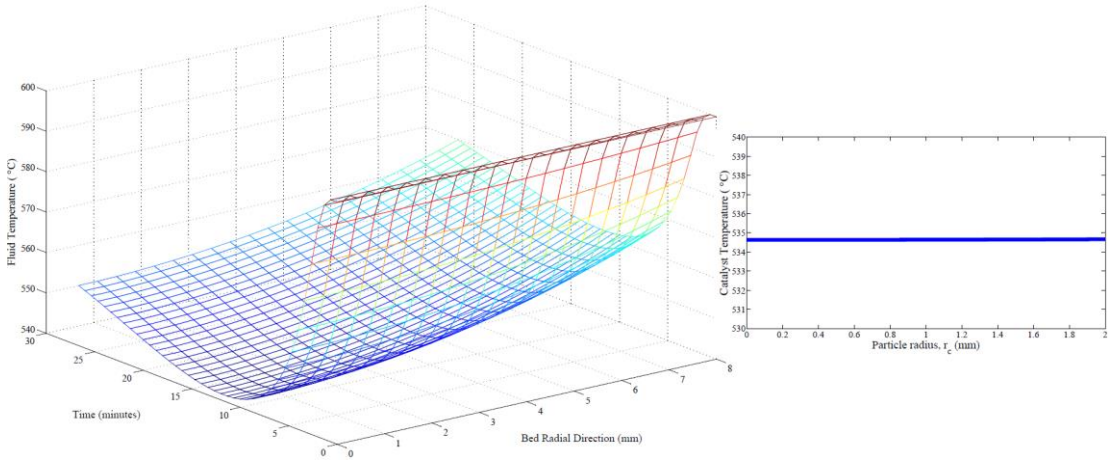

Figure 4.8: Radial fluid and particle temperature profile predicted by the 2D heterogeneous model for the experiment conducted by Jin and Ishida [171]. Results are reported at half bed height, and the solid temperature is at half reactor radius and 500 seconds. Chemical-looping combustion reforming at 600°C, 1 bar, and 33% CH_4 in H_2O.

4.3.4. Investigation of internal and external mass transport effects

In view of heat and mass transfer limitations, the experiment by Jin and Ishida [171] is well represented using the heterogeneous model. A lack of significant intraphase diffusion effects on an n^{th}-order irreversible reaction in a spherical catalyst pellet can be assessed by the Weisz-Prater criterion,

$$\frac{r_{obs}\,\rho_c\,a_l^2}{D_{e,i}\,C_i^S} < \frac{1}{n}, \tag{4.49}$$

where the observed rate, r_{obs}, and the concentration of the reactant at the external surface C_i^S are used [162]. This criterion has to be modified for a first-order reversible reaction and cylindrical particle,

$$\frac{r_{obs}\,\rho_c\,a_l^2}{D_{e,i}\left(C_i^S - C_i^{EQ}\right)} < 1, \tag{4.50}$$

where C_i^{EQ} is the concentration of the reactant if the reactor were at equilibrium and the coordinates for C_i^S are taken to be at the particle radius and mid-particle length.

The influence of mass transfer through the film surrounding a spherical catalyst particle can be examined using a similar expression. Satisfaction of the Mears criterion can be used to determine if interphase mass transfer is not significantly affecting the measured rate,

$$\frac{r_{obs}\,\rho_b\,a_l}{k_f C_i} < \frac{0.15}{n}, \tag{4.51}$$

in which case the observed reaction rate deviates less than 5% from the reaction calculated assuming a homogeneous mixture [169]. The Mears criterion can be modified for a reversible first-order reaction in a likewise manner to the Weisz-Prater criterion,

$$\frac{r_{obs}\,\rho_b\,a_l}{k_f\,(C_i - C_i^{EQ})} < 0.15. \tag{4.52}$$

Satisfaction of the Mears and Weisz-Prater criteria are determined for each reactant and corresponding reaction. Specifically, Eqs.(4.49) and (4.51) are used for R1-4 and Eqs.(4.50) and (4.52) for R5-R10 of

Table 4.1. The equilibrium concentrations are calculated from the equilibrium constants and the corresponding species concentration at the fluid or solid phase. The reaction rates of the forward reactions are integrated over the particle volume to give the observed rates.

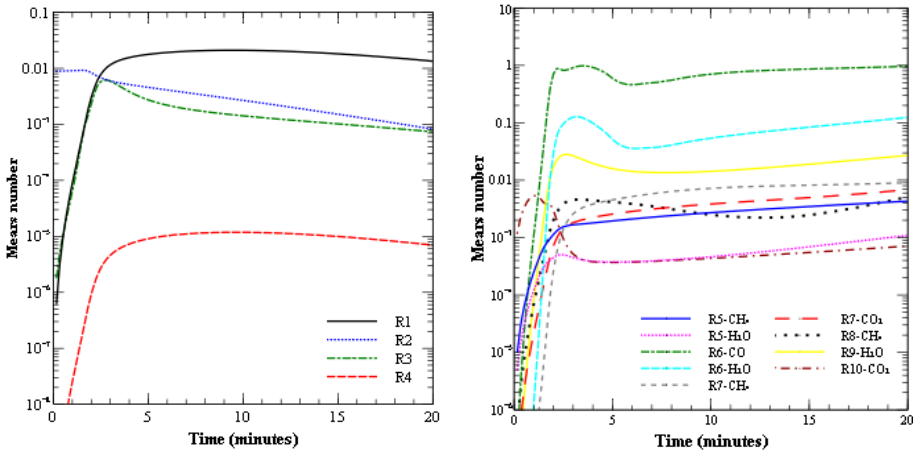

Figure 4.9: Mears numbers reported for R1-R4 (left) and R5-R7 (right). Reactions are assumed first order inside an isothermal particle. For reactions with two reactants, Mears numbers vary by reactant. Fixed bed unit operated by Jin and Ishida [171] is simulated using the heterogeneous model.

A common finding by investigators is that if mass interphase gradients occur, then mass intraparticle gradients would occur as well, which both have to be negligible to apply a homogeneous model [174]. The calculated Mears numbers for interphase concentration gradients for the experiment by Jin and Ishida [171] are shown in **Figure 4.9**. The observed rates for the methane conversion reactions are very slow during the onset of reduction, which explains the very small Mears numbers at $t < 2$ min. For the entire reduction period, negligible film transfer resistance is observed for all the reactions with the exception of CO consumed by R6. Mears numbers for R1-R4 generally decrease over time due to the decrease in reaction rates from NiO conversion. Because R4 is the least significant reaction among R1-R4 in terms of rate, Mears numbers reported for R4 are the smallest. In comparison, the catalytic reactions observe a

gradual increase in Mears numbers over reduction time, because the reaction rates show no tendency of diminishing while there are active catalytic surfaces (Ni), reforming fuel (CH_4), and oxygen sources (H_2O). The Mears numbers of R6 reveal that the reaction rate is high at the particle surface but limited by interphase transport of CO from the bulk, due to overall low concentrations and small gradients.

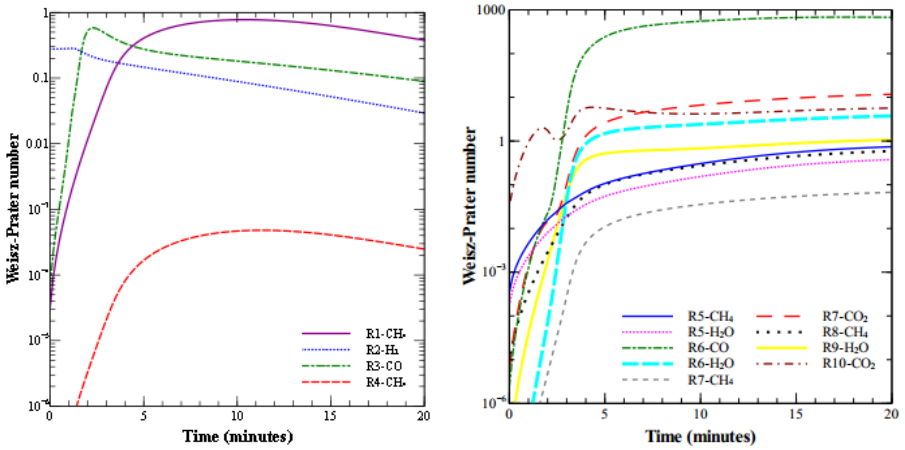

Figure 4.10: Wesiz-Prater numbers reported for R1-R4 (left) and R5-R10 (right). Reactions are assumed first order inside an isothermal particle. For reactions with two reactants, WP numbers vary by reactant. Fixed bed unit operated by Jin and Ishida [171] is simulated using the heterogeneous model.

In a similar analysis, the importance of internal diffusion limitations can be evaluated by fulfillment of the Wesiz-Prater criteria, as shown in **Figure 4.10**. A Wesiz-Prater number of greater than one indicates that the rate of reaction is much greater than the rate of diffusion, and that internal diffusion is limiting the overall reaction scheme. The rates of diffusion of CH_4, H_2, and H_2O through the pores are generally higher than the rates of CO and CO_2 due to higher effective diffusivities. Therefore, if internal transport resistance is significantly controlling a reaction, it is expected that the slower diffusing reactant will observe higher Wesiz-Prater numbers. By analysis of **Figure 4.10**, the NiO reduction reactions satisfy the Wesiz-Prater criteria, and a few catalytic reactions are limited by internal diffusion. The reaction most

affected by internal transport resistance is R6, with the diffusion rate of CO to be the most limiting. This finding is expected as film resistance is also detected from analysis of the Mears number. R6 is close to equilibrium inside the particle and thus is controlled by the slow rate of diffusion of CO through the particle. Other reactions that are limited by internal limitations are the CO_2 consuming reactions, R7 and R9, which exhibit slightly greater than one Wesiz-Prater numbers. This is likely due to a slow diffusion rate CO_2 leading to high concentration gradient and non-uniform reaction rates. As shown, the internal mass transport, as determined by the Wesiz-Prater number, plays a critical role on the reaction rates, as concentrations deviate much from the bulk.

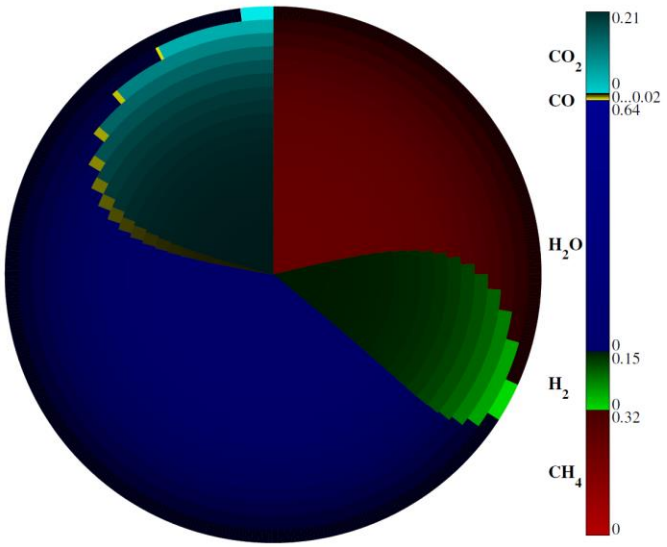

Figure 4.11: Radial variation of gas concentration inside the particle at $z_c=L_p/2$. At each r_c, concentration of species is denoted by the color bar where at the surface represents $r_c=R_p$ and the center represents $r_c=0$. Fixed bed unit operated by Jin and Ishida [171] is simulated using the heterogeneous model.

This analysis reveals the importance of internal and external mass transfer in chemical-looping reduction reactions. The former is primarily associated with the oxygen carrier properties, like particle size and pore size, and the latter to flow characteristics. To visualize the variation of solid concentration inside a

particle at any given time, the mole fraction of the gas is plotted with respect to the radius of the cylindrical particle (**Figure 4.11**). The arc length at each radial coordinate represents the fraction of each individual gas species inside the particle (excluding inert gas). For instance, at positions close to the inlet of the reactor, the surface concentration is mainly H_2O and CH_4 because of the direct transfer with the bulk fluid. Approaching $r_c \rightarrow 0$, the conversion of CH_4 and H_2O and corresponding production of H_2, CO, and CO_2 is depicted by the decreasing arc length of CH_4 and H_2O and increasing arc length for H_2, CO and CO_2. As discussed, intraparticle gradients arising large particle dimensions and slow diffusion rates lead to non-uniform reaction rates and departure from optimum performance. In the next section, the limits due to internal diffusion are explored through design optimization of the oxygen carrier geometry to meet chemical-looping standards.

4.3.5. Optimization of particle size

As an effective design tool, heterogeneous modeling can be used to determine an optimal oxygen carrier particle size for a fixed bed CLR system, in which CH_4 conversion and H_2 selectivity are maximized. The dynamic optimization problem is formulated in gPROMS in which keeping the experimental conditions used by Jin and Ishida [171], the initial particle size is set to the literature value and then bounded by +/- 10 times the initial value. The two-dimensional form of the process model outlined in Section 4.2 is used. The objective function to be maximized is defined for methane conversion, Eq.(4.53) and overall H_2 selectivity, Eq.(4.54), which are investigated separately. The diameter and length of the cylindrical pellet are treated as time-invariant variables to be optimized.

$$X_{CH_4} = \frac{F_{CH_4,in} - F_{CH_4,\text{out}}}{F_{CH_4,in}}, \tag{4.53}$$

$$S_{H_2} = \frac{F_{H_2,out}}{2F_{CH_4,\text{in}} + F_{H_2\text{O,in}}}. \tag{4.54}$$

Model results reveal that the reaction rates are highly sensitive to particle diameter, and insensitive to length. Transport resistance is mainly associated with radial diffusion within the particle due to good

mixing in the axial direction. Therefore, a range of particle lengths can be utilized without decreasing the oxygen carrier performance. A smaller particle diameter should be selected to limit the effect of internal transport resistance on reaction rates and increase CH_4 conversion and H_2 selectivity. A decrease from 4.0 mm to 0.8 mm in particle diameter brought significant changes, shown in **Figure 4.12**. The optimal particle size produces a 12% increase in CH_4 conversion and 7.7% increase in H_2 selectivity (

Table 4.8). Further decrease of D_p did not produce any measureable concentration differences, indicating a homogeneous reaction regime. Furthermore, overall improvements to the catalytic reaction rates are a result of reducing the diffusion barrier. The rate of methane conversion is enhanced and the overall reactions are more selective toward hydrogen production. Intraparticle concentration and temperature gradients are also minimized. The proposed particle size is realistic, does not create issues in experimental operation, and results in valuable benefits in the reactor performance. It is worth mentioning that after reducing the particle diameter, the pressure drop marginally increased from 0.0011 to 0.0086 bar. Close-to-isobaric conditions are maintained for this particular experimental apparatus; however, this should not be expected for a larger-scale commercial process.

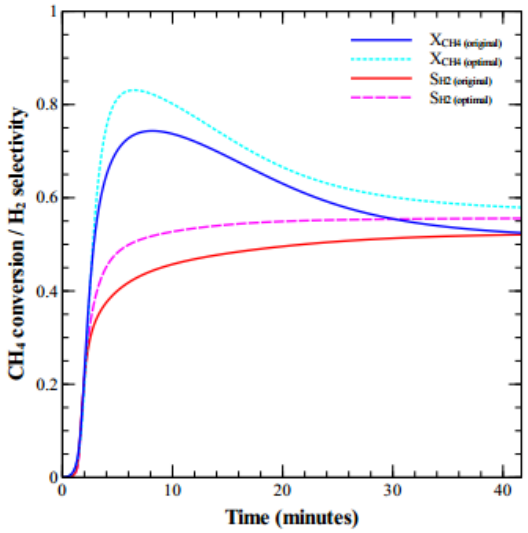

Figure 4.12: Heterogeneous model predictions for the effect of particle size on the CLR fixed bed experiment conducted by Jin and Ishida [171]. Solid lines represent the reference particle and dashed lines represent the optimal particle.

Table 4.8: Effect of particle size on X_{CH_4} and S_{H_2} for CLR fixed bed setup reported by Jin and Ishida [171] at 600°C.

	Length (mm)	*Diameter (mm)*	X_{CH_4}	S_{H_2}
Original	1.5	4	0.74	0.52
Optimal size	0.4 - 2.0	0.8	0.83	0.56

4.4. Conclusions

The dynamic behavior of a fixed-bed reactor for chemical-looping reduction is examined by a heterogeneous model, which is shown to agree very well with literature data, for a variety of Ni-based oxygen carriers, operating conditions, and reaction temperatures. As large particles are found to be affected by intra- and inter- diffusion limitations, more accurate predictions are obtained using the heterogeneous model. Differences between kinetic parameters estimated from the homogeneous model and the heterogeneous model are attributed to the extent of diffusion limitations in the experiments. For large oxygen carriers that are millimeters in size, diffusion limitations on some of the catalytic reactions are found to be severe. Furthermore, temperature fluctuations in the fixed-bed reactor are minimized by high rates of dispersion and small reactor scales. While intraparticle temperature gradients are found to be negligible for most cases, interphase heat exchange can be a limiting factor and should be accounted for in modeling. Application of the heterogeneous model is extended to optimize the particle size in order to improve chemical-looping performance. Through reduction of the particle diameter, diffusion-limited barriers are relaxed and as a result, CH_4 conversion and H_2 selectivity are enhanced. This reactor model, which combines particle and fluid effects, should enhance the design of chemical-looping in fixed-bed reactors and pave the way for feasibility analysis of the chemical-looping technology. In Part II of this work, a particle model will be used to analyze experiments performed in thermo-gravimetric analyzers. Physical and chemical changes incurring to the Ni-based oxygen carrier due to interaction with Al_2O_3 and from prolonged exposure to CLC conditions will be discussed.

Chapter 5 HETEROGENEOUS MODELING OF CHEMICAL-LOOPING COMBUSTION: PART 2: PARTICLE MODEL

The primary objective of this chapter is to showcase the ability of a particle model to predict the influence of varying particle properties on the reactivity of Ni-based oxygen carriers undergoing chemical-looping combustion (CLC). The particle model, which considers the effects of internal, interparticle and external diffusion limitations and reaction kinetics for NiO/Ni systems, is applied to reactivity investigations performed in the TGA. The reliability of the model to predict the observed reactivity responses to variations in particle size, microstructure, and chemical deactivation is analyzed in this work. Simulation results for a range of particle sizes reveal that the impact of intraparticle diffusion on reaction rates is accurately modeled. Furthermore, the effect of gradual changes in the particle microstructure due to redox cycling is analyzed through a sensitivity analysis of these physical and chemical changes. The framework of this analysis assumes that by incorporating these measured changes, it is possible to model the CLC performance over the lifespan of the oxygen carrier. Experimental data from the literature and performed in this work are utilized to demonstrate how the model can be utilized to gain a better understanding of the experiments. Simultaneously, the model can be implemented to be predictive of the changes in reactivity and selectivity as a function of time by manipulating the particle properties in accordance with experimental data.

5.1. Introduction

Research in CL is very active and largely focused on the development of suitable oxygen carriers, characterized by high rates of oxidation and reduction, high oxygen carrying capacity, high melting temperature, low tendency for attrition and fragmentation, low toxicity, and low cost [81]. Generally, oxygen carriers are formulated by depositing the active metal (Co, Cu, Fe, Ni, and Mn,) over an inert support, such as Al_2O_3, SiO_2, TiO_2, yttrium-stabilized zirconia (YSZ), and bentonite [57,175]. Dispersing the active metals offers advantages, such as improved particle stability, durability, fluidizability, and

surface area [176]. In particular, the Ni/Al_2O_3 materials demonstrate superior reactivity, high H_2 selectivity, resistance to agglomeration, and favorable fluidization properties [49,56,57,59–69,73,76]. The high melting temperatures of NiO (T=1955˚C) and Ni (T=1455˚C) allow for operation at higher working temperatures (900-1100˚C) than other oxides, such as CuO. Once reduced to metallic form, Ni catalyzes a series of reactions that are important in industrial applications, including reforming and partial oxidation of methane [54,55,177–181], partial oxidation of light paraffins [182], and methane cracking [183]. The products from the catalytic reactions are a mixture of syngas and solid carbon, which are adverse in CLC operation by reducing CO_2 selectivity and capture efficiency.

Table 5.1: Physical property changes of different oxygen carriers from continuous CLC operation.

Ref:	*Oxygen carrier*	*Size (μm)*	*Reactor*	*Temp. (°C)*	*Surface area (m^2/g)*		*Porosity*		*Density (kg/m^3)*	
					Fresh	Used	Fresh	Used	Fresh	Used
[71]	$NiO/NiAl_2O_4$	90-120	10 kW	750-900	0.4	0.7	0.36	0.53	3447	--
[80]	$NiO/NiAl_2O_4$	125-180	10 kW	750-900	0.75	1.4	--	--	3600	--
	$NiO/NiAl_2O_4/MgAl_2O_4$	125-180	10 kW	750-900	0.91	2.3	--	--	3250	--
[72]	$NiO/\gamma\text{-}Al_2O_3$	250-350	900 W	800-900	83	29	0.51	0.48	1700	1900
	$NiO/\alpha\text{-}Al_2O_3$	250-350	900 W	800-900	7.0	5.4	0.42	0.41	2400	2500

In performance testing of Ni/Al_2O_3 oxygen carriers, the reactivity and selectivity have been observed to deviate from that of the fresh materials (**Table 5.1**). In some cases, increasing surface area and pore size were attributed to Ni accumulation and formation of cracks and craters on the particle surface [37,73,80,184,185], leading to higher methane conversion and/or CO_2 selectivity. The chemical stability of the Ni-based oxygen carriers is another important parameter that needs to be preserved over multiple redox cycles. Interaction between NiO and Al_2O_3 forms $NiAl_2O_4$ spinel [70,71], which is very difficult to reduce and lowers the oxygen carrier reactivity [66]. Some authors proposed to use excess Ni [56,63], or

use $NiAl_2O_4$ as the support [60,62,65,66,73–76]. However, these approaches are not practical because Ni is highly toxic and expensive. Chemical additives, such as MgO and CaO, and thermal treatment of the Al_2O_3 have been shown to reduce the NiO-Al_2O_3 interaction [70,72,77–80,114,186,187].

In summary, the physical and chemical properties of Ni-based oxygen carriers are liable to change depending on the reactor and operating conditions. In this context, particle modeling can provide valuable insights in the investigations of oxygen carrier reactivity conducted in thermogravimetric analysis (TGA). The rate of oxygen carrier conversion is a function of the reaction scheme and the transport resistances around and within an oxygen carrier particle. A good understanding of these phenomena at the particle-scale is necessary for the adequate development of reactor models. The most frequently used kinetic models for CLC are the changing grain size model, shrinking core model, volumetric model, and nucleation and nuclei growth models [23]. García-Labiano et al. [156] applied the changing grain size model to simulate the mass and heat transfer resistances of Cu, Co, Fe, Mn, and Ni oxygen carriers. They observed that oxygen carriers can be considered isothermal and the intraparticle heat balance can be ignored to model the reactions. Noorman et al. [154] investigated the effect of diffusion limitations for a Cu-based oxygen carrier undergoing reduction by H_2 and CH_4. From their analysis, Knudsen diffusion is significantly limiting the reduction rate for particles larger than 1.0 mm in diameter.

In this work, the reactivity of Ni-based oxygen carriers measured from TGA is interpreted with a model to evaluate the effects of physical and chemical properties on observed rates. Unlike the aforementioned modeling studies, this work is experiment-driven and the results provide practical information about the underlying mechanisms affecting particle behavior. Section 5.3.1 introduces the experimental studies and the modeling approaches taken to simulate TGA results. Sections 5.3.2-5.3.4 use literature data to investigate the effects of particle size, number of redox cycles, and NiO-Al_2O_3 interaction in Ni-based systems. In Section 5.3.5, in-house TGA experiments with a Ni/Al_2O_3-SiO_2 oxygen carrier are studied. The variation of the reduction rates over redox cycles is presented, complemented by SEM, BET, and XRD characterization of the fresh and used particles. Modeling analysis is performed for every reduction

cycle, by taking into account the progressive physical and chemical changes accrued over each redox cycle.

5.2. Model description

In a typical TGA experiment, the sample is placed inside a crucible and a reducing agent flows across the mouth of the crucible at a fixed concentration and temperature (**Figure 5.1**). The fundamental mass transfer effects limiting the chemical reactions of TGA experiments can be categorized as (1) the transport of gas from the bulk TGA phase to the upper surface of the sample (external diffusion), (2) the diffusion of gas through the bed of particles (interparticle diffusion), and (3) the diffusion of gas within the pores of the particles (intraparticle diffusion) [188]. To reduce the extent of external diffusion limitations, a short and wide crucible can be used to limit the stagnant gas volume above the bed. High gas flows are commonly used to reduce external mass transfer resistance [114,189–191]. However, Gómez-Barea et al. [192] stated that this method cannot eliminate all external diffusion effects because if the sample lies partially below the crucible mouth, a stagnant gas region may still exist even at high gas flow rates. Secondly, interparticle mass transfer is related to the diffusion through the macrovoids surrounding the particles and is limiting for large bed heights. Lastly, interparticle mass transport effects can be prominent for large particles [193]. At the high working temperatures of CLC, the reaction rates are enhanced by fast kinetics but may be limited by the rate of gas diffusion through the porous particle.

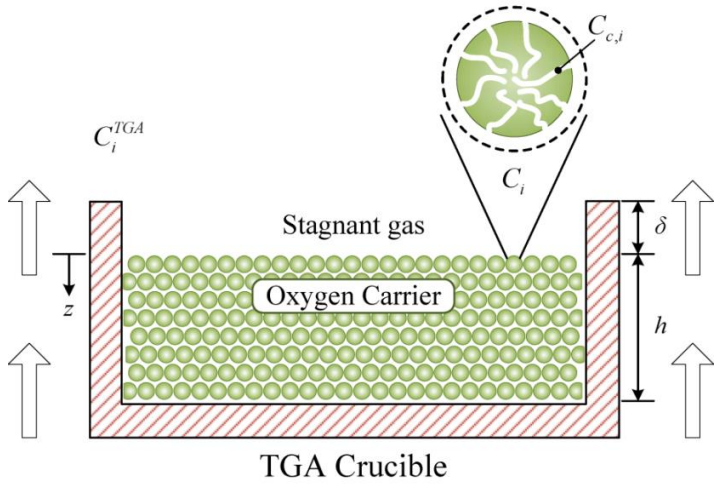

Figure 5.1: Gas concentration distribution in and around the crucible.

The present model is developed to simulate CLC experiments performed in the TGA crucible filled with oxygen carrier with a bed height of *h*. The height of the stagnant region above the sample, δ, is calculated by the difference between the height of the crucible and the calculated bed height from the mass of the sample and bulk porosity. The reactant gas flow is assumed a constant at the concentration of the TGA, C_i^{TGA}, and temperature fluctuations are neglected. This is valid because of the high convection inside the TGA. A two-phase model is used to describe the interactions between the crucible gas (C_i) and the particle gas ($C_{c,i}$). The transport of the crucible gas within the voids in the bed (ε_b) is controlled by axial dispersion and mass exchange with the particle gas. The conservation for the crucible gas is written as:

$$\varepsilon_b \frac{\partial C_i}{\partial t} = \varepsilon_b \frac{\partial}{\partial z}\left(D_{ax,i} \frac{\partial C_i}{\partial z} \right) + k_{c,i} a_v (C_{c,i}\big|_{r_c=r_p} - C_i) \,, \tag{5.1}$$

where ε_b is the bulk porosity of the TGA crucible, $D_{ax,i}$ is the axial diffusivity, $k_{c,i}$ is the mass transfer coefficient, and a_v is the external surface area per unit volume of the particle. Mass exchange between the main gas flow of the TGA, C_i^{TGA}, and the crucible gas occurs by external diffusion at z=0 across the boundary layer with thickness δ. At the base of the crucible (z=h), a zero flux condition is applied. The boundary conditions are:

$$\varepsilon_b D_{ax,i} \left(\frac{\partial C_i}{\partial z} \right)\Big|_{z=0} = \frac{D_{m,i}}{\delta} (C_i|_{z=0} - C_i^{TGA}), \tag{5.2}$$

$$\left(\frac{\partial C_i}{\partial z} \right)\Big|_{z=h} = 0. \tag{5.3}$$

The oxygen carrier is modeled as a homogeneous mixture of the solid phase with porosity ε_c filled by the gas phase. Structural changes in the particle during the course of reduction are not considered (unless otherwise mentioned). Moreover, the particle is modeled as isothermal, which has been demonstrated to be valid due to the high conductivity of the solid particle [193]. Viscous flow inside the particle is negligible and isobaric conditions are assumed. Mass transfer through the particle occurs by diffusion and convection. The diffusion flux is modeled by the Wilke-Bosanquet equation, which considers the contribution of molecular and Knudsen diffusion. Convective transport is induced by the non-equimolar stoichiometry of reaction which results in a net flow of gas molecules during chemical-looping reduction. The contribution of intraparticle convective transport is relevant for CH_4-NiO systems in which there is an increase in the number of gas molecules. The mass balance for the gaseous component inside a spherical oxygen carrier:

$$\varepsilon_c \frac{\partial C_{c,i}}{\partial t} + \frac{1}{r_c^2} \frac{\partial}{\partial r_c} \left(r_c^2 v_c C_{c,i} \right) = \frac{1}{r_c^2} \frac{\partial}{\partial r_c} \left(r_c^2 \frac{\partial}{\partial r_c} \left(D_{e,i} C_{c,i} \right) \right) + \rho_s \sum R_j \ . \tag{5.4}$$

The intraparticle velocity v_c can be determined from the continuity equation [194],

$$\frac{\partial v_c}{\partial r_c} = \frac{\sum_{j=1} R_j}{\sum_{i=1} C_{c,i}}. \tag{5.5}$$

The boundary conditions at the particle–bulk interface (r_c=R_p) are:

$$-D_{e,i} \left(\frac{\partial C_{c,i}}{\partial r} \right)\Big|_{r_c=R_p} + (v_c C_{c,i})\Big|_{r_c=R_p} = k_{c,i} \left(C_{c,i}\Big|_{r_c=R_p} - C_i \right). \tag{5.6}$$

At the particle center (r_c=0), the fluxes are zero:

$$\left.\frac{\partial C_{c,i}}{\partial r_c}\right|_{r_c=0} = v_c|_{r_c=0} = 0. \tag{5.7}$$

Convection inside the particle can be neglected for H_2-NiO systems because there is no molar expansion and hence the mass balance equations can be formulated based solely on the diffusive flux:

$$\varepsilon_c \frac{\partial C_{c,i}}{\partial t} = \frac{1}{r_c^2}\frac{\partial}{\partial r_c}\left(r_c^2 \frac{\partial}{\partial r_c}\left(D_{e,i} C_{c,i}\right)\right) + \rho_s \sum R_j \ , \tag{5.8}$$

with the following boundary conditions:

$$-D_{e,i}\left.\frac{\partial\left(C_{c,i}\right)}{\partial r_c}\right|_{r_c=R_p} = k_{c,i}(C_{c,i}|_{r_c=R_p} - C_i), \tag{5.9}$$

$$\left.\frac{\partial C_{c,i}}{\partial r_c}\right|_{r_c=0} = 0. \tag{5.10}$$

Recently, the kinetics of supported Ni-based oxygen carriers undergoing CLC with CH_4 as the reducing gas has been investigated in fixed bed and fluidized bed reactors [58,119]. The reaction scheme considers the NiO reduction by CH_4, H_2, and CO and a series of Ni-catalytic reactions following our previous work [119]. The conversion rate for NiO is expressed in terms of the sum of the NiO reduction reaction rates, $\sum R_j$:

$$dX_{NiO} / dt = \sum R_j / C'_{NiO}, \tag{5.11}$$

The integral of Eq.(5.11) over the particle volume and bed height is taken to be the solid conversion inside the TGA at any instance of time. A complete description of the mass transfer correlations, diffusion coefficients, and relevant physical properties used here are presented in the **Appendix**.

5.3. Results and discussion

5.3.1. Introduction to the experiments studied

The model is applied to published TGA experimental data utilizing Ni-based oxygen carriers, analyzing the effects of particle size (Section 5.3.2), microstructural changes (Section 5.3.3), and NiO-support

interaction (Section 5.3.4) on the rate of reduction. In Sections 5.3.1-5.3.2, the experimental data published by Ishida et al. [47], are modeled. In their work, five types of Ni/YSZ oxygen carriers were prepared using different methods and their reactivity towards H_2 reduction at 600°C was investigated in TGA. To be consistent with Ishida et al. [47] in notation, the oxygen carriers are referred to as 'A'-'D'. The reactivity of 'A'-'D' oxygen carriers was affected by the preparation procedure, thus different sets of kinetics and physical properties are used in this work to characterize the behaviors of each oxygen carrier. Their so-called 'D' particles is discussed and modeled in Section 5.3.2, with the objective of validating the mass diffusion model over a range of particle sizes. Furthermore, the 'E' particles were subject to performance testing and the model is used to correlate the variations in observed reactivity to possible changes occurring within the particle microstructure in Section 5.3.3.

Ishida et al. [47] minimized the effects of external diffusional limitations in their TGA experiments through the use of a pan crucible (5 mm-diameter) and large oxygen carriers (d_p=1.0-3.2 mm). By reducing the height of the crucible, the stagnant volume above the bed is reduced, which enhances the mass transport across the boundary layer. Interparticle diffusion is also fast because of the large voids that exist in between the large particles. Ishida et al. (1996) [47] observed a linear relationship between conversion and reducing gas concentration, which confirmed that the reduction rate was kinetically controlled (reaction rate is first order with respect to reducing gas according to Zhou et al. [119] and Iliuta et al. [58]). Thus in the absence of external and interparticle diffusion limitations, the particle model, as written in Eqs.(5.4)-(5.6), is sufficient to model their TGA experiments.

In Sections 5.3.4-5.3.5, the effect of NiO-support interaction on reactivity is studied for two Ni/Al_2O_3 systems. The model is extended to take into account $NiAl_2O_4$ which is simultaneously reduced with NiO in the presence of reducing gases. The kinetic model is validated against the TGA data published by de Diego et al. [72], utilizing α and γ-Al_2O_3 supports. Furthermore, the predictability of the model to capture the changes in reactivity is explored in Section 5.3.4 as a function of the reported differences in particle properties. Diffusion limitations around the crucible can be neglected in their experiments because of the

wire mesh sample holder (14 mm in diameter, 8 mm in height) and the high gas flow rate (25 nL/h). Dueso et al. [114] analyzed the effect of flow rate in the same TGA and found that when the flow was 20 nL/h or higher, there was no effect on the reaction rate. Furthermore the reactivity was unaffected by variations in the sample weight (30-70 mg) [114]. Thus, only particle equations are needed to model the TGA experiments by de Diego et al. [72].

In Section 5.3.5, an in-depth analysis is performed using a Ni/Al_2O_3-SiO_2 oxygen carrier over multiple redox cycles in the TGA. Fresh and used particles after each cycle are examined with scanning electron microscopy (SEM), powder X-ray diffraction (XRD), and Brunauer-Emmett-Teller (BET) surface area analysis by means of N_2 physisorption. With empirical evidence of the largest changes to the particle microstructure, the model is applied to predict the observed conversion profiles for each cycle spent in the TGA. Results from preliminary experiments using the fresh carriers revealed that the reactivity is affected by changes in the gas flow rate and initial sample weights. Due to operational constraints of our TGA, it is not possible to further increase the gas flow rate until no diffusion effects are observed. Thus, the complete model is used in order to take into account the resistances due to external, interparticle, and internal diffusion. The novelty of this work lies in the combination of experimental findings with modeling to develop a comprehensive understanding for the causes of reactivity changes in chemical-looping materials.

5.3.2. Effect of particle size

The effect of particle size was studied with TGA by Ishida et al. [47] under H_2 reduction at 600 °C using their 'D' Ni/YSZ oxygen carriers ranging in diameter from 1.0 to 3.2 mm. Ishida et al. [47] observed significant particle size effects and found that the NiO conversion rate was inversely proportional to the power of 1.1 of the particle diameter. The reaction rate is limited by the internal transport resistance of the gas phase to diffuse through the porous particle. A higher rate of reaction to internal diffusion leads to intraparticle variations in the H_2 partial pressure, which makes only a fraction of the surface area available to chemical reactions at any given time. The extent of diffusion limitations is more pronounced for larger

particle sizes, in which the time required for gases to diffuse to the active sites is longer.

Table 5.2: Model parameters for the reduction of Ni/YSZ oxygen carriers at 600°C in TGA under H_2 [47]. Particle 'D' was used to evaluate particle size effects and particle 'E' for the recycle tests. The kinetic rate constant (k_2) is lumped with the surface area, representing the NiO reduction reaction by H_2.

	k_2 [$m^3/s \cdot g$]	LL	UL	ε_c	ρ_c [kg/m^3]	d_p [mm]
Particles "D"	3.36E-04	2.31E-04	4.41E-04	0.4	4800	1.0-3.2
Particles "E"	5.90E-05	5.52E-05	6.28E-05	0.2	5400	1.4

LL, lower limit; UL upper limit of approximate 95% confidence interval.

In this work, the particle model is used to explore the dependency of oxygen carrier reactivity on the extent of intraparticle diffusional limitations. The reactivity data reported by Ishida et al. [47] for their 'D' oxygen carrier of one size is used to estimate model parameters, which are then applied to predict the reactivity of particles of different sizes, while keeping the kinetics and physical properties the same (with the exception of d_p). The particle porosity is assumed to be 0.4 for all sizes, which is reasonable for this type of support [62]. Reaction rate constants lumped with surface area k_j' $\left(k_j' = a_0 k_j\right)$ are estimated from the conversion data of the 1.8 mm-diameter particles (**Table 5.2**). Using the parameters from **Table 5.2**, the reactivity of the 'D' oxygen carrier (d_p=1.8 mm) can be well-represented by the particle model (**Figure 5.2**). Upon validation, the model is utilized to predict the rate of NiO reduction by H_2 encompassing the range of particle sizes experimentally measured by Ishida et al. [47] to explore if internal diffusion is correctly captured in the model and if it is the main reason for the differences in observed reactivity. **Figure 5.3** shows the comparison between experimental and model-predicted NiO conversion rates (dX_{NiO}/dt at X_{NiO} =0.5) as a function of the reciprocal of particle diameter ($1/d_p$). As shown, the model very accurately predicts the reduction behavior of the oxygen carriers for a wide range of particle sizes without any fitting. Furthermore, this analysis confirms the validity of the particle model to be applied to this TGA study. The effect of diminishing reactivity due to increasing particle size is

attributed to a combination of greater diffusion resistance inside the particle and interfacial mass transfer resistance with the surrounding gas [193].

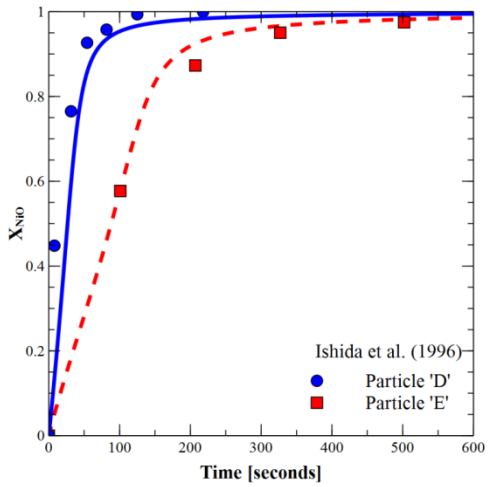

Figure 5.2:Model simulations (lines) of the TGA experimental data by Ishida et al. [47] (symbols). Ni/YSZ oxygen carriers (d_p=1.8 mm) of type 'D' and 'E' are reduced in H_2 at 600°C [47].

It is observed that reducing the particle size produces a dramatic improvement in the overall reaction rate. This effect can be quantified with an internal effectiveness factor written as:

$$\eta_j = \frac{3\int_0^{R_p} r_c^2 R_j dr_c}{r_p^3 R_j(r_p)}, \tag{5.12}$$

for a spherical particle. Under the assumption of isothermal conditions in the TGA, $\eta_j < 1$ indicates that the reactions are diffusion-limited and $\eta_j \approx 1$ indicates that the reactions are kinetically-controlled. Evaluating the data of Ishida et al. [47], internal effectiveness factors vary from 0.26 for the largest particle (d_p=3.2 mm) to 0.65 for the smallest particle (d_p=1.0 mm). While the extent of internal transport resistance is lowered using smaller particles, the overall rate is still controlled by a combination of chemical reaction and diffusion inside the particle. This is expected from observing **Figure 5.3**, where the conversion rate is still increasing and does not appear to stabilize as $d_p \rightarrow 1.0$ mm ($1/d_p \rightarrow 1000$ m^{-1}). Gas

concentration profiles inside the particle show that while X_{NiO} is low, H_2 is immediately consumed at the particle surface and does not diffuse very far into the particle. The rate at which NiO is reduced is hence limited by the rates of diffusion of H_2 and H_2O. Local variations in the reaction rate produce a clear conversion front that first appears at the particle surface and slowly moves toward the particle center. With this model, we arrive at a good understanding of the intraparticle mass transport mechanisms inside the oxygen carrier. Therefore, heterogeneous models provide a more realistic description than pseudo-homogeneous models out of consideration of the solid phase transport resistances [193]. As explained by Noorman et al. [154] and Pantoleontos et al. [195], if the effectiveness factors are known a priori, then it is possible to reduce the heterogeneous model to a pseudo-homogeneous model, however treating the effectiveness factor as a constant can lead to false predictions of the concentration profiles of the solid and bulk phases.

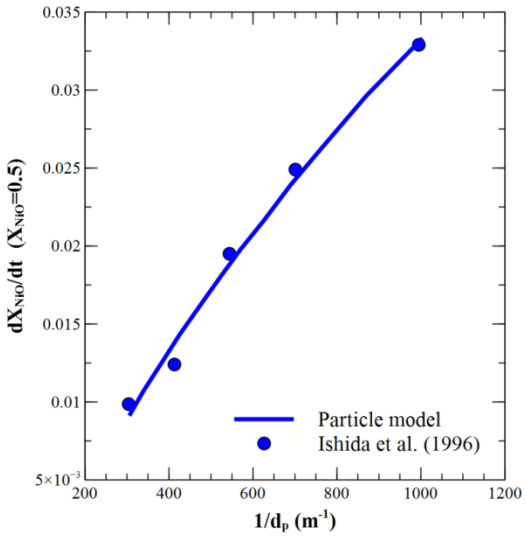

Figure 5.3: Comparison of NiO conversion rate (dX_{NiO}/dt at X_{NiO} = 0.5) for various particle sizes experimentally measured by Ishida et al. [47] in TGA (symbols) and predicted by the model (line). Reduction rates (dX_{NiO}/dt) of Ni/YSZ 'D' oxygen carriers with diameters 1.0 – 3.2 mm are calculated at X_{NiO}=0.5 under H_2 fuel and 600°C.

5.3.3. Effect of cyclic testing

In the literature, changes in the particle microstructure have been documented for Ni-based oxygen carriers from performance testing in TGA [47,114], batch fluidized bed reactors [37,80], and prototype reactors [73,185]. Changes to the pore structure of the particle were commonly observed, and believed to be caused by the oxygen carrier preparation, attrition or fragmentation, and migration of Ni [80,196]. The increasing oxygen carrier conversion rate as a function of the reduction cycle was correlated to the structural changes occurring within the particle. The exact mechanisms of these changes are not well-understood, and they can vary for different oxygen carriers and operating conditions. Nonetheless, modeling the impact of these progressive changes in the particle microstructure on the oxygen carrier reactivity can improve our understanding of the effect of the number of cycles on CLC performance. If these physical changes can be measured or correlated, then the reactivity behavior can be evaluated over the lifetime of an oxygen carrier. Alternatively, the model can be used to suggest changes occurring within the particle microstructure in the absence of BET or SEM data to account for the variations in reactivity.

Here, the model is used to analyze the effect of redox cycles on the structural properties of the 'E' Ni/YSZ oxygen carrier tested by Ishida et al. [47]. TGA data showed that the conversion rate increased over eight redox cycles at 600 ˚C. Ishida et al. [47] attributed the enhancement in reaction rate to slight enlargements of the grain and pore sizes, which exhibited negligible change after the first seven cycles. The reactivity stabilized after the seventh cycle, probably because a stable microstructure had been attained. Based on their observations, we hypothesize that a gradual increase in the mean pore size over increasing redox cycles is the reason for the observed reactivity behavior. Unlike Section 5.3.2, the capability of the model is limited by the availability of the data because any information regarding the pore size distribution or the variation after cycles was not reported in their work. Hence, the objective of this section is to utilize the model to conduct a sensitivity analysis of the mean pore size on the oxygen carrier conversion, to determine if the hypothesis can explain the experimental results.

The modeling approach follows establishing the kinetics from the conversion data of the fresh oxygen carrier and evaluating the reactivity to changes in the mean pore size. The rate constant, k_j', is estimated (**Table 5.2**) to match the experimental data of the fresh material (**Figure 5.2**). The pore size of the fresh 'E' particle is determined to be 4.5 nm assuming a cylindrical pore structure and uniform distribution. The porosity is assumed 0.2 (since it is denser than the 'D' particles) for all cycles. A sensitivity analysis of the pore size within a range of 4-25 nm is conducted. The model results show that the reactivity, taken as the time to reach 95% NiO conversion, increases with increasing pore size (**Figure 5.4a)**. The greatest improvement occurs when the pore diameter is increased from 4 to 10 nm. As discussed in Section 5.3.2, internal diffusion effects are important for oxygen carriers of this size, however by increasing the pore size, diffusion limitations are reduced. At a pore diameter > 15 nm, the rates are predominately controlled by kinetics. This finding somewhat contradicts the conclusion of Section 5.3.2 where all the particles were found to be diffusion-limited. However, modeling the intraparticle gradients of the 'E' particles provided a reasonable explanation, wherein internal transport was clearly enhanced by the increase in pore size and reaction rates were reduced by the 50% by the dilution of the reducing gas. Observing the agreement between model and experiment, we surmise that the pore size experienced an increase after 8 cycles (**Figure 5.4b**). Conclusively, on the basis of the (commonly observed) hypothesis of increasing pore size over redox cycles, we show that transport-limited oxygen carriers can gain reactivity over time due to surface restructuring and pore opening. In Section 5.3.5, the effect of number of cycles is analyzed through experimentation and modeling of the fresh and used carriers, where evidence of particle restructuring are quantified and modeled in detail.

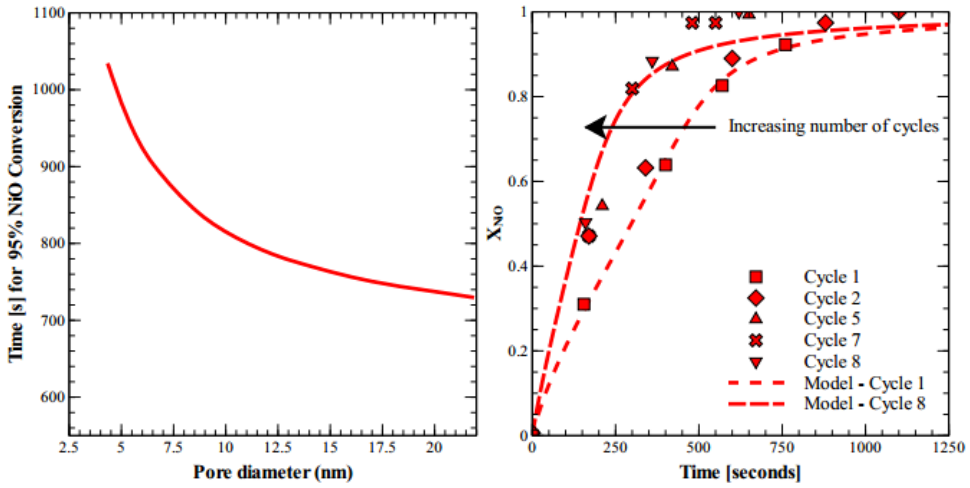

Figure 5.4: (a) Effect of particle porosity on NiO reduction for Ni/YSZ 'E' oxygen carrier evaluated at 600°C in 50 vol.% H_2 in N_2; (b) Comparison of reactivity of Ni/YSZ 'E' oxygen carrier at 600°C in 50 vol.% H_2 in N_2 gas experimentally measured by Ishida et al. [47] after eight reduction cycles (symbols) with model predictions for d_{pore} = 4.40 nm (cycle 1) and 10 nm (cycle 8) using the kinetic parameters obtained from the fresh particles (**Table 5.2**).

5.3.4. Effect of Ni-support interaction and spinel reduction

As shown, the variations in oxygen carrier reactivity can be accounted for in the model by modifying the physical parameters such as surface area and porosity to reflect the actual changes occurring within the microstructure. When the support is Al_2O_3, typically there is a loss of free NiO to form the less reactive $NiAl_2O_4$ spinel during calcination or oxidation at high temperatures for long periods. Since the spinel phase takes much longer to reduce than the NiO, extensive formation of $NiAl_2O_4$ essentially deactivates the oxygen carrier. Thermal pretreatment of γ-Al_2O_3 to form α-Al_2O_3 has been investigated as a route to minimize the extent of Ni-Al_2O_3 interaction and produce a higher fraction of the active NiO phase in the oxygen carrier [49,79,118,197,198]. De Diego et al. [72] tested dispersed Ni oxygen carriers over γ- and α-Al_2O_3 in a continuous CLR pilot plant for 50 h with a mixture of CH_4 and H_2O as the reducing gas operating in the range of 800-880 °C. The reactivity of the fresh and used oxygen carriers was then

investigated by TGA at 900 °C, under reduction with CH_4 and H_2O. The reduction rate was much slower on the γ-Al_2O_3 due to significant formation of $NiAl_2O_4$. De Diego et al. (2009) [72] observed that after 50 h in the CLR unit, the Ni/γ-Al_2O_3 oxygen carrier became more readily reduced because of a higher NiO content. The relative amount of free NiO was estimated from the TGA reduction data (**Figure 5.5**) to be approximately 25% for the fresh and 65% for the used Ni/γ-Al_2O_3 oxygen carrier. Increasing NiO content over redox cycles can be explained by the progressive reduction of the spinel phase in the CLR Reducer. The reduction of spinel was more extensive than the oxidation because of the longer residence times in the Reducer with a high H_2 concentration that further promotes the reduction reaction. In the case of Ni/α-Al_2O_3, the NiO content did not change with operation (~82% of the impregnated nickel remained as free NiO and slightly increased to 85% after 50 h). The physical characteristics of the fresh and used Ni/α-Al_2O_3 and Ni/γ-Al_2O_3 oxygen carriers reveal that the most noticeable change after 50 h of operation was the decrease in surface area for Ni/γ-Al_2O_3 from 83.4 to 29 m^2/g (**Table 5.1**).

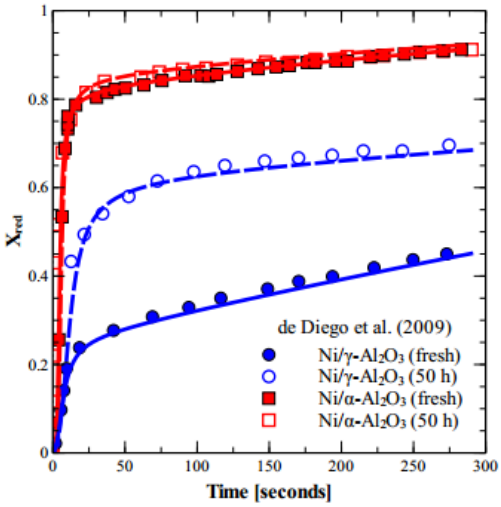

Figure 5.5: Reduction data (symbols) of Ni/γ-Al_2O_3 and Ni/α-Al_2O_3 oxygen carriers [100-300 μm] measured by TGA at 900°C in 15% CH_4, 20% H_2O, and 65% N_2 before and after 50 h of operation in a 900Wth CLR pilot plant [72]. Lines represent model predictions using the kinetic parameters obtained from the fresh particles (**Table 5.3**).

The particle model is applied to predict the reduction behavior of the Ni/α-Al_2O_3 and Ni/γ-Al_2O_3 oxygen carriers tested by de Diego et al. [72] before and after 50 h of operation. The overall solid conversion of the oxygen carrier (X_{red}) is a function of the NiO conversion, X_{NiO}, and the $NiAl_2O_4$ conversion, $X_{NiAl_2O_4}$:

$$X_{red} = X_{NiO} f_{NiO} + X_{NiAl_2O_4} \left(1 - f_{NiO}\right), \tag{5.13}$$

where f_{NiO} denotes the nickel fraction inside the oxygen carrier in the form of free NiO. This value is estimated from the TGA reduction data, corresponding to the inflection point in the solid conversion where NiO reduction ends and $NiAl_2O_4$ begins [72,114]. Dueso et al. [114] proposed that the reduction reactions of $NiAl_2O_4$ by CH_4, H_2, and CO can be described by the shrinking core model. The conversion of $NiAl_2O_4$ is expressed as a function of the sum of the $NiAl_2O_4$ reduction reaction rates, $\sum R_j'$:

$$dX_{NiAl_2O_4} / dt = \sum R_j' / C'_{NiAl_2O_4}. \tag{5.14}$$

The simultaneous reduction of NiO and $NiAl_2O_4$ is modeled using the rate expressions from Zhou et al. [119] and Dueso et al. [114]. The contribution of Ni-catalytic reactions is also taken into account using the proposed kinetics by Zhou et al. [119]. In general, the NiO reactions are dominant in the beginning of the reduction cycle because of fast kinetics. Once the NiO is converted, this is followed by a second, much slower reduction period to convert the remaining $NiAl_2O_4$.

The reactivity of the Ni/α-Al_2O_3 and Ni/γ-Al_2O_3 oxygen carriers is simulated under the TGA reduction conditions of de Diego et al. [72] using the physical properties from **Table 5.1** and the f_{NiO} values estimated from the data. The objective of this case study is to utilize the particle model to examine the effect of NiO/$NiAl_2O_4$ ratio and support (α-Al_2O_3, γ-Al_2O_3) on the overall solid reduction. Reduction rate constants for NiO and $NiAl_2O_4$ are estimated from the data of the fresh oxygen carriers (**Table 5.3**). As shown in **Figure 5.5**, the model predictions achieve an acceptable fit with the experimental data. Internal diffusional resistance was not significant in their experiments because of the small particle size (100-300 μm). For both oxygen carriers, the reduction of NiO is complete within approximately 20 s of reaction.

Table 5.3: Estimated kinetic parameters for the reduction of Ni/γ-Al_2O_3 and Ni/α-Al_2O_3 oxygen carriers at 900°C in TGA under 15% CH_4, 20% H_2O, and 65% N_2 [72]. Rate constants (k_1-k_4) correspond to NiO reduction kinetics published by Zhou et al. [119] and rate constants (k_1'-k_3') correspond to the $NiAl_2O_4$ reduction kinetics published by Dueso et al. [114]. f_{NiO} = 25% and 65% for fresh and used Ni/γ-Al_2O_3; f_{NiO} = 82% and 84% for fresh and used NiO/α-Al_2O_3.

	Ni/γ-Al_2O_3	*LL*	*UL*	*Ni/α-Al_2O_3*	*LL*	*UL*
k_1	9.15E-04	8.85E-04	9.45E-04	1.06E-02	1.03E-02	1.10E-02
k_2	5.03E-05	4.27E-05	5.79E-05	1.09E-04	5.82E-05	1.60E-04
k_3	3.19E-08	1.02E-08	5.28E-08	2.16E-06	4.53E-07	3.86E-06
k_4	6.14E-06	3.21E-06	9.07E-06	4.42E-05	1.56E-05	7.28E-05
k_1'	1.46E-09	1.40E-09	1.52E-09	6.51E-09	5.71E-09	7.30E-09
k_2'	5.11E-08	4.90E-08	5.32E-08	2.43E-07	2.23E-07	2.62E-07
k_3'	3.20E-08	2.83E-08	3.57E-08	1.56E-07	1.13E-07	2.00E-07

LL, lower limit; UL upper limit of approximate 95% confidence interval.

However, a longer time is required to completely convert the remaining $NiAl_2O_4$ in the Ni/γ-Al_2O_3 because of the higher fraction of $NiAl_2O_4$. The rate constants for the NiO reduction reactions are generally higher over α-Al_2O_3 because the NiO conversion is enhanced by the higher fraction of active NiO in its composition. Although γ-Al_2O_3 has a higher surface area, the faster kinetics of Ni/α-Al_2O_3 is more dominant. As a result, a higher overall NiO reduction rate is obtained using the α-Al_2O_3. For the reduction of $NiAl_2O_4$, the differences in rate constants between α-Al_2O_3 and γ-Al_2O_3 are relatively small. This reveals that the reactivity of the $NiAl_2O_4$ phase is unaffected by thermal pretreatment of the Al_2O_3. The higher surface area of γ-Al_2O_3 leads to the faster reduction rate of $NiAl_2O_4$ over γ-Al_2O_3. Similar trends in reactivity between α-Al_2O_3 and γ-Al_2O_3 have been reported by Dueso et al. [114], though for different carriers.

To simulate the effect of 50 h of operation on the reduction rate, the f_{NiO} parameter is increased to 65% for Ni/γ-Al_2O_3 and to 85% for Ni/α-Al_2O_3 to reflect the reduction of the $NiAl_2O_4$ phase over the redox cycles. Without additional fitting of the kinetics, the model predictions successfully capture the observed rise in reactivity. The increase in the free NiO content directly increases the overall solid conversion at the

end of reaction time, which is significant in the case of the used Ni/γ-Al_2O_3 oxygen carrier, notwithstanding that reduction rates are negatively affected by the decrease in surface area reported for both carriers. This finding validates not only the kinetic model but also the structural model of the oxygen carrier solid matrix. Thus, the reduction behavior of oxygen carriers taken from different periods of operation can be accurately predicted with the model by incorporating the important changes in physical and chemical properties from the experimental analysis.

5.3.5. Experiments performed in-house

In the preceding discussion, the reactivity of Ni-based oxygen carriers is shown to increase as the internal transport resistance is decreased, which can be achieved by decreasing particle size or increasing pore volume. Performance testing over multiple redox cycles can reveal changes in the oxygen carrier reactivity, caused by physical and chemical changes in the particle microstructure. The physical changes are primarily related to the changes in surface texture and solid structure of the support, such as sintering and agglomeration phenomena, while chemical changes can be the result of NiO interaction with the support layer. For the Ni/YSZ particles tested by Ishida et al. [47], increasing reducibility with H_2 can be explained by the gradual enlargements of the mean pore size occurring over increasing number of redox cycles. Chemical changes are not modeled because of the low reactivity of YSZ. In the study by de Diego et al. [72], the reactivity of the Ni/α-Al_2O_3 and Ni/γ-Al_2O_3 oxygen carriers was enhanced over time by a gradual conversion of the $NiAl_2O_4$ spinel phase and deteriorated by a loss of surface area due to agglomeration and sintering of the Ni. Ni/α-Al_2O_3 was not affected by the duration of operation, while Ni/γ-Al_2O_3, which was calcined at 950 ˚C for 1 h, significantly gained reactivity after 50 h in the CLR unit. The observed changes in reactivity are successfully predicted by the model. The focus of this section is to analyze the effect of redox cycling on the reactivity behavior of fresh γ-Al_2O_3-SiO_2 supported Ni-based oxygen carriers. The aim of this section is to present a comprehensive analysis of the important changes in reactivity, surface texture, and solid structure of the oxygen carriers after each redox cycle in the TGA through modeling and experimentation.

5.3.5.1. Materials and method

The Ni/γ-Al_2O_3-SiO_2 oxygen carrier was prepared using the incipient wetness impregnation method and the reactivity over four redox cycles was measured in the TGA at 950˚C under reduction in 4 vol.% H_2 in Ar and oxidation in air. The details of the preparation and TGA methods are given in Chapter 3. To ensure that the TGA experiments were not significantly affected by transport resistances, we analyzed the effect of flow rate (80-240 sccm) and initial sample weights (15-80 mg) on the observed reactivity. The reactivity increased with higher flows and smaller sample weights; however we were unable to operate at a condition where no influence could be detected due to constraints of our system. Based on those tests, we chose to conduct the experiments at a total flow rate of 240 sccm and an initial sample weight of 15 mg. This reduced the extent of external and interparticle diffusion, but did not completely eliminate them. For these reasons, the full TGA model presented in Section 5.2 is applied to the experiments performed here.

5.3.5.2. Experimental and model results

The rate constants for the reduction for NiO and $NiAl_2O_4$ by H_2 are estimated from the TGA conversion data measured from cycle 2 (**Table 5.4**). The reactivity for the first cycle is much lower compared to the other cycles because of the activation step required to expose the Ni grains to the surface. The Ni/γ-Al_2O_3-SiO_2 oxygen carrier prepared in this work has a similar rate constant for the $NiAl_2O_4$ reduction reaction and a lower rate constant for the NiO reduction reaction, compared with the Ni/γ-Al_2O_3 oxygen carriers used by de Diego et al. [72]. This can be explained by the differences in preparation method and presence of SiO_2 in our oxygen carriers. Our experiments require longer reduction times compared to the data reported by de Diego et al. [72] because our feed gas is much more dilute. Moreover, unlike **Figure 5.5**, it is hard to discern the NiO and $NiAl_2O_4$ reduction stages in the conversion data because they are overlapped. This can be explained by the relatively higher reaction temperature, more dilute H_2 concentration, and smaller particle size. Therefore, it is of interest to deconvolute the diffusion resistances associated with the TGA from the reduction reactions of NiO and $NiAl_2O_4$ in order to better understand the reactivity of these carriers.

Table 5.4: Estimated kinetic parameters for the reduction of Ni/γ-Al_2O_3-SiO_2 oxygen carrier at 950°C in 4 vol.% H_2 in Ar. Rate expressions k_2 correspond to the NiO reduction with H_2 kinetics published by Zhou et al. [119] and k_2' correspond to the $NiAl_2O_4$ reduction with H_2 kinetics published by Dueso et al. [114].

	NiO/γ-Al_2O_3	*LL*	*UL*
k_2	2.58E-05	2.47E-05	2.68E-05
$k_{2'}$	9.20E-08	8.76E-08	9.65E-08

LL, lower limit; UL upper limit of approximate 95% confidence interval.

The extent of diffusion limitations in the TGA is analyzed with the experimental results from cycle 2. The effect of each diffusion resistance on the reactivity is examined for different conditions in which a single diffusion resistance is isolated. The results modeled for reaction kinetics is determined by simulating a monolayer bed of particles with a negligible stagnant gas boundary layer and fast internal diffusion through the pores. The external diffusion effect is simulated using the reaction-controlled model with the experimental stagnant boundary layer thickness δ. Similarly, the diffusion limitations through the bed (interparticle effects) are evaluated by simulating the reaction-controlled model using the experimental bed height h, and limitations through the particle (intraparticle effects) by simulating the reaction-controlled model using the effective diffusion relationships. The conversion as a function of these diffusion resistances is depicted for $X_{red} < 0.7$ in **Figure 5.6**, where we approximate weight loss is primarily due to NiO reduction. This is justified later in our analysis (**Figure 5.12**). Comparing the three types of diffusion control, the interparticle diffusion is the most limiting step in the reduction rate. These results are consistent with Ollero et al. [188], who analyzed the diffusional limitations in TGA gasification studies. The overall prediction is lower than the interparticle diffusion-limiting case, indicating that all the diffusional effects are relatively important to model the TGA reduction behavior. Nonetheless, the dominant contribution comes from the kinetic terms, and diffusion resistances are of minor significance. In a separate study, an analysis of the kinetic models relevant in supported and

unsupported NiO reduction reactions is presented [132] and it is based on the observation that diffusion resistances are not dominant in TGA studies, even when they are present.

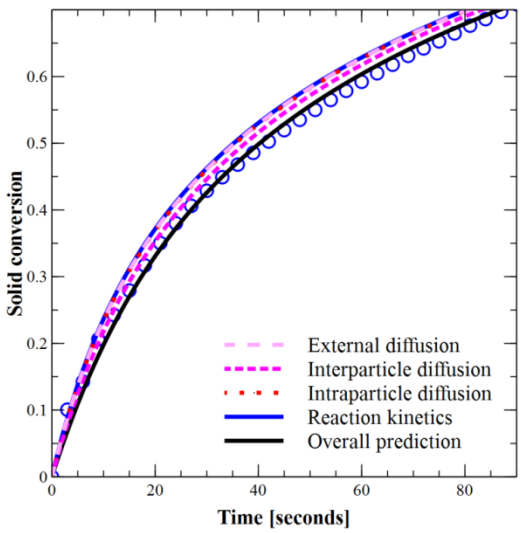

Figure 5.6: The effect of external, interparticle, and intraparticle diffusion in the modeling of TGA experiments. Model predictions under different diffusion resistances (lines) are compared with experimental results (symbols) from cycle 2.

The effect of the number of redox cycles on oxygen carrier reactivity is shown in **Figure 5.7**. As the cycle number is increased, there is an observed decrease in reactivity. The oxygen carrier was characterized by several techniques to identify the causes for the reactivity decline. Focused ion beam (FIB) scanning transmission electron microscopy (STEM) was used to identify the Ni distribution inside the particle. Shown in **Figure 5.8**, the images of the fresh and used materials show that Ni is distributed uniformly everywhere inside the particle and slightly more concentrated on the surface. **Table 5.5** shows the variation of BET surface area and mean pore size over various cycles spent in the TGA. There is an observed difference in the surface area and pore size between the fresh oxygen carrier and after cycle 1. However from cycle 2 to 4, no significant changes are measured, which suggests that the internal pore

structure is stable over these cycles. This agrees with the pore size distribution shown in **Figure 5.9**. The structural integrity of the support is observed in SEM (**Figure 5.10**), revealing that some sintering and agglomeration had occurred. Moreover, the XRD patterns obtained from cycles 2 and 4 show an increase in the NiO grain size from 0.0173 μm to 0.0252 μm.

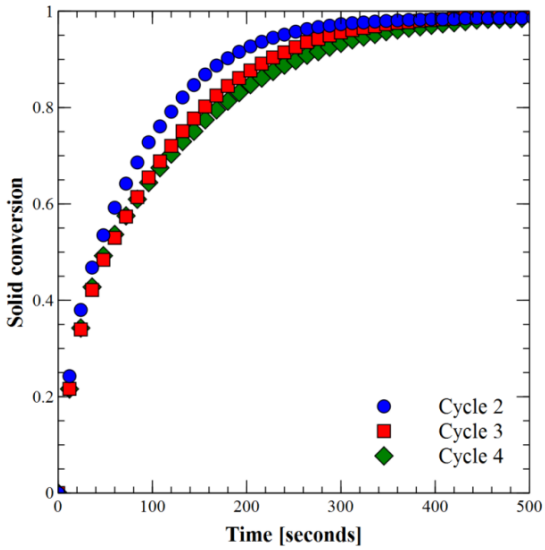

Figure 5.7: Reduction of Ni/Oγ-Al_2O_3-SiO_2 at 950°C in 4 vol.% H_2 in Ar over redox cycles in TGA.

Table 5.5: Properties of the Ni/γ-Al_2O_3-SiO_2 oxygen carrier after various cycles tested in TGA at 950°C. Reduction in 4 vol.% H_2 in Ar and oxidization in 100% air.

Properties	*Fresh*	*Cycle 1*	*Cycle 2*	*Cycle 6*
BET surface area (m^2/g)	93.7	68.1	68.1	69.2
Pore size (nm)	11.6	14.2	14.2	13.9
XRD phases	γ-Al_2O_3, SiO_2, NiO, $NiAl_2O_4$	γ-Al_2O_3, SiO_2, NiO, $NiAl_2O_4$	γ-Al_2O_3, SiO_2, NiO, $NiAl_2O_4$	γ-Al_2O_3, SiO_2, NiO, $NiAl_2O_4$

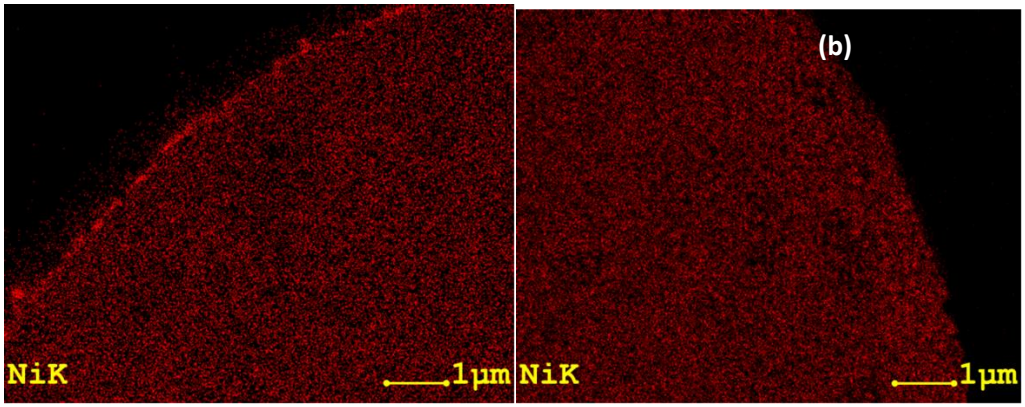

Figure 5.8: FIB/STEM images of the Ni distribution inside the (a) fresh Ni/γ-Al_2O_3- SiO_2 oxygen carrier and (b) after four cycles.

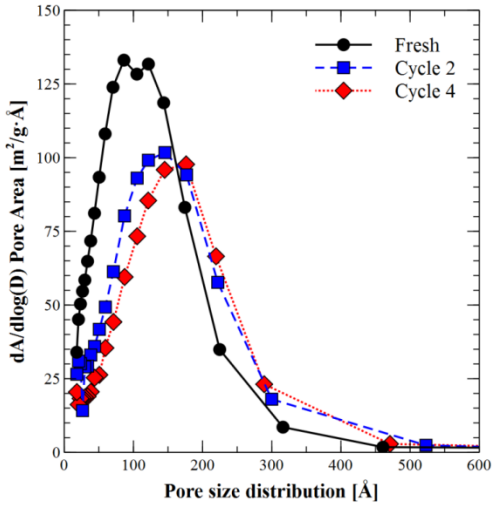

Figure 5.9: Pore size distribution of the Ni/γ-Al_2O_3-SiO_2 after various cycles in the TGA at 950°C.

Based on the materials characterization data, we postulate that the decline in oxygen carrier reactivity can be attributed to either (1) chemical deactivation due to progressive $NiAl_2O_4$ formation during oxidation or (2) loss of active surface area due to accumulative thermal sintering of the Ni grains. To address the former hypothesis, in-situ XRD is performed to analyze the effect of calcination for 3 h at 950 ˚C on the relative compositions of NiO and $NiAl_2O_4$ in the oxygen carrier. The method of this analysis is provided in the supplementary material. The assigned peaks corresponding to NiO, Al_2O_3, and $NiAl_2O_4$ are clearly

visible on the diffraction patterns presented in **Figure 5.11**. Comparison of the XRD patterns before and after extended oxidation reveals an increase in the $NiAl_2O_4$ intensity, indicating the formation of larger spinel crystals with oxidation time. Therefore, we surmise that the fraction of $NiAl_2O_4$ has increased over each redox cycle, resulting in a progressively decreasing conversion rate. The model predictions from cycle 2 are in good agreement with the experimental results and the subsequent cycles are simulated by varying the $NiO/NiAl_2O_4$ ratio (**Figure 5.12**). The contributions of NiO and $NiAl_2O_4$ reduction to the overall solid conversion can be observed in the X-time and dX/dt-time profiles. A similar trend in the time derivative of the conversion (dX/dt) can be observed for all cycles in which the conversion rate is characterized by the immediate reduction of NiO followed by the slow reduction for $NiAl_2O_4$. The fraction of NiO over NiO plus $NiAl_2O_4$ is estimated at 67 wt.% in cycle 2, 57 wt.% in cycle 3 and 54 wt.% in cycle 4. As can be observed, the reactivity loss can be captured by the increase in $NiAl_2O_4$ over cycles and by modeling this effect, we are able to match the experimental data very closely.

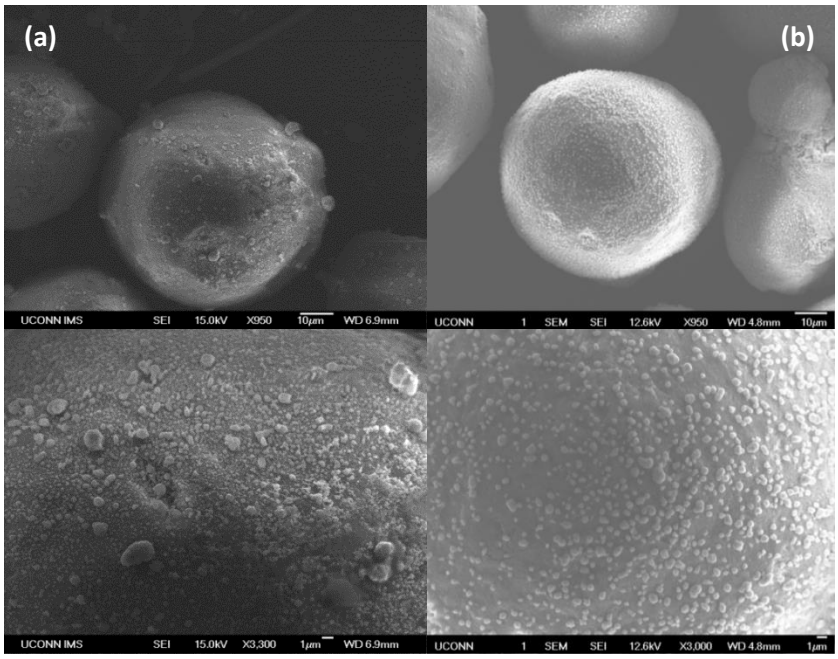

Figure 5.10: SEM images of the oxidized $Ni/SiO_2/\gamma\text{-}Al_2O_3$ oxygen carrier after 1 (a) and 4 (b) cycles in the TGA at 950°C.

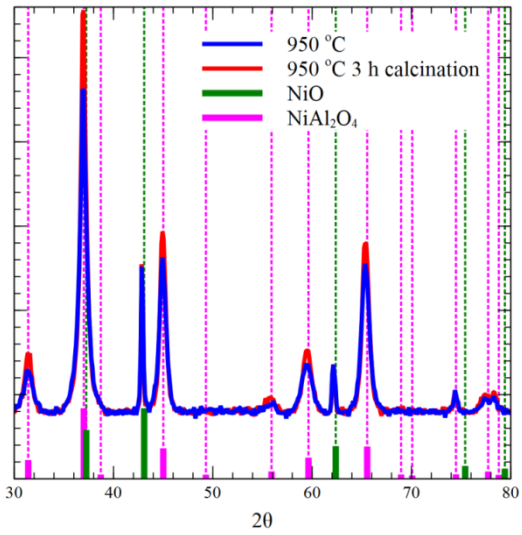

Figure 5.11: Evolution of $NiAl_2O_4$ in the Ni/γ-Al_2O_3-SiO_2 oxygen carrier from in-situ XRD.

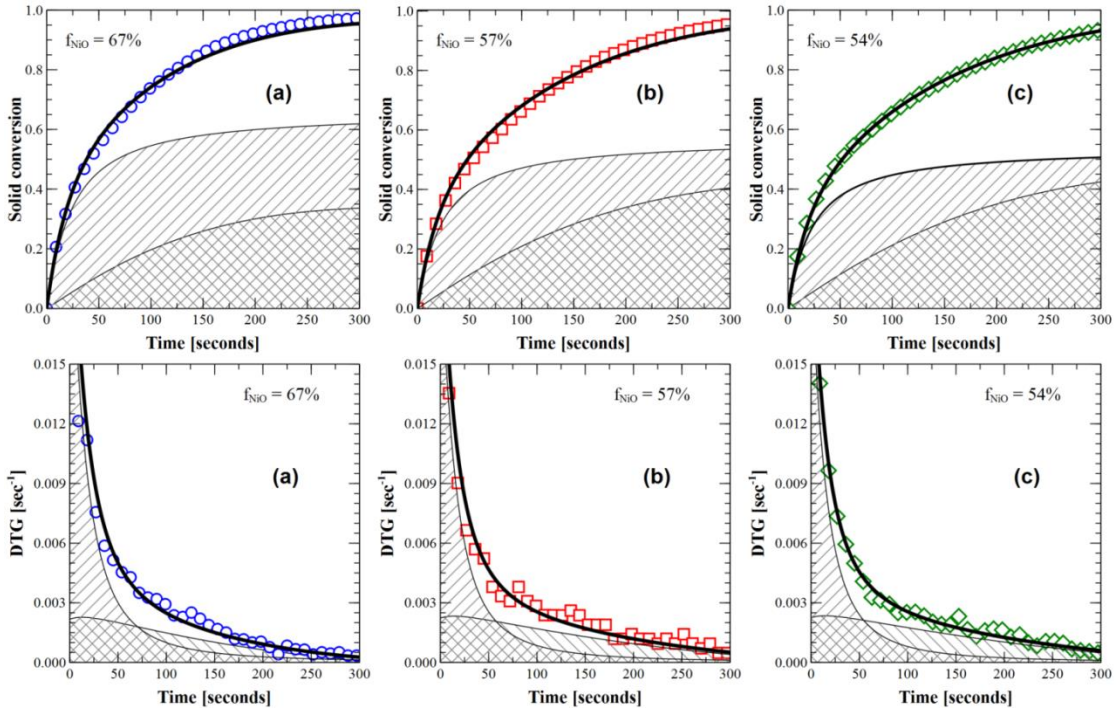

Figure 5.12: Comparison of reactivity of Ni/γ-Al_2O_3-SiO_2 oxygen carrier experimentally determined (symbols) with the model predictions (lines) using the kinetic parameters presented in **Table 5.4** obtained in this work. (a) - cycle 2; (b) - cycle 3; (c) - cycle 4. (▨) denotes NiO reduction and (▨) denotes $NiAl_2O_4$ reduction.

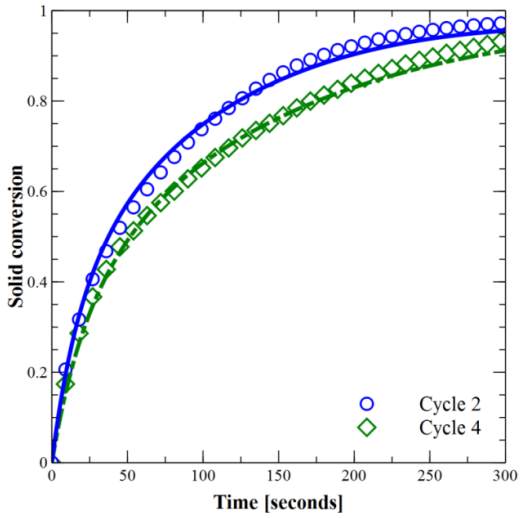

Figure 5.13: Comparison of reactivity of Ni/γ-Al_2O_3-SiO_2 oxygen carrier experimentally from cycles 2 and 4 (symbols) with the model predictions of cycle 2 (blue line) and after reducing the surface area (green line).

As stated earlier, a loss of active surface area can also reduce the oxygen carrier reactivity. The SEM images revealed that the Ni grains on the surface of the oxygen carrier grew in size with increasing number of redox cycles. Thus, it is reasonable to assume that the Ni grains inside the oxygen carrier grew as well, as evidenced by the NiO XRD patterns. This effect was not detected in the BET because the pore volume is much larger than the NiO grain volume. However Ni sintering can lead to substantial changes in the reaction rates. The increase in the NiO grain size from 0.0173 μm (cycle 2) to 0.0252 μm (cycle 4) is calculated to reduce the active NiO/$NiAl_2O_4$ surface area (68.1 m^2/g) by a factor of 0.69. This assumes that the dispersed NiO particles on the Al_2O_3 are full spheres and the total mass of the Ni-containing grains remains the same. **Figure 5.13** shows the effect of the active surface area change on the model-predicted conversion rate. It can be seen that the *predicted* reactivity with the decreased surface area is in reasonable agreement with the experimental data from cycle 4. These results suggest that a structural change in the oxygen carrier is also a reasonable explanation for the reactivity decline over redox cycles. It is difficult to provide experimental verification for these changes, whether they are due to solely

physical or chemical mechanisms or their combinations. Even so, the modeling analysis performed here demonstrates that both accounts can be practically implemented and realistic predictions can be made. In a future work we will employ XPS analysis to identify the extent of each phenomenon on the surface of the oxygen carrier, as successfully performed by Cabello et al. [116].

5.4. Conclusions

A particle model was used to predict experimental data in which the particle properties, such as size, microstructural properties, and support interaction, were subject to change. The model was proven to be predictive of the effects of particle size on the oxygen carrier reactivity over the range of diameters experimentally tested. The internal diffusion resistance, which was quantified with an effectiveness factor, was found to be significant for all particles with a mean diameter greater than 1.0 mm. The effect of redox cycling on the particle reactivity was evaluated by a sensitivity analysis of the observed changes of the microstructural properties. Furthermore, chemical deactivation due to Ni-support interaction was analyzed for oxygen carriers prepared on α-Al_2O_3 and γ-Al_2O_3. The observed reactivity changes due to differences in spinel fraction and sintering effects were well-predicted by the model, proving that the model can be used to track the performance of oxygen carriers throughout their use. Experimental tests performed using our Ni/γ-Al_2O_3-SiO_2 oxygen carrier revealed that the gradual reactivity decline could be modeled, whether the effects were due to $NiAl_2O_4$ formation or Ni sintering. The results from this work highlight the significance of dynamic modeling at the particle-scale for the interpretation of experiments and accurate design of CLC systems. While this study focuses on Ni-based systems, the model can be practically applied to any oxygen carrier system, by including the relevant reaction scheme and material properties.

Chapter 6 MODEL-BASED DESIGN OF CHEMICAL-LOOPING COMBUSTION EXPERIMENTS

To guide the design of chemical-looping combustion (CLC) systems, the use of accurate models is crucial. The reduction kinetics between NiO and CH_4 is uncertain, in regards to the most suitable kinetic mechanism and reaction network. A framework for structural identifiability analysis is developed and applied to evaluate the candidate kinetic models for the NiO-CH_4 reaction. The identifiability of kinetic parameters of different model structures is analyzed and compared. Models that lack structural identifiability of their kinetic parameters are rejected in the analysis. From a total of 160 possible candidate models, 4 kinetic models are found to be identifiable with respect to their kinetic parameters and distinguishable from different model structures. This structural identifiability analysis paves the way for model-based optimal design of experiments. First, optimal experiments are designed and executed to reject inadequate models and to determine a true model structure for the reaction kinetics of the CH_4-NiO system. Then, kinetics with statistical significance is estimated from experiments aimed at reducing parameter uncertainty. To maximize the observability of the NiO reduction reactions, fixed bed experiments should exhibit a peak separation of the concentration profiles, an initial high methane slip, and low overall CO_2 selectivity. Several case studies are presented to check the adequacy of the recommended model and evaluate its predictive ability and extrapolation capabilities. The model resulting from this work is validated and suitable for application in process design and optimization.

6.1. Introduction

Chemical-looping combustion (CLC) is a promising method for inexpensive CO_2 capture, accomplished by the sequential reduction and oxidation of a metal oxygen carrier by a hydrocarbon fuel and air, respectively [23,81]. Common oxygen carriers for CLC include supported metals, such as Ni, Cu, Mn, and Fe [34,44,60,62,65,66,73–77,79,93,175,176,199–203] or natural ores containing the same [32,204–211]. The oxidation of these metals is relatively easy to understand and simulate, in terms of their reaction kinetics, as there is typically one or a few sequential oxidation reactions occurring. The reduction kinetics

of these metals is, however, more complicated and less certain. During reduction, the bare metal form of the oxygen carrier can catalyze several heterogeneous reactions (*e.g.*, reforming, water gas shift, methanation, etc.), as well as a series of carbon formation reactions (*e.g.*, methane decomposition or cracking and Boudouard reactions). The challenge therein, is that these reactions have not been studied extensively at the very high temperatures of CLC and more importantly at the co-existence of metal oxides. In addition to the lack of certainty of the reactions catalyzed by the metals, there exists significant controversy in terms of understanding and determining reaction networks [49,56,58,60,72,73,77,114,118,119,142,171,198,212,213] and kinetic mechanisms [35,47,65,69,73,114,132,153,214,215] to describe the heterogeneous reduction of the metal oxide by reducing agents (CH_4, H_2, CO). It is unclear whether complete or partial fuel oxidation pathways are dominant, and what solid-state kinetic models can describe these reactions.

The reactivity and selectivity of the oxygen carrier are typically studied in experimental setups that provide information diluted by the unavoidable hydrodynamic effects associated with each CLC reactor. These setups commonly include fixed bed reactors, fluidized bed reactors and thermo-gravimetric analyzers. In these laboratory reactors, dominant reaction networks and kinetic mechanisms are developed and determined on the basis of experiments, designed according to common practice and experimental intuition. Thus, the proposed models are often selected from a limited number of possibly sub-optimal experiments. Here, experimental sub-optimality is defined as a range of experimental conditions derived from experimentalists' intuition or "rules of thumb," but not necessarily optimized for the task at hand: determination of a statistically significant, representative and accurate reaction kinetics scheme for the reduction step of NiO-based CLC. As a result, there exists uncertainty and controversy in the conclusions on the reaction networks, mechanisms and kinetics of the reduction step of chemical-looping combustion.

A better approach to extract information on the reactions, their network, and dominant kinetics from experiments is to follow a model-based framework. One such methodology is developed and applied in this work, to address the contradictions and inconsistencies in the CLC literature pertinent to the reaction

models governing the reduction of NiO. Namely, model-based identifiability analysis and design of optimal experiments is used here, with the objective to address literature controversies and arrive at statistically significant model structures and kinetic parameters for CLC reduction. For the present exercise, the reduction of NiO by CH_4 is explored, for which there exists profound controversy in the literature, noted by the wealth of independent research studies and considerable number of different reaction kinetics and schemes proposed. Nonetheless, the methodology proposed herein, can be applied to any other reaction system and should be viewed as a structured model-based methodology for systems with uncertainty, regardless of their domain, structure, specificity and particularities.

The structure of this document is as follows: first, we explain in detail the current state of understanding of the reaction system of CH_4 with NiO and the controversy governing the existing literature. The motivation behind a model-based approach to study the CLC kinetics of NiO with CH_4 is illustrated with a dynamic sensitivity analysis of the important kinetic parameters using a previously validated CLC model. Existing reactor designs are evaluated, in which potential issues with the estimation of kinetic parameters are discussed. Then, we introduce the application of a structured model-based design of experiments approach to solve the specific problem in the reaction kinetics of the NiO-CH_4 system. For each section of the methodology, the statistical theory and mathematical formulation is reviewed and presented. In a later analysis, we demonstrate the applicability of the methodology to tackle the model controversy with the NiO-CH_4 reduction kinetics and show the systematic reduction of models by the design and execution of highly informative experiments.

6.2. Problem statement

Existing studies of the NiO-CH_4 system at CLC conditions focus mostly on the comparison between fresh and used oxygen carriers, since the reactivity of oxygen carriers tends to depart from that of the fresh materials with time [128]. The derived rate constants from oxygen carriers of varying metal loading, synthesis methods, and testing conditions can exhibit differences that are magnitudes apart

[49,57,126,127]. For catalytically active oxygen carriers, such as NiO, the reduced metal promotes catalytic reactions that complicate kinetic parameter estimation efforts, due to the consideration of multiple, inter-related reactions. A generalized CLC kinetic model for NiO and CH_4, typically includes a set of heterogeneous NiO reduction reactions, reforming reactions catalyzed by the reduced metal, and carbon formation reactions. Typically, investigators interested in CLC reactor design or reactivity evaluations select the reaction model on the basis of *a priori* assumptions of the phenomenological proceedings of the gas-solid reactions with respect to the metal oxide [42,47,114,153] or results of parameter estimation of a few arbitrarily designed experiments [58,119]. The results from these kinetic studies are often unreliable if any deviation in the operating conditions exists, which in turn makes them inappropriate for reactor and process design analyses. In order to procure a reliable model, it is necessary to a) identify the possible models that can describe the system of interest; b) utilize a statistical procedure to identify and discriminate among candidate models; c) systematically reject the inadequate models; and d) enhance the precision of the model parameters. Here, we first assess the current state of understanding of the reactions of NiO with CH_4 and then describe a systematic framework for improving the existing knowledge.

6.2.1. Rival kinetic models

Previously, we reviewed reaction schemes for a CH_4-fed, Ni-based CLC system, finding inconsistency in the solid-state reaction models and reaction pathways proposed by different research groups [119]. **Table 6.1** presents the various proposed pathways in which CH_4, H_2 and CO react with NiO during a reduction cycle. All the reaction schemes model the reduction of NiO by H_2 and CO. However, three possible reaction pathways for the reaction between CH_4 and NiO have been proposed, involving partial and/or complete fuel oxidation pathways. Reaction Schemes (RS) II and III utilize different, single pathways for the reaction of NiO with CH_4, while RS I and IV consider different two-step pathways. A single global reaction between NiO and CH_4 has also been proposed [35,73], but is not considered in this work, because it is known that NiO has different reactivity in the presence of different reducing gases [114].

Table 6.1: Literature-proposed reaction pathways for the heterogeneous reduction of NiO by CH_4 and its partial oxidation derivatives.

RS I [58]	**RS II** [212]	**RS III** [114,118,216,217]	**RS IV** [79,213]
R1. $CH_4+2NiO\rightarrow 2Ni+2H_2+CO_2$	R2. $H_2+NiO\rightarrow Ni+H_2O$	R2. $H_2+NiO\rightarrow Ni+H_2O$	R2. $H_2+NiO\rightarrow Ni+H_2O$
R2. $H_2+NiO\rightarrow Ni+H_2O$	R3. $CO+NiO\rightarrow Ni+CO_2$	R3. $CO+NiO\rightarrow Ni+CO_2$	R3. $CO+NiO\rightarrow Ni+CO_2$
R3. $CO+NiO\rightarrow Ni+CO_2$	R4. $CH_4+NiO\rightarrow Ni+2H_2+CO$	R5. $CH_4+4NiO\rightarrow 4Ni+2H_2O+CO_2$	R4. $CH_4+NiO\rightarrow Ni+2H_2+CO$
R4. $CH_4+NiO\rightarrow Ni+2H_2+CO$			R5. $CH_4+4NiO\rightarrow 4Ni+2H_2O+CO_2$

In terms of the solid-state models for these heterogeneous reactions and in the absence of micro-kinetic analyses, such as density functional theory, the intrinsic kinetics of the non-catalytic reactions is commonly derived from empirical correlations and supported by materials characterization. These reaction models can be classified according to their mechanistic basis, such as nucleation, geometrical contraction, diffusion, and reaction order [132]. As these models vary in their degree of complexity and number of empirical parameters, statistical approaches were used to identify an overall best-suited model for the simplest CLC system: the reduction of NiO by H_2 [132]. Three adequate models were proposed for this system, out of 20 candidate solid-state kinetic models, by analyzing the statistical confidence of the model predictions, using all the experimental information available in the literature [132]. However, there exists uncertainty in this conclusion, in that the clear winner model was selected on the basis of a limited number of possibly sub-optimal experiments. The purpose of this work is to increase the scope of the work of Zhou et al. [132] to a CH_4-fed system, which is among the target feedstocks for gaseous CLC. To simplify the problem, the three best models selected by Zhou et al. [132] are designated as the candidate mechanistic solid-state reaction models, motivating the need for model discrimination. **Table 6.2** shows the rate expressions of these solid-state kinetic models: Avrami-Erofe'ev (AE), shrinking core (SC) and volumetric (V) models. A modified form of the V model was proposed by Iliuta et al. [58] to account for the commonly observed activation step in the reduction of NiO by CH_4. The modified volumetric model (MV) was previously used to arrive at accurate predictions of several literature-reported CLC and CLR

data [119,128,193]. For completeness, a similarly modified form of the SC model (MSC) is also introduced.

Table 6.2: Candidate solid-state reaction models for CLC, based on Zhou et al. (2014) [132].

Reaction model	**Rate expression**
Avrami-Erofe'ev (AE)	$\frac{dX}{dt} = kn(1-X)\left[-\ln(1-X)\right]^{(n-1)/n}$
Volumetric (V)	$\frac{dX}{dt} = k(1-X)^2$
Modified V (MV)	$\frac{dX}{dt} = kX(1-X)^2$
Shrinking core (SC)	$\frac{dX}{dt} = 3k(1-X)^{2/3}$
Modified SC (MSC)	$\frac{dX}{dt} = 3kX(1-X)^{2/3}$
Zero order*	$dX/dt = k$

*This mechanistic model was used only in the SLI analysis and not included among the candidate mechanistic models because it was previously rejected by Zhou et al. [132].

It is important to clarify that in these modified models (MV and MSC) only CH_4 is considered to be capable of being "activated" by bare Ni, affecting its reactivity with NiO. This is based on the experimental observations by Iliuta et al. [58], where a CH_4 activation step was seen to precede its reaction with NiO. This is commonly referred to as "methane slip" in CLC systems [39,127,184,202,212], where CH_4 is observed to escape the reactor unreacted during the initial stages of NiO reduction. Some CLC and CLR studies [40,73,121] assume CH_4 steam reforming as the main mechanism for CH_4 conversion, explaining "methane slip" as the result of the initial low reforming activity, driven by the absence of metallic Ni. With the AE model, the activation barrier is inherently captured, determined by the value of the Avrami-Erofe'ev parameter, *n*. Generally, *n* can be assumed to be independent of the reacting gas species and specific to the active metal in the oxygen carrier. Thus, a single value of *n* can be used to represent all the heterogeneous reduction reactions of interest for the NiO

system. The mechanistic models of **Table 6.2** are used to describe the rate of the oxygen carrier reactions found in **Table 6.1**. So far, 20 literature-reported kinetic models are possible for modeling of the NiO reduction by CH_4.

Table 6.3: Candidate catalytic reactions for CLC reduction with a Ni-based oxygen carrier and CH_4 fuel [119].

Reaction	**Stoichiometry**
R6. Steam methane reforming (SMR)	$CH_4 + H_2O \leftrightarrow CO + 3H_2$
R7. Water gas shift (WGS)	$CO + H_2O \leftrightarrow CO_2 + H_2$
R8. Overall SMR	$CH_4 + 2H_2O \leftrightarrow CO_2 + 4H_2$
R9. Methanation	$CO + 3H_2 \rightarrow CH_4 + H_2O$
R10. Dry reforming	$CH_4 + CO_2 \leftrightarrow 2CO + 2H_2$
R11. Methane cracking	$CH_4 \leftrightarrow C + 2H_2$
R12. C gasification by H_2O	$C + H_2O \leftrightarrow CO + H_2$
R13. C gasification by CO_2	$C + CO_2 \leftrightarrow 2CO$

The problem is made significantly more complex by the introduction of the Ni-catalyzed reactions of CH_4 and its gaseous and solid products, which cannot be neglected as Ni is the product of NiO reduction. First, we explore the uncertainty in the relevant reaction schemes and later we discuss the issue of describing the catalytic reactivity of Ni, when it coexists with NiO. **Table 6.3** summarizes all the relevant catalytic reactions reported to occur in the presence of Ni. It is noteworthy that most investigators do not use all of the reactions listed in **Table 6.3** in their kinetic models [119]. In particular, there are inconsistencies between investigators on which combination of steam CH_4 reforming and side reactions should be used (R6-R13 in **Table 6.3**) [49,58,72,118,119,171,212,218].

Table 6.4: Possible reforming schemes used in the CLC literature.

RS I [171]	**RS II** [118,218]
R6. $CH_4+H_2O\leftrightarrow CO+3H_2$	R6. $CH_4+H_2O\leftrightarrow CO+3H_2$
R7. $CO+H_2O\leftrightarrow CO_2+H_2$	R7. $CO+H_2O\leftrightarrow CO_2+H_2$
R8. $CH_4+2H_2O\leftrightarrow CO_2+4H_2$	R8. $CH_4+2H_2O\leftrightarrow CO_2+4H_2$
R9. $CO+3H_2\rightarrow CH_4+H_2O$	
RS III [49,58]	**RS IV** [72,119,212]
R6. $CH_4+H_2O\leftrightarrow CO+3H_2$	R6. $CH_4+H_2O\leftrightarrow CO+3H_2$
R7. $CO+H_2O\leftrightarrow CO_2+H_2$	R7. $CO+H_2O\leftrightarrow CO_2+H_2$
R9. $CO+3H_2\rightarrow H_4+H_2O$	

Table 6.4 illustrates the reaction networks typically considered in steam methane reforming (SMR) [49,58,72,118,119,171,212,218]. The most basic scheme (RS IV) consists of the SMR reaction in conjunction with the water gas shift (WGS) reaction, usually considered at equilibrium. Additional side reactions are the overall SMR and methanation reactions, which added to RS IV lead to RS II and III. The most comprehensive CH_4 reforming reaction network (RS I) under CLC conditions was proposed by Jin et al [171] Nonetheless, RS II reflects the most widely used reaction network for CH_4 steam reforming over a Ni catalyst [219,220]. Xu and Froment [219] expressed the three reversible reactions, SMR, WGS, and overall SMR, of RS II, based on a Langmuir-Hinshelwood reaction mechanism. In Zhou et al. [119], the overall SMR and methanation reactions were omitted because those reaction rates can be obtained by a combination of the first two reactions (SMR and WGS). However, the methanation reaction is often postulated to occur irreversibly as a separate reaction [221], justifying RS III. If either the overall SMR or the methanation reaction is not statistically significant to the overall CLC reaction scheme, similar predictions can be attained by a simpler model from adjusting the kinetic rates of the SMR and WGS. Therefore, the challenge that needs to be addressed is in the identification of the most statistically-rich reaction scheme at the conditions relevant to CLC. Augmentation of the 20 feasible NiO reduction kinetic models with the 4 reported reaction pathways for the catalytic reactions results in 80 possible reaction

kinetic models for CLC of CH_4 with NiO.

The continuous conversion of NiO to Ni in the CLC system (owed to the NiO reduction reactions) dynamically alters the content and possibly the catalytic activity of Ni. This joint effect on the rate of the catalytic reactions, r_{cat}, as compared to that of a completely reduced oxygen carrier, r_{cat}^0, is often expressed as a function of the instantaneous concentration of Ni, c_{Ni}, as:

$$r_{cat} = c_{Ni} r_{cat}^0. \tag{6.1}$$

Eq.(6.1) was successfully used by various authors [58,119,193] for simulating CLC with a Ni-based oxygen carrier. Ortiz et al. [118] used an alternate form of Eq.(6.1), Eq.(6.2), to include additional parameters that provided better predictions of their experimental data.

$$\begin{aligned} r_{cat} &= \alpha_{cat} r_{cat}^0, \\ \alpha_{cat}(X) &= a + bX + cX^2. \end{aligned} \tag{6.2}$$

The catalytic activity term α_{cat} was assumed a function of the instantaneous conversion of NiO to Ni, X, and multiplied to the rate of the catalytic reactions over a reduced Ni catalyst, r_{cat}^0, noting that the empirical parameters were specific to the type of oxygen carrier used, including the effect of the NiO support [118]. For the NiO/α-Al_2O_3 oxygen carrier of Ortiz et al. (2012) [118], the α_{cat} parameters of Eq.(6.2) were $[a = 0, b = 1, c = 0]$, which reduces Eq.(6.2) to Eq. (6.1). An activation barrier was observed with the NiO/γ-Al_2O_3 oxygen carrier, which was modeled by Ortiz et al. [118] by modifying the α_{cat} parameters to $[a = 0, b = 0.19, c = 0.81]$. It remains unclear whether using α_{cat} to account for the catalytic activity provides a statistical advantage over Eq.(6.2), or it is simply an artifact of over-parameterizing the model.

In summary, the inconsistencies listed in **Tables 6.1-6.4** and Eqs.(6.1)-(6.2) amount to 160 candidate models to describe the CLC reduction of NiO by CH_4. Given this size of problem, it becomes necessary to use a systematic framework for model elimination, to eventually arrive at a single, statistically significant model. We note again, that this winner or true model would not be the derivative of fundamental micro-kinetics analyses. Instead, it will reflect the most valuable model from the process engineering

perspective; the one that can be used in process and reactor design without the bottlenecks of uncertainty and arbitrary experimental bias. For convenience, the models are referred throughout the rest of the paper as $\mathbf{M}_{A-B-C-D}$, where *A* denotes the NiO reduction reaction pathway (RS I-IV) of **Table 6.1**, *B* the reaction models (AE, SC, V, SCM, VM) of **Table 6.2**, *C* the catalytic reforming scheme (RS I-IV) of

Table 6.4, and *D* the function capturing the effect of Ni on the catalytic reactivity (1→ Eq.(6.1); 2→ Eq.(6.2)). Section 6.2.2 discusses the conventional CLC experiments used to extract kinetic parameters and compares their capability to identify each reaction using a previously validated kinetic model. To meet the target of identifying a single "true" model, the experimental investment would be large and does not guarantee statistically significance in the model structure or parameters. Thus, an optimal way to design experiments is needed. Section 6.3 details the proposed solution approach to address the reaction kinetics problem, based on a model-based experiment design framework.

6.2.2. Ill-designed experiments

In this section, we motivate the design of experimental setups and conditions by analyzing the sensitivity of the product gases in a fixed bed CLC reactor, operated with a NiO oxygen carrier and CH_4 reducing feed [128,193]. The objective is to illustrate the dynamic sensitivity of typical fixed bed CLC measurements with respect to the kinetic parameters of a given model in various reactor designs. In essence, we explore the impact of experimentation apparatus and its design, before entering the discussion of how to design optimal experiments for it. Potential deficits of conventional experiment designs are identified, on the basis of low sensitivities of the measured variables to the kinetic parameters. From these case studies, it becomes evident that the "rules-of-thumb" of traditional experiment designs are inadequate to derive precise estimates of model parameters, within a reasonable timeframe and effort.

6.2.2.1. Sensitivity analysis of NiO reduction by CH_4 in existing reactor designs

The reduction of NiO by CH_4 was previously [128,193] described by a 1-D heterogeneous reactor model described in Chapter 5 with the kinetic model with structure $\mathbf{M}_{I-III-IV-I}$. The same model was applied to

the literature-reported experimental designs of **Table 6.5**, and accurate predictions of CLC reduction experimental data were obtained (**Figure 6.1**), after fitting the kinetic rate constants for the inherent differences in the oxygen carrier. The data of **Figure 6.1** show the transient evolution of the gas concentrations during a single reduction step. As shown in **Figure 6.1(a)**, a high fraction of unconverted CH_4 escapes the system of Iliuta et al. [58] at the beginning of reduction, due to an initial activation barrier between NiO and CH_4. Afterwards, complete combustion products (H_2O, CO_2) are produced from the NiO reduction reactions with CH_4, H_2, and CO. Over time, the conversion of NiO to Ni favors the catalytic reactions, forming H_2 and CO in addition to H_2O and CO_2. The so-called CH_4 slip is less significant in **Figure 6.1(b)** and completely absent in **Figure 6.1(c)**, which can be explained by the differences in Péclet numbers between the units. We note that in **Figure 6.1(b)**, the elongated CH_4 peak is due to the mixing downstream of the reactor, which was not significant in the setup of Iliuta et al. [58] (**Figure 6.1(a)**). Nonetheless, from the close agreement between model and experiments (**Figure 6.1**), we could assume that this kinetic model is correct. In the next series, we challenge the accuracy and statistical significance of the previously used models on the basis of theoretical identifiability analyses and optimally designed experiments for model discrimination. Here, we illustrate some issues with the data and models shown in **Figure 6.1**, through a dynamic sensitivity analysis.

Table 6.5: Design of the CL fixed bed units in the literature.

	Iliuta et al. [58]	Zhou et al. [119]	Rydén et al. [172]
L [mm]	7.65	21.7	5.66
D [mm]	4	9.9	15
Q [ml min^{-1}]	100	100	60
Reducing gas	10% CH_4 /Ar	10% CH_4/ Ar	25% CH_4 /Ar
Oxidizing gas	21% O_2/Ar	10% O_2/Ar	Air
T [°C]	800,900	800	900
d_p [μm]	140	100	120
Re_p	0.5	0.07	0.02
Pe	>200	~200	~1

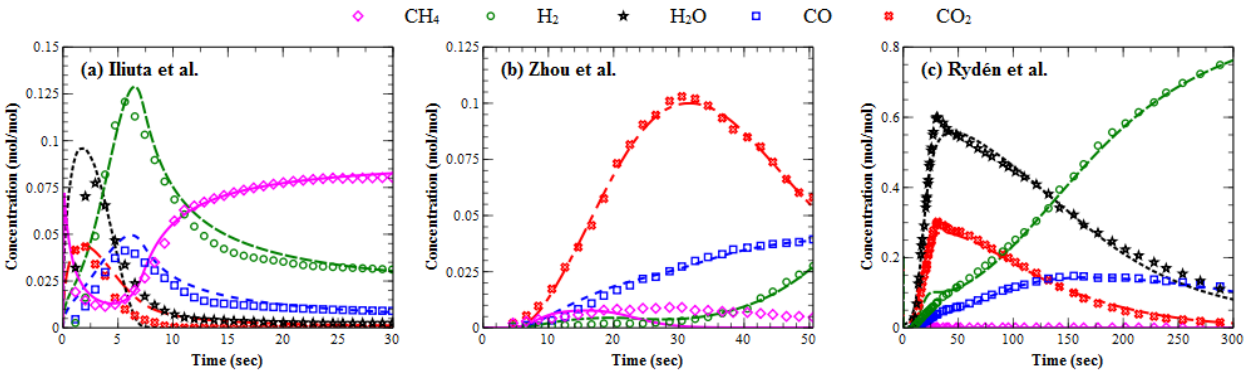

Figure 6.1: Experimental data and model predictions of reduction of NiO by CH_4 in the fixed bed reactor of (a) Iliuta et al. [58] at 900°C, (b) Zhou et al. [119] at 800°C, and (c) Rydén et al. [172] at 900°C.

Figure 6.2 presents the log-normalized dynamic sensitivities of the exit CH_4 concentration with respect to the frequency factor of the kinetic rate constants $\left(\frac{\partial C_{CH_4}(t,L)}{\partial k_{j,0}}\right)$ for the reactor designs of **Table 6.5** at 800°C. The dynamic sensitivities were computed using the direct differentiation method outlined in Atherton et al [222]. In the case of **Figure 6.2(c)**, a high degree of back-mixing in the reactor (due to very low Péclet numbers) results in insensitive measurements (with respect to the kinetics of interest) and leads to large uncertainty in their estimation precision. As the Péclet number increases, such as in **Figures 6.2(a)-6.2(b)**, the sensitivity of $C_{CH_4}(t,L)$ with respect to the kinetic parameters increases, because of the enhanced plug flow behavior. The experimental designs of Iliuta et al. [58] and Zhou et al. [119] are not practical for commercial CLC applications because of their low CH_4 conversion and CO_2 capture efficiency; but they are more suitable for estimating the kinetic parameters of the NiO reduction reactions. Conversely, the design of Rydén et al. [172] achieves almost 100% CH_4 conversion, but is not adequate for kinetic parameter estimation because of its lack of parameter sensitivity. Thus, kinetic parameters derived from the experimental data of Rydén et al [172]. will be statistically insignificant and different parameter values can essentially lead to the same model response.

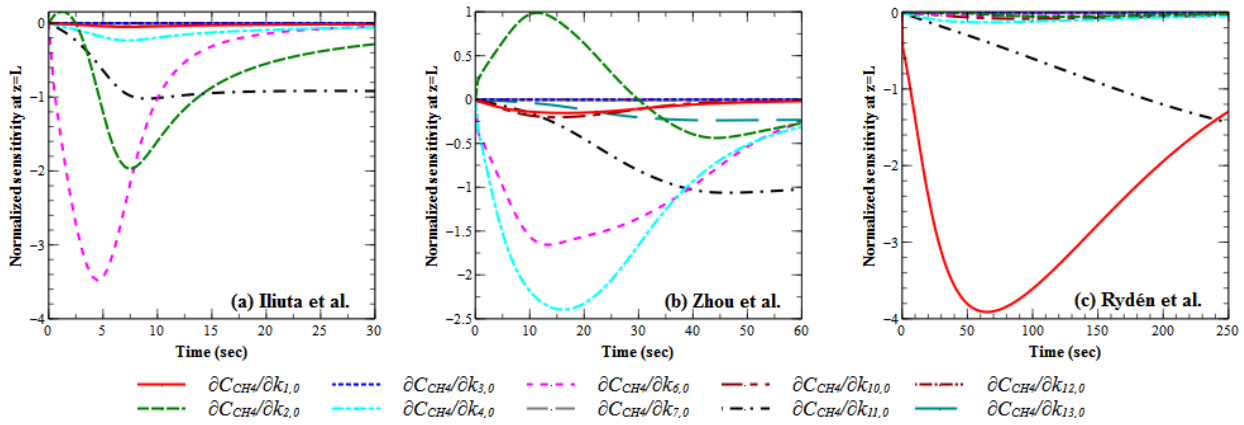

Figure 6.2: Normalized sensitivity functions of CH_4 concentration at the reactor exit with respect to the relevant CLC kinetic parameters for the fixed bed designs of (a) Iliuta et al. [58], (b) Zhou et al. (2013) [119], and (c) Rydén et al. (2008) [172] at 800°C.

As shown in **Figure 6.2(a)**, the exit CH_4 concentration is initially sensitive to the methane steam reforming reaction ($k_{6,0}$) and then it is sensitive to the NiO reduction reactions ($k_{2,0}$ and $k_{4,0}$). This separation of the sensitivity peaks is beneficial for de-convoluting the CLC reduction kinetics, by reducing the covariances of the parameter estimates [223]. Still, the design is not optimal, since only two of the four NiO reduction reactions are observable in the sensitivity analysis. In the case of **Figure 6.2(b)**, more NiO reduction reactions are potentially identifiable ($k_{1,0}, k_{2,0}$ and $k_{4,0}$) because the design yields more observable sensitivities in relation to the catalytic reactions. Still, this does not guarantee statistical significance of the estimated kinetics because of the lack of peak separation. The sensitivity profile of **Figure 6.2(c)** characterizes a design where the system is essentially insensitive to the reaction kinetics. In summary, it is not feasible to uniquely and precisely identify all the kinetic parameters from the studied experiment designs of **Table 6.5**. Evaluation of the dynamic sensitivities of **Figure 6.2** motivates the need to find an experiment design that maximizes the information available for identification and estimation of kinetic parameters.

6.2.2.2. Sensitivity of kinetic parameters of a given model with respect to the reactor and experimental design

Here, we show how the kinetic information in the form of parameter sensitivities can be used to design bench-scale fixed bed CLC reactors. For this exercise, the kinetic model and corresponding kinetic parameters used to predict the data of **Figure 6.1** are assumed correct. We focus on the reactor design of Zhou et al. [119] (**Figure 6.1(b)**) and explore the sensitivity of the measurable gas species with respect to the NiO reduction kinetic parameters over time and axial direction of the fixed bed. Analysis of the axial profile of the parameter sensitivities is valuable because the length of the fixed bed can be easily manipulated in the experimental design by adjusting the loading of the oxygen carrier. Simply put, for a bench-scale system the reactor design problem is often identical to the experiment design problem.

The normalized dynamic sensitivities of the gas concentrations (CH_4, H_2, CO, CO_2) with respect to the NiO reduction frequency factors *vs.* the reactor length and experiment time are shown in **Figure 6.3**. The sensitivity of CH_4 with respect to the NiO reduction reactions ($k_{1,0}$ and $k_{4,0}$) is initially very low, but increases over the reactor length and reduction time, as shown in **Figure 6.3(a)** and **Figure 6.3(d)**. At any time and position, the CH_4 concentration is much more sensitive to $k_{4,0}$ than $k_{1,0}$. The partial products (H_2, CO) generated from the reduction reactions are subsequently oxidized to H_2O and CO_2 by the downstream NiO. This is shown in the sensitivity profiles of H_2 with respect to $k_{2,0}$ (**Figure 6.3(f)**) and that of CO and CO_2 with respect to $k_{3,0}$ (**Figure 6.3(k)** and **Figure 6.3(o)**). The concentration of CO_2 is more sensitive to $k_{4,0}$ and $k_{1,0}$ (**Figure 6.3(m)** and **Figure 6.3(p)**), which is unexpected because R4 produces CO and H_2 and R1 produces CO_2 and H_2 (**Table 6.1**). This can be explained by the co-existence of the catalytic reactions such as the steam reforming or water gas shift, impacting the reaction equilibria. As discussed previously, conversion of CH_4 is highly sensitive to the steam reforming reaction and so production of CO_2 follows a combination of the NiO reduction and reforming reactions (and simultaneous water gas shift). The high sensitivity of CO_2 with respect to $k_{2,0}$ and $k_{4,0}$ (**Figure 6.3(n)** and **Figure 6.3(p)**) indicates that most of the CO_2 produced is from the catalytic reactions, rather than the oxidation

reactions with NiO.

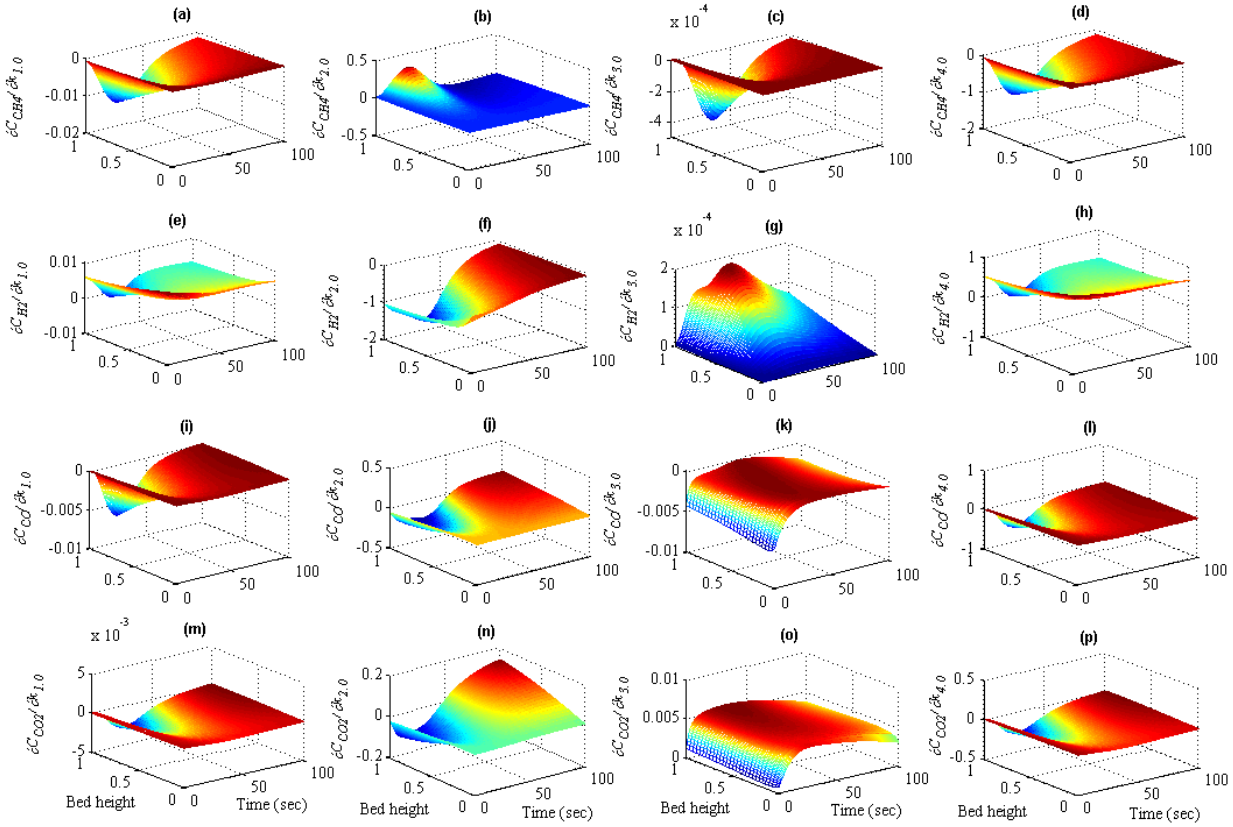

Figure 6.3: Surface plot of the normalized dynamic sensitivity of gases (CH_4, H_2, CO and CO_2) to the NiO reduction kinetic parameters, for the experimental setup of Zhou et al. [119].

Based on **Figure 6.3**, we can design an optimal reactor length and experiment duration that maximizes the sensitivities of the measured gases with respect to the NiO reduction kinetics in an effort to improve the precision of the parameter estimates. The absolute maximum of the sensitivity functions is generally located at the reactor exit for the design of Zhou et al. [119]. This is advantageous from the experimental perspective, because the exhaust gases are measured downstream the reactor. Furthermore, it is possible that increasing the reactor length can increase the dynamic sensitivity response of the exhaust gas with

respect to the NiO reduction kinetic parameters. Even so, it is challenging to identify $k_{1,0}$ and $k_{3,0}$ because they generally exhibit lower sensitivities as compared to $k_{2,0}$ and $k_{4,0}$. Thus, a different solution approach is needed to estimate all the uncertain kinetic parameters, beyond simply examining the sensitivity responses. In the next section, we introduce model-based experiment design methods as the solution approach to design better experiments to study the reduction of NiO by CH_4.

6.3. Design of experiments

6.3.1. State of the art of model-based methods

Methods for design of experiments (DOE) have been widely used to provide rich experimental information at minimum effort. The objective of DOE is to minimize uncertainty and maximize the useful information that can be extracted from the experiment. Early applications of DOE, such as factorial methods, randomized blocks, and Latin squares, viewed experiments as a series of inputs and outputs and selected the best combination of inputs to maximize the information about their relationship in the presence of experimental variance [224–227]. These classical design techniques are commonly referred to as black-box methods and are still widely used, because they are easy to implement, their results are easily interpreted, and allow the study of interactions between factors [228–231]. However, these methods are not well-suited for dynamic experiments and can be expensive in terms of experimental resources [232].

Model-based DOE relies on the explicit use of a mathematical model with some uncertainty in its parameters and/or model structure, cast as an optimization problem to predict the information content of the next series of experiments. These model equations reflect our current state of understanding of the process being investigated, wherein the use of unknown parameters and semi-empirical model structures denotes incomplete knowledge. Early applications of model-based DOE in the field of chemical kinetics were conducted for steady-state systems [233–237]. These concepts were extended to dynamic processes by Mehra [238], Shirt et al. [239], and Macchietto et al. [240–243]. Similar problems in the field of bio-

kinetics were treated within the model-based DOE framework to address the lack of parameter identifiability [244–247]. More recent work on model-based experimental design techniques is focused on developing new objective functions [248–250], robust algorithms [251–254], and efficient methods to handle uncertainty [255]. The model-based designs have been successfully applied to a wide range of systems to facilitate and improve the modeling of chemical kinetics [223,256–262], biochemical networks [263,264], and biological processes [265–267]. The potential applications are abundant across all engineering disciplines and can be applied to any system (linear, non-linear, steady-state or dynamic). In this work, we apply the model-based DOE to partially address the controversy of the kinetic models for the NiO-CH_4 system in order to minimize the experimental effort required to construct a sufficiently accurate and statistically significant model. In the next section, we provide the complete mathematical background for this analysis.

6.3.2. Mathematical formulation

The general representation of a CLC process model with structure **M** is written as a set of differential and algebraic equations (DAEs), as shown in Eq.(6.3):

$$\mathbf{M}: \begin{cases} \mathbf{f}\left(\dot{\mathbf{x}}\left(t\right), \mathbf{x}\left(t\right), \mathbf{u}\left(t\right), \boldsymbol{\theta}, t\right) = 0, \\ \hat{\mathbf{y}}\left(t\right) = \mathbf{h}\left(\mathbf{x}\left(t\right)\right), \end{cases} \tag{6.3}$$

where **f** is the system of differential equations describing the conservation of mass, energy, and momentum for the gas and solid phases, $\mathbf{x}(t)$ is the vector of the time-dependent state variables, such as concentration, temperature, and pressure, $\mathbf{u}(t)$ is the manipulated process variables (*e.g.*, gas flow rate and composition), $\boldsymbol{\theta}$ is the set of kinetic parameters to be estimated, and *t* is the time. The vector of measured variables, $\hat{\mathbf{y}}(t)$, is a function of the state variables, selected by $\mathbf{h}(\mathbf{x}(t))$ to match the sampling times of the measurement device $\mathbf{t}_{sp}$. The system of equations is constrained by algebraic and differential constraints, marked by the equation of state, flux balances, molar expansion terms, thermodynamic calculations, etc.

Let us define a generic experiment design vector $\boldsymbol{\phi}'$, containing the set of manipulated variables:

$$\boldsymbol{\varphi}' = [\mathbf{u}(t), \mathbf{t}_{sp}, \mathbf{y}_0, \tau]^T \in \boldsymbol{\Phi}', \tag{6.4}$$

where $\mathbf{y}_0$ is the set of initial conditions controlled by the manipulated variables $\mathbf{u}(t)$ and τ is the experiment duration. The design variables of $\boldsymbol{\phi}'$ are constrained within the design space $\boldsymbol{\Phi}'$, defined by the upper and lower bounds of the system. This design vector is modified for experiments performed in a standard fixed bed reactor to estimate kinetics. In most cases, the controls cannot be altered dynamically during a fixed bed experiment, so $\mathbf{u}(t)$ is simply taken as $\mathbf{u}(t_0)$. Also, the sampling times $\mathbf{t}_{sp}$ are often fixed by the measurement device and cannot be controlled. Thus, a simplified experiment design vector is used for the remainder of this work, as shown in Eq.(6.5):

$$\boldsymbol{\varphi} = [\mathbf{u}(t_0), \mathbf{y}_0, \tau]^T \in \boldsymbol{\Phi}. \tag{6.5}$$

6.3.3. Model-based experimental design framework

The model building procedure by Macchietto and co-workers [232,240,241] is adapted here to statistically verify and discriminate among the candidate kinetic models discussed in Section 6.2.1. Depicted in **Figure 6.4**, this procedure is divided into three consecutive stages:

Stage 1: First, models are proposed and are subsequently evaluated on the basis of their structural identifiability and distinguishability. The uncertainty in the Ni-catalytic reactions, NiO reduction reactions, and their interaction is treated separately.

Stage 2: Optimal experiments are designed and performed to discriminate among the candidate models that passed the preliminary analysis of Stage 1. The first experiment is designed under the worst-case criterion assumption where the candidate models are equally likely to be the true model. The best model is re-evaluated in a subsequent experiment design before concluding to a final model structure.

Stage 3: Optimal experiments are designed and performed to estimate the kinetic parameters of the winner model from Stage 2.

Typically, iteration between the interior loops or between the stages is required if the desired criteria are not met.

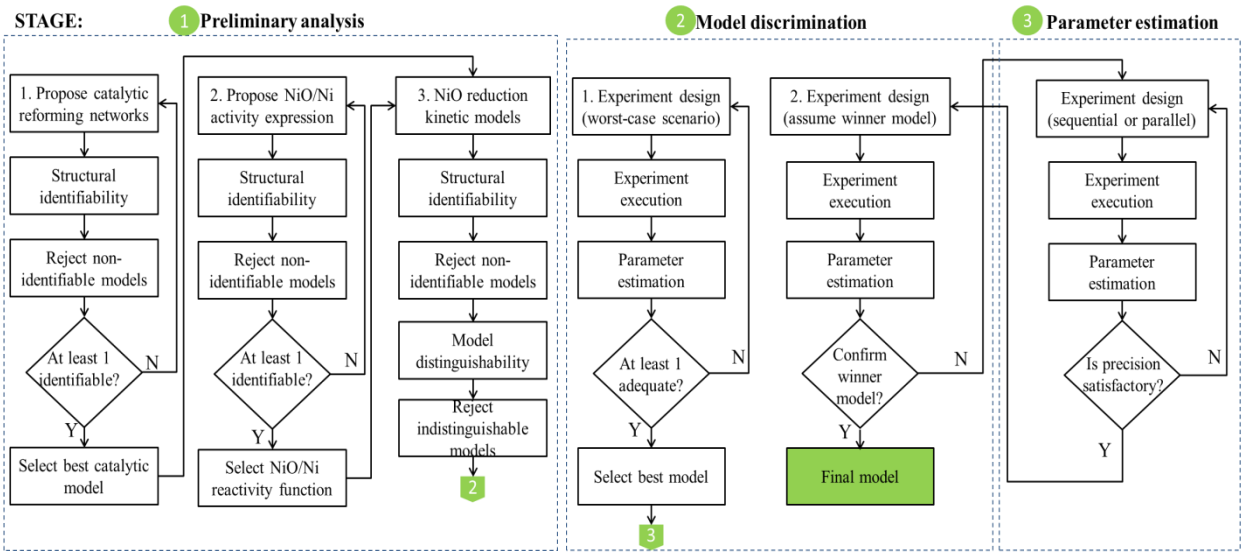

Figure 6.4: The overall model-based experimental design framework adapted from Macchietto et al. [232,240,241] as the solution approach to the problem statement of Section 6.2.

6.3.3.1. Stage 1: Preliminary analysis

In the development of a model, the mechanisms of the system under investigation are not always fully understood and experiments are needed to better understand them. Often, several plausible models can be conceptualized to describe the physical phenomena. During the preliminary model analysis, identifiability tests are conducted to assess the structure of the proposed model(s) [268,269]; specifically, to confirm in principle if an experiment design exists such that the parameters can be given unique values for a certain model structure. It is often argued that issues encountered during parameter estimation by means of data fitting are originated from the lack of identifiability of the unknown parameters [270]. To overcome this issue, theories of identifiability analysis have been postulated, including structural (theoretical) identifiability, practical identifiability, and sensitivity matrix analysis [271–273]. If a lack of identifiability is encountered from the structural analysis, it necessitates the rejection or reformulation of the model structure [270]. Practical identifiability, on the other hand, deals with the issue of limited, noise-corrupted data, which can be overcome via increasing the number of sampling times, measurement

devices, or their precision [274]. Here, structural identifiability analysis is used to check for potential non-identifiability of the CLC kinetic parameters of the set of possible model structures. If lack of identifiability is encountered from the structural analysis, it necessitates the rejection or reformulation of the model structure [270]. In practice, this means that for a given model structure, if parameters cannot be uniquely identified, then experimentation is going to be inconclusive. In this work, the structural identifiability analysis is used to check the selection of the kinetic models and ensure that the kinetic parameters they contain are mathematically distinct, following the steps of Stage 1 (**Figure 6.4**). Kinetic models with non-identifiable parameters are rejected in this preliminary analysis, while remaining models are then evaluated in terms of model distinguishability.

6.3.3.1.1. Structural identifiability analysis

Structural identifiability methods were reviewed in detail by Miao et al. [271]. The simplest method is the analytical direct test [275,276], which is argued to have limited applications because of the advanced methods needed to obtain analytical solutions [277]. More promising methods have been developed to detect structural non-identifiability, such as the power series expansion [278], the generating power series approach [279], the similarity transform approach [280,281], differential algebraic methods [272,282], and a method based on the implicit function theorem [283]. An optimization-based approach was proposed by Asprey et al. [241,284] to test for global structural identifiability. Vikhansky [258] modified the optimization problem proposed by Asprey et al. [241,284] to reduce the computation difficulties in finding a global minimum. Raue et al. [285] proposed a profile likelihood approach to infer parameter uncertainties in a higher-dimensional parameter space. Unfortunately, the applicability of these methods rapidly becomes infeasible with increasing model complexity [286].

Structural identifiability of the kinetic models is analyzed on the basis of the local and global identifiability tests, as outlined by Galvanin et al. [287]. First, the S*tructural Local Identifiability* (SLI) of the parameters is checked by the correlation matrix approach [288,289]. A correlation matrix of the parameters ($\widehat{\boldsymbol{\theta}}^0$) is calculated from the Fisher information matrix, given in Eq.(6.6):

$$\mathbf{H}_{\theta}(\hat{\boldsymbol{\theta}}^{0},\boldsymbol{\varphi}^{0})=\sum_{r=1}^{N_y}\sum_{s=1}^{N_y}\sigma_{rs}\mathbf{Q}_{r}^{T}\mathbf{Q}_{s}, \tag{6.6}$$

where σ_{rs} represents the *rs*-th element of inverse of the matrix of experiment errors and $\mathbf{Q}_r$ is the $N_{sp} \times N_\theta$ matrix of the dynamic sensitivity evaluated around the initial values of the parameters $\hat{\boldsymbol{\theta}}^0$ for the r-th response variable, as defined in Eq.(6.7):

$$\mathbf{Q}_{r}=\begin{bmatrix} \left.\frac{\partial\hat{y}_r}{\partial\hat{\theta}_1^0}\right|_{t_1} & \cdots & \left.\frac{\partial\hat{y}_r}{\partial\hat{\theta}_{N_\theta}^0}\right|_{t_1} \\ \vdots & \ddots & \vdots \\ \left.\frac{\partial\hat{y}_r}{\partial\hat{\theta}_1^0}\right|_{t_{N_{sp}}} & \cdots & \left.\frac{\partial\hat{y}_r}{\partial\hat{\theta}_{N_\theta}^0}\right|_{t_{N_{sp}}} \end{bmatrix}. \tag{6.7}$$

If the measurement errors are uncorrelated and follow a normal distribution with a zero mean, it can be proved from the Cramèr-Rao theorem [239,290] that the inverse of $\mathbf{H}_\theta$ is equal to the variance-covariance matrix $\mathbf{V}_\theta$ [271]. The correlation matrix is constructed from the elements of $\mathbf{V}_\theta$, as shown in Eq.(6.8):

$$\begin{aligned} r_{ij}&=\frac{V_\theta(\theta_i,\theta_j)}{\sqrt{V_\theta(\theta_i,\theta_i)}\sqrt{V_\theta(\theta_j,\theta_j)}}, i\neq j, \\ r_{ij}&=1, i=j. \end{aligned} \tag{6.8}$$

If θ_i and θ_j are strongly correlated, their correlation coefficient r_{ij} is close to ±1, and they are thus non-identifiable [253,287,291,292]. For most cases, non-singularity of $\mathbf{H}_\theta$ is also accepted as a criterion for satisfying the SLI test [293].

We note that the information matrix has an important role in optimizing experiment designs for parameter estimation, which is relevant to the question of identifiability. The SLI test performed in this work takes advantage of the information matrix, by solving a D-optimal design problem, to seek a hypothetical design that minimizes the correlation between the kinetic parameters [294], shown in Eq.(6.9). If the parameters are still highly correlated under the best-case scenario of the D-optimal design, then it warrants the rejection of the respective kinetic model from the analysis.

$$\boldsymbol{\varphi}_{SLI} = \arg\max_{\boldsymbol{\varphi}\in\boldsymbol{\Phi}} \left\{ \det\left[\mathbf{H}_{\theta}(\hat{\boldsymbol{\theta}}^{0}, \boldsymbol{\varphi}^{0}) \right] \right\}$$

$$\begin{aligned} &\textit{subject to :} \\ &\mathbf{f}\left(\dot{\mathbf{x}}(t), \mathbf{x}(t), \mathbf{u}(t_0), \hat{\boldsymbol{\theta}}^{0}, t\right) = 0, \\ &\hat{\mathbf{y}}\left(t\right) = \mathbf{h}\left(\mathbf{x}\left(t\right)\right), \\ &\mathbf{u}_{\min} \le \mathbf{u}(t_0) \le \mathbf{u}_{\max} \qquad \forall t \in [0, \tau], \\ &0 < t \le \tau. \end{aligned} \tag{6.9}$$

SLI is a necessary but not sufficient condition for identifiability because it is solved over the initial parameter estimates, $\hat{\boldsymbol{\theta}}^{0}$. Thus, it is important to ensure parameter identifiability over the entire parameter space $\boldsymbol{\Theta}$, which is the objective of the S*tructural Global Identifiability* (SGI) test [272]. Correspondingly, the model with structure $\mathbf{M}$ is said to be globally identifiable if [272]:

$$\mathbf{M}(\mathbf{u}(t), \boldsymbol{\theta}, t) = \mathbf{M}(\mathbf{u}(t), \boldsymbol{\theta}^{*}, t) \;\Leftrightarrow\; \boldsymbol{\theta} = \boldsymbol{\theta}^{*}, \forall \boldsymbol{\theta}, \boldsymbol{\theta}^{*} \in \boldsymbol{\Theta},\ \boldsymbol{\Theta} \in \Re^{N_\theta}. \tag{6.10}$$

Satisfaction of Eq.(6.10) ensures that different parameter sets do not provide the same model response within the entire variability domain of the model parameters. The optimization-based approach proposed by Asprey and Macchietto [241] is applied here, wherein a kinetic model is deemed globally identifiable with respect to its parameters $\boldsymbol{\theta}$, if for two parametric sets, $\boldsymbol{\theta} \in \boldsymbol{\Theta}$ and $\boldsymbol{\theta}^{*} \in \boldsymbol{\Theta}^{*}$, Eq.(6.11) yields a global maximum that satisfies $\Phi_{SGI} \le \varepsilon_{\Phi_{SGI}}$:

$$\Phi_{SGI} = \max_{\boldsymbol{\theta}\in\boldsymbol{\Theta}, \boldsymbol{\theta}^{*}\in\boldsymbol{\Theta}^{*}} \left(\boldsymbol{\theta} - \boldsymbol{\theta}^{*}\right)^{T} \mathbf{W}_{\theta} \left(\boldsymbol{\theta} - \boldsymbol{\theta}^{*}\right)$$

$$\begin{aligned} &\textit{subject to :} \\ &\int_{0}^{\tau} \left(\hat{\mathbf{y}}\left(\mathbf{u}(t_0), \boldsymbol{\theta}, t\right) - \hat{\mathbf{y}}\left(\mathbf{u}(t_0), \boldsymbol{\theta}^{*}, t\right)\right)^{T} \mathbf{W}_{y} \left(\hat{\mathbf{y}}\left(\mathbf{u}(t_0), \boldsymbol{\theta}, t\right) - \hat{\mathbf{y}}\left(\mathbf{u}(t_0), \boldsymbol{\theta}^{*}, t\right)\right) dt < \varepsilon_{y}, \\ &\mathbf{f}\left(\dot{\mathbf{x}}\left(t\right), \mathbf{x}\left(t\right), \mathbf{u}\left(t_0\right), \boldsymbol{\theta}, t\right) = 0, \\ &\mathbf{f}\left(\dot{\mathbf{x}}\left(t\right), \mathbf{x}\left(t\right), \mathbf{u}\left(t_0\right), \boldsymbol{\theta}^{*}, t\right) = 0, \\ &\hat{\mathbf{y}}\left(t\right) = \mathbf{h}\left(\mathbf{x}\left(t\right)\right), \\ &\theta_{i,\min} \le \theta_{i} \le \theta_{i,\max} \qquad i=1,...,N_{\theta}, \\ &\theta^{*}_{i,\min} \le \theta^{*}_{i} \le \theta^{*}_{i,\max} \qquad i=1,...,N_{\theta^{*}}. \end{aligned} \tag{6.11}$$

Eq.(6.11) is solved over a time horizon of interest, $[0, \tau]$, and the optimal design determined from the SLI test, constrained by ε_{y}, being the time integral of the differences in model responses with $\boldsymbol{\theta}$ and $\boldsymbol{\theta}^{*}$. Weighting matrices on $\boldsymbol{\theta}$ and $\hat{\mathbf{y}}$ are $\mathbf{W}_{\theta} \in \Re^{N_\theta \times N_\theta}$ and $\mathbf{W}_{y} \in \Re^{N_y \times N_y}$, respectively and $\varepsilon_{\Phi_{SGI}}$ and ε_{y} are taken as small positive values. The optimization results of Eq.(6.11) can be influenced by the choice of $\varepsilon_{\Phi_{SGI}}$, and a generalized approach was proposed by Walter et al. [277] to make $\varepsilon_{\Phi_{SGI}}$ a function of a

specific weighting factor given to each parameter. No weighting function is required for $\hat{\mathbf{y}}$ in this study because they are molar fractions of the exit gas stream. To treat kinetic parameters equally, $\mathbf{W}_\theta$ normalizes the kinetic constants to a reference temperature.

6.3.3.1.2. Model distinguishability

Another possible scenario in the analysis of the kinetic models is that some of these models provide practically the same responses, within the input and parameter space determined. In practice, this means that two different models are indistinguishable if their responses overlie, for any $\boldsymbol{\theta} \in \boldsymbol{\Theta}, \boldsymbol{\theta}^* \in \boldsymbol{\Theta}^*, \boldsymbol{\phi} \in \boldsymbol{\Phi}$, and the same initial conditions.[241] Therefore, the test for model distinguishability is formulated as a semi-infinite max-min optimization problem, that maximizes (with respect to $\boldsymbol{\phi}$) the minimum (with respect to $\boldsymbol{\theta}, \boldsymbol{\theta}^*$) of the time integral of the differences between the responses of different model structures, $\hat{\mathbf{y}}$ and $\hat{\mathbf{y}}^*$, as shown in Eq.(6.12):

$$
\begin{aligned}
\Phi_D = \max_{\boldsymbol{\varphi}\in\boldsymbol{\Phi}} \min_{\boldsymbol{\theta}\in\boldsymbol{\Theta},\boldsymbol{\theta}^*\in\boldsymbol{\Theta}^*} & \int_0^{\tau} \left(\hat{\mathbf{y}}\left(\mathbf{u}\left(t_0\right),\boldsymbol{\theta},t\right) - \hat{\mathbf{y}}^*\left(\mathbf{u}\left(t_0\right),\boldsymbol{\theta}^*,t\right)\right)^T \\
& \times \mathbf{W}_y \left(\hat{\mathbf{y}}\left(\mathbf{u}\left(t_0\right),\boldsymbol{\theta},t\right) - \hat{\mathbf{y}}^*\left(\mathbf{u}\left(t_0\right),\boldsymbol{\theta}^*,t\right)\right) dt \\
& \textit{subject to :} \\
& \mathbf{f}\left(\dot{\mathbf{x}}\left(t\right),\mathbf{x}\left(t\right),\mathbf{u}\left(t_0\right),\boldsymbol{\theta},t\right) = 0, \\
& \hat{\mathbf{y}}\left(t\right) = \mathbf{h}\left(\mathbf{x}\left(t\right)\right), \\
& \mathbf{f}^*\left(\dot{\mathbf{x}}\left(t\right),\mathbf{x}\left(t\right),\mathbf{u}\left(t_0\right),\boldsymbol{\theta}^*,t\right) = 0, \\
& \hat{\mathbf{y}}^*\left(t\right) = \mathbf{h}^*\left(\mathbf{x}\left(t\right)\right), \\
& \theta_{i,\min} \le \theta_i \le \theta_{i,\max} \qquad i=1,\ldots,N_\theta, \\
& \theta^*_{i,\min} \le \theta^*_i \le \theta^*_{i,\max} \qquad i=1,\ldots,N_{\theta^*}, \\
& \mathbf{u}_{\min} \le \mathbf{u}(t_0) \le \mathbf{u}_{\max} \qquad \forall t \in [0,\tau].
\end{aligned}
\tag{6.12}
$$

The two models can be deemed distinguishable if $\Phi_D \geq \varepsilon_{\Phi_D}$. Asprey and Macchietto[241] recommended that ε_{Φ_D} be the integral of the expected variance of the measured $\mathbf{y}$.

6.3.3.2. Stage 2: Experiment design for model discrimination

With a collection of competing models with structures that have been deemed identifiable and distinguishable, experimental evidence is necessary to extract a winner model that best represents the physical system. In this stage, an optimal experiment is specifically designed to for the task of optimizing the discriminability between competing models. This approach finds an optimum design which

maximizes the divergence of the model trajectories, whereby poorly representative models are easily detected and thusly rejected. Assuming that the lack-of-fit of a model to the experimental data is attributed to experimental noise, parameter uncertainty, and inadequacy of the model structure, this stage maximizes the contribution of the latter and facilitates a comparison between rival models and selection of a winner model [295]. Several authors have addressed the problem of constructing optimum designs for this purpose [296–299]. This criterion was termed, T-optimality following the fundamental work by Atkinson and Fedorov [297,298] who applied it in the discrimination between two competing regression models. Various procedures and implementation of T-optimum designs have been considered (see for instance Uciński and Bogacka [300], Dette and co-workers [301,302], Tommasi and López-Fidalgo [303], and Waterhouse et al. [304] among others).

In the literature, many contributions to the design of experiments for model discrimination were conducted via the Bayesian [305–308] and frequentist approaches [252,309–311]. Under the Bayesian approach, the models are translated into Bayesian probability models, of which parameters are treated as random variables with a prior distribution. A utility function, which quantifies the discriminability of the rival models, is optimized with respect to the new decision variables. Within the Bayesian framework, randomness in experiment outcomes and uncertainty in model parameters are considered. After the n^{th} experiment stage, posterior distributions for parameters and models from the proceeding n-1 stage are taken as the new prior distributions for the n^{th} trial.

In contrast to the Bayesian approach, model selection from the frequentist perspective is focused on comparison of the sum of squares achieved with each model against the data. All the models are assigned an equal probability and an optimal experiment is designed to maximize the dissimiarility of the models. Upon execution of the frequentist designed experiments, the candidate models are assessed based on the statistical tests, such as the classical χ^2 test, in the data analysis [312]. Models can be rejected if the sum of the weighted residuals is unacceptably high, or retained if it is within statistical acceptable limits of the process. Various authors have found that despite the inherent differences between the Bayesian and

frequentist methods, the resulting differences between experiments designed with either criterion are very minor, if applied correctly [311,313,314]. Thus, the simpler frequentist method is applied here.

Under the frequentist approach, the T-optimum experiment is formulated as a dynamic optimization problem. The conventional T-optimal objective criterion was developed for the discrimination between two competing models, based on the assumption that one is initially considered as the "true" model with known parameters [298]. A second model is proposed, motivating an experiment to confirm the better model. This T-optimal criterion seeks a design that maximizes (with respect to $\boldsymbol{\phi}$) the minimum (with respect to $\boldsymbol{\theta}^{(2)}$) of the time integral of the differences between the model responses:

$$\begin{aligned}
&\boldsymbol{\varphi}_{T(1)} = \arg\max_{\boldsymbol{\varphi}\in\boldsymbol{\Phi}} \min_{\boldsymbol{\theta}^{(2)}\in\boldsymbol{\Theta}^{(2)}} \int_0^{\tau} \left(\hat{\mathbf{y}}^{(1)}\left(\mathbf{u}(t_0), \hat{\boldsymbol{\theta}}^{(1)}, t\right) - \hat{\mathbf{y}}^{(2)}\left(\mathbf{u}(t_0), \boldsymbol{\theta}^{(2)}, t\right)\right)^2 dt \\
&\quad \textit{subject to :} \\
&\quad \mathbf{f}^{(1)}\left(\dot{\mathbf{x}}(t), \mathbf{x}(t), \mathbf{u}(t), \hat{\boldsymbol{\theta}}^{(1)}, t\right) = 0, \\
&\quad \hat{\mathbf{y}}^{(1)}\left(t\right) = \mathbf{h}^{(1)}\left(\mathbf{x}\left(t\right)\right), \\
&\quad \mathbf{f}^{(2)}\left(\dot{\mathbf{x}}(t), \mathbf{x}(t), \mathbf{u}(t), \boldsymbol{\theta}^{(2)}, t\right) = 0, \\
&\quad \hat{\mathbf{y}}^{(2)}\left(t\right) = \mathbf{h}^{(2)}\left(\mathbf{x}\left(t\right)\right), \\
&\quad \hat{\theta}^{(1)}_{i,\min} \le \hat{\theta}^{(1)}_{i} \le \hat{\theta}^{(1)}_{i,\max} \qquad i=1,\ldots,N_{\theta^{(1)}}, \\
&\quad \theta^{(2)}_{i,\min} \le \theta^{(2)}_{i} \le \theta^{(2)}_{i,\max} \qquad i=1,\ldots,N_{\theta^{(2)}}, \\
&\quad \mathbf{u}_{\min} \le \mathbf{u}(t_0) \le \mathbf{u}_{\max} \qquad \forall t \in [0,\tau].
\end{aligned} \tag{6.13}$$

Heidebrecht et al. [223] proposed the simplified objective function of Eq.(6.14), in which the model parameters are constant. This assumes that both sets of parameters, $\boldsymbol{\theta}^{(1)}$ and $\boldsymbol{\theta}^{(2)}$**,** are known or estimated *a priori*. The solution of Eq.(6.13) or Eq.(6.14) is local, because it relies on the prior knowledge of the parameter estimates of the model considered as "true."

$$\begin{aligned}
&\boldsymbol{\varphi}_{T(2)} = \arg\max_{\boldsymbol{\varphi}\in\boldsymbol{\Phi}} \int_0^{\tau} \left(\hat{\mathbf{y}}^{(1)}\left(\mathbf{u}(t_0), \hat{\boldsymbol{\theta}}^{(1)}, t\right) - \hat{\mathbf{y}}^{(2)}\left(\mathbf{u}(t_0), \hat{\boldsymbol{\theta}}^{(2)}, t\right)\right)^2 dt \\
&\quad \textit{subject to :} \\
&\quad \mathbf{f}^{(1)}\left(\dot{\mathbf{x}}(t), \mathbf{x}(t), \mathbf{u}(t), \hat{\boldsymbol{\theta}}^{(1)}, t\right) = 0, \\
&\quad \hat{\mathbf{y}}^{(1)}\left(t\right) = \mathbf{h}^{(1)}\left(\mathbf{x}\left(t\right)\right), \\
&\quad \mathbf{f}^{(2)}\left(\dot{\mathbf{x}}(t), \mathbf{x}(t), \mathbf{u}(t), \hat{\boldsymbol{\theta}}^{(2)}, t\right) = 0, \\
&\quad \hat{\mathbf{y}}^{(2)}\left(t\right) = \mathbf{h}^{(2)}\left(\mathbf{x}\left(t\right)\right), \\
&\quad \mathbf{u}_{\min} \le \mathbf{u}(t_0) \le \mathbf{u}_{\max} \qquad \forall t \in [0,\tau].
\end{aligned} \tag{6.14}$$

Cooney and McDonald [315] proposed another type of T-optimum design that does not declare a winner

model *a priori*. A max-min problem similar to Eq.(6.13) is solved, with the exception that the minimization step is taken with respect to all the model parameters. This is referred to as the worst-case criterion by Asprey and Macchietto [241], who extended the formulation by Cooney and McDonald [315] to account for discrete sampling times, as given in Eq.(6.15):

$$
\begin{aligned}
\boldsymbol{\varphi}_{T(3)} = \arg\max_{\boldsymbol{\varphi}\in\boldsymbol{\Phi}} \min_{\substack{\boldsymbol{\theta}^{(j)}\in\boldsymbol{\Theta}^{(j)},\\ \boldsymbol{\theta}^{(k)}\in\boldsymbol{\Theta}^{(k)}}} & \sum_{i=1}^{N_{sp}}\sum_{j=1}^{N_M}\sum_{k=j+1}^{N_M} \left(\hat{\mathbf{y}}^{(j)}\left(\mathbf{u}(t_0),\boldsymbol{\theta}^{(j)},t_i\right)-\hat{\mathbf{y}}^{(k)}\left(\mathbf{u}(t_0),\boldsymbol{\theta}^{(k)},t_i\right)\right)^T \\
& \times\mathbf{W}_y\left(\hat{\mathbf{y}}^{(j)}\left(\mathbf{u}(t_0),\boldsymbol{\theta}^{(j)},t_i\right)-\hat{\mathbf{y}}^{(k)}\left(\mathbf{u}(t_0),\boldsymbol{\theta}^{(k)},t_i\right)\right) \\
& \textit{subject to :} \\
& \mathbf{f}^{(j)}\left(\dot{\mathbf{x}}(t),\mathbf{x}(t),\mathbf{u}(t_0),\boldsymbol{\theta}^{(j)},t\right)=0, \\
& \hat{\mathbf{y}}^{(j)}\left(t\right)=\mathbf{h}^{(j)}\left(\mathbf{x}\left(t\right)\right), \\
& \mathbf{f}^{(k)}\left(\dot{\mathbf{x}}(t),\mathbf{x}(t),\mathbf{u}(t_0),\boldsymbol{\theta}^{(k)},t\right)=0, \\
& \hat{\mathbf{y}}^{(k)}\left(t\right)=\mathbf{h}^{(k)}\left(\mathbf{x}\left(t\right)\right), \\
& \theta_{\min}^{(j)} \le \theta^{(j)} \le \theta_{\max}^{(j)} \qquad i=1,\ldots,N_{\theta^{(j)}}, \\
& \theta_{\min}^{(k)} \le \theta^{(k)} \le \theta_{\max}^{(k)} \qquad i=1,\ldots,N_{\theta^{(k)}}, \\
& \mathbf{u}_{\min} \le \mathbf{u}(t_0) \le \mathbf{u}_{\max} \qquad \forall t\in[0,\tau] \\
& t_{sp,1} \ge \Delta t_1, \\
& \Delta t_{sp}^{\min} \le t_{sp,i} - t_{sp,i-1} \le \Delta t_{sp}^{\max}, \qquad i=1,\ldots,N_{sp}.
\end{aligned}
\tag{6.15}
$$

A potential weakness of Eq.(6.15) is that kinetic parameters can be adjusted in a manner that the corresponding models lose accuracy. Thus, the designed experiment does not guarantee model discriminability for the competing kinetic models. Nonetheless, Eq.(6.15) is used in the foremost model discrimination of Stage 2 of **Figure 6.4** in an effort to not introduce bias, when selecting a true model. Once a winner model is deduced, precise estimates of the kinetic parameters are obtained from D-optimal designs, discussed in the following section. Then, it is necessary to return to the model discrimination stage to confirm that the winner model is indeed the best model to fit the data. This is carried out using Eq.(6.13), under the assumption that the previously selected model is the true model. If the model deemed "true" by Eq.(6.15) does not provide the best fit of the experimental data from the subsequent T-design from Eq.(6.13), it could mean that the selected model and/or parameter estimates are not adequate, necessitating the T-optimal/D-optimal designs to be reiterated until the process converges to a "true" winner model [316]. After completion of this model analysis step, there should exist only one winner model out of the original 160 possible CLC kinetic models.

6.3.3.3. Stage 3: Experiment design for parameter estimation

With a winner CLC kinetic model selected from Stage 2, the goal of Stage 3 is to design optimal experiments for the purpose of obtaining precise estimates of the kinetic parameters. The procedure shown in Stage 3 of **Figure 6.4** outlays three consecutive steps: (1) design of experiment(s) based on current knowledge; (2) execution of experiment(s); and (3) estimation of kinetics parameters and test for statistical significance. Iteration between steps (1)-(3) in a sequential manner provides a progressive reduction in parameter uncertainty, by exploiting new information from previous experiments [266]. This sequential approach is historically used, but may not be optimal in terms of time and resources. In particular, CLC processes require substantial time to initially reach the temperature set-point and oxygen carrier stability, but afterwards, useful data can be generated quickly, given that gas flows can be easily changed to initiate the reduction, purge, and oxidation cycles. Thus, it can be more advantageous to propose multiple experimental conditions at once to reduce the total experimental effort. Recently, parallel approaches were used to propose multiple experiments with one design.[266] A potential advantage of the parallel design is that each experiment can be designed to maximize a specific aspect of the information, rather than the overall set, which decreases the size of the optimization problem and increases the effectiveness of the design. In this work, sequential and parallel approaches are explored to propose optimal experiments for kinetic parameter estimation.

The information matrix, introduced in Stage 1, plays a central role in this type of optimum designs, because its inverse (the variance-covariance matrix) is directly related to the statistical confidence of the parameter estimates. The objective function, therefore, seeks to minimize a function of the variance-covariance matrix $\mathbf{V}_\theta(\hat{\boldsymbol{\theta}}, \boldsymbol{\phi})$, as given in Eq.(6.16):

$$\mathbf{V}_\theta(\hat{\boldsymbol{\theta}}, \boldsymbol{\varphi}) = \mathbf{H}_\theta(\hat{\boldsymbol{\theta}}, \boldsymbol{\varphi})^{-1} = \left[\sum_{k}^{N_{exp}} \sum_{r}^{N_y} \sum_{s}^{N_y} \sigma_{rs|k} \mathbf{Q}_{r|k}^T \mathbf{Q}_{s|k} + \boldsymbol{\Sigma}_\theta(\hat{\boldsymbol{\theta}})^{-1} \right]^{-1} . \quad (6.16)$$

Eq.(6.16) is augmented from Eq.(6.6) to include an initial approximation of the parameter uncertainty $\left(\boldsymbol{\Sigma}_\theta(\hat{\boldsymbol{\theta}})\right)$, and to evaluate the information content over a number of different experiments, N_{exp}.

There are three standard design criteria to maximize parameter precision: D-optimal (minimizes the determinant of $\mathbf{V}_\theta$), A-optimal (minimizes the trace, *i.e.* sum of eigenvalues, of $\mathbf{V}_\theta$), and E-optimal (minimizes the largest eigenvalue of $\mathbf{V}_\theta$). The main distinction between the design criteria is that A- and D-optimal designs minimize the arithmetic and geometric mean of the identification errors, respectively; whereas the E-optimal design minimizes the largest error [253]. Less common design criteria include G-, L-, C-, and Ds- designs, which are summarized by Walter and Pronazto [317]. The D-optimal design (Eq.(6.17)) is the most popular criterion, with several applications in chemical processes [260,318–322]. A potential disadvantage of the D-optimal design is that the calculated design vector is catered to the most sensitive model parameters, resulting in low parameter confidence for the remaining parameters [323]. It is advantageous in that it minimizes the correlation between model parameters, which is of interest here because of the inherent similarity of the reduction and catalytic reactions in CLC.

$$
\begin{aligned}
\boldsymbol{\varphi}_D = \arg\min_{\boldsymbol{\varphi}\in\boldsymbol{\Phi}} & \left\{ \det\left[\mathbf{V}_\theta(\hat{\boldsymbol{\theta}}, \boldsymbol{\varphi}) \right] \right\} \\
& \textit{subject to}: \\
& \mathbf{f}\left(\dot{\mathbf{x}}(t), \mathbf{x}(t), \mathbf{u}(t_0), \hat{\boldsymbol{\theta}}, t \right) = 0, \\
& \hat{\mathbf{y}}\left(t\right) = \mathbf{h}\left(\mathbf{x}\left(t\right)\right), \\
& \mathbf{u}_{\min} \le \mathbf{u}(t_0) \le \mathbf{u}_{\max} \qquad \forall t \in [0, \tau] \\
& t_{sp,1} \ge \Delta t_1, \\
& \Delta t_{sp}^{\min} \le t_{sp,i} - t_{sp,i-1} \le \Delta t_{sp}^{\max}, \qquad i = 1, \ldots, N_{sp}.
\end{aligned}
\tag{6.17}
$$

The selected CLC kinetic model analyzed here should contain kinetic parameters that are estimable from experiments (guaranteed by the analysis in Stages 1 and 2). Thusly, the D-optimal criterion of Eq.(6.17) can be effectively used in this work to enhance the statistical significance of the CLC kinetic parameters. In summary, the methods presented in each stage of the model-based framework provide a systematic procedure for comparing the possible combinations of kinetic models and identifying a "true" reaction kinetics scheme. In this work, we present the application of these methods to devise novel CLC experimental designs to improve the understanding of the reaction networks, mechanistic models, and kinetic parameters governing the NiO-CH_4 reaction system.

6.4. Process model

The foundation of the following analysis is a 1-D heterogeneous model presented previously [128,193], which incorporates the conservation balances of mass, energy, and momentum in a fixed bed reactor undergoing CLC reduction. This process model with the kinetic model $\mathbf{M}_{\mathrm{I-III-IV-I}}$ of Zhou et al. [119,141,324] successfully predicted experimental data reported in the literature for the reduction of NiO by CH_4 [58,171,172] under different hydrodynamic conditions, particle sizes, and operating temperatures. The main assumptions of the model are that reactions occur on the Ni/NiO sites inside the particle, pore diffusion is the only mechanism for transport within the particle, film resistance occurs at the outer layer of the particle, the flow in the bulk phase follows an axially dispersed plug flow with no radial variations, constant temperature at the wall, and atmospheric outlet pressure. A summary of the conservation equations and boundary conditions used in the 1-D heterogeneous model is provided in Chapter 4. The initial conditions pertain to the experimental conditions prior to the reduction experiment. Usually, the reactor is purged with inert gas, the temperature is at the set-point of the furnace, and the oxygen carrier is fully oxidized. For a bench-scale fixed bed reactor, such as the one used in this work, the hydrodynamic model described in Chapter 4 is sufficient. Expanding the complexity of the process model, by increasing its scope to 2-D [193] or employing Maxwell-Stefan diffusion [325–327] does not yield significant benefits in accuracy. Thus, within the context of this work, we assume that any model-experiment deviation can be attributed to inadequacies in the structure and parameter values of the kinetic model. The kinetic rate constants are described by the reparameterized form of the Arrhenius equation (Eq. (6.18)) to reduce the correlation between the pre-exponential factors $k_{i,0}$ and activation energies Ea_i [209,328–332]. The reference temperature T_{ref} in Eq.(6.18) is set to 500°C for the catalytic reforming reactions and 700°C for the NiO reduction reactions. The model was implemented and solved using the commercial software package gPROMS 4.0.0 [170].

$$k_i = k_i^{T_{ref}} \exp\left[-\frac{Ea_i}{R}\left(\frac{1}{T}-\frac{1}{T_{ref}}\right)\right], \qquad k_i^{T_{ref}} = k_{i,0}\exp\left(-\frac{Ea_i}{RT_{ref}}\right). \tag{6.18}$$

6.5. Experimental methods

The fixed bed reactor used in this study is illustrated in **Figure 3.1** and was described in detail in Chapter 3. **Table 6.6** summarizes the design variables that can be manipulated within the optimal experimental design framework. It should be noted that due to experimental constraints and measurement uncertainty (thermocouple delays, back-mixing in the spectroscopic device, furnace lag, etc.), the control variables (gas flows, temperature, solid loadings) are treated as time-invariant variables $\left(\mathbf{u}(t) \to \mathbf{u}(t_0)\right)$, where t_0 denotes the initial time of the reduction cycle. The sampling times are also fixed by the mass spectroscopic device. The experimental design vector is hence, $\boldsymbol{\phi} = [\mathbf{u}(t_0), \mathbf{y}_0, \tau]^T$, where $\mathbf{y}_0$ is the vector of the conditions after the previous purging step (following oxidation) and τ is the reduction step duration. The selection of the admissible experiment controls, $\mathbf{u}(t_0)$, of **Table 6.6** contains systems variables that can be manipulated easily and accurately during (or prior to) the execution of the cyclic experiment. These were the fraction of the fraction of CH_4 in the reducing feed, the initial oxygen carrier loading, and the temperature of the isothermal reactor.

Table 6.6: Time-invariant controls for the in-house CLC fixed bed experiments.

Design variables, $\boldsymbol{\phi_i}$	unit	$\boldsymbol{\phi_{i,\min}}$	$\boldsymbol{\phi_{i,\max}}$
Fraction of CH_4 in Ar	[mol/mol]	0	0.30
Oxygen carrier loading	[g]	0.80	2.20
Temperature	[ºC]	500	850
τ	[sec]	0	60

6.6. Results and discussion

The sequence of this section follows the methodology presented in Section 6.3, consisting of a (1)

preliminary analysis testing the uniqueness of the model with respect to its parameters, (2) identification and subsequent rejection of inadequate models, and (3) maximization of the statistical significance of the uncertain kinetic parameters [232,240,241]. In this section, we present the results of each method and show their effectiveness in reducing the uncertainty in the candidate CLC kinetic models.

6.6.1. Preliminary analysis

With the model of a CLC process defined in Eq.(6.3) and the experiment design vector of Eq.(6.5), we first need to confirm whether the kinetic parameters of the candidate model structures are structurally identifiable. Specifically, we need to find if, in principle, an experiment design exists, in which the model parameters can be uniquely identifiable, given a certain model structure. We applied the framework for structural identifiability analysis presented in **Figure 6.5**, following the sequence of local and global approaches proposed by Galvanin et al. [287] The controversies in the NiO reduction kinetics of **Table 6.1**-

Table 6.4 are deconstructed in **Figure 6.5**, whereby we evaluated independently the uncertainty associated with the catalytic activity of Ni (Eq.(6.1) or Eq.(6.2)), the catalytic reforming kinetics, and the NiO reduction kinetics.

First, structural local identifiability (SLI) of the model parameters of **M** with Eq.(6.2) was analyzed. We used literature sources to define the design space, $\boldsymbol{\Phi}$, and get initial estimates of $\boldsymbol{\theta}$ for the SLI analysis. Secondly, we analyzed the SLI of the candidate reforming reaction networks, using initial estimates of $\boldsymbol{\theta}$ and definitions of $\boldsymbol{\phi}$ and $\boldsymbol{\Phi}$ according to relevant literature studies. For the locally identifiable models, we performed the F-test and AICc test, following the procedure of Zhou et al. [132] to select the most suitable reforming network. In the third step shown in **Figure 6.5**, we studied the structural identifiability of the NiO reduction kinetic models, using the models determined from previous steps for the catalytic activity of Ni and reforming reaction network. The kinetic parameters were estimated from an in-house NiO reduction experiment, with a defined design space, $\boldsymbol{\Phi}$. The locally identifiable models were then

analyzed in terms of their structural global identifiability (SGI). Globally identifiable models were then evaluated in terms of model distinguishability. If two models were deemed indistinguishable, then the more globally identifiable model was retained, while the other model was rejected. At the conclusion of the framework of **Figure 6.5**, we have systematically identified a set of identifiable and distinguishable kinetic models that is fit for model-based design of experiments.

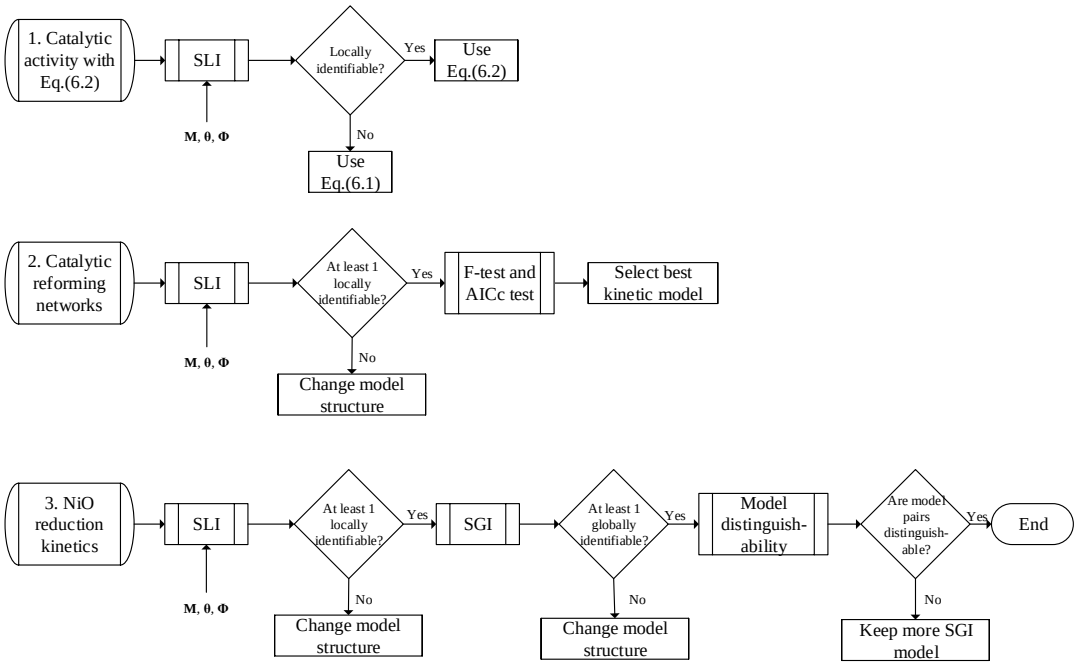

Figure 6.5: Procedure for structural identifiability analysis and model distinguishability analysis, adapted from the work of Galvanin et al. [287] and Asprey and Macchietto [241].

Ni contribution on the catalytic activity

The empirical expression of Eq.(6.2) was originally proposed by Ortiz et al. [118] to simulate the catalytic activity of Ni in CL reduction experiments using NiO/α-Al_2O_3 and NiO/γ-Al_2O_3 oxygen carriers. In their analysis, Ortiz et al. [118] modeled the reduction of NiO using $\mathbf{M}_{\mathrm{III-VI-II-II}}$. This kinetic model is not considered among the 160 candidate models shown in **Table 6.2**, because Zhou et al.[132] rejected the

zero order mechanistic model due to poor data fitting. Nonetheless, we show in **Figures 6.6(a)-6.6(b)** the validation of the reported kinetic model, $\mathbf{M}_{\mathrm{III-VI-II-II}}$, with the reported kinetic parameters, $\widehat{\boldsymbol{\theta}}^{0}$, of Ortiz et al. [118] to accurately predict the reduction data. The design vector $\boldsymbol{\phi}$ is constrained by the experimental design space of Ortiz et al. [118], being the gas fraction of the feed ($H_2O/CH_4/H_2$=3:1:1-7:1:1), reactor temperature (500-900°C), and space time (0.1-0.4 g h/mol CH_4). The experiment duration was fixed as in Ortiz et al. (2012) [118] to 100 sec. We assumed that data was collected every 1 sec with a variance of 0.01. Ortiz et al. [118] performed one reduction experiment for each oxygen carrier.

Using $\mathbf{M}$, $\widehat{\boldsymbol{\theta}}^{0}$, and $\boldsymbol{\phi} \in \boldsymbol{\Phi}$ from Ortiz et al. [118] we solved Eq.(6.9) to determine an optimal design that maximizes the local identifiability of the kinetic parameters of $\mathbf{M}_{\mathrm{III-VI-II-II}}$ and the empirical parameters of Eq.(6.2) for the NiO/γ-Al_2O_3 oxygen carrier. At the optimal design point, the correlations between the parameters were computed (**Table 6.7**). The correlation analysis of **Table 6.7** reveals that the model structure of $\mathbf{M}_{\mathrm{III-VI-II-II}}$ is not identifiable, as the empirical parameters used to describe the catalytic activity of Ni are perfectly correlated with the kinetic parameters of the catalytic reactions (**Table 6.7**). However, it is possible that the model structure could be locally identifiable with information from additional experiments. Thus, we extended the SLI analysis to simultaneously optimize the design of up to 3 reduction experiments. These results also showed that this model structure is not identifiable. Therefore, Eq.(6.1) is more appropriate (from the statistical point of view) to characterize the effect of Ni on the catalytic activity.

Other model structures were tested to simulate the reduction behavior of the NiO/α-Al_2O_3 and NiO/γ-Al_2O_3 oxygen carriers reported by Ortiz et al. [118]. Zhou et al. [132] showed that the best solid-state mechanistic model for NiO reduction is the Avrami-Erofe'ev model. In **Figures 6.6(c)-6.6(d)**,the kinetic parameters of $\mathbf{M}_{\mathrm{III-I-II-I}}$ were tuned to match the experimental data. We found that accurate representation of the data is feasible with Eq.(1), because the activation barrier observed in the NiO/γ-Al_2O_3 experiments by Ortiz et al. [118] is inherently captured by the Avrami-Erofe'ev exponent. Finally, the model predictions of the winner model from this analysis ($\mathbf{M}_{\mathrm{II-I-IV-I}}$) are shown in **Figures 6.6(e)-**

6.6(f), which is also in agreement with the data. This multiplicity of good agreement with the data illustrates the difficulty in identifying correct model structures in unguided experimental efforts. In summary, the SLI analysis found an instance of over-parameterization in the mathematical representation of reaction kinetics, reducing the problem size from 160 possible combinations of kinetic models to 80 candidate kinetic models for the reduction of NiO by CH_4.

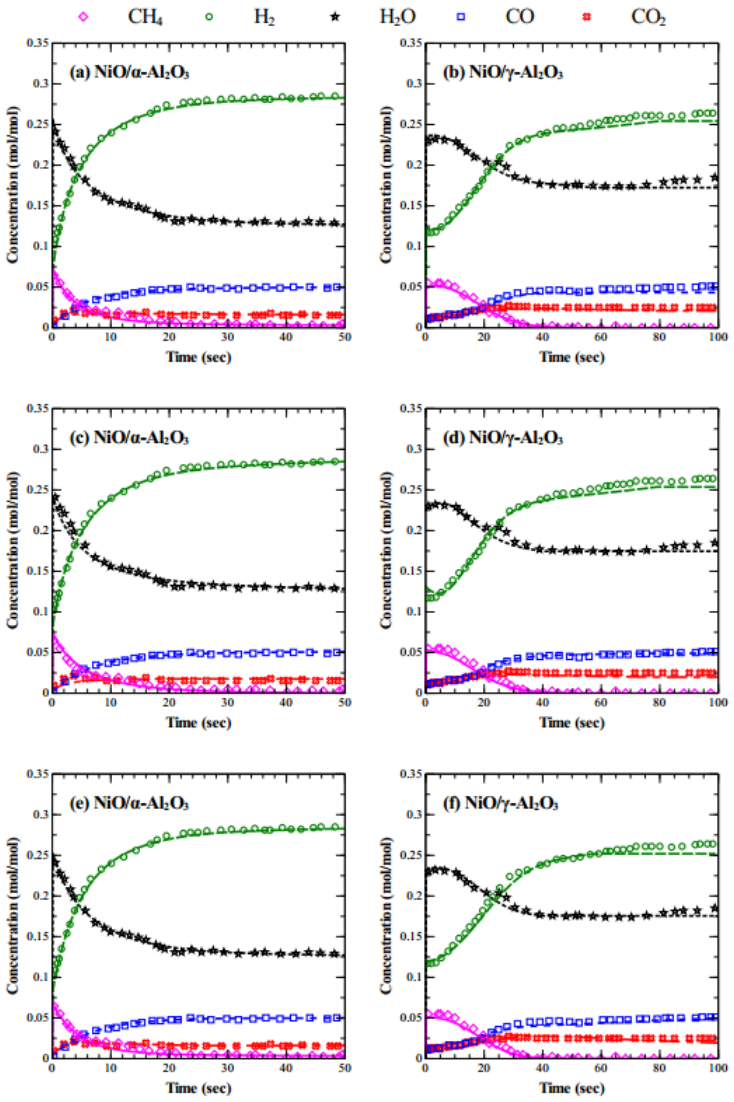

Figure 6.6: Experimental data and model predictions of the exit gas fractions for the CLC reforming experiments at 900°C with the NiO/α-Al_2O_3 (left column) and NiO/γ-Al_2O_3 (right column) oxygen carriers of Ortiz et al. [118]. **Figures 6.6(a)-6.6(b)** show predictions with $\mathbf{M}_{\mathrm{III-VI-II-II}}$, where

a=0,b=1,c=0 for NiO/α-Al_2O_3 and *a=0,b=0.19,c=0.81*for NiO/γ-Al_2O_3. **Figures 6.6(c)-6.6(d)** show predictions with $\mathbf{M}_{\mathrm{III-I-II-I}}$ and **Figures 6.6(e)-6.6(f)** show predictions with $\mathbf{M}_{\mathrm{II-I-IV-I}}$.

Table 6.7: Correlation matrix of the parameter estimates for NiO/γ-Al_2O_3 oxygen carrier with $\mathbf{M}_{\mathrm{III-VI-II-II}}$ at the calculated design that maximizes SLI.

Parameter	*b*	*c*	$k_2^{T_{ref}}$	$k_3^{T_{ref}}$	$k_5^{T_{ref}}$	$k_6^{T_{ref}}$	$k_7^{T_{ref}}$	$k_8^{T_{ref}}$
b	1.000							
c	1.000	1.000						
$k_2^{T_{ref}}$	0.000	0.000	1.000					
$k_3^{T_{ref}}$	0.000	0.000	0.140	1.000				
$k_5^{T_{ref}}$	0.000	0.000	-0.407	-0.145	1.000			
$k_6^{T_{ref}}$	-1.000	-1.000	0.000	0.000	0.000	1.000		
$k_7^{T_{ref}}$	0.000	0.000	-0.099	-0.054	-0.110	0.000	1.000	
$k_8^{T_{ref}}$	-1.000	-1.000	0.000	0.000	0.000	1.000	0.000	1.000

Catalytic reforming network

The task of this section is to select one catalytic reforming model among the 4 candidate models listed in

Table 6.4, $\mathbf{M}_{\mathrm{Ø-Ø-I-Ø}} - \mathbf{M}_{\mathrm{Ø-Ø-IV-Ø}}$. We are only concerned with the catalytic reforming reactions occurring over a reduced Ni oxygen carrier, so Ø denotes that the corresponding reduction reactions are absent. The kinetic parameters for $\mathbf{M}_{\mathrm{Ø-Ø-I-Ø}}$, $\mathbf{M}_{\mathrm{Ø-Ø-III-Ø}}$, and $\mathbf{M}_{\mathrm{Ø-Ø-IV-Ø}}$ were fitted to the reforming data of Ortiz et al. [118]. The results of the kinetic parameter estimation are shown in **Figure 6.7** and the kinetic parameters used to fit the data are provided in Table S.3 of the Supplementary Information of [333]. Ortiz et al. [118] used the kinetic model represented here as $\mathbf{M}_{\mathrm{Ø-Ø-II-Ø}}$ to predict their experiments, which we replicated in this work using their reported parameters. The close agreement of the model predictions with the experimental data (**Figure 6.7**) reveals that the catalytic kinetic models $\mathbf{M}_{\mathrm{Ø-Ø-I-Ø}} - \mathbf{M}_{\mathrm{Ø-Ø-IV-Ø}}$ are all adequate to represent this set of data. The design space for the SLI

analysis (**Table 6.8**) was chosen in accordance with Ortiz et al. [118] and others [219–221], who performed a series of catalytic experiments in fixed bed reactors at different temperatures, space times, and fuel to catalyst ratios. An additional set of experimental conditions was included to study the methanation reaction (R9) of

Table 6.4, which is relevant for models $\mathbf{M}_{\text{Ø}-\text{Ø}-\text{I}-\text{Ø}}$ and $\mathbf{M}_{\text{Ø}-\text{Ø}-\text{III}-\text{Ø}}$, and was not studied in the work of Ortiz et al. [118]. It was assumed that the outlet gases are measured every 30 sec with a variance of 0.01.

SLI analysis showed that in principle it is possible to identify each catalytic reaction, but the experimental effort required to achieve structural identifiability is dependent on the parameterization of the model and number of states and unknown parameters. **Table 6.8** presents the results of the SLI analysis in the form of the minimum number of experiments required to precisely estimate all the kinetic parameters of each model. As the reaction scheme increases in complexity (*i.e.*, $\mathbf{M}_{\text{Ø}-\text{Ø}-\text{IV}-\text{Ø}} \rightarrow \mathbf{M}_{\text{Ø}-\text{Ø}-\text{I}-\text{Ø}}$), more experiments are necessary to achieve SLI of the kinetic parameters. The simplest model structure, $\mathbf{M}_{\text{Ø}-\text{Ø}-\text{IV}-\text{Ø}}$, requires the least experimental effort (4 experiments in total), whereas $\mathbf{M}_{\text{Ø}-\text{Ø}-\text{I}-\text{Ø}}$ requires at least 12 experiments. We note that that the minimum number of experiments required for SLI is smaller than that performed by Ortiz et al. [118], because of the wider design space used in the SLI test and the fact that Ortiz et al. [118] performed experiments at evenly spaced intervals within their experimental design space, which is not necessarily optimal. Additional information supporting the results presented in **Table 6.8** is provided in Tables S.4-S.6 of the Supplementary Information of [333], showing the calculated optimal design variables, correlation analysis, and the statistical significance of each catalytic model.

Subsequently, the candidate model structures, $\mathbf{M}_{\text{Ø}-\text{Ø}-\text{I}-\text{Ø}} - \mathbf{M}_{\text{Ø}-\text{Ø}-\text{IV}-\text{Ø}}$, were assessed by the F-test and the Corrected Akaike Information Criterion (AICc), following the procedure of Zhou et al. [132]. The quality of fit of the simplest model, $\mathbf{M}_{\text{Ø}-\text{Ø}-\text{IV}-\text{Ø}}$, was compared with the more complicated models,

$\mathbf{M}_{\emptyset-\emptyset-\mathrm{I}-\emptyset} - \mathbf{M}_{\emptyset-\emptyset-\mathrm{III}-\emptyset}$, to explore if there was a statistical advantage in increasing the model size. The results of these analyses are shown in Table S.7 of the Supplementary Information of [333]. To summarize, the F-test and the AICc test found that $\mathbf{M}_{\emptyset-\emptyset-\mathrm{IV}-\emptyset}$ was the most statistically significant model, as equally good fits were obtained with fewer number of reactions and estimated parameters. Thus, $\mathbf{M}_{\emptyset-\emptyset-\mathrm{IV}-\emptyset}$ was selected as the most suitable catalytic reforming scheme for the CLC kinetic model. This is in agreement with Rostrup-Nielsen and co-workers [334–337], who found accurate representation of their reformers utilizing this reaction scheme. For the remainder of this work, the NiO-CH_4 reduction kinetics is modeled with the simplest catalytic reaction scheme ($\mathbf{M}_{\emptyset-\emptyset-\mathrm{IV}-\emptyset}$) with Eq.(6.1). The problem size is subsequently reduced from 80 to 20 candidate kinetic models.

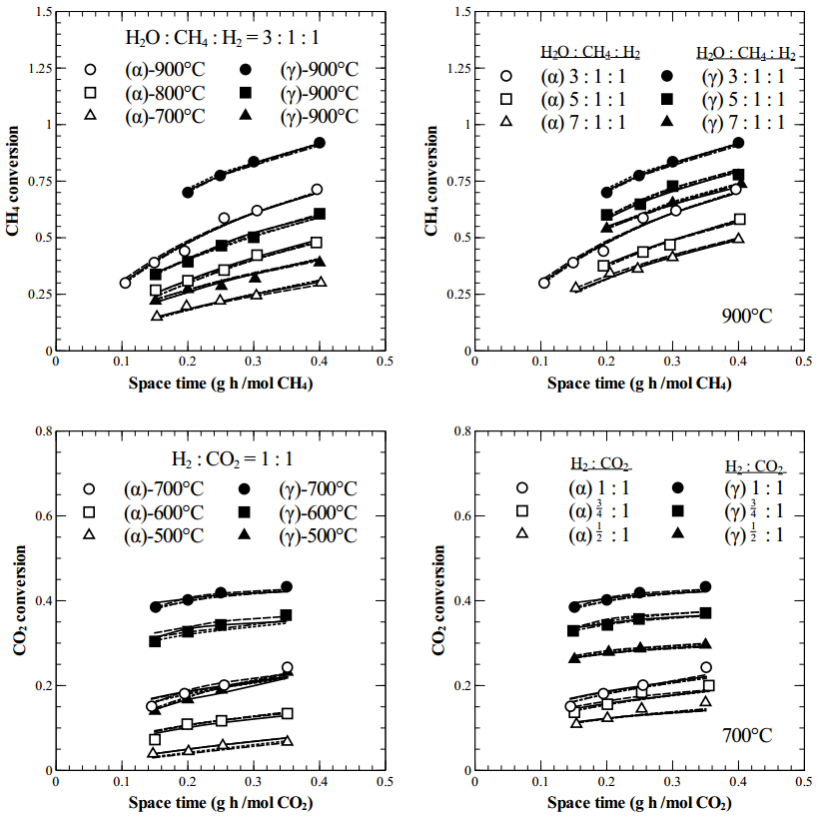

Figure 6.7: Experimental data and model predictions of the steady-state CH_4 and CO_2 conversion profiles for the set of (top row) steam methane reforming and (bottom row) reverse water gas shift experiments

conducted with the Ni/γ-Al_2O_3 (full symbols) and Ni/α-Al_2O_3 (empty symbols) oxygen carriers by Ortiz et al. [118] The model predictions with $\mathbf{M}_{\emptyset-\emptyset-\mathrm{I}-\emptyset}$ are represented by solid lines, $\mathbf{M}_{\emptyset-\emptyset-\mathrm{II}-\emptyset}$ by dashed lines, $\mathbf{M}_{\emptyset-\emptyset-\mathrm{III}-\emptyset}$ by dotted lines, and $\mathbf{M}_{\emptyset-\emptyset-\mathrm{IV}-\emptyset}$ by dash-dot lines.

Table 6.8: Range of design variables for the steam methane reforming, reverse water gas shift, and methanation experiments and results of the SLI test in terms of the minimum N_{exp}. The results for the Ni/α-Al_2O_3 oxygen carrier are differentiated from Ni/γ-Al_2O_3 (in parentheses).

		Steam reforming	**Reverse WGS**	**Methanation**
Design variables, ϕ_i	Gas fraction	8vol.% CH_4	10vol.% CO_2	10vol.% CO
	Solid loading	0.2 g	0.2 g	0.2 g
	Temperature	400-900°C	400-900°C	400-900°C
	Molar ratio	$H_2O/CH_4/H_2$=2-8:1:1	H_2/CO_2=0.5-5	H_2/CO=1-5
	Space time	0.2-0.4 g-h/mol CH_4	0.15-0.4 g-h/mol CO_2	0.15-0.4 g-h/mol CO
	τ	30 min	30 min	30 min
Min. N_{exp} for SLI	$\mathbf{M}_{\emptyset-\emptyset-\mathrm{I}-\emptyset}$	4 (4)	4 (4)	4 (4)
	$\mathbf{M}_{\emptyset-\emptyset-\mathrm{II}-\emptyset}$	4 (3)	4 (3)	0 (0)
	$\mathbf{M}_{\emptyset-\emptyset-\mathrm{III}-\emptyset}$	3 (4)	3 (4)	0 (4)
	$\mathbf{M}_{\emptyset-\emptyset-\mathrm{IV}-\emptyset}$	2 (2)	2 (2)	0 (0)

NiO reduction kinetics

At this stage of the framework of **Figure 6.5**, we need to determine if the NiO reduction kinetics is structurally identifiable, with respect to the non-catalytic reaction pathway and solid-state reaction mechanism. The kinetic parameters of the 20 candidate models were estimated to a low-temperature CL reduction experiment, performed in the experimental setup of Zhou et al. [119] Shown in **Figure 6.8**, a low reaction temperature was used to slow down the reactions and better discern the products from the various reactions. As shown in **Figure 6.8**, there exists a wealth of models capable of fitting the data accurately. The models that use the V and SC mechanisms exhibit a high lack of fit and were thus rejected

from further analysis. The following 12 models: $\mathbf{M}_{\mathrm{III-V-IV-I}}, \mathbf{M}_{\mathrm{III-III-IV-I}}, \mathbf{M}_{\mathrm{I-I-IV-I}}, \mathbf{M}_{\mathrm{II-I-IV-I}}$, $\mathbf{M}_{\mathrm{II-III-IV-I}}, \mathbf{M}_{\mathrm{I-V-IV-I}}$, $\mathbf{M}_{\mathrm{IV-III-IV-I}}, \mathbf{M}_{\mathrm{IV-V-IV-I}}, \mathbf{M}_{\mathrm{III-I-IV-I}}$, $\mathbf{M}_{\mathrm{IV-I-IV-I}}, \mathbf{M}_{\mathrm{I-III-IV-I}}$, and $\mathbf{M}_{\mathrm{II-V-IV-I}}$, were retained.

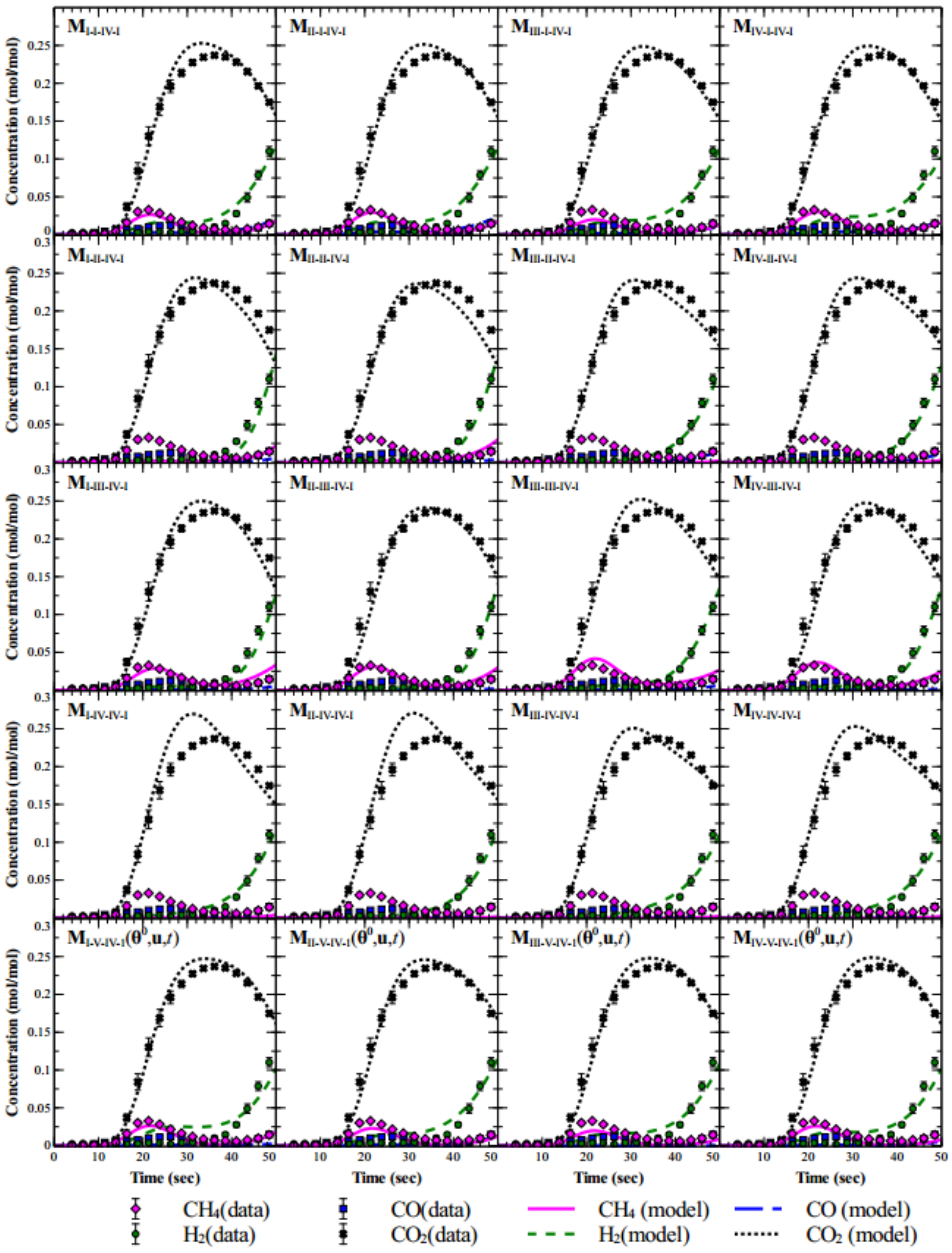

Figure 6.8: Experimental data and model predictions of a non-optimal, low temperature (500°C) experiment for preliminary inspection of the rival kinetic models, using the reactor design of Zhou et al. [119]. The Avrami-Erofe'ev exponent is assigned to 1.5.

For the 12 candidate reduction models, we maximized the identifiability of the dependent NiO reduction kinetics by solving Eq.(6.9), over the experimental design space of Zhou et al. [119], listed in **Table 6.6**. The results are presented in Tables S.9-S.10 of the Supplementary Information of [333], in terms of the optimized design vectors and correlation matrices. The results indicate that the estimability of the NiO reduction kinetics is maximized at high CH_4 feeds, low temperatures, and low solid loadings. In other words, the D-optimal design of the SLI analysis wants to bring the system to a state where CH_4 slip at the start of the batch experiment is more prominent and separable from the other reactions. Furthermore, operating at a low CH_4 conversion increases the selectivity to H_2 and CO, which improves the identifiability of the kinetic parameters of the partial NiO reduction and reforming reactions. In summary, we concluded that all of the NiO reduction kinetic model structures are satisfactory in terms of their local parameter identifiability.

It is also necessary to confirm structural identifiability of the model structure over a range of parameter values. Global identifiability of the candidate models was evaluated by solving Eq.(6.11) at the design determined from the SLI test. This analysis was performed with bounds on the parameter values $\theta_i, \theta_i^* \in \hat{\theta}_i \times [0.1\ ,10\ ]$. The optimization parameters were defined as arbitrarily small numbers: $\varepsilon_{\Phi_{SGI}} = 1 \times 10^{-10}$ and $\varepsilon_y = 5 \times 10^{-3}$, respectively. The results from the SGI analysis (Table S.11 of the Supplementary Information of of [333]) revealed that only 5 model structures were structurally globally identifiable with respect to their parameters: $\mathbf{M}_{\text{II}-\text{I}-\text{IV}-\text{I}}, \mathbf{M}_{\text{III}-\text{I}-\text{IV}-\text{I}}, \mathbf{M}_{\text{II}-\text{III}-\text{IV}-\text{I}}$, $\mathbf{M}_{\text{III}-\text{III}-\text{IV}-\text{I}}$ and $\mathbf{M}_{\text{II}-\text{V}-\text{IV}-\text{I}}$.

The final step of the framework of **Figure 6.5** is to evaluate whether different model structures are distinguishable from each other in the same input and output space. First, we analyzed the distinguishability between model structures with different NiO and CH_4 reaction pathways but the same mechanistic model, being $\mathbf{M}_{\text{II}-\text{I}-\text{IV}-\text{I}} - \mathbf{M}_{\text{III}-\text{I}-\text{IV}-\text{I}}$ and $\mathbf{M}_{\text{II}-\text{III}-\text{IV}-\text{I}} - \mathbf{M}_{\text{III}-\text{III}-\text{IV}-\text{I}}$. The results of this analysis (Table S.12 of the Supplementary Information of [333]) revealed that it is feasible to distinguish

$\mathbf{M}_{\mathrm{II-III-IV-I}}$ from $\mathbf{M}_{\mathrm{III-III-IV-I}}$, but infeasible to distinguish $\mathbf{M}_{\mathrm{II-I-IV-I}}$ from $\mathbf{M}_{\mathrm{III-I-IV-I}}$. The model structure of $\mathbf{M}_{\mathrm{II-I-IV-I}}$ was retained, because this model structure was shown previously to have higher SGI attributes (*i.e.*, smaller Φ_{SGI}) than $\mathbf{M}_{\mathrm{III-I-IV-I}}$. The procedure was then repeated for the remaining combinations of kinetic models. Model distinguishability was confirmed for all the remaining models (Table S.12 of the Supplementary Information of [333]).

In summary, 4 out of 160 candidate CLC models successfully passed through all stages of the preliminary analysis of parameter identifiability and model distinguishability. These 4 kinetic models demonstrate sufficient structural (local and global) identifiability and model distinguishability. In the next section, we show how experiments can be optimally designed in order to ensure the selection of the most accurate model and estimate kinetics with statistical precision. We conclude to an overall best kinetic model and demonstrate the applicability of this "true" model to predict CLC reduction data.

6.6.2. Optimal design of experiments

Figure 6.9 presents the framework applied in this work to identify and statistically validate a "true" kinetic model for the NiO-CH_4 system. As shown in **Figure 6.9**, optimal experiments are designed and executed to discriminate between the candidate model structures. The most accurate model structure to represent the data is selected as the "true" model. If none of the candidate models is adequate, then the model structure should be changed or another model should be proposed. Next, optimal experiments are designed to enhance the statistical significance of the kinetic parameters of the winner model. It is also important to check that the winner model with optimized kinetic parameters is the most adequate model. This is performed in a second model discrimination experiment, in which there exists one "true" model candidate and three alternatives. If the winner model is still the most adequate model, then we conclude to a final model structure with precise kinetic parameters. Otherwise, we need to reiterate between the exterior loops of **Figure 6.9**.

In the following, we present the numerical and experimental results of the sequence of steps outlined in

Figure 6.9. At the start of the framework, there are 4 candidate models, $\mathbf{M}_{\mathrm{II-I-IV-I}}$, $\mathbf{M}_{\mathrm{II-III-IV-I}}$, $\mathbf{M}_{\mathrm{II-V-IV-I}}$, and $\mathbf{M}_{\mathrm{III-III-IV-I}}$, to represent the reduction kinetics of NiO by CH_4. The reference rate constants for all the reactions, $k_i^{T_{ref}}$ of Eq.(6.18), were previously estimated from the nominal reduction experiment presented in **Figure 6.8**. The activation energies for R2-R4 of **Table 6.1** were fixed to the reported values of Zhou et al. [119] and for R5 to the reported value of Dueso et al. [114]. For the catalytic reactions, $k_i^{T_{ref}}$ was estimated in Section 6.6.1, keeping Ea_i fixed to the reported values of Zhou et al. [119] The results of the optimal experimental designs for model discrimination and parameter estimation are discussed. The posterior statistics of the parameter estimates are presented for each step of the framework. The fidelity of the final model to be used for interpolation and extrapolation is demonstrated.

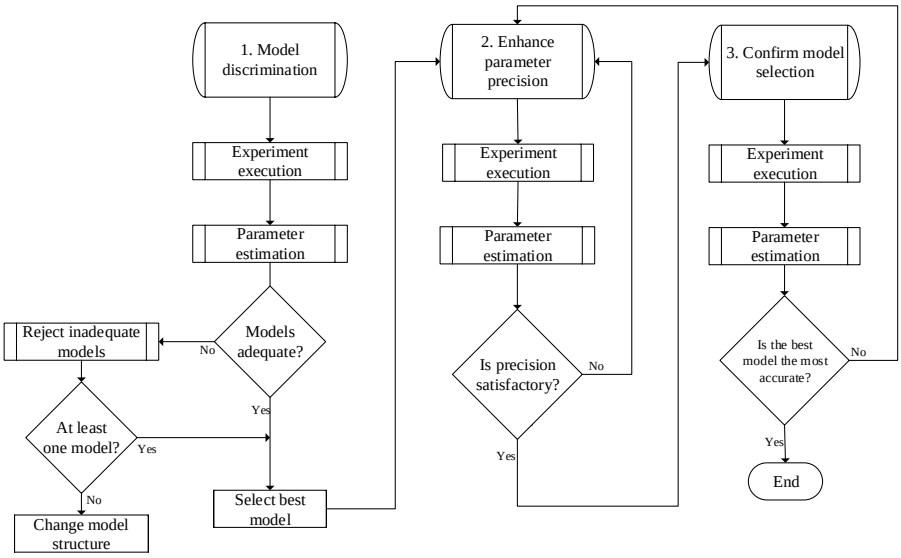

Figure 6.9: Framework for model-based design of experiments for model discrimination and parameter estimation, adapted from the work of Macchietto and co-workers [232,240,241].

Design of experiments for model discrimination

The first T-optimal design of **Figure 6.9** was calculated under the worse-case criterion of Eq.(6.15), in

which all models deemed identifiable in Section 6.6.1 were assumed equally likely to be the true model. Eq.(6.15) was solved over the 4 candidate models with bounds on the parameter values $\boldsymbol{\theta}^{(1)}, \ldots, \boldsymbol{\theta}^{(4)} \in \boldsymbol{\Theta}$ as [0.1, 10] times their estimated values from Section 6.6.1 and bounds on $\boldsymbol{\phi}$ as detailed in **Table 6.6**. The solution for the T-optimal design is shown in the caption of **Figure 6.10**.

Figure 6.10 presents the experimental data and model predictions of the proposed T-optimal design using Eq.(6.15). Compared to conventional CLC reduction experiments (such as **Figure 6.1(b)**), the T-optimal design of **Figure 6.10** led to a higher slip of converted CH_4, due to the higher CH_4 composition in the fuel, and lower CO_2 selectivity, due to the lower reaction temperatures. As evidenced by the initial CH_4 slip of **Figure 6.10**, this design separates the CH_4-NiO reduction reactions from the reduction reactions with H_2 and CO and the catalytic reactions, which is critical in discerning a statistically significant reaction mechanism. Furthermore, the dynamic profiles of CO and H_2 provide insight into the NiO-CH_4 reaction pathway and the conversion behavior of the oxygen carrier. For each candidate model, $k_i^{T_{ref}}$ of the NiO reduction reactions was estimated to the data of **Figure 6.10** and the results were analyzed by statistical tests. From visual inspection of **Figure 6.10,** the best model structure is clearly $\mathbf{M}_{\mathrm{II-I-IV-I}}$. The predictions of $\mathbf{M}_{\mathrm{II-III-IV-I}}$ are also close to the experimental data, but fail to match the rise in H_2 towards the end of the experiment. This indicates that the NiO conversion rate is under-predicted, because H_2 breakthrough usually occurs from the methane decomposition reaction, favorable when the NiO conversion is high. The worst fitting model is $\mathbf{M}_{\mathrm{III-III-IV-I}}$, with which the CO and CO_2 selectivities are severely mismatched.

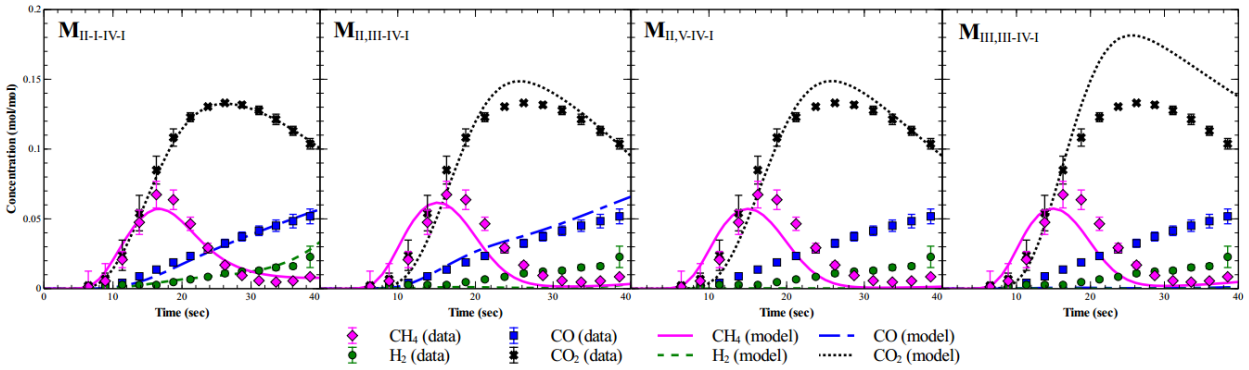

Figure 6.10: Experimental and model predictions for the first T-optimal design for model discrimination, using the parameters given in **Table 6.9**. $\square_{\square(3)} = \left[0.20\frac{\text{mol}}{\text{mol}}\ \text{CH}_4, 2.2\text{g}, 615^\circ\ \text{C}, 40\text{sec}\right]$

Table 6.9: Parameter estimates for the first T-design for model discrimination, $\square_{\square(3)} = \left[0.20\frac{\text{mol}}{\text{mol}}\ \text{CH}_4, 2.2\text{g}, 615^\circ\ \text{C}, 40\text{sec}\right]$.

Model	Set of **θ**	Estimates of **θ**	Confidence interval (95%)	95% *t*-value	χ^2-value (95% χ^2)
$\mathbf{M_{II-I-IV-I}}$	$\begin{bmatrix} k_2^{T_{ref}} \\ k_3^{T_{ref}} \\ k_4^{T_{ref}} \\ n \end{bmatrix}$	$\begin{bmatrix} 1.34\times10^{-5} \\ 5.64\times10^{-6} \\ 1.17\times10^{-7} \\ 0.83 \end{bmatrix}$	$\begin{bmatrix} \pm2.57\times10^{-6} \\ \pm7.20\times10^{-7} \\ \pm1.30\times10^{-7} \\ \pm0.099 \end{bmatrix}$	$\begin{bmatrix} 5.20 \\ 7.80 \\ 0.089^* \\ 8.33 \end{bmatrix}$	8.03 (68.87)
$\mathbf{M_{II-V-IV-I}}$	$\begin{bmatrix} k_2^{T_{ref}} \\ k_3^{T_{ref}} \\ k_4^{T_{ref}} \end{bmatrix}$	$\begin{bmatrix} 3.02\times10^{-4} \\ 2.77\times10^{-6} \\ 4.85\times10^{-6} \end{bmatrix}$	$\begin{bmatrix} \pm2.1\times10^{-3} \\ \pm4.14\times10^{-7} \\ \pm4.54\times10^{-6} \end{bmatrix}$	$\begin{bmatrix} 0.14 \\ 6.70 \\ 1.07^* \end{bmatrix}$	81.47 (74.47)
$\mathbf{M_{II-III-IV-I}}$	$\begin{bmatrix} k_2^{T_{ref}} \\ k_3^{T_{ref}} \\ k_4^{T_{ref}} \end{bmatrix}$	$\begin{bmatrix} 5.92\times10^{-5} \\ 3.82\times10^{-6} \\ 5.23\times10^{-6} \end{bmatrix}$	$\begin{bmatrix} \pm9.37\times10^{-5} \\ \pm4.38\times10^{-7} \\ \pm1.49\times10^{-6} \end{bmatrix}$	$\begin{bmatrix} 0.63^* \\ 8.71 \\ 3.50 \end{bmatrix}$	72.78 (74.47)
$\mathbf{M_{III-III-IV-I}}$	$\begin{bmatrix} k_2^{T_{ref}} \\ k_3^{T_{ref}} \\ k_5^{T_{ref}} \end{bmatrix}$	$\begin{bmatrix} 6.12\times10^{-4} \\ 3.08\times10^{-4} \\ 2.64\times10^{-4} \end{bmatrix}$	$\begin{bmatrix} \pm4.60\times10^{-3} \\ \pm4.80\times10^{-3} \\ \pm2.21\times10^{-4} \end{bmatrix}$	$\begin{bmatrix} 0.43^* \\ 0.064 \\ 1.19^* \end{bmatrix}$	391.97 (74.47)

*Indicates *t*-values are lower than the reference *t*-value (95%) from the Student's *t* distribution, 1.665.

The χ^2 goodness of fit test was used to evaluate the adequacy of each model to represent the data. An acceptable model fit is achieved when the obtained sum of residuals is below the χ^2 value at the 5% significance level for the corresponding degrees of freedom, calculated from the number of experimental

points minus the number of estimable parameters. From this statistical analysis (**Table 6.9**), $\mathbf{M}_{\mathrm{II-I-IV-I}}$ provides the best fit, while $\mathbf{M}_{\mathrm{III-III-IV-I}}$ and $\mathbf{M}_{\mathrm{II-V-IV-I}}$ fail the χ^2 test. The *t*-test was also used to check the statistical significance of the estimated kinetic parameters. As shown in **Table 6.9**, $\mathbf{M}_{\mathrm{II-I-IV-I}}$, $\mathbf{M}_{\mathrm{II-V-IV-I}}$, and $\mathbf{M}_{\mathrm{II-III-IV-I}}$ provide reliable estimates of 2 out of 3 NiO reduction kinetic parameters with *t*-values larger than the reference values, while the worst fitting model, $\mathbf{M}_{\mathrm{III-III-IV-I}}$, can only reliably estimate 1 kinetic parameter. We note that this T-optimal design was intended to solve the problem of multiplicity of rival models, rather than for parameter estimation. In the next section, experiments are designed exclusively for this purpose, to maximize the parameter precision of the winner model: $\mathbf{M}_{\mathrm{II-I-IV-I}}$. Once the parameters are estimated with statistical significance, a second T-optimal design is executed, to confirm that $\mathbf{M}_{\mathrm{II-I-IV-I}}$ is indeed the best overall model.

Design of experiments for parameter estimation

The next series of experiments is focused on improving the reliability of the model predictions of $\mathbf{M}_{\mathrm{II-I-IV-I}}$ by reducing uncertainty in the values of the kinetic parameters for the NiO reduction reactions, Ea_i and $k_i^{T_{ref}}$. For this purpose, three different design strategies were constructed. In the *sequential* design strategy, the first D-optimal experiment was determined around the most current values of $\widehat{\boldsymbol{\theta}}$, estimated from the T-optimal experiment. After executing this D-optimal experiment, the parameter values were re-estimated and used in the design of a subsequent D-optimal experiment. In the *parallel* design strategy, two D-optimal experiments were designed simultaneously, using the parameters estimated from the T-optimal experiment. Lastly, a *reference* design was considered in which we only varied the reaction temperature. This was based on the design strategies typically used to study the reactivity of oxygen carriers for CLC [58,119,171]. The reference design was used as a benchmark to qualitatively illustrate and quantitatively determine the benefits of D-optimal design of CLC bench-scale experiments. This reference design represents "normal" experiments resulting from experimental intuition. The success of each design strategy was assessed by analyzing the statistical significance of the

estimated kinetic parameters ($\square_{\square}^{\square}$, $\square\square_{\square}$). The reliability of the model-based approach was then demonstrated using the derived model parameters from each design for prediction of new and previous CLC data.

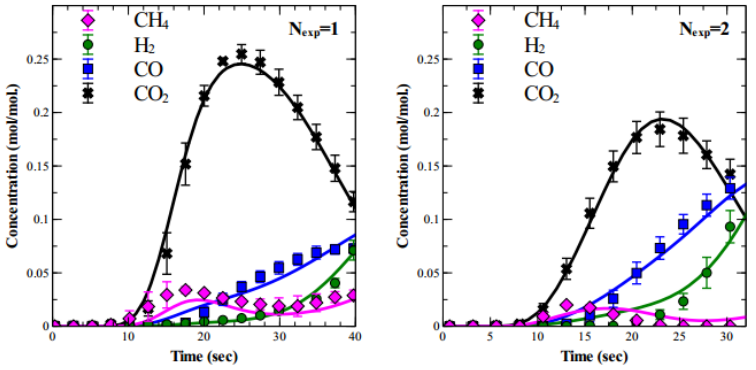

Figure 6.11: Data and model predictions of the *parallel* D-design strategy (Exp. 1: 30 mol.% CH_4, 1.67 g, 623˚C, 40 s; Exp. 2: 30 mol.% CH_4, 0.84 g, 768 ˚C, 32 s) with $\mathbf{M}_{\mathrm{II-I-IV-I}}$.

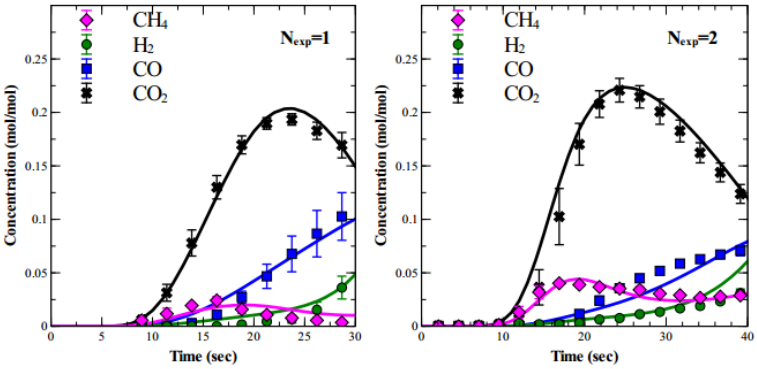

Figure 6.12: Data and model predictions of the *sequential* D-design strategy (Exp. 1: 30 mol.% CH_4, 0.85 g, 792˚C, 30 s; Exp. 2: 30 mol.% CH_4, 1.56 g, 648˚C, 40 s) with $\mathbf{M}_{\mathrm{II-I-IV-I}}$.

Figures 6.11-6.13 presents the proposed experimental designs. There are similarities between the sequential and parallel D-optimal designs, wherein one experiment at high temperature and low solid loading is paired with a second at low temperature and high solid loading. The D-optimal designs are at the maximum fraction of CH_4 feed, whereas the reference design uses a very dilute fuel. The latter fulfills

the objective of CLC by maintaining a high CO_2 selectivity during the reduction step, while the former is optimized for kinetic parameter estimation. The duration of the experiments was limited to 30-40 sec, depending on the oxygen carrier loading. This is a preemptive measure to prevent excessive solid carbon formation, as to avoid possible plugging inside the reactor and detriment to the oxygen carrier. **Figures 6.11-6.13** show model predictions with $\mathbf{M}_{\mathrm{II-I-IV-I}}$ after fitting $k_i^{T_{ref}}$ and Ea_i for the NiO reduction reactions to the experimental data. While the model predictions of each design strategy are in good agreement with the corresponding data, the D-optimal design experiments are more informative of the NiO reduction reactions, as compared to the reference experiments. This is evident by the simultaneous presence of partial and complete combustion products that evolve over the course of reduction. On the other hand, the only information that can be extracted from the reference experiments is the high CO_2

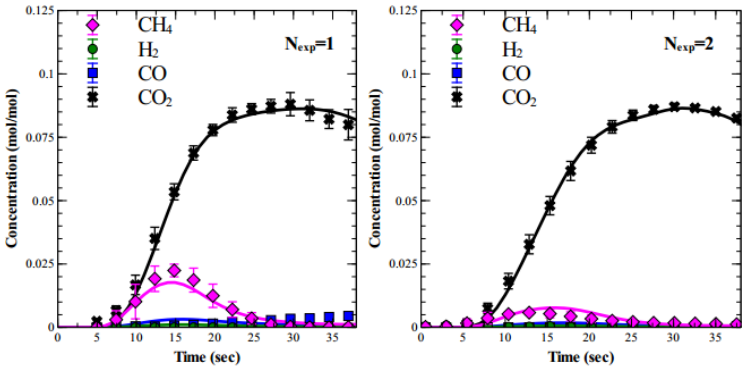

Figure 6.13: Data and model predictions of the *reference* experiment design (Exp. 1: 10 mol.% CH_4, 1.80 g, 700 ˚C, 38 s; Exp. 2: 10 mol.% CH_4, 1.80 g, 800 ˚C, 38 s) with $\mathbf{M}_{\mathrm{II-I-IV-I}}$.

The estimated values and posterior statistics of the NiO reduction kinetic parameters ($k_i^{T_{ref}}, Ea_i$) for each design strategy are summarized in **Tables 6.10-6.12**. The kinetic parameters estimated from the reference experiments were mostly unreliable (**Table 6.12**). In comparison, the D-optimal experiments by sequential and parallel approaches provided precise estimates of the kinetic parameters with statistical

certainty. The parameters for the reduction of NiO by H_2 (R2) are estimated more reliably than for R3 or R4 because the system is highly sensitive to R2, which was discussed in the Problem Statement section of this work. Comparing the sequential and parallel approaches, the values of the estimated parameters show only slight deviations, suggesting that both procedures were equally effective in estimating kinetic parameters, given our experimental design space and model structure.

Table 6.10: Results of the parameter estimation with the *parallel* D-design strategy (**Figure 6.11**). The reference *t*-value is 1.662.

Set of $\boldsymbol{\theta}$	Estimates of $\boldsymbol{\theta}$	Confidence interval (95%)	95% *t*-value
	9.02×10^{-6}	$\pm 7.22 \times 10^{-7}$	12.47
	3.89×10^{-6}	$\pm 2.53 \times 10^{-7}$	15.31
	3.05×10^{-7}	$\pm 1.41 \times 10^{-7}$	2.16
	7.09×10^{3}	$\pm 3.02 \times 10^{3}$	3.10
	7.12×10^{3}	$\pm 1.60 \times 10^{3}$	4.47
	1.08×10^{5}	$\pm 5.34 \times 10^{4}$	2.03

Table 6.11: Results of the parameter estimation with the *sequential* D-design strategy (**Figure 6.12**). The reference *t*-value is 1.662.

Set of $\boldsymbol{\theta}$	Estimates of $\boldsymbol{\theta}$	Confidence interval (95%)	95% *t*-value
	1.20×10^{-5}	$\pm 1.12 \times 10^{-6}$	10.77
	3.37×10^{-6}	$\pm 4.41 \times 10^{-7}$	9.02
	2.55×10^{-7}	$\pm 1.50 \times 10^{-7}$	1.70
	1.57×10^{4}	$\pm 1.11 \times 10^{4}$	1.46
	2.61×10^{4}	$\pm 1.31 \times 10^{4}$	1.99
	1.06×10^{5}	$\pm 5.84 \times 10^{4}$	1.82

Table 6.12: Results of the parameter estimation with the *reference* experiment (**Figure 6.13**). The reference *t*-value is 1.662.

Set of $\boldsymbol{\theta}$	Estimates of $\boldsymbol{\theta}$	Confidence interval (95%)	95% *t*-value
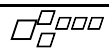	6.42×10^{-5}	$\pm 3.55 \times 10^{-5}$	1.81
	1.07×10^{-5}	$\pm 1.01 \times 10^{-5}$	1.06

□□□□□	1.00×10^{-6}	$\pm 4.07 \times 10^{-6}$	2.46
□□□	2.08×10^{4}	$\pm 7.64 \times 10^{4}$	0.27
□□□	2.86×10^{4}	$\pm 1.45 \times 10^{6}$	0.20
□□□	6.18×10^{4}	$\pm 5.28 \times 10^{4}$	1.17

* Indicates *t*-values are lower than the reference *t*-value (95%) from the Student's *t* distribution 1.674.

6.6.3. Validation of true model structure

With precise and accurate kinetic parameters from the previous D-optimal design, another T-optimal experiment was designed to confirm that $\mathbf{M}_{\mathrm{II-I-IV-I}}$ is indeed the best model structure. In this T-design problem, $\mathbf{M}_{\mathrm{II-I-IV-I}}$ was selected *a priori* as the "true" model structure, using $\widehat{\boldsymbol{\theta}}^{*}$ derived from the parallel D-design approach (**Figure 6.11**). Eq.(6.13) was solved over the set of candidate model structures ($\mathbf{M}_{\mathrm{II-III-IV-I}}, \mathbf{M}_{\mathrm{III-III-IV-I}}, \mathbf{M}_{\mathrm{II-V-IV-I}}$, and the true model, $\mathbf{M}_{\mathrm{II-I-IV-I}}$), using an augmented objective function to account for discrete sampling times and any number of rival models, N_M: $\boldsymbol{\varphi}_{T} = \arg\max_{\boldsymbol{\varphi}\in\boldsymbol{\Phi}} \min_{\boldsymbol{\theta}^{(j)}\in\boldsymbol{\Theta}^{(j)},} \sum_{i=1}^{N_{sp}} \sum_{j=1}^{N_M} \left(\hat{\mathbf{y}}^{*}\left(\hat{\boldsymbol{\theta}}^{*}, \mathbf{u}(t_0), t_i\right) - \hat{\mathbf{y}}^{(j)}\left(\boldsymbol{\theta}^{(j)}, \mathbf{u}(t_0), t_i\right)\right)^2$, where $\hat{\mathbf{y}}^{*}$ denotes the vector of responses of the true model structure with accurate parameter values $\widehat{\boldsymbol{\theta}}^{*}$, and $\hat{\mathbf{y}}^{(j)}$ is the vector of model responses for the possible model structures with adjustable parameter values $\boldsymbol{\theta}^{(j)}$. The resulting T-optimal design is shown in **Figure 6.14** and **Table 6.13**.

To evaluate the best possible fit of the candidate models, the values of $k_i^{T_{ref}}$ were tuned to the data of the new T-optimal design. **Figure 6.14** presents the results of the kinetic parameter estimation of the candidate model structures. The estimated parameter values and their statistical significance are shown in **Table 6.13**. From the analysis of the χ^2 test (**Table 6.13**), and quality of fits (**Figure 6.14**), we confirmed that $\mathbf{M}_{\mathrm{II-I-IV-I}}$ is indeed the best model. If a different model was found to be the true model, then under the model-based framework, we would need to propose a new D-optimal design to estimate the parameters of the new model, followed by another T-optimal design to validate the true model, until a model is deemed as true. In this case, no further iteration was required, as we arrived at a final model structure from the T-optimal design analysis. The results obtained from this systematic approach revise our previous work, wherein we used a less accurate modified volumetric mechanistic model with an

excessive number of reaction pathways for NiO to react with CH_4.

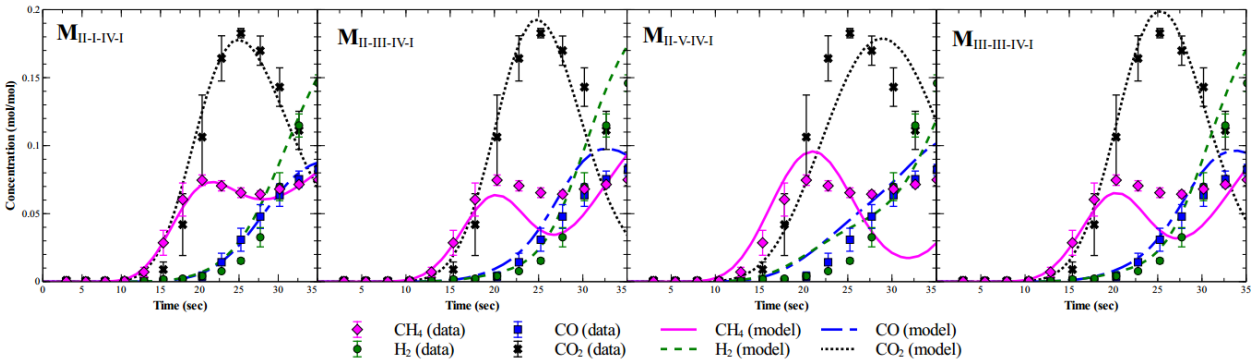

Figure 6.14: Experimental and model predictions for the second T-optimal design as validation of the true model structure. $\boldsymbol{\phi}_{T(1)} = \left[0.30\,\frac{\text{mol}}{\text{mol}}\ \text{CH}_4, 0.80\text{g}, 610°\text{C}, 35\text{sec}\right]$

Table 6.13: Parameter estimates for the second T-optimal design to validate model selection, $\square_{\square(1)} = \left[0.30\,\frac{\text{mol}}{\text{mol}}\ \text{CH}_4, 0.80\text{g}, 610°\text{C}, 35\text{sec}\right]$.

Model	Set of $\boldsymbol{\theta}$	Estimates of $\boldsymbol{\theta}$	Confidence interval (95%)	95% *t*-value	χ^2-value (95% χ^2)
$\mathbf{M_{II-I-IV-I}}$	$\begin{bmatrix} k_2^{T_{ref}} \\ k_3^{T_{ref}} \\ k_4^{T_{ref}} \\ n \end{bmatrix}$	$\begin{bmatrix} 1.37\times10^{-5} \\ 7.68\times10^{-6} \\ 4.37\times10^{-7} \\ 0.65 \end{bmatrix}$	$\begin{bmatrix} \pm1.90\times10^{-6} \\ \pm1.26\times10^{-6} \\ \pm2.45\times10^{-6} \\ \pm0.069 \end{bmatrix}$	$\begin{bmatrix} 7.22 \\ 6.08 \\ 0.18* \\ 9.46 \end{bmatrix}$	12.45 (69.83)
$\mathbf{M_{II-V-IV-I}}$	$\begin{bmatrix} k_2^{T_{ref}} \\ k_3^{T_{ref}} \\ k_4^{T_{ref}} \end{bmatrix}$	$\begin{bmatrix} 1.11\times10^{-5} \\ 6.38\times10^{-6} \\ 3.20\times10^{-3} \end{bmatrix}$	$\begin{bmatrix} \pm1.39\times10^{-6} \\ \pm8.68\times10^{-7} \\ \pm3.45\times10^{-3} \end{bmatrix}$	$\begin{bmatrix} 7.97 \\ 7.35 \\ 0.93* \end{bmatrix}$	325.74 (70.99)
$\mathbf{M_{II-III-IV-I}}$	$\begin{bmatrix} k_2^{T_{ref}} \\ k_3^{T_{ref}} \\ k_4^{T_{ref}} \end{bmatrix}$	$\begin{bmatrix} 3.90\times10^{-5} \\ 1.82\times10^{-5} \\ 7.10\times10^{-5} \end{bmatrix}$	$\begin{bmatrix} \pm6.19\times10^{-6} \\ \pm3.16\times10^{-6} \\ \pm4.81\times10^{-4} \end{bmatrix}$	$\begin{bmatrix} 6.31 \\ 5.70 \\ 0.0015* \end{bmatrix}$	96.24 (70.99)
$\mathbf{M_{III-III-IV-I}}$	$\begin{bmatrix} k_2^{T_{ref}} \\ k_3^{T_{ref}} \\ k_5^{T_{ref}} \end{bmatrix}$	$\begin{bmatrix} 4.17\times10^{-5} \\ 7.84\times10^{-6} \\ 1.27\times10^{-5} \end{bmatrix}$	$\begin{bmatrix} \pm4.51\times10^{-6} \\ \pm8.85\times10^{-7} \\ \pm8.81\times10^{-6} \end{bmatrix}$	$\begin{bmatrix} 9.25 \\ 8.85 \\ 1.44* \end{bmatrix}$	77.56 (70.99)

* Indicates *t*-values are lower than the reference *t*-value (95%) from the Student's *t* distribution 1.674.

6.6.4. Application of the final model

As a final step in the optimal experimental design framework, the final model, $\mathbf{M}_{\mathrm{II-I-IV-I}}$, using the optimally derived kinetics from the D-optimal experiments was used for predictive analyses of other types of CLC experimental data. It is important to note that no fitting of the kinetic parameters was performed in this step, as the aim was to check the applicability of the final model. As a basis for comparison, the derived kinetics from the reference experiment design was also used. The data under evaluation are taken from the experimental conditions of: (1) a nominal CLC experiment design at high temperature and (2) the first T-optimal design of **Figure 6.10**. The first experiment illustrates a realistic operation of CLC with CH_4 fuel and a NiO-based oxygen carrier. The capability of the model with parameters estimated from each design strategy to predict this experiment is depicted in **Figure 6.15**. Over this design, the model predicts the data equally well with all sets of parameters. This result validates the application of the D-optimal set of parameters to predict high temperature experiments, which were outside the range of the conditions used for the D-optimal kinetic parameter estimation.

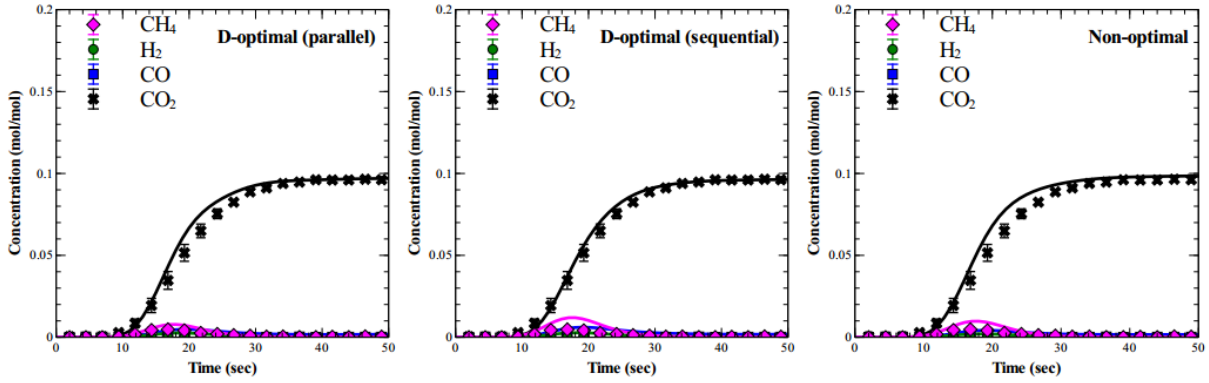

Figure 6.15: Model predictions of a normal CLC experiment using the final model $\mathbf{M}_{\mathrm{II-I-IV-I}}$ and the kinetic parameters obtained from the *parallel* D-design strategy (left), *sequential* D-design strategy (middle), and *reference* design strategy (right). $\square = \left[0.10\,\frac{\mathrm{mol}}{\mathrm{mol}}\ \mathrm{CH}_4, 2.2\mathrm{g}, 850^{\circ}\ \mathrm{C}, 50\square\square\square\right]$

In the second test, the kinetic parameters were used to predict the data of **Figure 6.10**. As shown in **Figure 6.16**, an acceptable agreement between model predictions and experimental data can only be achieved using the optimally-derived kinetics. The inadequacies of the model occurring at $t > 30$ sec are most likely not attributed to errors in the NiO reduction kinetics, rather to the catalytic reactions, which were determined from the nominal low-temperature experiment performed in Section 6.6.1. In both cases the CH_4 fraction was under-predicted, suggesting that the catalytic methane decomposition reaction could be ill-defined, which will be investigated in the future. These two case studies demonstrate that without a set of precise parameters, the predictive or extrapolation ability of a model is severely limited to the design space in which its parameters were estimated. This weakens the capacity of a model to be used for any other purpose, especially for process scale-up or design studies. However if the parameters are sufficiently precise and accurate, the reliability of a model is greatly increased, which is key for successful product and process design, control, and optimization applications.

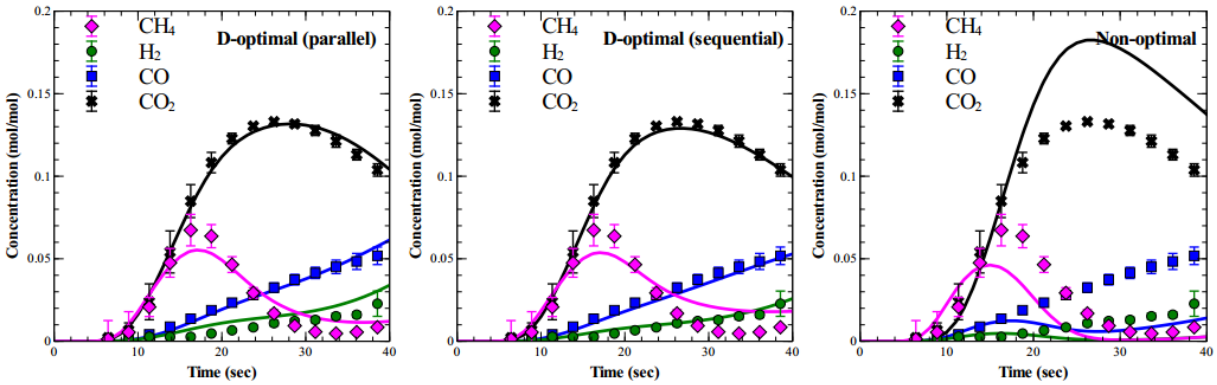

Figure 6.16: Model predictions of the first T-design experiment using the final model $\mathbf{M}_{\mathrm{II-I-IV-1}}$ and the kinetic parameters obtained from the *parallel* D-design strategy (left), *sequential* D-design strategy (middle), and *reference* design strategy (right). $\square_{\square(3)} = \left[0.20\frac{\mathrm{mol}}{\mathrm{mol}}\ \mathrm{CH_4}, 2.2\mathrm{g}, \mathit{615}^{\circ}\ \mathrm{C}, 40\mathrm{sec}\right]$.

6.7. Conclusions

The reduction of NiO by CH_4 is uncertain in regards to the most suitable reaction mechanism, reaction pathway, and contribution of the reactions catalyzed by Ni. In this series, a model-based framework for design of experiments was applied to identify and statistically validate a high fidelity kinetic model that is suitable for process engineering. In this work, we evaluated 160 possible kinetic models for the NiO-CH_4 system and found 4 model structures that were structurally identifiable with respect to its kinetics and distinguishable with respect to its model structure. In this paper, we optimized the design of CLC reduction experiments to facilitate model discrimination and parameter estimation. The differences between model structures were maximized in order to enable a clear discrimination of the most accurate model. The NiO reduction kinetic parameters were estimated from optimal experiments designed to minimize parameter uncertainty. The final model was shown to have predictive and extrapolation abilities, outside of the original experiment design space. Through this model-based methodology, we arrived at a high-fidelity kinetic model with precise parameters and at minimal experimental effort. The uncertainty of the NiO-CH_4 reduction kinetics is exemplary of the effectiveness of the presented framework applied to a relatively large problem with complex dynamic interactions.

Chapter 7 Dynamic Optimization of Fixed Bed Chemical-Looping Combustion Processes

The feasibility of incorporating chemical-looping combustion (CLC) into a combined cycle power plant is explored. We propose a model-based framework to optimally design the cycle strategy for a CLC system, composed of multiple fixed bed reactors. The CLC reactor system is optimally integrated with the downstream gas turbine of a combined cycle power plant, by solving a dynamic program to optimize the temperature profile of the heat removal step out of each reactor, with constraints on the system performance during reduction and oxidation. We demonstrate the feasibility of fixed bed CLC systems to achieve different exhaust temperatures, using synthetic Cu- and Ni-based oxygen carriers. The optimal operating strategy is scaled-up to a system of fixed bed reactors operating in parallel. We show that through process optimization, the batch-operation of fixed bed CLC reactors is void of significant exhaust gas temperature fluctuations and can reach high thermal efficiencies with in-situ CO_2 capture.

7.1. Introduction

The main application of chemical-looping combustion (CLC) will be in the power generation sector. Among the most energy efficient power cycles is the combined cycle power plant (CCPP), which is an arrangement of a gas turbine with a steam cycle. Combined cycles offer the advantage of high efficiencies, reduction in pollutant emissions, low capital and maintenance costs, and compatibility with natural gas and coal feedstocks [338–341]. In the natural gas fired combined cycle (NGCC), clean natural gas is combusted with air at high temperature and pressure in a gas turbine, producing electricity. Waste heat from the exhaust is then recovered through generation of high pressure steam, which powers steam turbines to produce more electricity. The exhaust gas contains CO_2 and steam, diluted in N_2 from the combustion air. To separate the CO_2 from the N_2, solvent-based absorption methods are usually preferred and afterward, the CO_2 is cooled and compressed to supercritical conditions [341,342]. Coal fired processes use the integrated gasification combined cycle (IGCC), wherein a synthesis gas mixture is

produced through gasification of the coal at high pressure with oxygen. After cleaning, the syngas is burned in the gas turbine and the exhaust gases are sent to the steam cycle. CO_2 removal from IGCC systems entails the addition of a shift converter unit (to convert the syngas into CO_2 and H_2) and/or a CO_2 separation and compression unit. The net power efficiency of conventional combined cycles without CO_2 capture is approximately 58%[338] using natural gas and 40-42% using coal [340,341]. Carbon capture by means of chemical absorption from the flue gases of the NGCC reduces the net plant efficiency and power output of the NGCC systems by about 10% [343]. The efficiency of IGCC with pre-combustion decarbonisation by physical absorption decreases the efficiency of the plant to 35%.[149] To reduce the energy expenditure of the CO_2 capture step, CLC can be used in these combined cycle plants [23].

One of the challenges in the commercialization of CLC technology is the integration of the CLC reactor with an existing power plant, from the process design perspective. The CLC unit can be integrated with a combined cycle by replacing the combustor of the gas turbine. In conventional syngas-fed and natural gas-fed gas turbines, the gas turbine pressure ratio is in the range of 10-20 with turbine inlet temperatures of 1100-1300°C [343–345]. The thermal efficiency of the gas turbine increases with the inlet temperature and pressure [346], which also benefits the steam cycle because the gas exiting the gas turbine is at higher temperatures. Therefore, CLC needs to be operated at elevated pressures, if integrated in a combined cycle power plant. From the efficiency perspective, the pressure drop across the CLC reactor should be low ($\Delta P/P<8\%$) [111], in order to conserve the energy spent in gas compression. In summary, high-pressure operation with low pressure drop is a requirement for high efficiency CLC integrated with a combined cycle.

The high-pressure requirement imposes constraints in the design and cycling sequence of CLC reactors. The most widely recognized design for CLC consists of interconnected fluidized bed reactors [23,81]. In this configuration, the solid oxygen carrier is physically transported between the so-called air and fuel reactors. This concept was successfully demonstrated in different prototypes with various oxygen carriers at atmospheric pressure [74,100,104,105,196,347–350]. The high-pressure fluidized bed concept is still

under development [351–353], due to the technical difficulties in gas/solid separations and the inherent challenges in achieving stable circulation of solids. Additionally, a high temperature and high pressure solids filtering system is required to remove the fines that result from the unavoidable particle attrition in fluidized bed systems [354]. The presence of particles in the outlet stream can negatively impact the performance of the gas turbine, as well as damage the thermal-barrier coatings on the surfaces of the gas turbine [355]. Alternatively, the fixed bed reactor configuration appears as a more practical option to accomplish high-pressure CLC. This concept was studied in several works for power generation and hydrogen production [96,108,354,356–360]. In the fixed bed design, the gas/solid separation problem is inherently avoided and no fines are sent to the gas turbine. The control and operation of fixed bed reactors under high-pressure operation is more straightforward than in the fluidized bed design. Due to its simplicity, the fixed bed design concept might serve well as an intermediate-scale technology deployment option for CLC.

In principle, the fixed bed CLC system is a batch process (**Figure 7.1**), that dynamically switches between consecutive reduction, oxidation, and heat removal phases. During the reduction phase, a hydrocarbon fuel is oxidized into CO_2 and steam, by reduction of the oxygen carrier. The reactor is briefly purged with an inert gas and the gas flow is switched to air to commence the oxidation step. Regeneration of the oxygen carrier is exothermic and produces a hot gas stream, which can be converted to electricity in a combined cycle power plant. Typically, oxidation and heat removal occur in succession without change of input parameters. In this cyclic process, the conversion and temperature profiles of the previous cycle influence the performance of the next. This, in addition to the effect of temperature on the oxygen carrier reactivity, impacts the switching scheme of the CLC process.

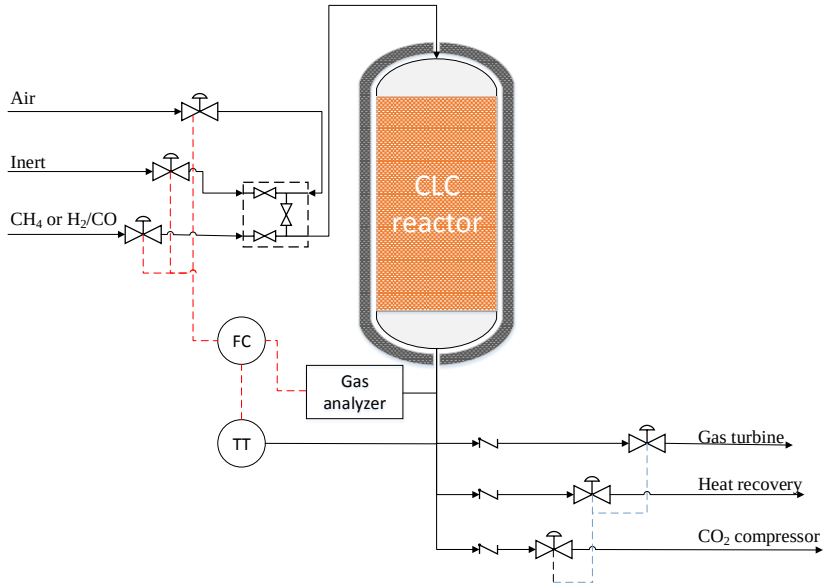

Figure 7.1: Schematic of a cycle strategy for a fixed bed CLC reactor.

The aim of this work is to showcase a model a model-based approach to optimally design and control such a batch process for power generation applications. We explore high-pressure fixed bed CLC reactors as a case study for this approach, where the process is heavily constrained in terms of performance and heat management. First, we discuss the formulation of a dynamic optimization problem for this batch heat generation process. The conditions of the CLC reactor that allow for seamless integration with a combined cycle are expressed as process constraints within the optimization problem. Optimal cycle strategies for fixed bed CLC with methane and syngas are presented and compared against a baseline design. We assess the feasibility of batch CLC processes utilizing synthetic Cu and Ni oxygen carriers, due to the availability of their kinetic data at high-pressure and their intrinsic differences in melting points, both of which impact the CLC performance and the efficiency of the power plant. The CLC process is evaluated on the basis of its compatibility with the combined cycle power plant, at different temperature set-points to feed the downstream gas turbine. Finally, the operation of a system of a series of fixed bed reactors working in parallel is calculated for a full-scale power plant.

7.2. Problem formulation

7.2.1. Process description

The CLC cycle in a batch fixed bed reactor consists of reduction, oxidation, and heat removal steps. To control this transient switching, a practical approach is to use the temperature and gas selectivity measurements of the exhaust stream to decide when to alternate the gas flow [108], as shown in **Figure 7.1**. **Figure 7.1** is not a real and complete controls diagram, but an illustration of a conceptual design strategy. In this strategy, the reduction cycle is stopped when: (a) fuel slip is detected or (b) the CO_2 capture efficiency is too low. Then the reactor switches to purging mode. After a brief purge, the oxidation cycle is initiated by feeding air into the reactor. When the front of the heat generated by the exothermic oxidation reaction reaches the reactor exit, the temperature of the exhaust stream rises and the exhaust gas is sent to the gas turbine. This is the heat removal stage and proceeds until the exhaust temperature reaches a temperature that is too low for the gas turbine. Some of the heat generated in the oxidation step is left in the bed and produces a moderate-temperature gas that can be used for heat recovery within the plant. After this, the reactor is purged and the cycle returns to the reduction step.

Temperature fluctuations occur in the reactor exhaust stream during the transient heat removal stage, which can negatively impact the operation of a downstream gas turbine. In particular, changes in turbine temperature can lead to thermal/mechanical cycling stress and differential expansion between stationary and rotating parts [358,361]. Both phenomena cause fatigue damage and reduce the lifetime of the turbine if they are not properly handled. Therefore, adequate heat management of the CLC reactor is needed for the gas turbine to operate efficiently and safely. In addition, it is best to maximize the solid conversion in the reduction and oxidation cycles to fully utilize the oxygen carrier, while maintaining high CO_2 capture efficiency. Due to these strict requirements and constraints, the design and operation of the batch CLC reactor is complex and requires a formal methodology that ensures system safety and reliability. In the following section, we propose a generic model-based formulation for the design and tuning of the switching strategy, with the objective of seamlessly integrating CLC into a combined cycle power plant.

7.2.2. Optimization problem formulation

The unit operations for the batch reactor are formulated as an optimal control problem, with the objective of maximizing the energy extracted from the CLC reactor to produce a gas steam suitable for power generation in the gas turbine. The control variables considered in this study are the flow rate and temperature of the feed air, time interval for the reduction, oxidation, and heat removal steps, and loading of the metal oxide in the oxygen carrier, listed in **Table 7.1**. Overall, this is a first-level exploratory work focused on the optimality of operation from the safety and turbine stability perspective. For a given reactor size and specific turbine inlet temperature, *TIT*, we explore the feasibility of operating a fixed bed CLC upstream a gas turbine, by manipulating all the controls available in **Table 7.1**. The composition of the feed gas is fixed to fuel during reduction (100% CH_4 or a syngas mixture), N_2 during purge and air during oxidation and heat removal. The control profile for the feed gas is modeled with piecewise constant functions, represented as $\mathbf{u}(\tau_i) = \mathbf{u}_i$, where $\mathbf{u}$ is the vector of temperature, flow, and composition of the gas stream and i is the index for the CLC step, *i.e.*, reduction, purge, oxidation, and heat removal. The duration for reduction, oxidation, and heat removal is τ_i and is considered as a control variable. The metal oxide content in the oxygen carrier, ω, is a time-invariant control variable, which can be tuned to achieve different exhaust temperatures during heat removal. The set of control variables is summarized in the design vector, $\boldsymbol{\phi}$, shown in Eq.(7.1), which is constrained by upper and lower limits permitted in the design space, $\boldsymbol{\Phi}$:

$$\boldsymbol{\varphi} = [\mathbf{u}_i, \tau_i, \omega] \ . \tag{7.1}$$

Table 7.1: Design variables in the dynamic operation of fixed bed CLC.

Design variables	*Notation*
Air feed rate	$\mathbf{u}_i$
Air temperature	
Reduction time interval	τ_i
Oxidation time interval	
Heat removal time interval	
Metal oxide content in oxygen carrier	ω

The objective function to be maximized is the time-integral of the temperature of the exhaust gas stream produced during heat removal, $T_{HR,out}(t)$. This can be interpreted as maximizing the time interval in which a high-temperature gas is generated for electricity production in the gas turbine. A normalization factor is used in the objective, $\alpha = \frac{1}{273.15}$. The temperature of the exhaust gas during the heat removal phase should be at or very close to a desired reference value of the turbine inlet temperature, *TIT*. To ensure that the *TIT* fluctuations are not significant, we impose an inequality path constraint on $T_{HR,out}(t)$ to not exceed $\pm$50°C of the *TIT* set-point. In this work, we consider two *TIT* set-points for the optimization study. While the state-of-the-art heavy-duty gas turbines can handle *TIT* values up to 1400°C [344,362,363], the CLC reactor can realistically operate at 800-1200°C, to prevent thermal damage of the oxygen carrier [34,364–366]. The temperature of the reactor always needs to be maintained below the melting or sintering points of the oxygen carrier, T^{max}. An inequality constraint is, thus, incorporated, where the temperature inside the reactor at any time and point must be less than 50°C below the melting point of the oxygen carrier, $T(t,z) \leq T^{max} - 50°C$. The CLC reactor during reduction also needs to achieve an acceptable level of performance in terms of emissions control. We impose inequality constraints during the reduction cycle to ensure that the process always behaves within commonly acceptable standards of fuel conversion ($X_{fuel}(t) \geq 98\%$) and CO_2 selectivity ($S_{CO_2}(t) \geq 90\%$) [149,341,367]. The pressure drop across the reactor must be below 8% of the inlet pressure [110], to avoid excess pressure losses ($\frac{\Delta P(t)}{P(t,z=0)} \leq 8\%$). These process constraints reflect the basic requirements of the CLC reactor according to the literature. The complete formulation for the discussed optimization problem is thus:

$$
\begin{aligned}
&\max_{\varphi\in\Phi} \int_{t_0}^{t_f} \alpha T_{HR,out}(t)dt \\
&\quad subject\ to: \\
&\quad \mathbf{f}\left(\dot{\mathbf{x}}(t),\mathbf{x}(t),\mathbf{u}(t),\boldsymbol{\theta},t\right)=0, \\
&\quad \mathbf{x}^{\min} \le \mathbf{x}(t) \le \mathbf{x}^{\max}, \\
&\quad \mathbf{u}_i^{\min} \le \mathbf{u}_i \le \mathbf{u}_i^{\max}, && i=1,\ldots,N_u \\
&\quad \tau_i^{\min} \le \tau_i \le \tau_i^{\max}, && i=1,\ldots,N_u \\
&\quad \omega^{\min} \le \omega \le \omega^{\max} \\
&\quad T_{HR,out}\left(t\right)=\mathbf{h}\left(\mathbf{x}\left(t\right)\right), && t\forall[t_0,t_f], \\
&\quad TIT-50°C \le T_{HR,out} \le TIT+50°C, && t\forall[t_0,t_f], \\
&\quad T(t_i,z)+50°C \le T^{\max}, && t\forall[t_0,t_f], z\forall[0,L], \\
&\quad S_{CO_2}(t) \ge 90\%, && t\forall[t_0,t_f], \\
&\quad X_{fuel}(t) \ge 98\%, && t\forall[t_0,t_f], \\
&\quad \Delta P(t)/P(t,z=0) \le 8\%, && t\forall[t_0,t_f],
\end{aligned}
\tag{7.2}
$$

where $X_{fuel}(t)$ and $S_{CO_2}(t)$ are the time-integrated fuel conversion and CO_2 selectivity, respectively as:

$$
S_{CO_2}(t)=\int_{t_0}^{t} F(t,z=L,CO_2)dt \Big/ \int_{t_0}^{t} (F(t,z=0,i)+F(t,z=0,CO_2))dt, \qquad i=\mathrm{CH_4}\ \text{or CO} \tag{7.3}
$$

$$
X_{fuel}(t)=1-\int_{t_0}^{t} F(t,z=L,i)dt \Big/ \int_{t_0}^{t} F(t,z=0,i)dt, \qquad i=\mathrm{CH_4}, \mathrm{H_2}, \text{or CO} \tag{7.4}
$$

As shown in Eq.(7.2), the batch reactor is represented by a system of differential and algebraic equations, **f**, where $\mathbf{x}(t)$ is the vector of state variables (*i.e.*, mass, temperature, and pressure), and $\boldsymbol{\theta}$ is the system parameters, including the kinetic constants, describing the reactivity of the oxygen carriers. The temperature measurement $T_{□□,□□□}(□)$ is a function **h** of the state variables, $\mathbf{x}(t)$. The underlying physics of the fixed bed CLC reactor is described by a heterogeneous reactor model presented previously [128,193]. The model incorporates the conservation equations of mass, energy, and momentum through the axial space of the fixed bed reactor. The dusty-gas diffusion model is used to capture the concentrated gas flows and internal diffusion limitations through oxygen carrier particles. External mass and heat transfer resistance is considered at the particle surface. In previous work, Zhou et al. [119,132,142] proposed a set of reaction kinetics for Cu- and Ni-based oxygen carriers, capable of predicting atmospheric fixed bed experiments reported in the open literature. We utilized optimal experimental design methods to statistically verify the CLC kinetic models and in turn, maximize the fidelity of the kinetic model to predict data outside of its design space [333,368]. We performed high-pressure fixed bed

experiments with Cu- and Ni-based oxygen carriers and matched the data using an empirical pressure correlation [65] and the optimized kinetic models derived at atmospheric pressure [369]. Thus, we can conclude that the reactor and kinetic models used here are realistic and accurate enough for depiction of the large-scale fixed bed systems analyzed here. The mathematical model was developed and solved using the commercial software package gPROMS [170]. We employed the control vector parameterization (CVP) with single-shooting algorithm to solve the dynamic optimization problem of Eq.(7.2). The complete mathematical model including the mass, energy and momentum balances, as well as the reaction kinetics and constants used in this work, are provided in Chapters 3-6.

7.3. Dynamic simulation of a nominal design

In this section, we describe the performance of a reactor with a nominal design, in order to establish a basis of comparison with the optimal solution determined from Eq.(7.2). For simplicity, we utilize the reactor design and operating conditions proposed by Spallina et al. [110] for CLC of syngas with an ilmenite oxygen carrier. The goal of this section is not to optimize the reactor design, but to illustrate a baseline performance with process conditions proposed in the literature for a large-scale fixed bed process. It is possible that this reactor design is sub-optimal for CLC with CuO and NiO oxygen carriers, but the focus here is on the optimality of operation and not the reactor design.

Table 7.2: Properties of the oxygen carriers simulated in this work.

Oxygen carrier		
Active metal	CuO	NiO
Support	SiO_2	α-Al_2O_3
Weight fraction of metal oxide (wt.%)	20	20
Solid porosity	0.40	0.40
Particle size (mm)	5	5
Melting point of reduced metal (°C)	1085	1455

Tables 7.2-7.3 summarize the nominal design parameters and operating variables used to establish a baseline performance of the fixed bed processes. The performance of the fixed bed reactor of **Table 7.3**, with the feedback control strategy discussed in **Section 7.2.1** is shown in **Tables 7.2-7.3**, presented in terms of the bed temperature *vs.* bed height, and exhaust gas temperature and composition *vs.* cycle time. The process decisions during the simulation sequence were to: (1) feed fuel (syngas or CH_4) until $X_{fuel}(t) < 98\%$ or $S_{CO_2}(t) < 90\%$; (2) switch to inert gas and purge the system for 300s, (3) feed air to oxidize the solids and produce a suitable gas for power generation, and (4) switch to purging mode when the reactor exhaust reaches the temperature set-point (T_{sp}=800°C for syngas-fed and T_{sp}=900°C for methane-fed processes). These steps are repeated for multiple redox cycles to achieve a cyclic steady-state, where the temperature and conversion profiles of one cycle are identical to the next. The results of **Figures 7.2-7.5** are presented for this cyclic steady-state condition, usually reached within 2-3 cycles. The heat removal duration, feeding the gas turbine (HR-1), was selected over the time interval in which the exhaust temperature was within 50°C of the turbine inlet temperature (*TIT).* For simplicity, we set the *TIT* set-point to 1000°C for both oxygen carriers. In the later sections, we incorporate different *TIT* set-points in the constraint of the optimization problem. As shown in **Figures 7.2-7.5**, the maximum temperature reached in the fixed bed process is dependent on the oxygen carrier material and fuel type. In **Figure 7.3**, the system overshoots the set-point and in **Figure 7.2**, **Figure 7.4**, and **Figure 7.5**, the system undershoots. The results shown here are used to illustrate the performance of a fixed bed process under a nominal design and operating conditions.

Table 7.3: Design and operating conditions of the studied fixed bed reactor configuration (adapted from Spallina et al. [110] suited for reduction by syngas-fuel and methane-fuel).

	Syngas-fuel	**Methane-fuel**
Reactor configuration		
Length (m)	11	11
Diameter (m)	5.5	5.5
Gas streams		
Air (Oxidation + Heat Removal)		
Mass flow (kg/s)	178	178
Pressure (bar)	17	17
Inlet Temperature (°C)	450	600
Composition (%.vol)	0.92 Ar; 0.03 CO_2; 1.03 H_2O; 77.28 N_2; 20.73 O_2	0.92 Ar; 0.03 CO_2; 1.03 H_2O; 77.28 N_2; 20.73 O_2
N_2 (Purge)		
Mass flow (kg/s)	577.5	577.5
Pressure (bar)	17	17
Inlet Temperature (°C)	450	450
Composition (%.vol)	1.016 Ar; 0.04 CO_2; 1.31 H_2O; 97.5 N_2	1.016 Ar; 0.04 CO_2; 1.31 H_2O; 97.5 N_2
Fuel (Reduction)		
Mass flow (kg/s)	152	15
Pressure (bar)	17	17
Inlet Temperature (°C)	450	450
Composition (%.vol)	1 Ar; 33.6 CO; 34 CO_2; 13.8 H_2; 16.4 H_2O; 1.3 N_2	100% CH_4

Figure 7.2 presents the complete CLC sequence with the CuO oxygen carrier and syngas fuel. When oxidation is started, energy is released from the exothermic reactions and the bed temperature increases. As air is continually fed to the reactor, the heat front travels axially through the bed and the cycle switches to heat removal when the exhaust temperature is high enough to feed a downstream gas turbine (**Figures 7.2(a)**-**7.2(b)**). The progression of the heat front can be seen in **Figure 7.2(a)**, by the location of the high temperature zones at the end of oxidation and at the end of heat removal. The exhaust temperature during the heat removal phase is relatively constant and flat during HR-1 and then steadily decreases during HR-2 (**Figure 7.2(b)**), because of the temperature profile inside the bed produced from the oxidation phase (**Figure 7.2(a)**). The exit gas concentration during oxidation is predominantly composed of N_2 with some unreacted O_2 (**Figure 7.2(c)**). The bed is completely regenerated at the end of the oxidation cycle, as inlet feed concentrations of the air are detected at the reactor exit (**Figure 7.2(c)**). After a brief purge, the cycle switches to reduction. The reduction of CuO by syngas is exothermic and

increases the internal bed temperature, which is shown in **Figure 7.2(a)** by comparing the temperature distribution at the end of heat removal (HR-2) with the distribution at the end of reduction. The exhaust temperature during reduction first decreases (**Figure 7.2(b)**), because the residual low-temperature heat from the previous heat removal step (**Figure 7.2(a)**) is being pushed out of the reactor. When the heat front from the reduction reactions reaches the exit of the reactor, the exhaust temperature increases (**Figure 7.2(b)**). The gas composition of the reduction exhaust is mostly H_2O and CO_2, with some minor slip of unconverted fuel occurring at the end of the reduction (**Figure 7.2(c)**).

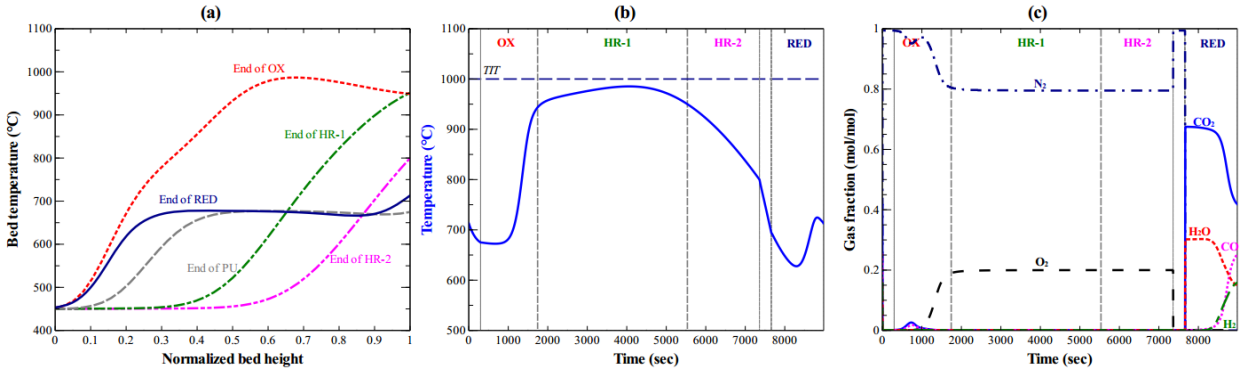

Figure 7.2: Profiles of the (a) internal solid temperature, (b) exit gas temperature and (c) exit gas composition of the CLC reactor with the CuO oxygen carrier and syngas fuel. The reactor design is reported in **Table 7.3**.

The dynamic behavior of the fixed bed reactor with the NiO oxygen carrier and syngas fuel is presented in **Figure 7.3**. In this process, the reduction step is less exothermic than with the CuO oxygen carrier, indicated by the lower temperatures inside the reactor at the end of reduction (**Figure 7.3(a)**). The exhaust gas during reduction, thus, exhibits smaller temperature fluctuations (**Figure 7.3(b)**) as compared to **Figure 7.2(b)**. During the reduction phase, complete conversion of the fuel is achieved with minor release of H_2 and CO **(Figure 7.3(c))**. After oxidation, the bed temperature is elevated (**Figure 7.3(a)**) and a

high-temperature gas is produced for heat removal (**Figure 7.3(b)**). The main heat removal phase is relatively longer in this process (**Figure 7.3(b)**), as compared to **Figure 7.2(b)**). This can be explained by the greater uniformity in bed temperature at the end of oxidation (**Figure 7.3(a)**), allowing for the heat removal stage to the gas turbine (HR-1) to proceed for longer times (**Figure 7.3(b)**).

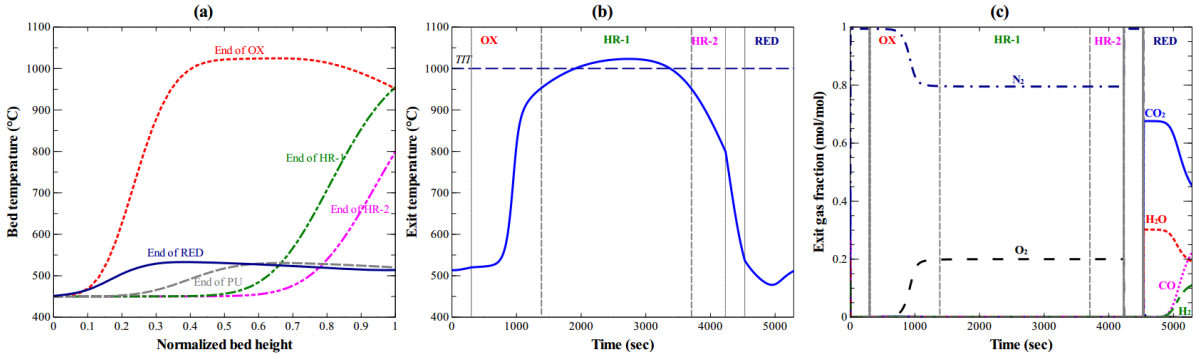

Figure 7.3: Profiles of the (a) internal solid temperature, (b) exit gas temperature and (c) exit gas composition of the CLC reactor with the NiO oxygen carrier and syngas fuel. The reactor design is reported in **Table 7.3**.

The performance of the fixed bed reactor under CuO reduction with methane is shown in **Figure 7.4**. When CH_4 is sent to the reactor, the entrance of the reactor is the first to be reduced. The reduced bed gets cooled down (**Figure 7.4(a)**) due to the endothermicity of the reduction reactions. The reduction of CuO by CH_4 produces partial combustion products (H_2 and CO) [142], which travel through the bed and get oxidized by the fresh oxygen carrier, liberating heat. Thus, the interior and exit regions of the reactor at the end of the reduction are warmer than at the end of heat removal, shown in **Figure 7.4(a)**. The temperature of the exhaust gas first decreases and then increases during reduction (**Figure 7.4(b)**). The temperature decrease (**Figure 7.4(b)**) is caused from the low-temperature heat front leaving the reactor and simultaneous cooling from the reduction reactions. Midway through reduction, temperature of the

exhaust gas rises (**Figure 7.4(b)**) because the reactor gets warmed up from the oxidation of H_2 and CO inside the bed. At the exit of the reactor, only CO_2 and H_2O are observed during reduction (**Figure 7.4(c)**), indicating complete conversion of the fuel. The subsequent oxidation and heat removal stages follow similar patterns as described in **Figures 7.2-7.3**.. At the end of oxidation, a high-temperature zone is formed inside the bed (**Figure 7.4(a)**), suitable for heat removal. The bed temperature near the reactor entrance slightly drops below the temperature of the inlet air at the end of oxidation (**Figure 7.4(a)**). The entrance was not fully reduced because of the slower reduction kinetics of CuO by CH_4 as opposed to syngas and the cooling effect of purge prior to reduction. Thus, less heat was liberated during oxidation and the feed of warm air slowly increases the temperature of the reactor entrance.

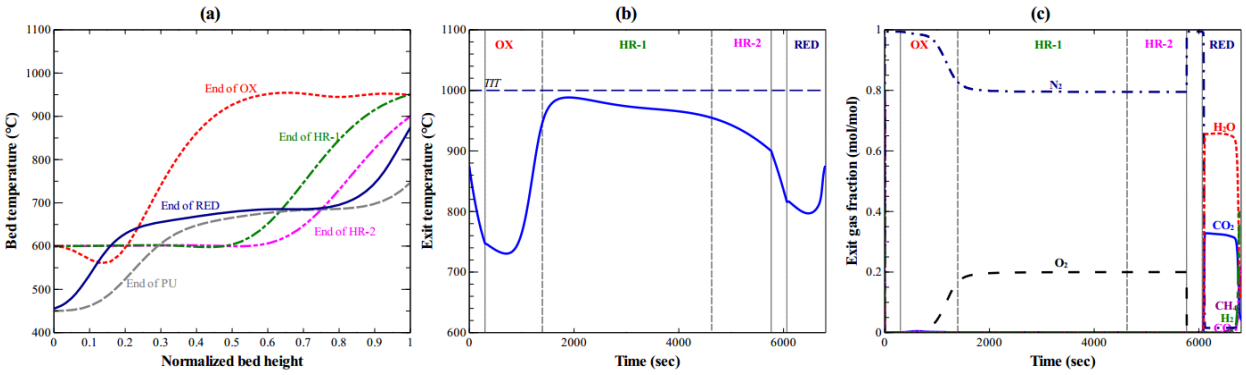

Figure 7.4: Profiles of the (a) internal solid temperature, (b) exit gas temperature and (c) exit gas composition of the CLC reactor with the CuO oxygen carrier and methane fuel. The reactor design is reported in **Table 7.3**.

Figure 7.5 presents the dynamic performance of the NiO oxygen carrier with methane fuel. Similar to **Figure 7.4(a)**, the reduction of the NiO by CH_4 is endothermic and decreases the temperature of the reactor (**Figure 7.5(a)**) as the conversion front moves through the bed. As a result, the temperature of the exhaust gas stream decreases over time during reduction and subsequent purge (**Figure 7.5(b)**). The

effluents of the reduction step are mostly CO_2 and H_2O, with a small amount of fuel slip occurring at the end of reduction (**Figure 7.5(c)**). During the oxidation cycle, heat is liberated by the exothermic reactions and a high-temperature zone is formed inside the reactor bed (**Figure 7.5(a)**). At the end of oxidation, the oxygen carrier is regenerated, indicated by the unconverted air leaving the reactor (**Figure 7.5(c)**), and the temperature of the exhaust gas is within 50°C of the *TIT* set-point (**Figure 7.5(b)**). The exhaust gas during heat removal exhibits a high temperature drop, restricting energy extraction to the gas turbine to ~50% of the total heat removal time **Figure 7.5(b)**).

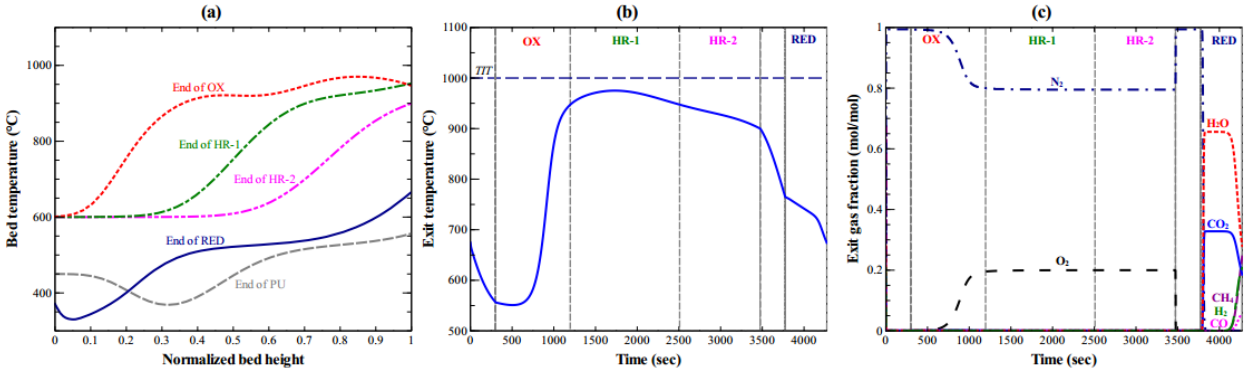

Figure 7.5: Profiles of the (a) internal solid temperature, (b) exit gas temperature, and (c) exit gas composition of the CLC reactor with the NiO oxygen carrier and methane fuel. The reactor design is reported in **Table 7.3**.

Figures 7.2-7.5 are representative of cycle strategies to conduct CLC in a large-scale fixed bed reactor. The issue with these nominal designs is the exit gas temperature and its fluctuations during the heat removal phase, which is not suitable for a downstream gas turbine. To find the optimal heat management strategy, we solve the optimization problem of **Section 7.2.2** for the reactor configurations of **Table 7.3**.

7.4. Results and discussion

7.4.1. Optimal fixed bed operation for CLC

The challenge in solving the optimization problem formulated in Section 7.2.2 is that the conversion and temperature profiles from the previous cycle impact the performance of the next cycles and it typically takes 2-3 cycles for the system to reach a cyclic steady-state condition after modifying the cycle strategy. Thus, the optimization procedure needs to be carried out for several redox cycles and the optimal cycle strategy should be extracted from the last cycle. In this analysis, we first initialize all state variables at the end of the heat removal phase of the nominal design point (shown in **Figures 7.2-7.5**) and perform the optimization procedure for 3 redox cycles. For each oxygen carrier, we consider two set-points for the turbine inlet temperature (*TIT*), being: 1100°C and 1000°C for NiO and 1000°C and 900°C for CuO. These reference values are exemplary of the existing, commercial gas turbines offered by Siemens [370,371] and GE [144,372,373]. As mentioned, smaller *TIT*s are required in CLC to protect the oxygen carrier from sintering or agglomeration. The results of this optimization are presented in **Figures 7.6-7.7** for the CuO oxygen carrier and in **Figures 7.8-7.9** for the NiO oxygen carrier. **Figures 7.6-7.9** showcase the optimal fixed bed performance with the low *TIT* set-point and in Figures SI.1-4 of the Supplementary Information of [374] we present the performance with the high *TIT*-set-point. For brevity, we will focus our discussion on **Figures 7.6-7.9**. The optimal operating strategies are presented in **Table 7.4.**

Figure 7.6 presents the optimal fixed bed performance with the Cu-based oxygen carrier and syngas fuel. With the *TIT* set-point of 900°C, the optimal configuration achieves a lower temperature rise during oxidation (**Figure 7.6(a)**), compared to the nominal design (**Figure 7.2(a)**). This was accomplished by using a reduced CuO loading. Shown in **Figure 7.6(b)**, the temperature of the gas steam starts below the *TIT* set-point at the start of heat removal to the gas turbine (HR-1), rises above the set-point, and then drops below the set-point at the end of HR-1. On average, the exhaust temperature with the optimal operating conditions is above the *TIT* set-point but within the 50°C variation allowed by Eq.(7.2). In the nominal design, the exhaust temperature during heat removal is always below the *TIT* set-point (**Figure**

7.2(b)). Another benefit with the optimal cycle strategy is the longer time interval to remove heat to the gas turbine (HR-1), from comparing **Figure 7.6(b)** with **Figure 7.2(b)**. At the same time, the duration of HR-2 is decreased and a higher bed temperature is available for reduction (indicated in **Figure 7.6(a)** and **Figure 7.2(a)**). The gas profiles during the entire CLC cycle (**Figure 7.6(c)**) follow the same trend as in **Figure 7.2(c)**, whereby high fuel conversion is achieved during the reduction and oxidation cycles and unconverted air leaves the reactor during the heat removal cycles.

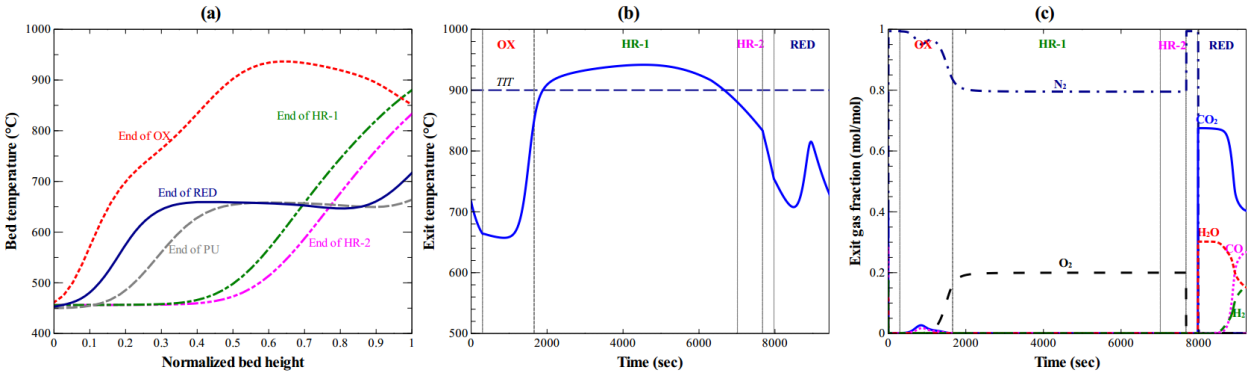

Figure 7.6: Profiles of the (a) internal solid temperature, (b) exit gas temperature, and (c) exit gas composition of the optimal operating strategy with the CuO oxygen carrier and syngas fuel, for a turbine inlet temperature (*TIT*) set-point of 900°C.

The optimal performance of the fixed bed reactor with the CuO oxygen carrier and methane is shown in **Figure 7.7**. Similar to the syngas-fed process, the optimizer reduced the CuO loading to achieve the turbine inlet temperature (*TIT*) set-point of 900°C. The air preheat temperature was increased, to improve the fuel conversion in the subsequent reduction step. The heat removal stage proceeds for longer times in the optimal design (**Figures 7.7(b)** and **7.7(c)**) as compared to the nominal design (**Figure 7.4(b)** and **Figure 7.4(c)**). Additionally, the temperature fluctuations of the reduction exhaust are suppressed in the optimal configuration (**Figure 7(b)**), which is the result of the better temperature uniformity inside the

bed at the end of heat removal (**Figure 7.7(a)**). The gas selectivity profile (**Figure 7.7(c)**) shows that during the reduction step, the methane feed is completely converted to CO_2 and H_2O (**Figure 7.7(c)**). During the oxidation cycle, no significant carbon oxides are released (**Figure 7.7(c)**), indicating that carbon formation was minor during the reduction step. A low-temperature zone is exhibited near the reactor entrance at the end of oxidation (**Figure 7.7(a)**), due to the locally incomplete conversion of solids in the previous reduction step, whereas the reactor entrance reaches the inlet gas temperature.

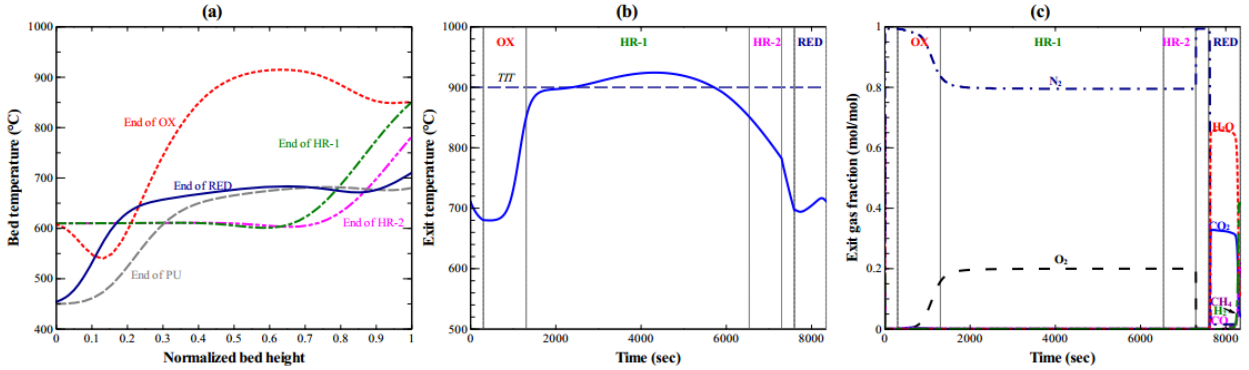

Figure 7.7: Profiles of the (a) internal solid temperature, (b) exit gas temperature, and (c) exit gas composition of the optimal operating strategy with the CuO oxygen carrier and methane fuel, for a turbine inlet temperature (*TIT*) set-point of 900°C.

Figure 7.8 shows the optimal performance for the NiO oxygen carrier with syngas fuel. The heat removal stage to the gas turbine was maximized to an extent that it was no longer necessary to consider a secondary heat removal step (HR-2). Instead only a purging step is shown in **Figures 7.8(b)-7.8(c)**, in between the HR-1 and reduction phase. Shown in **Figure 7.8(b)**, the gas temperature during heat removal satisfies the requirements for the gas turbine. This can increase the energy efficiency of the combined cycle power plant by sending more heat to the gas turbine. The reason for the better heat removal efficiency is the more uniform temperature distribution inside the reactor at the end of the oxidation step (**Figure 7.8(a)**), providing a flat temperature profile for the exhaust stream (**Figure 7.8(b)**). After heat

removal, the bed temperatures are higher in the optimal design (**Figure 7.8(a)**) compared to the nominal design (**Figure 7.3(a)**). This provides more heat for the reduction step and improves the conversion of the bed. The changes in the reduction cycle between the optimal and nominal designs can be seen by the higher temperature of the exhaust gas (**Figures 7.8(b)** and **7.3(b)**) and that of the solids at the end of the reduction step (**Figures 7.8(a)** and **7.3(a)**). The gas selectivity during reduction (**Figure 7.8(c)**) follows the same behavior as the nominal design (**Figure 7.3(c)**), satisfying the constraints of Eq.(7.2).

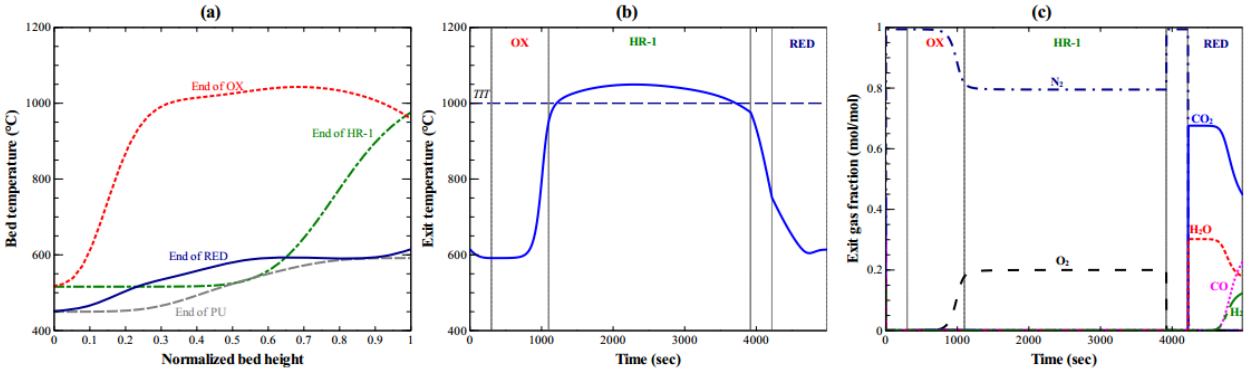

Figure 7.8: Profiles of the (a) internal solid temperature, (b) exit gas temperature, and (c) exit gas composition of the optimal operating strategy with the NiO oxygen carrier and syngas fuel, for a turbine inlet temperature (*TIT*) set-point of 1000°C.

For the reduction of NiO by methane, the optimal cycle configuration maximizes the heat removal step to the gas turbine and eliminates the HR-2 step entirely, as shown in **Figure 7.9**. The gas temperature during the heat removal step (**Figure 7.9(b)**) is on average higher than the turbine inlet temperature (*TIT*) set-point of 1000°C. This is mainly due to increasing the NiO loading, which favors a higher temperature rise inside the reactor after oxidation (**Figure 7.9(a)**). The reduction reaction for the NiO-CH_4 is highly endothermic and the kinetics is sensitive to the reaction temperature. Thus, the optimizer switches to reduction at a higher bed temperature (**Figure 7.9(a)**), compared to the nominal design (**Figure 7.5(a)**). More of the bed is able to be reduced and the gas selectivity (**Figure 7.9(c)**) indicates that the methane

feed is fully oxidized. The reduction gas stream leaves the reactor at higher temperatures (**Figure 7.9(b)**) compared to the nominal design (**Figure 7.5(b)**).

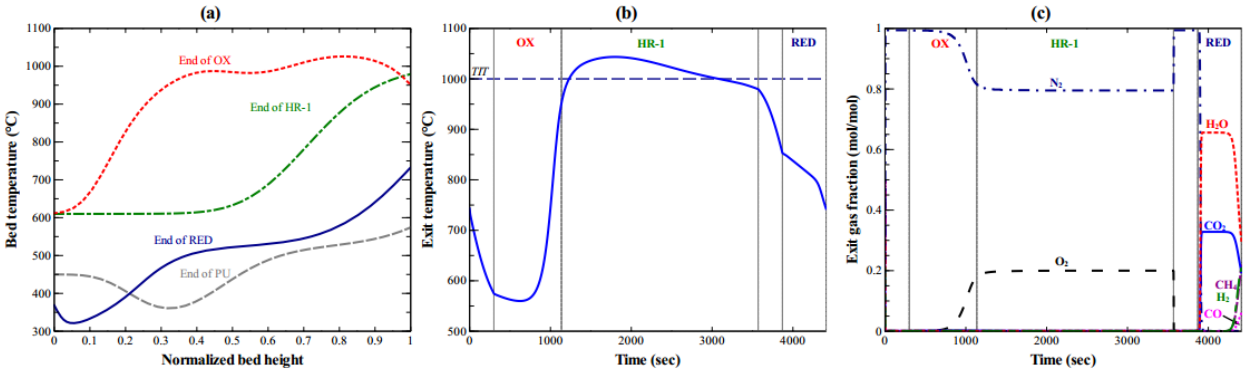

Figure 7.9: Profiles of the (a) internal solid temperature, (b) exit gas temperature, and (c) exit gas composition of the optimal operating strategy with the NiO oxygen carrier and methane fuel, for a turbine inlet temperature (*TIT*) set-point of 1000°C.

Table 7.4: Summary of the optimal operating strategy for the fixed bed processes with the NiO and CuO oxygen carriers over the reactor design of **Table 7.3**.

	CuO with syngas	**CuO with CH_4**	**NiO with syngas**	**NiO with CH_4**
TIT set-point (°C)	1000, 900	1000, 900	1100, 1000	1100, 1000
Reduction (RED)				
Cycle time (sec)	1612, 1549	830, 758	929, 764	633, 540
Oxidation (OX)				
Mass flow (kg/s)	142, 142	160, 160	160, 164	162, 167
Temperature (°C)	443, 456	610, 610	516, 516	650, 610
Cycle time (sec)	1553, 1359	1210, 1129	940, 799	941, 836
Heat removal 1 (HR-1)				
Mass flow (kg/s)	142, 142	160, 160	160, 160	160, 151
Temperature (°C)	443, 456	610, 610	516, 516	650, 610
Cycle time (sec)	5451, 5340	4500, 5236	2722, 2820	2445, 2434
Heat removal 2 (HR-2)				
Mass flow (kg/s)	178, 178	178, 178	178, N/A	N/A, N/A
Temperature (°C)	443, 456	610, 610	516, N/A	N/A, N/A
Cycle time (sec)	1540, 663	900, 758	378, N/A	N/A, N/A
ω (wt.%)	20.7, 17.6	21.5, 17.7	21.7, 20	23.2, 21.2

7.4.2. Comparison of the cycle strategies

We define three metrics to calculate the heat removal efficiency achieved with the optimal and nominal cycle strategies. The energy efficiency of the heat removal step, η_{HR}, was expressed as a ratio of the enthalpy of the high temperature gas stream for the gas turbine to the total enthalpy of one complete cycle:

$$\eta_{HR} = \frac{\int_{t_0=0}^{\tau_{HR1}} \left((\dot{m} \cdot h)\big|_{t,z=L} - (\dot{m} \cdot h)\big|_{t,z=0} \right) dt}{\int_{t_0=0}^{\tau_{cycle}} \left((\dot{m} \cdot h)\big|_{t,z=L} - (\dot{m} \cdot h)\big|_{t,z=0} \right) dt}, \tag{7.5}$$

where $\dot{m}$ and h are the time- and space-dependent mass flow rates and enthalpy of the gas stream, τ_{HR-1} is the time interval for the heat removal step to produce electricity in the gas turbine, and τ_{cycle} is the time interval for one complete redox cycle. The second metric used to evaluate the performance of CLC was the standard deviation of the exit gas temperature during the heat removal phase to the gas turbine, σ_{HR}. This performance evaluation quantifies the degree of temperature fluctuations experienced at the inlet of the gas turbine. The third metric was the fraction of time the process is in the main heat removal step (HR-1):

$$\chi_{HR} = \tau_{HR1} / \tau_{cycle} \ . \tag{7.6}$$

Table 7.5 summarizes the efficiencies calculated for the optimal case studies of **Figures 7.6-7.9** and Figures SI.1-SI.4 of the Supplementary Information of [374]. For comparison, we also report η_{HR}, σ_{HR}, and χ_{HR} for the nominal design (**Figures 7.2-7.5**). The CLC reactors with the optimal cycle strategies have higher values of η_{HR} for all the studied oxygen carriers, fuel types, and turbine inlet temperatures, indicating that more of the heat from the CLC reactions can be efficiently converted into electricity. The actual efficiency of the process can be higher because the remaining heat will be recovered in the steam cycle, but this was not considered in the present study. The standard deviation of the heat removal gas, σ_{HR}, is higher in the optimal designs. This can be interpreted as consequence of removing more heat to the gas turbine. Nonetheless, the maximum temperature change of the exhaust gas during the heat

removal phase is within the constraints of the problem. For a process to have smaller temperature fluctuations, the corresponding constraint can be adjusted to be tighter in the optimization problem. To maximize the energy efficiency of the gas turbine, the duration of the heat removal phase of the reactor was increased. Shown in **Table 7.5,** higher values of χ_{HR} were obtained for the optimized cases. Overall, dynamic optimization of the cyclic fixed bed operation increased the energy efficiency of the reactor while satisfying operating constraints.

Table 7.5: Heat removal coefficients computed for the optimal cycle strategies of **Figures 7.6-7.9** and for the nominal operation of **Figures 7.2-7.5**.

Case study		η_{HR}	σ_{HR} (°C)	χ_{HR}
CuO with syngas	Optimal design (*TIT*=1000°C)	6.30E-01	2.27E+01	5.07E-01
	Optimal design (*TIT*=900°C)	6.28E-01	1.72E+01	5.61E-01
	Nominal design (*TIT*=1000°C)	5.09E-01	1.15E+01	4.11E-01
NiO with syngas	Optimal design (*TIT*=1100°C)	7.82E-01	1.88E+01	4.62E-01
	Optimal design (*TIT*=1000°C)	8.36E-01	1.89E+01	5.66E-01
	Nominal design (*TIT*=1000°C)	6.34E-01	2.05E+01	4.37E-01
CuO with CH_4	Optimal (*TIT*=1000°C)	7.27E-01	1.86E+01	5.60E-01
	Optimal (*TIT*=900°C)	7.12E-01	9.76E+00	5.46E-01
	Nominal design (*TIT*=1000°C)	5.88E-01	1.02E+01	4.94E-01
NiO with CH_4	Optimal (*TIT*=1100°C)	8.25E-01	2.46E+01	4.43E-01
	Optimal (*TIT*=1000°C)	8.86E-01	2.02E+01	5.50E-01
	Nominal design (*TIT*=1000°C)	4.82E-01	7.62E+00	2.85E-01

A critical design variable that dictates the temperature rise during oxidation is metal loading in the oxygen carrier [96]. High metal loadings are desired for better bed utilization and process capacity. However, the process is also heavily constrained by the maximum temperature that can occur inside the reactor at any point and time. Oxygen carriers that have high carrying capacity and high oxidation enthalpy, such as NiO and CuO, are limited in the amount of active metal that they can use without undesirable hot spots [354]. The use of large particles can actually lower the extrema of the temperature fluctuations, by decreasing the reaction rates due to the intraparticle diffusion resistance [128,193]. In this analysis, we

found that as the *TIT* set-point increases, the maximum allowed metal oxide content increases (**Table 7.4**). To reach the same *TIT* set-point, a higher loading of CuO was needed as compared to NiO because of the higher heat of reaction of Ni (**Table 7.4**). There was also an effect of the fuel type on the optimal metal loading, for the same *TIT* values and materials. We found that CLC with methane can operate at higher loadings of CuO and NiO than CLC with syngas (**Table 7.4**), which can be the result of a higher diffusion resistance associated with CH_4 oxidation reactions and their slower kinetics.

In addition to optimizing the *TIT* value, the impact of the heat removal phase on the overall process efficiency is also a function of cycle duration of each CLC step. During heat removal, the total enthalpy of gas sent to the gas turbine can be increased by converting more of the oxygen carrier in the preceding reduction cycle. Hence, the exothermic reaction rate is higher and more heat is transferred to the heat removal gas. As discussed previously, the reduction cycle is highly constrained by the requirements in CO_2 capture efficiency and fuel conversion. If the reduction period continues for too long, solid carbon accumulates over the oxygen carrier, as shown in the work of Zhou et al. [324] and Nordness et al. [369]. Combustion of the solid carbon in the subsequent oxidation step produces temperature gradients inside the bed (for example, **Figure 7.2(a)**), resulting in unfavorable temperature fluctuations in the exhaust stream. The optimal cycle configuration shortens the secondary heat removal phase (HR-2) and manipulates the air temperature, so that reduction step occurs over a slightly hotter bed and a higher conversion can be obtained. It strikes a balance between the endothermicity and exothermicity of the CLC reactions to maximize the heat removal. By solving the dynamic optimization problem for the fixed bed CLC operation, we can find the optimal flow conditions and cycle times that maximize temperature uniformity, while maintaining high fuel combustion efficiency. The results show that despite the inherent reactor dynamics, the fixed bed system is a promising option for power generation in gas turbine-based power cycles.

7.4.3. Dynamics of the CLC reactor network

The next step of the analysis is to illustrate the scale-up of the CLC reactors for integration with a power

plant operating in continuous mode. We are interested in exploring how the dynamics of the each reactor will affect the downstream power plant components. We followed the procedure by Spallina et al. [110] to devise an operation strategy for a series of fixed bed reactors operated in parallel. According to Spallina et al. [110], the sequence is based on running the reactors with a phase displacement, ζ, equaling 1/3 of the time to compete the reduction step. The total number of reactors for the system is calculated from τ_{cycle}/ζ, to provide a constant input of fuel to the CLC reactor network. The performance of each reactor is based on the numerical results described in the preceding sections. The gas streams are mixed downstream of the reactors, assuming ideal gas behavior, into combined streams of CO_2/H_2O from reduction, N_2/O_2 from oxidation, and air from heat removal. These streams define the inputs to the power plant components, downstream of the CLC block.

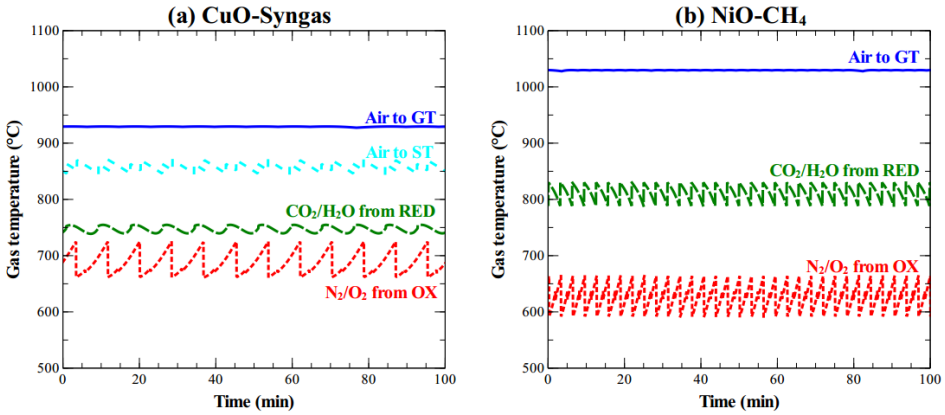

Figure 7.10: Gas temperature of the mixed gas streams leaving the system of fixed bed reactors for the (a) CuO process with syngas fuel and (b) NiO process with methane fuel.

We calculated a sequence of operation for the reactor systems with CuO and NiO oxygen carriers and syngas and methane reducing fuels and evaluated the behavior of the mixed streams leaving the reactor system. For brevity, we present the results for two dissimilar process operations: the CuO reactor with syngas fuel at the *TIT* set-point of 900°C (**Figure 7.10(a)**) and the NiO reactor with methane fuel at the

TIT set-point of 1000°C (**Figure 7.10(b)**). The performance of the reactors of **Figure 7.10** is evaluated over their optimal cycle strategies. As shown, the system generates a time-varying temperature profile for the mixed gas streams, as a result of the dynamic operation of each fixed bed reactor. The gas turbine receives a high-temperature gas that has practically no temperature fluctuations (**Figure 7.10(a)** and **Figure 7.10(b)**). The temperature fluctuations of the other gas streams are ~50°C or less. This illustrates that even though the temperature change experienced in each reactor is severe (around 500°C), running multiple reactors in parallel helps to equalize the temperature fluctuations so the power plant sees a more stable stream input. The extent of gas temperature fluctuations to the steam turbine can be reduced by use of an accumulator tank downstream the reactors to further mix the gases for a more uniform temperature profile.

To assess the feasibility of the fixed bed system, we discuss possible heat recovery opportunities for the lower-quality heat streams downstream the CLC reactors. As mentioned by Hamers et al. [356], preheating the syngas fuel before feeding the CLC reactors can be performed by cooling the CO_2/H_2O stream, which leaves the reactor at higher temperatures and mass flow rates compared to the inlet syngas. The depleted air stream produced from oxidation can be used to supplement the air stream used for heat removal to the gas turbine [111]. The temperature of the gas turbine exhaust is approximately 500-600°C [144], which provides the temperature differential to preheat the air stream, leaving the compressor at 450°C [111], before feeding the CLC reactors. To meet higher preheat temperature for the air, such as that shown in **Figure 7.10(b)**, the process can utilize the higher temperature gas streams, such as the reduction exhaust and a portion of the heat removal gas, noting that this would reduce the process efficiency. Preheating the inert gas for the purging steps is not expected to be problematic, because the N_2 is recycled through the system and can be used to preheat itself. From a qualitative point of view, the fixed bed reactor system optimized in this work shows promise for integrating into a combined cycle power plant. Future work is focused on the performance analysis of an integrated CLC-based combined cycle power plant, including thermal integration of the plant in the process design.

7.5. Conclusions

This work explored the optimality in integration of high-pressure fixed bed CLC reactors with combined cycle systems for power generation. One of most challenging aspects of the fixed bed process is the dynamic cycling between redox reactions and the resulting temperature fluctuations. This work formulated and solved a dynamic optimization problem to find operation strategies that enable the integration of the batch and transient operating profiles of fixed bed CLC reactors with the requirements for constancy and disturbance rejection of gas turbines. The results of this approach showed that fixed bed CLC reactors can provide a stable, high-temperature and high-pressure gas that is suitable for a downstream gas turbine, while accomplishing performance constraints in the reduction and oxidation cycles. The study focused on two synthetic oxygen carriers, two different gaseous fuels, and two set-points for the turbine inlet temperature. At the optimal conditions, the fixed bed reactor operates in its heat removal stage with a relatively flat exhaust gas temperature profile consistent with the requirements of the gas turbine of a combined cycle power plant. The oxygen carrier conversion during the reduction cycle was maximized, in order to generate a high-temperature gas stream to feed the gas turbine for longer periods. Optimization of the cycle strategy allowed for the fixed bed process to reach higher energy efficiencies than a baseline design. We extended the analysis to consider a system of reactors for an integrated large-scale power plant. The combination of multiple reactors decreased the temperature fluctuations of the gas streams sent to the power plant units. The drawbacks of this process are the high temperature variations inside the CLC bed between the redox cycles, the dynamic switching of reactors to achieve continuous operation for the power plant, and the corresponding need for high-temperature valves.

Chapter 8 A NOVEL REVERSE-FLOW FIXED BED REACTOR FOR CHEMICAL-LOOPING COMBUSTION

Chemical-looping combustion (CLC) is a promising technology for power generation with *in-situ* CO_2 capture. The most widely used process configuration for CLC is based on interconnected fluidized bed reactors. Although successfully demonstrated at the pilot scale, the interconnected fluidized-bed design encounters technical challenges, arising from the need for efficient gas-solid separation and the inevitable loss of particles due to attrition. These issues are intrinsically avoided in fixed-bed reactors by the nature of their stationary bed, which allows for compactness of design and better utilization of the oxygen carrier. However, fixed-bed reactors do not achieve the level of performance of their fluidized-bed counterparts, because of their lower CO_2 capture efficiency, and temperature and composition non-uniformity inside the bed. In this work, a novel fixed-bed configuration is presented, in which the fuel flow direction is periodically switched during the CLC reduction cycle. Simulations with an experimentally verified mathematical model demonstrate that the reverse-flow operation can significantly improve the performance of CLC fixed-bed reactors, making them competitive with their fluidized-bed equivalents, while addressing many of the bottlenecks in their operation. In reverse-flow mode, fixed-bed CLC systems achieve significant advantages, such as better gas-solids mixing, better CO_2 selectivity and capture efficiency, and lower temperature fluctuations.

8.1. Introduction

Chemical-looping combustion (CLC) has emerged as one of the most promising, low-cost CCS technologies [7,23,81], with the potential to reduce the cost of CO_2 capture by 50% [20]. Although CLC is an emerging technology, significant progress has been made over the last 10 years, with commercialization efforts anticipated shortly [7]. Comprehensive reviews covering the development of CLC were published by Adánez et al. [23], Hossain and de Lasa [81], and Lyngfelt et al. [375]. In CLC, a metal/metal oxide is used as an oxygen carrier that oxidizes a gaseous fuel, usually methane or natural gas. The looping schemes in **Figure 8.1** depict this cyclic process, involving an oxygen carrier reduction

step, where the fuel is oxidized to CO_2 and H_2O, and an oxidation step, where the reduced metal is regenerated in air. A pure stream of CO_2 is readily obtained in the reduction step, upon condensation of H_2O. The oxidation step produces a flue gas containing only N_2 and some unused O_2, which can be vented to the atmosphere. The metal oxide reduction reaction can be endothermic or exothermic depending on the active material, while the metal oxidation reaction is always exothermic. While there is no enthalpy difference between the overall CLC reaction and conventional combustion, the energy expenditure for CO_2 separation is significantly decreased in the CLC process. Thus, an overall higher thermal and electrical efficiency can be obtained compared to alternative CCS options [143,376].

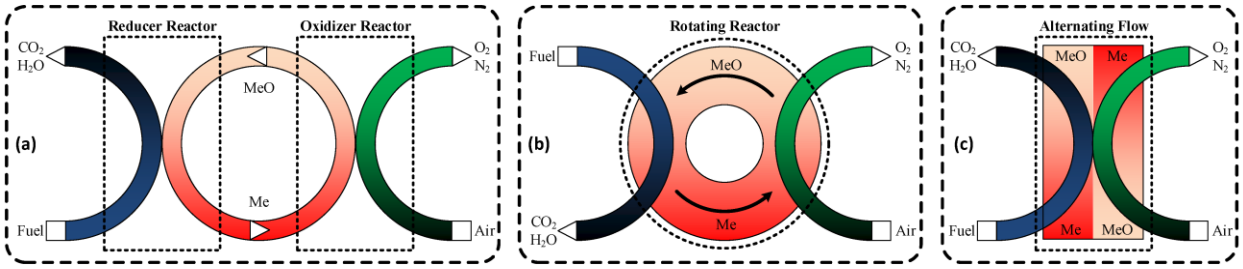

Figure 8.1: Reactor options for CLC: (a) circulating fluidized-bed; (b) rotating reactor; and (c) alternating flow over a fixed-bed.

The selection of suitable oxygen carriers is essential to the application of the CLC process. The desired characteristics are: high reactivity toward reduction and oxidation reactions; high CO_2 selectivity; stability over multiple cycles; low cost; and environmental benignity. The selection, preparation, and testing of oxygen carriers have been extensively studied in many publications [34,60,62,65,66,70,73–75,77,79,199–201,203,377,378]. Nickel-based oxygen carriers have received particular attention because of its high reactivity with CH_4 and durability in CLC systems [73,79,199,377,379]. Despite their excellent reactivity, Ni-based oxygen carriers are also responsible for H_2, CO and C products, because of the catalytic activity of Ni that promotes reforming, water-gas shift, and carbon formation reactions. Nonetheless, long-term

pilot-scale testing showed that Ni-based oxygen carriers exhibit high stability and reactivity over multiple redox cycles, while issues due to $NiAl_2O_4$ formation, sintering and agglomeration have been reported [66,70,72,114,197,379,380]. The drawbacks of using Ni include its high cost and toxicity, which makes it infeasible to operate at a commercial-scale, if particle attrition is significant. Ni can be potentially more favorable in fixed-bed CLC systems, where these issues are intrinsically avoided.

The process options for CLC can be categorized as circulating reactors, rotating reactors, and alternating flow reactors (**Figure 8.1**). The desired qualities of the CLC reactor system include: good mixing between fuel and solids; uniform distribution of temperature within the reactor; continuous operation; simplicity of scale-up; low pressure drop; limited attrition and creation of fines; and negligible leakage of fuel. The most widely used reactor technology is based on the interconnected fluidized-bed design [74,157,196,349,381] (**Figure 8.1(a)**). This CLC design has been successfully demonstrated in pilot plants ranging 0.3 – 140 kW, with 29 oxygen carriers, utilizing natural gas, methane and syngas, with a combined operation exceeding 4000 h [30]. Fluidization enables good contact between gas and solids, uniform temperature profiles, small pressure drop, and continuous operation [46,382]. Thus, the conversion of CH_4 to H_2O and CO_2 is always high and carbon deposition is marginal. Fluidized-bed reactors are, in general, commercially available and well-established in the petroleum refining industry. However, the dual-reactor configuration encounters various technical and operational issues. The circulation of solids between the two reactors requires energy-intensive cyclones and particle loop seals to prevent gas leakage, which is more problematic at elevated pressures [96,108]. Fragmentation and attrition of the oxygen carrier creates fines that need to be filtered, while fresh oxygen carrier needs to be continually added to the system [378,383]. The fragmented solids, in the form of fines, can be entrained and carried out of the fluidization vessel [157]. These issues drastically increase process operation costs, if an expensive oxygen carrier, such as Ni, is used. Moreover, they impact the environmental benignity of the CLC process, if harmful poisonous metals (*e.g.*, Ni) are to be emitted to the atmosphere in the form of fines.

Some of these issues are addressed in the moving bed reactor, proposed by Li and Fan [106], for the CL reduction of Fe-based oxygen carriers with syngas. Higher conversions can be obtained in the moving bed than in fluidized-beds thanks to the multiple oxidation states of Fe. The moving bed design reduces the solid circulation rate and minimizes the reactor volume. The concept was demonstrated in a 2.5 kW bench-scale unit for a combined operation of over 300 h, and was able to achieve complete conversion of the fuel (syngas, CH_4) with 100% CO_2 capture [384,385]. The reactor was operated isothermally using external heating, but this may not be feasible for a commercial process. Modelling and simulation was performed to optimize the moving bed design [386]. Similar technical issues such as attrition and gas leakage arise in this design due to the continuous circulation of solids between reactors. The use of large oxygen carrier particles (d_p=4 mm) is needed in the moving bed in order to resist fluidization, thereby potentially making reaction rates diffusion-limited [128,193].

Fixed-bed reactors have several advantages over alternative designs, of which the most important is the elimination of particle attrition and need for gas-solid separation [96,154,155]. The fixed-bed configuration (**Figure 8.1(c)**) consists of a stationary bed with alternating flows between reducing and oxidizing environments. By the simplicity of this design, fixed-beds are easier to scale-up, pressurize and operate, and can handle a relatively large range of particle sizes. The design is also more compact than a fluidized-bed reactor, which allows for better utilization of the oxygen carrier, lower capital cost, and smaller process footprint. CLC performance in a fixed-bed reactor was compared to an equivalent fluidized-bed in previous work and the results revealed a significant performance gap in terms of low CO_2 selectivity, severe temperature fluctuations, and high carbon formation [324]. Also, periodic operation can be undesirable because it requires the use of a high temperature, high gas flow switching system. Spallina et al. [109] demonstrated that switching the gas direction between oxidation and reduction cycles can improve the thermal management of the process. Hamers et al. [108] found that higher energy efficiency can be achieved by feeding the fuel in the opposite direction during reduction. However, this can lead to severe temperature fluctuations in the exhaust stream. Thus, a configuration with two fixed beds in series

was proposed to achieve the desired outlet temperature and improve the range of applicable oxygen carriers.

In rotating bed reactors (**Figure 8.1(b)**), an annulus fixed-bed is rotating between different sectors, where air and fuel are fed. Dahl et al. [97] designed a prototype CLC rotating reactor, which was able to achieve 90% methane conversion and over 90% CO_2 capture efficiency using a CuO/Al_2O_3 oxygen carrier [387]. The advantages of the rotating reactor design include compactness of design, continuous operation, limited energy for circulation, and feasibility of scale-up and commercialization, but the system is limited by the low CO_2 purity mostly due to gas leakage and mixing between fuel and air streams [23]. Simulations of the rotating reactor revealed that reducing the angular dispersion can increase the CO_2 purity [112]. In the work by Zhao et al. [98,99] a rotary-bed reactor was explored as an alternative to the rotating reactor design. The rotary-bed reactor consists of a rotary solid wheel, with micro-channels coated with oxygen carrier that rotates through reducing and oxidizing environments. With this design, mixing between air and fuel can be avoided with an efficient sealing system [388]. Potential drawbacks include high temperature fluctuations, thermal distortion and carbon deposition.

Given the process options for CLC, the fixed-bed reactor is a promising candidate, but significant improvements are needed to close the performance gap with the other higher-performing reactors. In this work, a novel reverse-flow concept is explored for CLC reduction in fixed-bed reactors. **Figure 8.2** shows the concept of a reverse-flow fixed-bed reactor, in which the operation is controlled by two valves, set to switch flow direction periodically. Flow reversal was originally employed in adiabatic fixed-bed reactors for exothermic reactions [158,389–391]. The principal advantages of flow reversal include improved heat transfer at the inlet and exit of the bed and formation of a hot zone in the middle section of the reactor [392]. The maximum temperature rise in the bed exceeds that of steady-state fixed-beds, which permits higher exit conversions [393,394], at lower heating demands [390]. Thus, reverse-flow operation made it possible to provide continuous autothermal operation without external gas preheating. This idea was extended for coupling endothermic (*e.g.*, methane steam reforming) and exothermic reactions (*e.g.*,

methane combustion) [391,394–399], which results in superior heat integration, higher thermal efficiency, and productivity [400,401]. Flow reversal can increase the conversion of reversible-reactions by shifting the equilibrium with the moving heat front [402–404]. Although cyclic, reverse-flow operation has been commercially demonstrated for processes such as the production of syngas from methane [405,406], oxidation of sulphur dioxide [407,408], methanol synthesis [409], treatment of waste air [410–422], and oxidation of o-xylene [423].

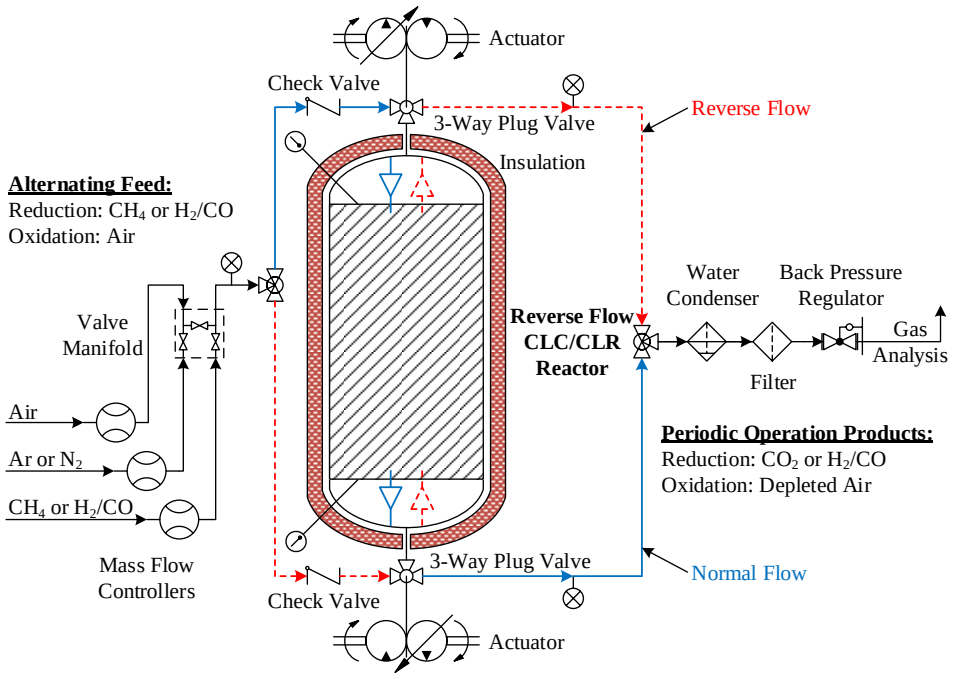

Figure 8.2: Diagram of bench-scale reverse-flow fixed-bed reactor

The scope of this paper is to provide proof of concept of the superiority of the reverse-flow operation for CLC fixed-bed reactors. The potential benefits of periodic reversal are explored for the oxygen carrier reduction cycle, in relation to the performance of conventional fixed-bed and fluidized-bed systems. Advantages of the reverse-flow reactor include simplicity of operation, compactness of design, feasibility of scale-up, straightforward gas-solid separation, and no particle attrition. Furthermore, the superior heat

integration and better gas-solid contact in the reverse-flow process can be beneficial to the feasibility and realizability of large-scale CLC systems.

8.2. Mathematical model

8.2.1. Background of CLC modeling

In previous work, we have investigated kinetic and reactor models for CLC applications in TGA, fixed-bed, and fluidized-bed reactors [119,128,132,193,424]. The appropriateness of modelling assumptions was extensively studied [193], showing the dependence of reaction rates on the extent of mass and heat transfer dominance inside the reactor and/or the oxygen carrier. As fixed-beds commonly operate with a range of particle sizes, accurate modelling of the diffusion limitations within and surrounding the particle is essential. We have developed and validated a particle model that was able to predict the extent of diffusion limitations over changing particle sizes [128,193]. The model was also predictive of the changes in the particle microstructure due to chemical and physical degradation [128]. At the reactor level, the heterogeneous model achieved not only superior predictions of the experimental data from various CLC units (**Table 8.1**), but also more realistic estimates of the kinetic parameters [193]. Modelling of the temperature gradients inside the fixed-bed gave valuable information about the dependence of reactions on mixing patterns. In most cases, intraparticle heat resistance was negligible, however interfacial heat transfer was found to limit CLC reaction rates with large particles [193]. For all simulations, mass and energy balances, as well as momentum balance, as approximated by the Ergun equation, were included. In summary, the models developed previously can be used with confidence for reactor analysis and process efficiency studies.

Moreover, Ni-based oxygen carrier reduction kinetics were analyzed, in terms of the applicability of known solid-state reaction models, such as the volumetric model, shrinking core, nuclei formation and growth, and power law [119,132]. Analysis of the reported CLC fixed-bed experimental data showed that, for supported NiO oxygen carriers, reduction by CH_4, H_2, and CO can be satisfactorily represented by a

previously reported, see Ref. [58], modified volumetric model [119]. A more detailed investigation was conducted in TGA and the superiority of the nuclei formation and growth model, as well as that of the modified volumetric model, was shown with statistical analysis over a range of flow rates, sample weights, and temperatures [132]. A universal CLC reaction scheme was proposed (**Table 8.2**) for a Ni-based oxygen carrier and CH_4 reducing fuel, which was validated against data collected from fixed-bed and fluidized-bed units in the literature [119,324,424]. The reaction scheme and kinetic parameters of (**Table 8.2**) were later refined in the work of Han et al. [333,368] by employing a model-based structural identifiability and optimal experimental design analysis.

Table 8.1: Operating conditions of the current CL fixed-bed units.

	Ref. [171]	*Ref.* [58]	*Ref.* [119]	*Ref.* [172]
L [mm]	250	7.65	21.7	5.66
D [mm]	16	4	9.9	15
Q [ml min^{-1}]	900	100	100	60
Fuel	33% CH_4/H_2O	10% CH_4 /Ar	10% CH_4 /Ar	25% CH_4 /Ar
T [°C]	600	900	800	900
Fr	0.34	6.3	0.055	0.0039
L/D	15.6	1.9	2.2	0.38
Re_p	10	0.5	0.07	0.02

Table 8.2: Chemical-looping Reducer reactions with NiO and CH_4 [119].

NiO reduction reactions	Partial CH_4 oxidation	$CH_4+2NiO \rightarrow 2Ni+CO_2+2H_2$
	H_2 oxidation	$H_2+NiO \rightarrow Ni+H_2O$
	CO oxidation	$CO+NiO \rightarrow Ni+CO_2$
	Partial CH_4 oxidation	$CH_4+NiO \rightarrow Ni+2H_2+CO$
Ni-catalyzed reactions in CL Reducer	Steam CH_4 reforming	$CH_4+H_2O \leftrightarrow 3H_2+CO$
	Water gas shift	$CO+H_2O \leftrightarrow H_2+CO_2$
	Dry reforming	$CH_4+CO_2 \leftrightarrow 2CO+2H_2$
	Methane decomposition	$CH_4 \leftrightarrow 2H_2+C$
	C gasification by H_2O	$C+H_2O \leftrightarrow CO+H_2$
	C gasification by CO_2	$C+CO_2 \leftrightarrow 2CO$

8.2.2. Background of reverse-flow modeling

Models of reverse-flow operation are primarily aimed at describing the principal heat and mass changes occurring during flow reversal. At the simplest, the model should consider convective mass transport, reaction kinetics, heat dissipation, and temperature transients for the solid phase [390]. Since its development, various plug-flow homogeneous models [425–428] and heterogeneous models [409,423,429,430] were used to provide a qualitative description of the reverse-flow phenomena. The indirect coupling of combustion and steam reforming reactions in a reverse-flow configuration was first simulated by Kulkarni and Duduković [395,398,399], who developed a numerical algorithm to accurately capture the moving temperature and concentration fronts. The simulations were used to propose possible ways for achieving high thermal efficiencies and heat integration with other process units [397]. This concept was applied to study temperature control for highly endothermic reactions by van Sint Annaland et al. [431,432]. In summary, the optimal design of the reverse-flow reactor relies on the adequate selection of reactor size, bed porosity, feed concentration and flow, and flow switching frequency [433]. For coupling endothermic and exothermic reactions, optimal performance lies in the maximization of the time-averaged endothermic reaction products, while minimizing the fuel expenditure for exothermic reactions. For CLC, optimal design of the reverse-flow reactor needs to effectively increase the conversion of fuel into CO_2 and minimize the temperature deviations throughout the bed.

8.2.3. Dynamic fixed-bed model

In this work, the heterogeneous modelling framework, previously developed [128,193], is chosen to simulate the reverse-flow reactor performance. The dynamic balance for the gaseous species through a spherical particle is:

$$\frac{\partial(\varepsilon_c C_{c,i})}{\partial t} + \frac{1}{r_c^{\,2}} \frac{\partial}{\partial r_c}\left(r_c^{\,2} J_i\right) = \rho_s \sum R_i \ , \tag{8.1}$$

where $C_{c,i}$ is the concentration of gas component i inside the particle, J_i is the flux of gas component i, and $\sum R_i$ is the sum of the intrinsic rates of the reactions given in **Table 8.2**. The flux of gas through the solid is described by the dusty-gas model, which provides a more realistic depiction of the intraparticle mass

transport in a multi-component mixture [326,327,434]. Due to the small scale of the pores, pressure gradients and convective forces inside the particle are assumed to be negligible to diffusive effects. The species flux is expressed as:

$$-\frac{\partial C_{c,\mathrm{i}}}{\partial r_c}=\sum_{j=1}^{N}\frac{1}{D_{\mathrm{ij}}^{e}}\left(y_k J_i-y_i J_k\right)+\frac{J_i}{D_{\mathrm{i}K}^{e}}, \tag{8.2}$$

where the structure of the oxygen carrier is assumed symmetrical and uniform, characterized by a void space ε_c and tortuosity τ. The effective diffusivities of gas through the void space, D_{ij}^{e} and $D_{\mathrm{i}K}^{e}$, are functions of the molecular diffusivity and the pore structure. The heat balance within the solid phase is described by Fourier's law:

$$\left(\left(1-\varepsilon_c\right)\rho_s C_{p,s}+\varepsilon_c C_{p,c} C_{T,c}\right)\frac{\partial T_c}{\partial t}=\frac{1}{r_c^{\,2}}\frac{\partial}{\partial r}\left(r_c^{\,2}\lambda_s\frac{\partial T_c}{\partial r_c}\right)+\rho_s\sum\left(-\Delta H_i\right)\left(R_i\right). \tag{8.3}$$

The boundary conditions at the particle center and surface are determined from the continuity of fluxes:

$$J_i\big|_{r_c=0}=\left.\frac{\partial T_c}{\partial r_c}\right|_{r_c=0}=0, \tag{8.4}$$

$$J_i\big|_{r_c=r_p}=k_{c,i}\left(C_{c,i}\big|_{r_c=r_P}-C_i\right), \tag{8.5}$$

$$-\lambda_s\left(\frac{\partial T_c}{\partial r_c}\right)\bigg|_{r_c=r_p}=h_f\left(T_c\big|_{r_c=r_p}-T\right). \tag{8.6}$$

The reactor model assumes an axially dispersed plug flow for the bulk transport of mass and heat. The reactor is operated without external heating and thus, radial temperature gradients are neglected. The 1D model is written as:

$$\frac{\partial(\varepsilon_b C_i)}{\partial t}+\frac{\partial(uC_i)}{\partial z}=\varepsilon_b\frac{\partial}{\partial z}\left(D_{ax,i}\frac{\partial C_i}{\partial z}\right)+k_{c,i}a_v\left(C_{c,i}\big|_{r_c=r_P}-C_i\right), \tag{8.7}$$

$$\frac{\partial(\varepsilon_b C_{p,f} C_T T)}{\partial t}+\frac{\partial(\mathrm{C}_T\, C_{p,f} uT)}{\partial z}=\varepsilon_b\frac{\partial}{\partial z}\left(\lambda_{ax}\frac{\partial T}{\partial z}\right)+h_f a_v\left(T_c\big|_{r_c=r_P}-T\right), \tag{8.8}$$

where ε_b is the bulk porosity, C_i is the concentration of species i in the bulk phase, u is the superficial gas velocity, T is the temperature of the bulk fluid, $C_{p,f}$ is the heat capacity of the bulk fluid, $k_{c,i}$ and h_f are the

mass and heat transfer coefficients between the bulk gas and the particle surface, a_v is the total external surface area per unit volume, $D_{ax,i}$ is the effective axial dispersion coefficient in Eq.(8.9) estimated by the Bischoff and Levenspiel correlation [159], and λ_{ax} is the effective thermal conductivity in Eq.(8.10) by Yagi et al. [163].

$$\frac{1}{Pe_{ax}} = \frac{\varepsilon_b}{\tau Re_p Sc} + \frac{0.45}{\left(1+\frac{7.3}{Re_p Sc}\right)}, \tag{8.9}$$

$$\frac{\lambda_{ax}}{\lambda_m} = \frac{\lambda_e^0}{\lambda_m} + 0.7 Pr\, Re_p. \tag{8.10}$$

The momentum balance through the fixed-bed is expressed by the Ergun equation:

$$\frac{dP}{dz} = -\left(\frac{1-\varepsilon_b}{\varepsilon_b{}^3}\right)\left(\frac{\rho u_0^2}{d_p}\right)\left(\frac{150}{Re_p}+1.75\right), \tag{8.11}$$

where P is the total pressure in the bed, ρ is the density of the bulk fluid, u_0 is the superficial gas velocity, d_p is the particle diameter and Re_p is the particle Reynolds number. The appropriate boundary conditions for the reactor equations under one-directional flow are:

$$\varepsilon_g D_{ax,i} \left.\frac{\partial C_i}{\partial z}\right|_{z=0} = \left[u(C_i - C_{i,in})\right]\Big|_{z=0}, \tag{8.12}$$

$$\varepsilon_g \lambda_{ax} \left.\frac{\partial T}{\partial z}\right|_{z=0} = \left[(uC_T C_{p,\mathrm{f}})(T_i - T_{in})\right]\Big|_{z=0}, \tag{8.13}$$

$$\left.\frac{\partial C_i}{\partial z}\right|_{z=L} = \left.\frac{\partial T}{\partial z}\right|_{z=L} = 0, \tag{8.14}$$

$$P\big|_{z=L} = P_{out}. \tag{8.15}$$

8.2.4. Reverse-flow operation

In reverse-flow operation, the gas velocity, U, changes in sign for every t_s seconds, with t_s being the switch time, or time interval between subsequent switches of the flow direction. When the flow is entering at $z=0$, the gas velocity is defined as a positive number, and when flow is entering at $z=L$, it is defined as a negative number. The changes in velocity due to dynamic flow reversal are shown in Eqs.(8.16)-(8.17), where n is the number of switches [390]. To differentiate the gas velocities, U refers to

the reverse-flow process, while *u* refers to the one-directional process.

$$U(t) = \kappa(t) u, \tag{8.16}$$

$$\kappa(t) = \begin{cases} 1, \ t \in \left[(n-1)t_s, (n-1/2)t_s \right] \\ -1, \ t \in \left[(n-1/2)t_s, nt_s \right] \end{cases}. \tag{8.17}$$

The boundary conditions in the revere-flow operation are:

$$\varepsilon_b D_{ax,i} \frac{\partial C_i}{\partial z} = \begin{cases} \dfrac{1+\kappa(t)}{2} u\left(C_i - C_{i,in}\right), \ z = 0 \\ -\dfrac{1-\kappa(t)}{2} u\left(C_i - C_{i,in}\right), \ z = L \end{cases} \tag{8.18}$$

$$\varepsilon_b \lambda_{ax} \frac{\partial T}{\partial z} = \begin{cases} \dfrac{1+\kappa(t)}{2} u\left(T - T_{in}\right) C_T C_{p,f}, \ z = 0 \\ -\dfrac{1-\kappa(t)}{2} u\left(T - T_{in}\right) C_T C_{p,f}, \ z = L \end{cases}. \tag{8.19}$$

The dynamic model is implemented and solved in gPROMS 4.0 [435]. The finite difference method is used to discretize the partial differential equations along the axial bed direction and the radial particle direction.

8.3. Reactor design and operation

To explore the advantages of reverse-flow reactors for CLC, two conceptual reactors are simulated: (a) a bench-scale reactor, designed to represent a conceptual "average" of experimental setups reported in the literature; and (b) a scaled-up version of the bench-scale reactor, to explore the theoretical benefits of flow reversal at larger scale. A CH_4-fed system with a Ni-based oxygen carrier is studied, for which existing models were validated previously [119,128,132,193,424]. Demonstration of the performance of the reverse-flow CLC system with Ni is valuable, due to the fact that the constraints imposed by fluidized-bed reactors, such as attrition, cost and pollution due to lost Ni, invalidate this otherwise excellent oxygen carrier. Nevertheless, the modelling approach is extendable and applicable to other gaseous fuels and oxygen carriers.

8.3.1. Design parameters

The reduction of a Ni-based oxygen carrier by CH_4 is simulated following the reaction scheme of **Table 8.2**. For the theoretical analysis presented here, the Ni-based oxygen carrier studied by Chandel et al. [127] (**Table 8.3**) is used, because we were able to successfully predict the oxygen carrier reduction characteristics reported for their batch fluidized-bed reactor [436]. The NiO loading was changed from the original value of 60 wt.% to 20 wt.% in order to limit the temperature rise during the subsequnt oxidation cycle. The typical temperature of reduction for a continuous CLC plant is 900°C [437], and it is assumed that the inlet fuel is pre-heated by the exhaust stream of the Oxidizer to 900°C. The reducing gas is pure CH_4. The initial bed temperature prior to reduction is slightly above 900°C (assumed 950°C), because of the heat liberated from the previous oxidation cycle [108]. No external heating is applied and adiabatic conditions are assumed, in order to represent a hypothetical commercial process [392]. In the simulation of reverse-flow operation, the boundary conditions are periodically altered as shown in Eqs. (15-18). Different switch time intervals are investigated to explore their effect on performance optimality. To clarify the terminology used in the remaining of this paper, "switching frequency" refers to the number of flow reversals during the reduction period, while "switch interval" refers to the time between each flow reversal. These two terms are obviously correlated by the time required for one reduction cycle, which was set to 250 s, to ensure complete reduction of the oxygen carrier. Complete oxygen carrier reduction is, of course, unrealistic, but it is studied here to explore the extrema of advantages of the reverse-flow concept. The performance of the reverse-flow reactor is compared to the traditional one-directional process, where any differences in the gas, bed temperature or conversion profiles are attributed only to flow reversal (*i.e.*, all other process conditions are kept identical).

8.3.2. Design of the bench-scale reactor

A bench-scale reactor is designed on the basis of previously studied CLC/CLR fixed-bed units (**Table 8.1**), to serve as a benchmark for the advantages of reverse-flow operation. The reactor dimensions are chosen with an average length to diameter (L/D) ratio consistent with the CLC units of **Table 8.1**. The corresponding gas velocity should promote convective flow to increase reactor output, while providing

sufficient residence time to completely convert the fuel. The mixing patterns inside the reactor can be characterized by the Froude number, and for the bench-scale reactor studied here, a similar Froude number to that of Jin and Ishida [62] is selected. For higher Froude numbers, as in the case of Iliuta et al. [58], the residence time is too short and unconverted fuel escapes the reactor. A very small Froude number is also undesirable, because of back-mixing and low output. Thus, matching the hydrodynamics of the Jin and Ishida [62] unit is appropriate. The gas flow rate is then calculated based on the target Froude number and reactor dimensions. The operating conditions and sizing of the bench-scale reactor are presented in **Table 8.4**

Table 8.3: Properties of the oxygen carrier studied [127].

Surface area (m^2/g)	7
Ni loading (wt.%)	20
Density (kg/m^3)	3960
Porosity	0.37
Size [μm]	300

Table 8.4: Design and operating parameters for the case studies examined.

	Bench-scale reactor	*Industrial-scale reactor*
L [m]	0.22	1.0
D [m]	0.055	0.25
Q (L/min)	16.68 (100% CH_4)	3000 (100% CH_4)
Fr	0.34	0.39
L/D	4	4
Re_p	0.80	6.9
ΔP [bar]	0.3	4

8.3.3. Scale-up to industrial size

Scaling laws based on geometric similarity and dimensionless numbers are commonly used to design large-scale reactors to maintain the same flow patterns, heat and mass transfer, and product selectivity of laboratory reactors [394,438]. Glicksman [439] developed a set of scaling laws for fluidized-bed reactors based on equal particle Reynolds number, Froude number, particle size distribution, bed geometry, and

particle sphericity. For fixed-bed reactors, the scale-up task is relatively more straightforward [440]. Nauman [441] proposed that fixed-bed reactors should be scaled-up according to either geometrical similarity, where the *L*/*D* ratio is kept constant, or constant pressure drop, which can be achieved by increasing the diameter while maintaining the same superficial velocity. It is not recommended to scale-up a fixed-bed with a constant Reynolds number, because it will lead to a short and wide reactor, and higher Reynolds numbers enhance the heat transfer characteristics at the wall [441]. Simulation and optimization have also been used in the scale-up of fixed-bed reactors in order to mitigate temperature fluctuations, which in turn can severely impact the fuel conversion and product selectivity [436,442].

The reverse-flow concept is demonstrated for a commercially realistic industrial-scale fixed-bed reactor. To establish a basis for a realistic reactor size, commercial steam reforming and water-gas shift reactors used for H_2 production [195,443] are used to determine the anticipated capacity of a single commercial CLC reactor. These industrial fixed-bed reactors typically range $6-15$ m in length and $0.01-4$ m in diameter. To maintain a reasonable pressure drop across the fixed-bed at $2-3$ atm, large catalyst particles with an equivalent diameter of 1 cm are commonly used [443]. In this study, a particle size of 300 μm is chosen, in order to minimize diffusion effects through the oxygen carrier, but at the same time it imposes a significant pressure drop in the system. For the pressure drop to be within reasonable bounds, the bed height should not exceed 1 m. The scaling factors that are kept constant in the design are the *L*/*D* ratio and Froude number. The reactor diameter is calculated, given the bed height limit and the equivalent *L*/*D* of the bench-scale reactor. The gas flow rate is then calculated to match the Froude number of the bench-scale reactor. Following this rationale and procedure, the reactor size and operating conditions for the industrial-scale reactor are calculated as shown in **Table 8.4**. It should be noted that the strategy of reactor design (both for bench- and industrial- scale systems) is aimed at showcasing the advantages of reversing the flow in CLC reduction. These systems can be further optimized by studying different oxygen carriers, particle sizes, and different geometries, but this optimization is outside the scope of this paper. In Chapter 9, the cycle configuration and reverse-flow strategy is optimized for maximal heat removal efficiency.

8.4. Results and discussion

Reverse-flow operation is investigated as a novel configuration for CLC fixed-bed systems, with the potential to improve the CO_2 capture efficiency and temperature profile uniformity. This is illustrated for the bench-scale reactor, for which the performance using an one-directional feed is compared to that with flow reversal. The principle of the reverse-flow operation is then demonstrated for an industrial-scale reactor to explore whether the calculated bench-scale benefits are realistic at larger scales.

8.4.1. Design study for the bench-scale reactor

In the one-directional fixed-bed process, a conversion front moves in the axial direction through the bed. The reduction of the oxygen carrier by the fuel generates partial and complete combustion products (CO, CO_2, H_2, and H_2O) that subsequently participate in reforming, water-gas shift, and carbon formation reactions. The initially generated syngas can be further oxidized to CO_2 and H_2O *via* reactions with the downstream oxygen carrier. As the oxygen supply in the bed becomes progressively depleted over time, catalytic reactions become significant, resulting in diminishing fuel conversion to CO_2 and greater carbon deposition. If the contact between fuel and converted oxygen carrier can be reduced, then the formation of syngas and solid carbon can be effectively lowered in the fixed-bed process. This can be accomplished by periodically switching the direction of the fuel. The conversion profile with the reverse-flow process differs from the one-directional flow, in which two conversion fronts uniformly move toward the center of the bed (**Figure 8.3**).

The impact of flow reversal on CO_2 selectivity and CH_4 conversion is shown in **Figure 8.4** for different switch intervals. In all cases, the reverse-flow reactor achieves higher CO_2 selectivity for oxygen carrier conversions below 0.8. The performance of the reverse-flow reactor reverts to that of the one-directional process at higher conversions due to significant carbon build-up at both ends of the bed. Operating at longer switch intervals, such as 40 s, limits the efficiency of the reverse-flow reactor, because the bed is appreciably converted (~35%) by the fuel, prior to the first flow reversal. Hence, a sharp rise in the CO_2 profile is exhibited when the gas direction is reversed and the fuel contacts the fresh oxygen carrier. More

frequently reversing the flow can provide a more uniform conversion profile inside the bed and an overall higher CO_2 selectivity. In regards to CH_4 conversion, both reactors exhibit a minor initial CH_4 slip due to the absence of Ni, which activates the CH_4 conversion reactions [58,119]. The reverse-flow reactor achieves higher or equally high fuel conversions. The steep drops and jumps shown in **Figure 8.4** are the result of instantly pushing the gaseous contents to the opposite direction of the reactor when the flow is reversed. They are the least realistic aspect of the simulations preformed, as these discontinuities are attributed to the model boundary conditions when the flow direction is periodically changed and do not account for momentary gas compressibility and dispersion.

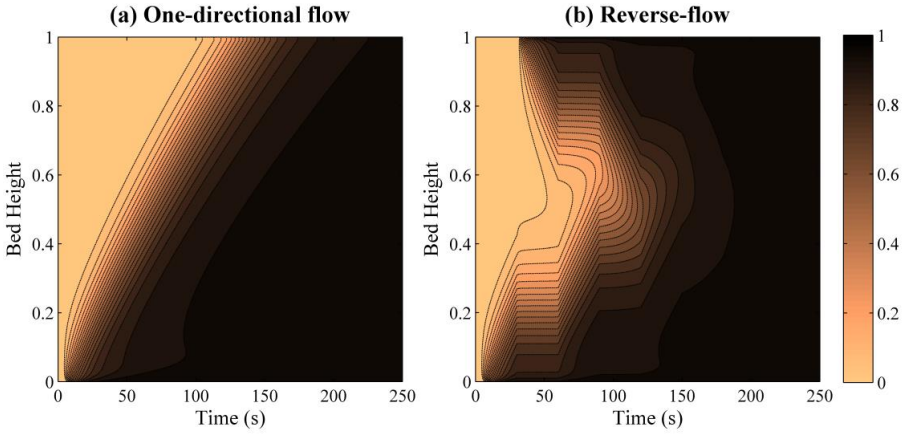

Figure 8.3: Oxygen carrier conversion as a function of reduction time and dimensionless bed height for the bench-scale reactor. Switch interval is 30 s for the reverse-flow operation.

From the analysis of **Figure 8.4**, the optimal flow reversal scheme for the bench-scale reactor corresponds to a switch interval of ~30 s, which can achieve CO_2 selectivity >90% with the lowest switching frequency. The utilization of the oxygen carrier is substantially increased in the reverse-flow process. For instance, the reduction cycle using an one-directional flow must be terminated when the bed is 22% converted to maintain 90% CO_2 selectivity in the exhaust stream. To operate at the same selectivity in the reverse-flow reactor, with a 30 s switch interval, reduction can be continued until the bed is 42%

converted. This is a significant improvement, addressing specifically one of the major bottlenecks of current CLC fixed bed reactors. It also offers advantages in terms of mitigating carbon formation in the reactor.

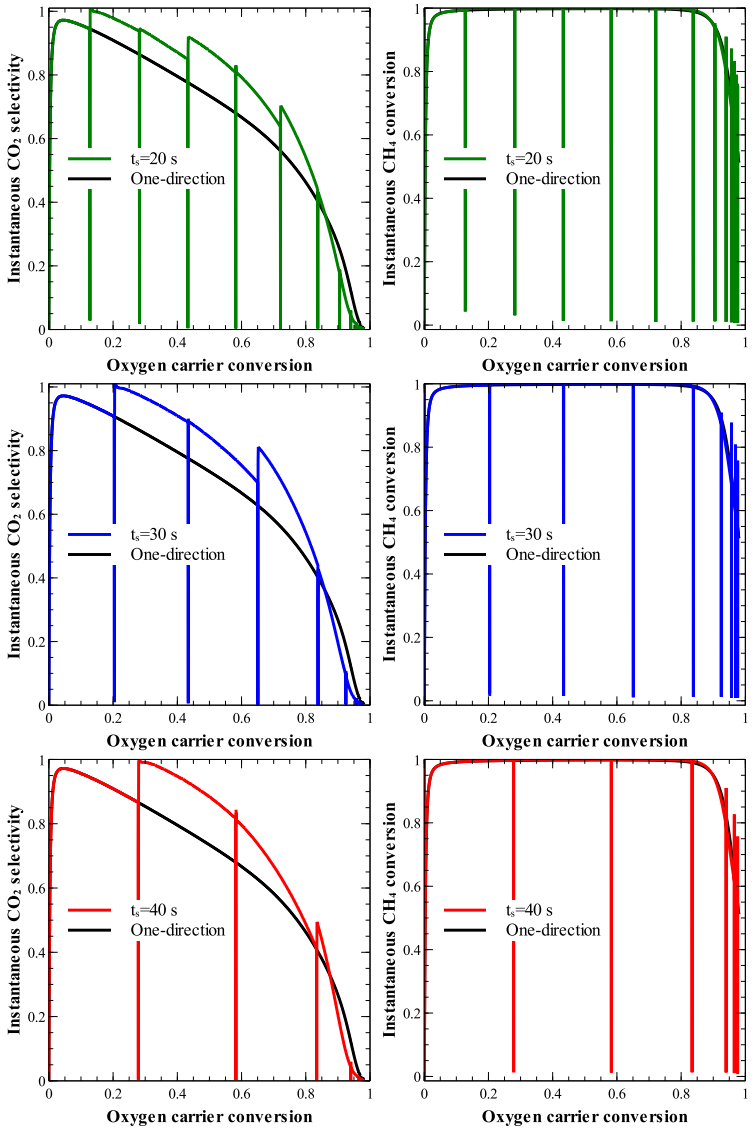

Figure 8.4: Comparison of the CO_2 selectivity and CH_4 conversion for the bench-scale reactor under one-directional flow and reverse-flow operation at different switch intervals.

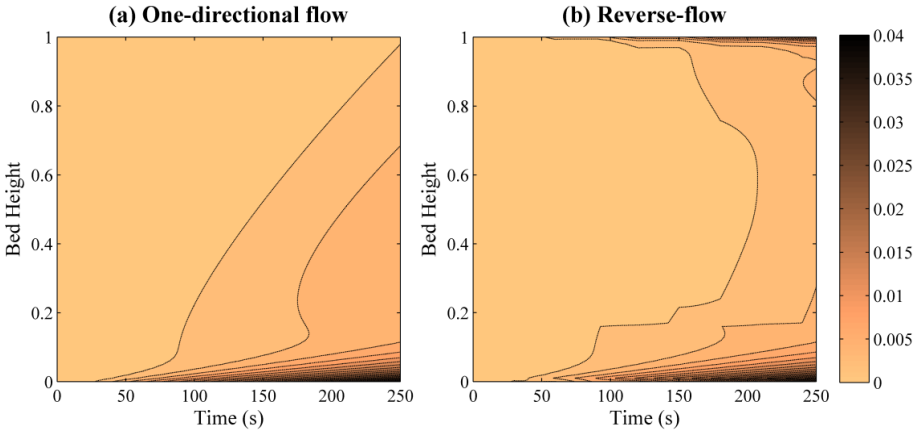

Figure 8.5: Amount of carbon deposited (kg C/kg OC) as a function of reduction time and normalized bed height for the bench-scale reactor. Switch interval is 30 s for the reverse-flow operation.

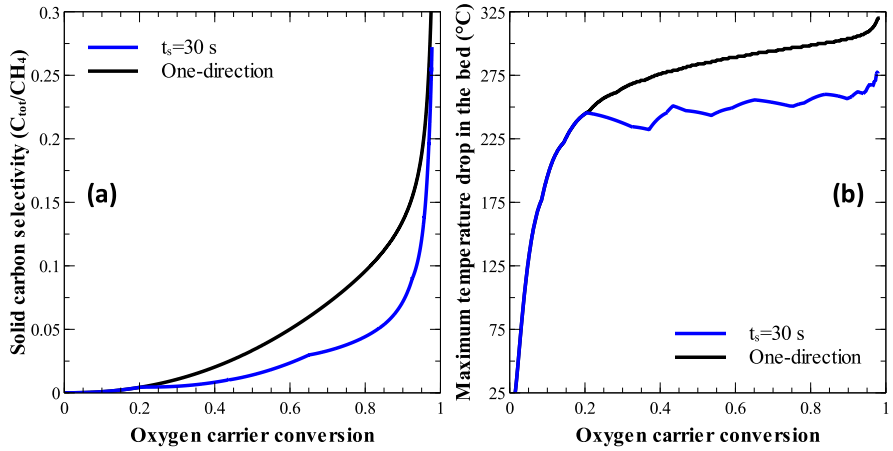

Figure 8.6: (a) Selectivity to solid carbon in the bed for the reverse-flow (t_s=30 s) and one-directional bench-scale reactor; (b) Maximum bed temperature drop for the reverse-flow (t_s=30 s) and one-directional bench-scale reactor.

In CLC with Ni-based oxygen carriers, CH_4 decomposition on the catalytic surface is inevitable and severely lowers the CO_2 capture efficiency of the process. Carbon formed during the reduction step is converted into CO_2 during oxidation and vented to the atmosphere, thus lowering the overall CO_2 capture efficiency. The extent of carbon formation is studied for the bench-scale reactor by evaluating the amount of C deposited in the bed and the efficiency of the total CO_2 capture (η_{CO_2}) of the process. Solid carbon deposits on the reduced surfaces that are devoid of oxygen sources. This phenomenon occurs at the inlet

of the one-directional reactor and at both ends of the reverse-flow reactor (**Figure 8.5**). Due to the improvement in fuel contacting patterns, the reverse-flow reactor achieves superior selectivity to solid carbon for all practical oxygen carrier conversions (**Figure 8.6(a)**). This effect is strongly correlated with the CO_2 capture efficiency of the process, calculated in terms of the CO_2 and CH_4 flow rates as follows:

$$\eta_{CO_2} = \frac{\int_0^t F_{CO_2}|_{z=L}}{\int_0^t F_{CH_4}|_{z=0}}. \tag{8.20}$$

The CO_2 capture efficiency η_{CO_2} is different from the CO_2 selectivity: the former is the time-integral of the moles of CO_2 captured per moles of CH_4 fed into the system, while the latter is the instantaneous ratio of CO_2:CH_4. These two metrics provide an integrated understanding of the overall reactor performance. **Table 8.5** presents the η_{CO_2} values calculated at different times to meet a range of oxygen carrier conversions. For all the listed conversions, the CO_2 capture efficiency is higher in the reverse-flow reactor. Comparison of these results to a circulating fluidized-bed unit, which can achieve 94% CO_2 gas yield with negligible carbon build-up and a solid conversion of 0.6 [185], shows that the concept of a reverse-flow reactor is a promising alternative to the commonly employed fluidized-bed processes. Moreover, the CO_2 capture efficiency shown in **Table 8.5** is likely sub-optimal. The observed benefits of the reverse-flow process can be further improved by optimization of the reactor dimensions. This optimization would ask the contour lines of **Figures 8.3**, **8.5**, and **8.7** to be vertical (flat) as early as possible, which would signify composition and temperature uniformity. Nonetheless, this is outside the scope of this work, since it would yield a biased comparison with conventional fixed-bed CLC systems.

As demonstrated, flow reversal allows for better utilization of the available oxygen sources in the bed. This effect is also exhibited in the temperature profiles. As most of the CLC reduction reactions are endothermic, the formation of cold spots inside the reactor always coincides with the conversion front (**Figure 8.7**). The largest temperature drop for the one-directional reactor appears at the inlet and for the reverse-flow reactor at both ends. Better heat utilization is achieved by reversing the fuel direction, whereby a larger volume of the bed can be used to provide conductive heat for the reduction reactions.

This results in milder cold spots and faster conversion rates under the reverse-flow process. Approximately, a 50°C improvement in the maximum temperature drop is achieved with the reverse-flow concept at the bench-scale (**Figure 8.6(b)**).The non-uniformities in the maximum temperature drop shown in **Figure 8.6(b)** are due to the periodic flow reversal, which causes the position of the cold spot to vary from inlet to exit. Nonetheless, reverse-flow operation improves the thermal management of the process, which is more important in large-scale systems, where the divergence of temperature can cause substantial losses in product selectivity, material activity and lifespan [440].

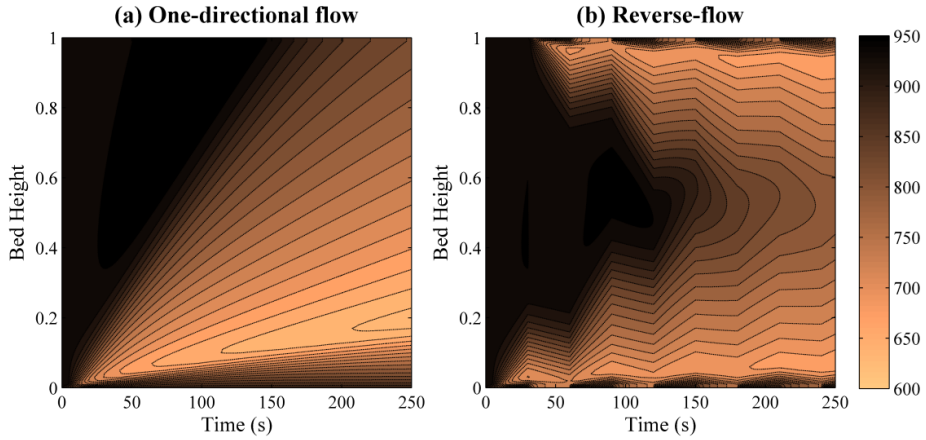

Figure 8.7: Bed temperature (°C) as a function of reduction time and normalized bed height for the bench-scale reactor. Switch interval is 30 s for the reverse-flow operation.

Table 8.5: CO_2 capture efficiency η_{CO_2} for varying oxygen carrier conversion in the bench-scale fixed-bed reactor under one-directional flow and reverse-flow operation with a switch interval of 30 s.

Solid conversion	***One-directional***	***Reverse-flow***
0.3	0.9238	0.9561
0.4	0.9873	0.9515
0.5	0.8688	0.9348
0.6	0.8383	0.9107
0.7	0.8043	0.8854
0.8	0.7630	0.8507

8.4.2. Application to an industrial-scale reactor

The reverse-flow concept is demonstrated for a scaled-up, industrial equivalent fixed-bed reactor. The effect of reactor scale-up on the oxygen carrier conversion was studied for the one-directional system, showing shorter reaction times for the industrial-scale reactor. The reaction rates are enhanced by the higher partial pressures at the inlet, due to the larger pressure drop across the bed. Nonetheless, the product selectivity and bed temperature profile are not affected by the reactor scale-up because of the similar mixing patterns to the bench-scale reactor. While the total carbon deposition in the bed is much greater compared to the bench-scale reactor (because of the higher flow rate of fuel), the rate of carbon deposition is proportional to the bench-scale reactor by the change in reactor volume and the selectivity to solid carbon is about the same.

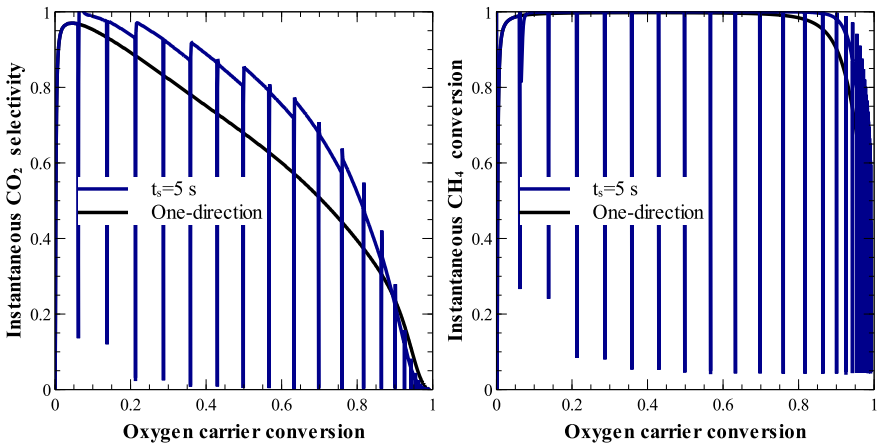

Figure 8.8: CO_2 selectivity and CH_4 conversion for the industrial-scale reactor under one-directional flow and optimal reverse-flow operation (t_s=5 s).

The effect of switching frequency on CO_2 selectivity and CH_4 conversion was analyzed in a similar method described for the bench-scale reactor. Shorter switch intervals are needed for the industrial-reactor in order to meet the high CO_2 selectivities of the bench-scale reactor, because of the faster reaction rates. The optimal switch interval, providing CO_2 selectivity >90% over a range of oxygen carrier conversions,

was estimated at ~5 s. **Figure 8.8** presents the results of the optimal industrial-scale reverse-flow operation in comparison to the one-direction flow system. The reverse-flow reactor achieves higher CO_2 selectivity for any oxygen carrier conversion below 0.85, with the improvement being more significant in the range of conversions from 0.4 to 0.8. The high CO_2 selectivity can be sustained for higher oxygen carrier conversions in the reverse-flow reactor. Assuming a 90% CO_2 selectivity as the benchmark, the one-directional flow reactor can operate until only 25% of the bed is reduced, whereas at optimal reverse-flow operation, the bed can be progressively reduced up to 45% conversion. There is some improvement in the CH_4 conversion due to flow-reversal at oxygen carrier conversions above 0.8, but the reduction period would normally be terminated prior to that. The oxygen carrier conversion in the bed (**Figure 8.9**) follows similar patterns as the bench-scale case, with the only difference being that complete conversion occurs sooner. Again, a large-scale reverse-flow reactor can be designed optimally for CLC, focusing on maximizing CO_2 selectivity and bed utilization, which will be the subject of our future work.

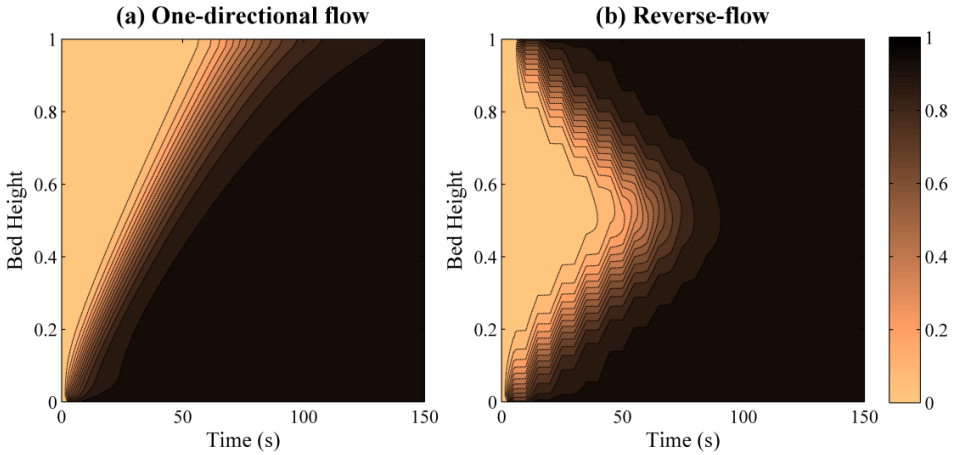

Figure 8.9: Oxygen carrier conversion as a function of reduction time and normalized bed height for the industrial-scale reactor. Switch interval is 5 s for the reverse-flow operation.

The CO_2 capture efficiency of the industrial-scale reactor is heavily dependent on the amount of carbon deposited during reduction. As shown in **Figure 8.10**, the location of the greatest carbon deposition in the

fixed-bed is at the first point of contact between fuel and oxygen carrier. The reverse-flow reactor has less accumulated solid carbon, because of the better utilization of the oxygen carrier, as discussed previously. In total, the selectivity to solid carbon is lower in the reverse-flow reactor (**Figure 8.11(a)**). Another advantage of reversing the flow is the prevention of excess carbon build-up at the one end, which can eventually clog the reactor.

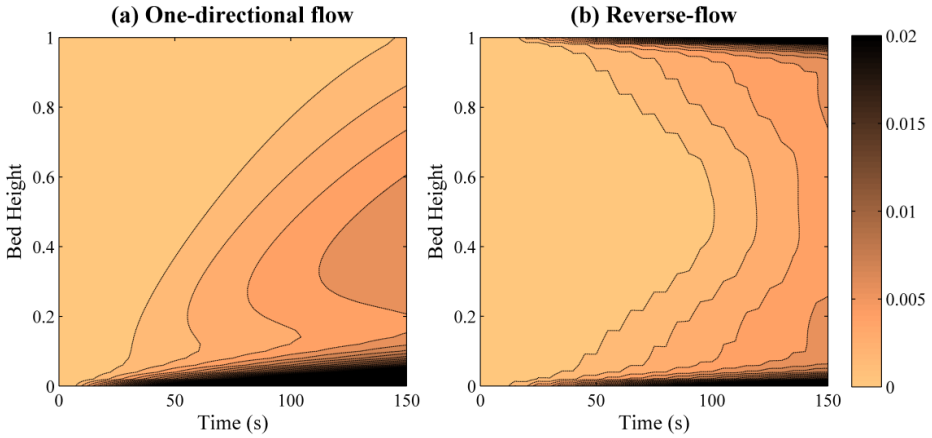

Figure 8.10: Amount of carbon deposited (kg C/kg OC) as a function of reduction time and normalized bed height for the industrial-scale reactor. Switching time is 5 s for the reverse-flow operation.

Table 8.6: CO_2 capture efficiency η_{CO_2} for varying oxygen carrier conversion for the industrial-scale fixed-bed reactor under one-directional flow and reverse-flow operation with a switching time of 5 s.

Solid conversion	***One-directional***	***Reverse-flow***
0.3	0.9128	0.9446
0.4	0.8787	0.9309
0.5	0.8432	0.9128
0.6	0.8042	0.8893
0.7	0.7614	0.8616
0.8	0.7099	0.8179

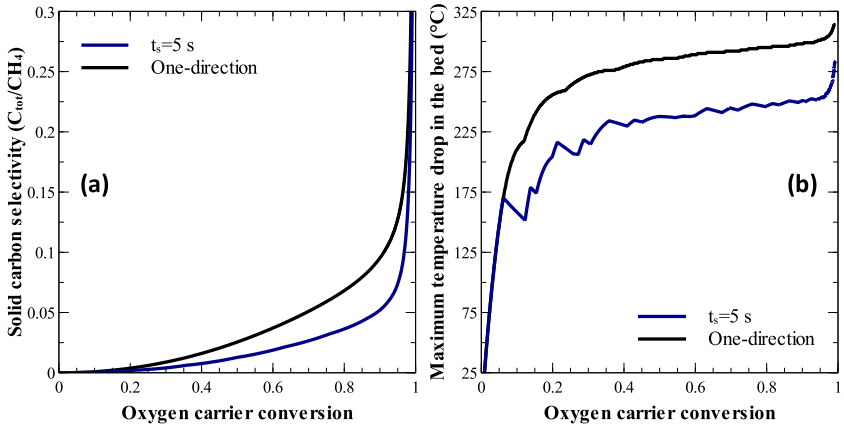

Figure 8.11: (a) Selectivity to solid carbon in the bed for the reverse-flow (t_s=5 s) and one-directional industrial-scale reactor; (b) Maximum bed temperature drop for the reverse-flow (t_s=5 s) and one-directional industrial-scale reactor.

The improvement in CO_2 capture efficiency (**Table 8.6**) yields equally promising results compared to the bench-scale reactor. For all oxygen carrier conversions, η_{CO_2} is higher in the reverse-flow reactor and the difference becomes noticeably larger at higher oxygen carrier conversions. Practically, the oxygen carrier utilization can be improved by 60% with the reverse-flow process operating at over 90% CO_2 capture efficiency. The temperature profile inside the industrial-scale reactor (**Figure 8.12**) is similar to that of the bench-scale reactor, due to the appropriateness of scale-up. A more uniform temperature profile can be achieved by reversing the fuel direction. The maximum temperature drop along the bed is reduced by 50°C with the reverse-flow process (**Figure 8.11(b)**). By lowering the intensity of cold spots during reduction, the reverse-flow operation improves the thermal management of the CLC reactor which has positive effects on the overall heat integration of the entire process.

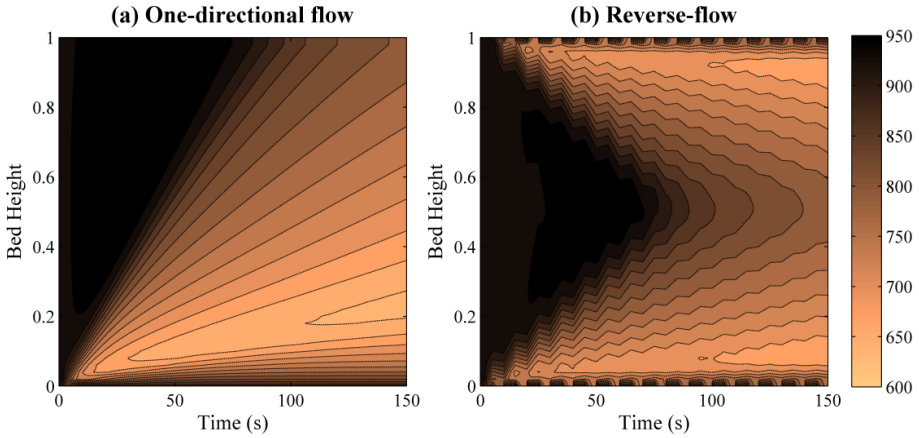

Figure 8.12: Bed temperature (°C) as a function of reduction time and normalized bed height for the industrial-scale reactor. Switch interval is 5 s for the reverse-flow operation.

8.5. Conclusions

The performance of CLC in reverse-flow fixed-bed reactors was evaluated for a bench-scale reactor and its industrial scale-up equivalent, using a previously validated heterogeneous CLC model. For the theoretical analysis, the bench-scale reactor was designed according to CLC/CLR fixed-bed units reported in the literature, operating in one-directional flow, and was compared to its reverse-flow equivalent operating at identical conditions. The results of this analysis demonstrate that periodic reversal of the gas flow during CLC reduction leads to significant improvements in reactor performance, in terms of CO_2 selectivity, CO_2 capture efficiency, and bed temperature fluctuations. By scaling-up the bench-scale reactor, it was shown that the advantages of the reverse-flow operation can be exploited at the industrial-scale. This fixed-bed design avoids the issue of attrition and gas-solid separation commonly found in circulating fluidized-bed units. Furthermore, the simplicity of the process makes it easily applicable to existing bench-scale units without considerably complicated equipment, for which scale-up does not entail significant challenges. For an optimized design, the switch interval should vary over the course of reduction to maximize the performance gains at the minimum amount of switches, which will be studied in the future. In addition, the topic of heat management in the fixed-bed will be investigated by coupling

reverse-flow of the reduction and oxidation cycles. Flow reversal done at the oxidation conditions can potentially be used to alter and manipulate the location of hot spots inside the fixed-bed. Thus, coupling these phenomena together can reduce the energy expenditure for oxidation, while sufficiently regenerating the fixed-bed.

Chapter 9 Optimal Control of a Reverse-Flow Chemical-Looping Fixed Bed Reactor

A reverse-flow fixed bed reactor concept for chemical-looping combustion (CLC) is explored. The limitations of conventional fixed bed reactors, as applied to CLC, are overcome by reversing the gas flow direction periodically to enhance the mixing characteristics of the bed, thus improving oxygen carrier utilization and reactor efficiency. The reverse-flow reactor is simulated by a dusty-gas model and compared with an equivalent fixed bed reactor without flow reversal. Dynamic optimization is used to calculate conditions at which each reactor operates at maximum efficiency. Several cases studies illustrate the benefits of reverse-flow operation for the CLC with CuO and NiO oxygen carriers and methane and syngas fuels. A major advantage of the proposed reactor design is the better utilization of the oxygen carrier bed and improved uniformity of the exhaust gas temperature during heat removal. The results show that implementing CLC in a reverse-flow reactor has the potential to achieve higher power generation efficiency than conventional fixed bed CLC reactors.

9.1. Introduction

Chemical-looping combustion (CLC) is a promising technology for power generation with cost effective CO_2 capture. CLC is a two-step combustion process that produces a high purity stream of CO_2, ready for compression and sequestration. A solid oxygen carrier, in the form of metal oxide particles, transports the oxygen from air to combust a gaseous fuel. Since the fuel is never mixed with air, the combustion products (H_2O/CO_2) are not diluted in N_2 and CO_2 can be captured after condensing the water vapor. CLC is a pre-commercialization technology, but simulation studies on its integration with power plants indicate that it has the potential to be more efficient than all other CO_2 capture technologies [26,47,444–448]. The overall efficiency of the corresponding power plant would be higher if CLC was to be integrated with combined cycle (CC) power plants that take advantage of the high efficiencies of the Brayton cycle. Therefore, several process configurations have been proposed that integrate CLC reactors with CC power

plants utilizing natural gas and synthesis gas fuels. The thermal efficiency of natural gas-fired CC with CLC is 52-53% [143–145], which is about 3-5% higher than that of post-, oxy-fuel, or pre-combustion CO_2 capture methods [449]. For coal feedstocks, the efficiency of CLC combined with an integrated gasification combined cycle (IGCC) was estimated to be close to that of conventional IGCC without CO_2 capture [450] and about 2% higher than IGCC with pre-combustion CO_2 capture [111,149].

CLC reactors must operate at high pressures (>20 bar) and high temperatures (>1200°C) [451,452] for their seamless integration with downstream gas turbines. A major challenge in the development of CLC reactors, in the case of the more conventional fluidized bed configurations, is the establishment and maintenance of stable fluidization at high-pressure and at large-scale. Therefore, the design of the main candidate reactor configuration for commercial CLC realization, consisting of two interconnected fluidized beds between which the oxygen carrier is circulating [23,30,46,74,157,196,349,381,382], suffers from immaturity of its fluidization technology. The main advantages of fluidized bed implementations of CLC are the high gas/solid heat and mass transfer rates, stable operating temperature, and continuous operation. Most of the operational experience of fluidized bed CLC units was gained at atmospheric pressure and research is on-going to design and operate reactors that can accomplish stable circulation and fluidization of the oxygen carrier at the scale conceptualized for power generation [351,353,453].

An alternative to interconnected fluidized bed CLC configurations is the much simpler fixed bed design [108,154,354,364]. In a fixed bed reactor configuration for CLC, the oxygen carrier is statically contained and alternatively exposed to oxidizing and reducing gases. Since solid circulation (and thus gas-solid separation) is not required, high-pressure operation can be achieved without much difficulty. The fixed bed reactor is more compact than the fluidized bed, which offers potential for better utilization of the oxygen carrier, lower capital cost, and smaller process footprint. The main disadvantages of the fixed bed reactor are its dynamic operation and the necessity of high temperature valves. The main challenge of interest to this work is the batch operating principle of a fixed bed CLC reactor configuration, in conjunction with the requirement for stable, smooth steady state operation of power plants. This is a

traditional chemical engineering challenge, but relatively new to the power generation sector.

In previous work, we used dynamic models to study and compare the performance of fixed bed and fluidized bed reactors for gaseous CLC [119,128,132,141,142,193,324,333,368,369]. We showed that the fixed bed reactor can operate at near 100% CH_4 conversion, but the reduction cycle needs to be controlled to ensure high CO_2 capture efficiency [324]. In other relevant work, Hamers et al. [108] and Spallina et al. [358] showed that a proper heat management strategy is essential to the integration of fixed bed CLC into a power plant. Spallina et al. [111] estimated the overall process efficiency of a CLC-based IGCC plant using fixed bed reactors to be 40-41%, which was similar to an IGCC-CLC plant with fluidized bed reactors [356]. Heat management in the form of CLC operating strategy was formulated as an optimization problem by Han and Bollas [374], with the objective of maximizing energy efficiency as a function of the CLC cycling procedure. Here, we expand upon previous work by allowing the operating strategy of CLC to change the direction of the gas flow during each cycle.

9.2. Basic operating principle of fixed bed CLC

The fixed bed CLC reactor is a batch process, operated in successive cycles of reduction, oxidation, and heat removal. During reduction, a gaseous fuel (such as natural gas or syngas) is fed to a fully oxidized bed, where the oxygen carrier is reduced and the fuel is converted mainly to CO_2 and H_2O. The reduction of the oxygen carrier is usually a combination of endothermic and exothermic reactions, depending on the fuel and metal oxide. The reduction phase is stopped when either the fuel conversion or CO_2 selectivity reaches a lower bound, determined by efficiency and environmental requirements, and the reactor is purged with inert gas for a short period. Next, air is fed to the reactor to commence the oxidation cycle and regenerate the oxygen carrier. The reactor is heated up to high temperatures due to the exothermic reactions and the heat from the solids is transferred to the gas phase by continually blowing air through the reactor. This is commonly referred to as the heat removal phase. Once most of the heat is pushed out of the reactor, the reactor is purged briefly and the cycle returns to reduction.

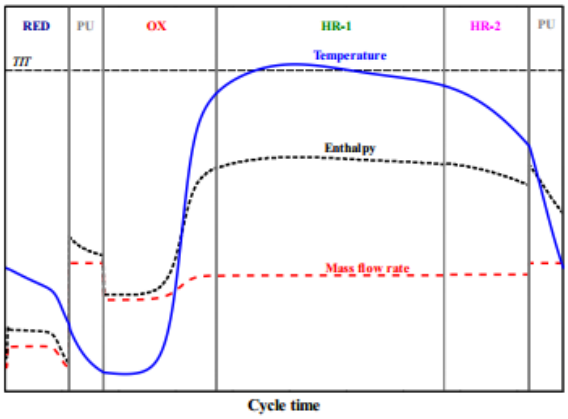

Figure 9.1: Schematic of a typical cyclic operation of CLC in a fixed bed reactor in terms of the temperature, total enthalpy, and mass flow rate of the exhaust gas stream.

Figure 9.1 presents common profiles of the exhaust gas temperature, mass flow rate, and enthalpy during cyclic operation of a fixed bed CLC reactor. Details on how these profiles are calculated can be found in the following Section; here, we focus on the main principles of operation of a fixed bed CLC reactor. As shown, the maximum gas temperature and enthalpy occur during the primary heat removal phase (HR-1). In an integrated CLC-CC plant, downstream the CLC reactor is a gas turbine, which expands the hot, pressurized CLC exhaust to produce electricity. Temperature fluctuations at the inlet of the gas turbine should be minimized to preserve the integrity of the turbomachinery. Thus, at the onset of the temperature decrease in **Figure 9.1**, the exhaust gas is diverted to the steam cycle and a secondary heat removal stage (HR-2) is initiated. The steam cycle is less efficient than the gas turbine cycle of the CC. Therefore, the dynamic operation of the fixed bed reactor creates a source of efficiency penalty for the CLC system. This penalty can be more easily understood if we think of the non-constancy of the temperature of the exhaust gas during heat removal and understand that the lower temperature portion (time-wise) of the stream is of lower quality for power generation. Here, it is also critical to remember that because of the one-reactor configuration of the fixed bed CLC, the temperature of the bed after oxidation needs to be lowered before initiating reduction. In contrast, if CLC is implemented in two pressurized fluidized bed reactors, all of the air exhaust can be used to generate electricity in a gas turbine. To overcome this problem associated

with the fixed bed system, we need to optimize the reactor configuration and process operation and ensure high thermal and CO_2 capture efficiencies.

9.3. Novelty and scope of this work

To summarize the scope of this work, we are interested in fixed bed reactors, because of their capability to operate at high pressures, with gaseous fuels and we wish to explore the optimality of reactor design and operation strategy for the maximization of process efficiency and CO_2 capture. The basic process elements that control these efficiencies are the uniformity of the bed in terms of temperature and oxygen carrier conversion profiles. In an effort to impose uniformity to the fundamentally axially distributed fixed bed reactor, we explore the use of reverse-flow operation. **Figure 9.2** shows a simplified process scheme of a reverse-flow CLC reactor. At normal flow conditions, the flow passes through 1-2-R-3-4 and when the direction is switched, the gas flows through 1-2'-R-3'-4. In this investigation, we examine if reverse-flow operation can enhance the contact between fuel and oxygen carrier during reduction. There might exist benefits, in terms of a more uniform bed conversion and temperature distribution, which could lead to better oxidation cycle efficiency and heat removal performance.

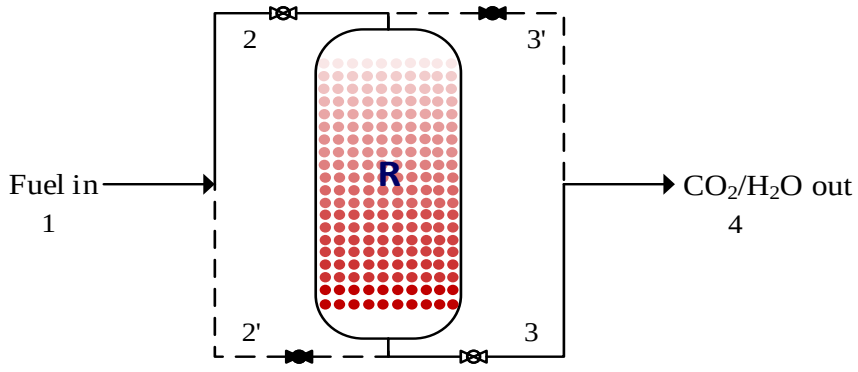

Figure 9.2: Simplified diagram of revere-flow operation in a fixed bed CLC reactor. Forward flow pass is 1-2-R-3-4 and backward flow pass is 1-2'-R-3'-4.

To calculate an operating strategy for the reverse-flow reactor, we propose an optimization problem to maximize the energy efficiency of the heat removal step, in which the reactor exhaust can be used for electricity generation in a downstream gas turbine. This energy efficiency is expressed as the fraction of the enthalpy sent to the gas turbine over the energy output of the reactor, as shown in Eq.(9.1):

$$\eta_{HR} = \frac{\int_{t_0}^{\tau_{HR-1}} \left(\dot{m}_{out}(t) \cdot h_{out}(t)\right) dt}{\int_{t_0}^{\tau_{cycle}} \left(\dot{m}_{out}(t) \cdot h_{out}(t)\right) dt}, \tag{9.1}$$

where $\dot{m}_{out}$ and h_{out} are the time-dependent mass flow rate and enthalpy of the exhaust gas stream, τ_{HR-1} is the time interval for the heat removal step to produce electricity in the gas turbine, and τ_{cycle} is the time interval for one complete redox cycle. To maximize η_{HR}, we can optimize the number of flow switches n_{sw} and the time interval for each flow switch $\tau_{n_{sw}}$ during reduction, the time interval of each oxidation and heat removal stages τ_i, the flow rate and temperature of the inlet air $\mathbf{u}_i$, and metal oxide content in the oxygen carrier ω. The dynamic switching between different gases is modeled with piece-wise constant functions. These variables are contained in the design vector of the process, shown in **Table 9.1**.

Table 9.1: Design variables for the problem formulation to optimize the heat removal efficiency of a reverse-flow CLC reactor.

Design variables	$\boldsymbol{\phi}$
Number of flow switches during reduction	n_{sw}
Time interval for each flow switch during reduction	$\tau_{n_{sw}}$
Oxidation time interval Heat removal-1 time interval Heat removal-2 time interval	τ_i
Air feed rate Air temperature	$\mathbf{u}_i$
Metal oxide content in oxygen carrier	ω

The CLC reactor must satisfy the input boundary conditions of the power plant, achieve high fuel conversion efficiency, and operate within constraints related to power plant safety and oxygen carrier stability. The temperature of the gas feeding the gas turbine should be at or close to the turbine inlet temperature (*TIT*) set-point with minimal fluctuations. Inequality path constraints are incorporated to keep the temperature of the reactor exhaust during heat removal, $T_{HR,out}(t)$, within $\pm$50°C of the *TIT* set-point. Additionally, the temperature inside the bed, $T(t,z)$, is constrained to always be less than 50°C below the melting point of the metal oxide, T^{max}. Of course, the CLC reactor must comply with acceptable levels of emissions control. Specifically, the CLC reactor needs to achieve ≥90% CO_2 capture efficiency [96] and ≥98% fuel conversion [149] during the reduction phase. The CO_2 capture efficiency, $S_{CO_2}(t)$, and fuel conversion, $X_{fuel}(t)$, are computed from the time-integral of the molar flow rates of the gas stream. The pressure drop across the reactor must be within $\left(\frac{\Delta P}{P_{in}(t)}\right) \leq 8\%$ [111] at any time, to avoid excess pressure losses and maximize plant efficiency. All these requirements are captured as constraints in the optimization problem of Eq.(9.2), which presents the complete formulation to optimize the operating strategy for a reverse-flow fixed bed CLC reactor.

$$
\begin{aligned}
&\max_{\varphi\in\Phi}\ \eta_{HR} \\
&s.t. \quad \mathbf{f}\left(\dot{\mathbf{x}}(t),\mathbf{x}(t),\mathbf{u}(t),\boldsymbol{\theta},t\right)=0, \\
&\quad \mathbf{x}^{\min} \le \mathbf{x}(t) \le \mathbf{x}^{\max}, \\
&\quad \mathbf{u}_i^{\min} \le \mathbf{u}_i \le \mathbf{u}_i^{\max}, && i=1,\ldots,N_u \\
&\quad \tau_i^{\min} \le \tau_i \le \tau_i^{\max}, && i=1,\ldots,N_u \\
&\quad \omega^{\min} \le \omega \le \omega^{\max}, \\
&\quad \tau_{n_{sw}}^{\min} \le \tau_{n_{sw}} \le \tau_{n_{sw}}^{\max}, \\
&\quad n_{sw}^{\min} \le n_{sw} \le n_{sw}^{\max} \\
&\quad TIT - 50°C \le T_{HR,out}(t) \le TIT + 50°C, \forall t \in [t_0, t_f], \\
&\quad T(t_i,z) + 50°C \le T^{\max}, && \forall t \in [t_0, t\theta_f], \forall z \in [0,L], \\
&\quad S_{CO_2}(t) \ge 90\%, && \forall t \in [t_0, t_f], \\
&\quad X_{fuel}(t) \ge 98\%, && \forall t \in [t_0, t_f], \\
&\quad \Delta P(t) / P_{in}(t) \le 8\%, && \forall t \in [t_0, t_f].
\end{aligned}
\tag{9.2}
$$

In Eq.(9.2), the CLC reactor is modeled as a system of differential and algebraic equations, **f**, where $\mathbf{x}(t)$ is the vector of state variables (*i.e.*, mass, temperature, and pressure), and $\boldsymbol{\theta}$ is the system parameters, including the kinetic constants describing the reactivity of the oxygen carriers. **Section 8.2** describes in more detail the design equations, **f**, of the fixed bed CLC reactor. The mathematical model was developed

and solved using the commercial software package gPROMS [170]. We employed the control vector parameterization (CVP) with single-shooting algorithm to solve the above stated dynamic optimization problem.

9.4. Model Validation

The process model written in Eqs.(8.1)-(8.15) was successfully used to predict CLC experimental data collected from an in-house fixed bed reactor and data reported in the literature. **Figure 9.3** presents the model validation of the model described in Section 8.2.3 to match experimental data reported by Ishida et al. [47], Han et al. [368], and Nordness et al. [369]. Specifically, **Figure 9.3(a)** illustrates the accurate simulation of internal mass transfer effects through the oxygen carrier particle, for a range of particle sizes. **Figure 9.3(b)** demonstrates the accuracy of the reaction scheme and kinetics derived from experiments optimally designed for kinetic parameter estimation [333,368] in predicting CLC experiments using NiO and CH_4 fuel, in an atmospheric fixed bed reactor. A similar approach was taken by Zhou et al. [142] to estimate the reduction kinetics of CuO and CH_4. The kinetic models of Han et al. [333,368] and Zhou et al. [142] were then extended to high-pressure conditions, by fitting a pressure dependency term using the correlation proposed by García-Labiano et al. [89]. **Figures 9.3(c)-9.3(d)** show that the models developed previously are sufficient for predicting pressurized fixed bed experiments for the complete redox cycle (reduction, purge, and oxidation), performed by Nordness et al. [369]. In summary, the described process model provides a sufficient level of accuracy and can be used with confidence for reactor analysis and process efficiency studies.

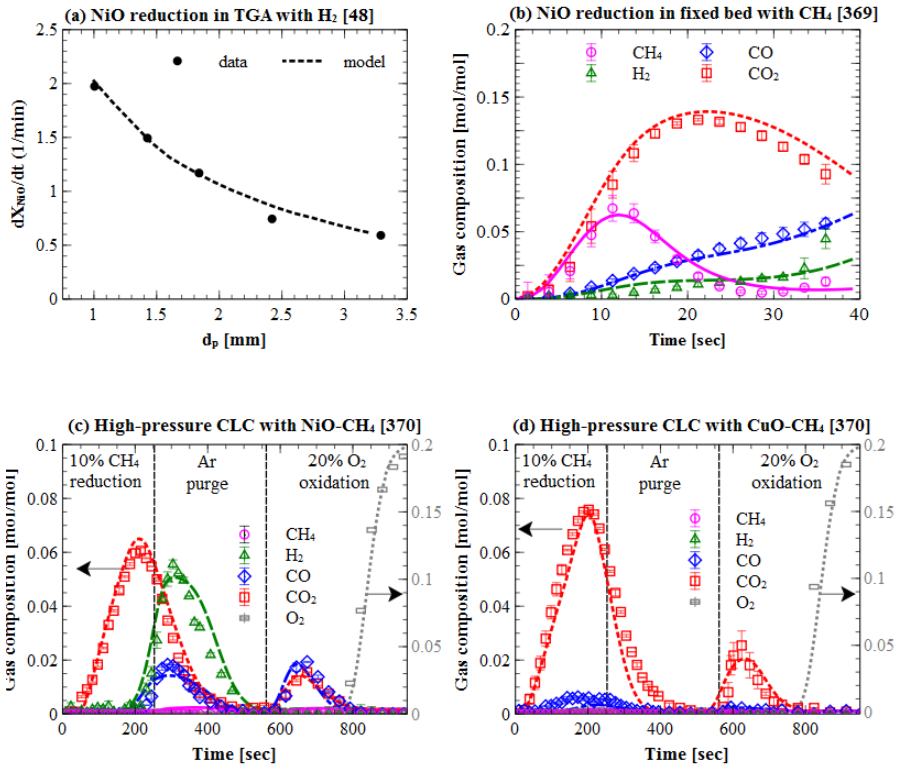

Figure 9.3: Model predictions of CLC experimental data performed in TGA (a) and in fixed bed (b,c,d) using the dusty-gas model. In **Figure 9.3(a)**, the particle model is predicative of the effect of intraparticle diffusion limitations over a range of particle sizes (d_p=1.0-3.2 mm), measured by Ishida et al. [47]. **Figure 9.3(b)** shows the validation of the model to predict fixed bed CLC in atmospheric pressure [368]. **Figure 9.3(c)-Figure 9.3(d)** show the validation of the model to describe high-pressure CLC with NiO and CuO oxygen carriers, as described in Nordness et al. [369].

9.5. Base case for comparative analysis of the reverse-flow reactor

In this Section, the reverse-flow reactor performance is compared against an equivalent one-directional flow fixed bed reactor. This comparison assumes a clean methane and syngas fuel source, from natural gas or coal gasification respectively. Synthetic oxygen carriers of supported CuO and NiO were used to improve reactivity and selectivity of the reactor and reduce its footprint. Oxygen carrier reduction and oxidation kinetics were adapted from Nordness et al. [369], who experimentally studied high-pressure

CLC of CH_4 and syngas with CuO and NiO and devised high-pressure kinetics. The reactor specifications and operating conditions shown in **Table 9.2** were used for the stimulation of the reverse-flow and one-directional reactors. A base-case scenario of reactor geometry, operating pressure, syngas and purge flow rate was taken from the work of Spallina et al. [110], who analyzed the feasibility of integrating an ilmenite-containing fixed bed reactor into an IGCC process. We extended the work of Spallina et al. [110] to a methane-fed process, with a flow rate 10% of the syngas flow rate, as suggested by Norman et al. [155].

Table 9.2: Reactor design and operation, adapted from the work of Spallina et al. [110].

Reactor configuration		
Length (m)		11
Diameter (m)		5.5
Pressure (bar)		17 bar
Gas streams		
Syngas-fuel		
Composition	(vol.%)	1 Ar; 33.6 CO; 34 CO_2; 13.8 H_2; 16.4 H_2O; 1.3 N_2
Temperature	(°C)	450
Mass flow	(kg/s)	152
Methane-fuel		
Composition	(vol.%)	100% CH_4
Temperature	(°C)	450
Mass flow	(kg/s)	15
Purge		
Composition	(vol.%)	1.016 Ar; 0.04 CO_2; 1.31 H_2O; 97.5 N_2
Temperature	(°C)	450
Mass flow	(kg/s)	577.5
Cycle time	(s)	300

For each oxygen carrier and fuel type, we considered two set-points for the *TIT:* being: 1100°C and 1000°C for NiO and 1000°C and 900°C for CuO. Preliminary analysis showed that the reverse-flow reactor performance was more sensitive to the timing of the flow reversal, rather than the total number of switches. Generally, fewer flow switches are preferred in order to relax the mechanical stress on the high-temperature switching valves. Thus, we assigned n_{sw}=2 (flow direction is changed twice during the reduction cycle) in **Table 9.1** and then solved Eq.(9.2) to find the optimal cycle conditions for the reverse-

flow reactor. We also optimized the cycle strategy for the one-directional fixed bed reactor, by solving Eq.(9.2) without flow reversal. **Tables 9.3-9.4** present the optimal design variables for the one-directional and reverse-flow processes.

Table 9.3: Optimized cycle strategy and operating conditions for the one-directional reactor.

	CuO oxygen carrier		**NiO oxygen carrier**	
	Syngas-fuel	*Methane-fuel*	*Syngas-fuel*	*Methane-fuel*
TIT set-point (°C)	1000, 900	1000, 900	1100, 1000	1100, 1000
Reduction (RED)				
Cycle time (sec)	1300, 1200	838, 950	913, 770	609, 550
Air temperature (°C)	443, 456	610, 610	514, 516	650, 610
Oxidation (OX)				
Mass flow (kg/s)	214, 160	160, 160	160, 164	165, 178
Cycle time (sec)	1346, 1463	1306, 1000	838, 802	963, 848
Heat removal 1 (HR-1)				
Mass flow (kg/s)	214, 185	185, 187	186.4, 214	214, 182
Cycle time (sec)	3273, 4883	4220, 4490	2500, 2200	1805, 2400
Heat removal 2 (HR-2)				
Mass flow (kg/s)	160, N/A	169, 169	169, 160	151, 174
Cycle time (sec)	670, N/A	1275, 1440	597, 200	194, 490
MeO (*wt.%*)	20.7, 17.6	21.8, 17.7	21.7, 19.6	22.4, 20.9

Table 9.4: Optimized cycle strategy and operating conditions for the reverse-flow reactor.

	CuO oxygen carrier		**NiO oxygen carrier**	
	Syngas-fuel	*Methane-fuel*	*Syngas-fuel*	*Methane-fuel*
TIT set-point (°C)	1000, 900	1000, 900	1100, 1000	1100, 1000
Reduction (RED)				
Semi-cycle 1(sec)	626, 481	418, 319	378, 406	327, 250
Semi-cycle 2(sec)	394, 186	193, 363	217, 180	100, 100
Semi-cycle 3 (sec)	437, 627	222, 288	220, 120	200, 233
Air temperature (°C)	440, 456	600, 600	500, 500	620, 615
Oxidation (OX)				
Mass flow (kg/s)	160, 214	156, 142	154, 157	169, 183
Cycle time (sec)	1340, 900	1275, 1108	904, 757	850, 710
Heat removal 1 (HR-1)				
Mass flow (kg/s)	214, 214	214, 214	214, 214	214, 214
Cycle time (sec)	4525, 4480	4000, 4400	2147, 2250	2075, 2200
Heat removal 2 (HR-2)				
Mass flow (kg/s)	142, N/A	151, 160	142, 142	142, 160
Cycle time (sec)	700, N/A	500, 500	300, 270	200, 400
MeO (*wt.%*)	21.8, 19.0	23.0, 20.1	22.2, 20.6	24.0, 22.3

9.6. Results and discussion

In Section 9.5, we proposed reverse-flow fixed bed reactors as a process intensification option for CLC. Here we evaluate the advantages of reversing the feed flow operation during the reduction step, which was shown as the most impactful on the overall CLC performance. The benefits of reversing the feed flow in the reduction step are illustrated for the entirety of the CLC sequence (oxidation, heat removal and reduction), at cyclic steady-state conditions. Cyclic steady-state refers to the condition of the entire CLC system, in which the temperature and concentration profiles are identical for repeated redox cycles. The cyclic results for all of the case studies are shown in the Supplementary Information of this work [454]. For brevity, we focus on the major findings from the comparative analysis by examining each case study at the lower *TIT* set-point.

9.6.1. Reduction phase

During reduction, a gaseous fuel is fed to a reactor of fully oxidized oxygen carrier. In normal flow conditions, a reaction front is formed and moves in the axial direction through the reactor oxidizing the fuel, while reducing the bed. **Figures 9.4Figure 9.4(a)-9.4(c)** show the performance of the one-directional fixed bed reduction of NiO by syngas fuel, in terms of spatial and temporal bed conversion, bed temperature, and solid carbon formation. As shown in **Figure 9.4(a)**, the reactor entrance was the first to be reduced, followed by the interior and exit regions of the bed, due to the progression of the reaction front. The reduction was stopped before complete conversion of the bed, to ensure acceptable levels of fuel conversion and CO_2 capture efficiency. The bed temperature increased slightly, due to the reduction reactions that, in the case of NiO reduction by syngas, are overall exothermic. A weak heat front was formed at the entrance of the reactor and moved through the bed (**Figure 9.4(b)**). The entrance of the reactor was eventually cooled to the temperature of the feed gas, once reduction of the oxygen carrier in the entrance zone of the reactor was complete. As shown in **Figure 9.4(c)**, solid carbon was formed on the reduced oxygen carrier and was kinetically favored at the interior regions of the bed, where the temperature was higher.

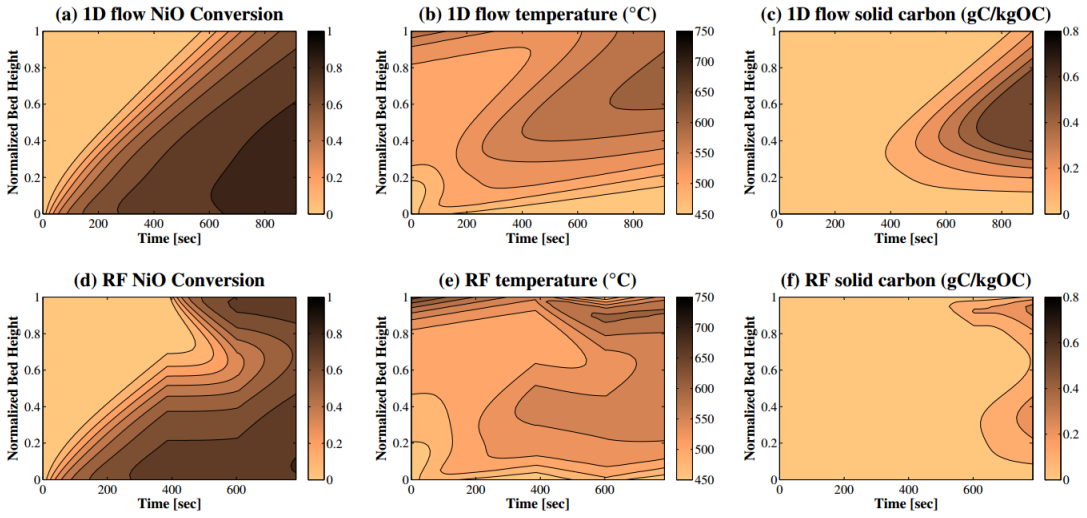

Figure 9.4: Profiles of the internal bed conversion, bed temperature, and solid carbon selectivity in the one-directional (1D) and reverse-flow (RF) reactors for the syngas-fed reduction with NiO. Conversion of 0 refers to NiO and conversion of 1 refers to Ni.

Figures 9.4(d)-9.4(f) show the reduction performance of the same system under reverse-flow operation. As shown in **Figure 9.4(d)**, the flow direction was reversed for the first time when the reaction front reached the middle of the reactor. After the first flow switch, the fuel entered the reactor at $z=L$ (reactor end) and reduced the unconverted oxygen carrier. A second reaction front was formed, moving toward the center of the bed (**Figure 9.4(d)**). Simultaneously, the temperature of the reactor exit was increased due to the exothermic reduction reactions (**Figure 9.4(e)**). After the second flow switch, the oxygen carrier was reduced from the forward flow pass. By periodically reversing the flow direction, we can enhance the contact between the fuel and the fresh oxygen carrier. This can be beneficial in suppressing catalytic reactions, which reduce CO_2 selectivity and increase carbon deposition. Comparing **Figure 9.4(c)** with **Figure 9.4(f)**, solid carbon started to deposit in the reactor about 100 s later in the reverse-flow reactor. At the end of reduction, less solid carbon was accumulated in the reverse-flow reactor (**Figure 9.4(f)**). In addition, reverse-flow operation provided a more uniform bed conversion (**Figure 9.4(d)**), due to the periodic switching between inlet and outlet ports. The temperature fluctuations were smaller in the

reverse-flow reactor (**Figure 9.4(e)**), as noted by the warmer reactor entrance and smaller hot spots as compared to **Figure 9.4(b)**. The same benefits were seen for the CLC with CuO, shown in Fig SI.1 of the Supplementary Information of this work [454].

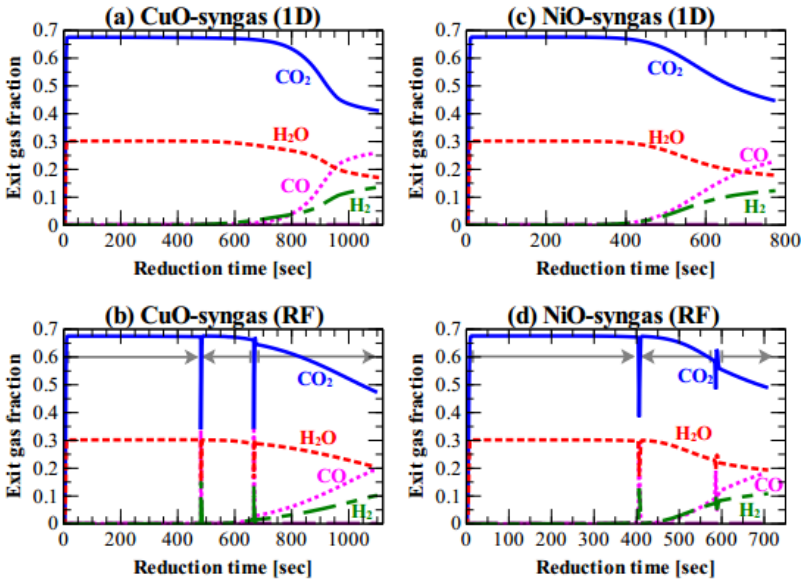

Figure 9.5: Exit gas fraction of the syngas-fed fixed bed reactors with CuO and NiO oxygen carriers under one-directional (1D) flow and reverse-flow (RF) with syngas fuel. The results are presented for the reduction phase at the *TIT* set-point of 900°C for CuO and 1000°C for NiO.

Figure 9.5 shows the dynamic exhaust gas profiles of the reduction with syngas fuel under one-directional flow and reverse-flow. When fuel was fed from one direction (**Figures 9.5(a)** and **9.5(c)**), the oxygen carrier was reduced by CO and H_2 following the axial fronts shown in **Figures 9.4(a)-9.4(c)**, producing CO_2 and H_2O. For most of the reduction period, complete conversion of the fuel was obtained. The optimizer stopped the reduction step before fuel slip became significant, as a consequence of the constraints on CO_2 capture efficiency and fuel conversion (Eq.(9.2)). The reduction time was shorter for the NiO process (**Figure 9.5(c)**) than for the CuO process (**Figure 9.5(a)**), mainly because the loading of

the NiO in the oxygen carrier was estimated by the optimizer to be lower than that of CuO (**Table 9.3**), for the same fuel and *TIT* set-point. This was due to the higher heat of oxidation of Ni, which bounded the NiO loading to lower levels, to satisfy the temperature constraints of Eq.(9.2).

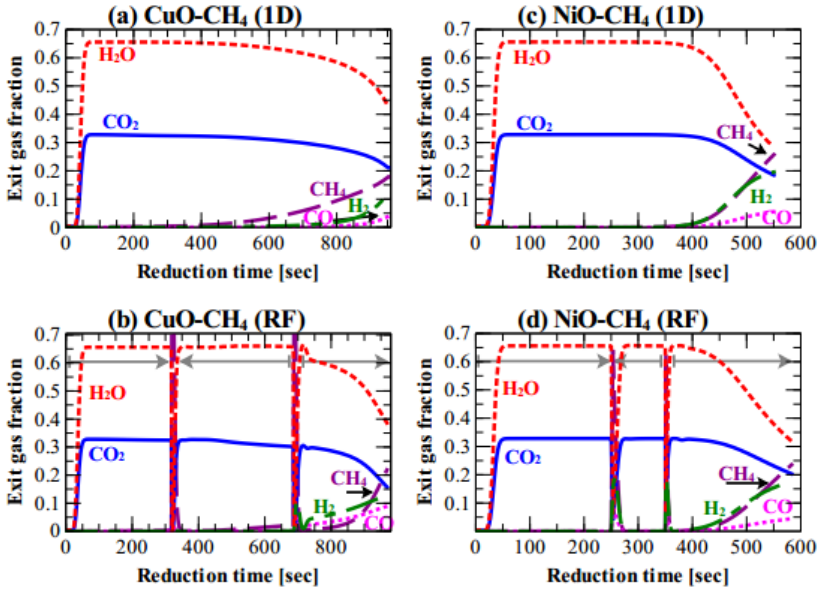

Figure 9.6: Exit gas fraction of the methane-fed fixed bed reactors with CuO and NiO oxygen carriers under one-directional (1D) flow and reverse-flow (RF) with CH_4 fuel. The results are presented for the reduction phase at the *TIT* set-point of 900°C for CuO and 1000°C for NiO.

Figures 9.5(b) and **9.5(d)** show the reduction of the equivalent processes during reverse-flow operation. The flow direction (forward and backward) is indicated by the gray horizontal lines. There was an instantaneous release of unconverted fuel when the flow was reversed, as indicated by the vertical jumps in **Figures 9.5(b)** and **9.5(d)**. However, this impact was minor compared to the total amount of gaseous CO_2 produced during the reduction step. The reverse-flow reactor achieved the same emissions control as the one-directional process, since the same constraints were used in the optimization problem. As shown in **Figure 9.5(b)**, **Figure 9.5(d)** and **Table 9.4,** the optimal flow switching strategy for the process was to

operate in forward flow for a longer period than in backward flow. This can be explained by the temperature distribution inside the bed during reduction. The entering syngas was reacting with a relatively hotter bed during backward flow in comparison with forward flow, as shown in **Figure 9.4**. The higher bed temperatures promoted a faster rate of solid conversion, as well as favored the formation of solid carbon. Thus, the optimizer reduced the time interval for backward flow in relation to forward flow, leveraging gas/solid kinetics to satisfy the constraint on CO_2 capture efficiency.

Figure 9.6 shows the results of the reduction of CuO and NiO by CH_4 in one-directional and reverse-flow. As shown in **Figures 9.6(a)** and **9.6(c)**, the CH_4 fuel was oxidized into CO_2 and H_2O and the reduction of CuO or NiO was stopped before the release of unconverted gases (CH_4, H_2 and CO) became significant (satisfying the CH_4 conversion and CO_2 capture constraints). The reverse-flow processes shown in **Figures 9.5(b)** and **9.5(d)** achieved the same gaseous fuel conversion and CO_2 capture efficiency as their equivalent one-directional flow reactors. A negligible amount of unconverted CH_4 fuel escaped the reactor when the flow was reversed. The optimal reverse-flow strategy for the reduction with CH_4 fuel was similar to that with syngas fuel, in which the total duration for the forward flow pass was longer than for the backward flow pass, as shown in **Tables 9.3-9.4** and **Figures 9.5-9.6**.

9.6.2. Oxidation/Heat removal phase

The oxidation stage of the reduced Ni oxygen carrier, shown in **Figure 9.7,** exhibited significantly axially distributed bed conversion, solid carbon and temperature. As shown, application of reverse-flow operation during the previous reduction step generated a more uniform distribution of Ni in the reactor with less solid carbon. As air was fed to the reactor, reaction and temperature fronts were formed and travelled axially through the bed, converting Ni to NiO (**Figures 9.7(a)-9.7(d)**), increasing the bed temperature (**Figures 9.7(b)-9.7(e)**), and oxidizing the solid carbon to gaseous carbon (**Figure 9.7(c)** and **Figure 9.7(f)**). At the end of oxidation, both reactors were fully oxidized with no residual solid carbon. Much of the heat produced from the oxidation reactions was still retained in the bed (**Figure 9.7(b)** and **Figure 9.7(e)**). As a result, air needed to be continually fed to the reactor in order to transfer the heat

stored in the solids to the gas phase. The heat produced from the oxidation of the reactor exit was first to be pushed out of the bed, followed by the heat from the interior and inlet regions of the bed.

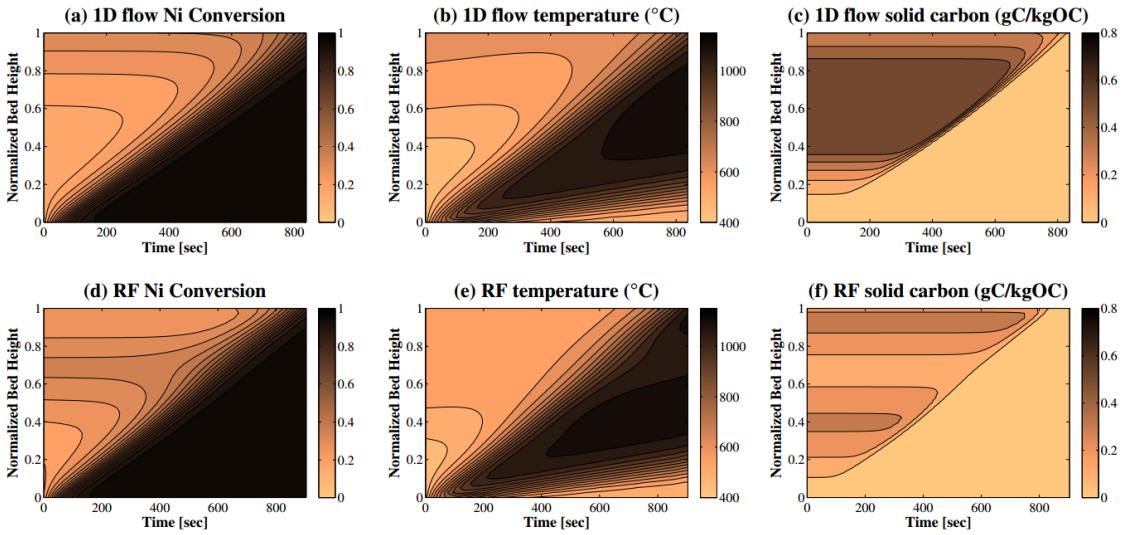

Figure 9.7: Profiles of the internal bed conversion, bed temperature, and solid carbon selectivity in the one-directional (1D) and reverse-flow (RF) reactors during oxidation with NiO oxygen carrier. The reactor was previously reduced by syngas and results are shown in **Figure 9.4**. Conversion of 0 refers to Ni and conversion of 1 refers to NiO.

The temperature profiles of the exhaust gas are shown in **Figures 9.8-9.9** for the entire sequence of each CLC cycle. The results presented in **Figure 9.8(a)** are for the one-directional reactor with CuO and CH_4. As shown in **Figure 9.8(a)**, at the start of oxidation, the gas leaving the reactor was at similar temperatures to the reduction exhaust, because the heat front was developing inside the reactor and the residual heat from the previous reduction cycle was still being pushed out. Quickly after, the exhaust temperature started to rise, when the exothermic heat front reached the exit of the reactor. When the exhaust gas temperature reached a temperature 50°C lower than the *TIT* set-point (900°C in **Figure 9.8(a)**), the heat removal step was initiated. The temperature profile shown in **Figure 8(a)** was relatively

stable during the main heat removal cycle (HR-1). When the lower threshold of the *TIT* (850°C) was crossed the secondary heat removal step (HR-2) was started, followed by a brief purging and the oxygen carrier reduction step. With the reverse-flow process, the system was able to operate at a shortened duration of HR-2, as shown in **Figure 9.8(b)**. This improved the energy efficiency of the process, by increasing the ratio of the heat sent to the gas turbine, relative to the heat lost in the other exhaust streams. As shown in **Figure 9.8(b)**, the temperature of the reduction exhaust sharply decreased when the flow direction was reversed. The reactor temperature was lower near the reactor entrance due to the endothermicity of the reduction reactions and the heat transferred to the cold feed. During the backward flow pass, the gas was cooled to the temperature of the solids at the reactor entrance before leaving the reactor from what was the reactor entrance a few seconds ago. When the flow direction returned to the forward path, the exhaust temperature increased significantly (**Figure 9.8(b)**), pushing the heat concentrated in the reactor center (because of the flow reversals) out of the reactor.

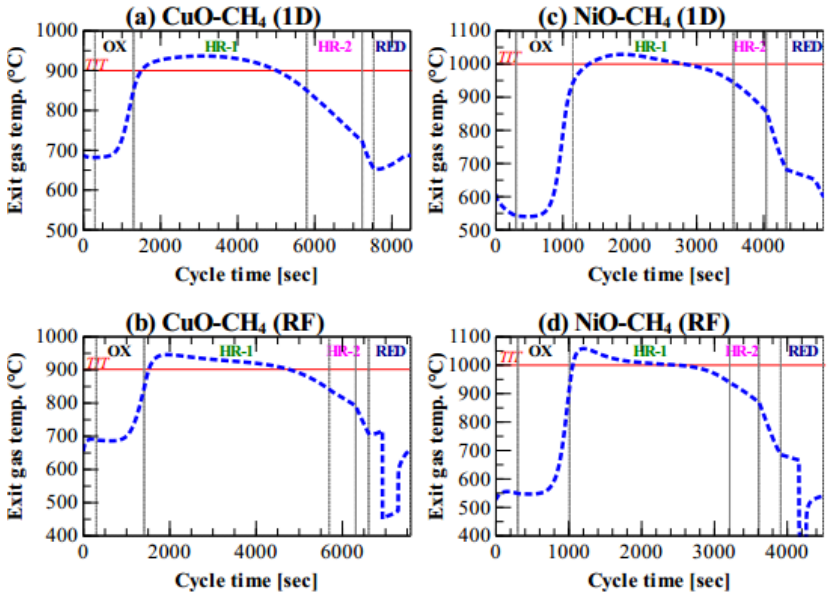

Figure 9.8: Temperature profiles of the exhaust gas stream for the entire CLC sequence under one-directional (1D) flow and reverse-flow (RF) with CH_4 fuel. The results are presented for the CLC sequence at the *TIT* set-point of 900°C for CuO and 1000°C for NiO.

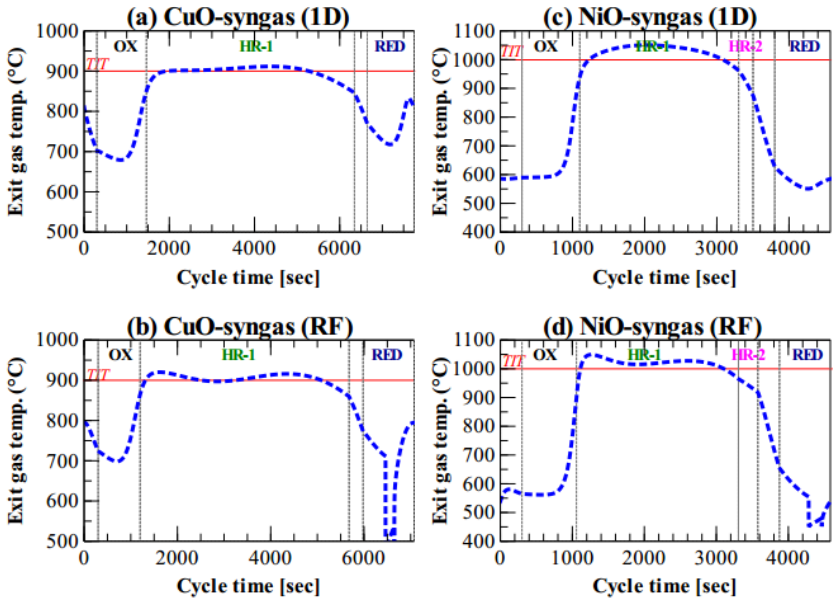

Figure 9.9: Temperature profiles of the exhaust gas stream for the entire CLC sequence under one-directional (1D) flow and reverse-flow (RF) with syngas fuel. The results are presented for the CLC sequence at the *TIT* set-point of 900°C for CuO and 1000°C for NiO.

Figure 9.8(c) presents the temperature profile for the case study with NiO and CH_4 under one-directional flow. The temperature swing between oxidation and reduction was larger in **Figure 9.8(c)** than in **Figure 9.8(a)**, because of the higher heat of reaction of Ni/NiO as compared to Cu/CuO and the higher *TIT* set-point. A noticeable difference between the one-directional process (**Figure 9.8(c)**) and the reverse-flow process (**Figure 9.8(d)**) was the gas temperature profile at the end of oxidation. The reverse-flow process had a sharper temperature rise and as a result, the oxidation cycle was shorter and the heat removal cycle was longer (**Figure 9.8(d)**). The faster temperature rise indicated a higher rate of reaction during oxidation, attributed to the higher Ni concentration at the reactor exit, shown previously in **Figure 9.4(d)**. In the one-directional process, lack of Ni at the reactor exit (shown in **Figure 9.4(a)**) lowered the oxidation reaction rate and produced a more gradual temperature rise inside the bed and thus, a slower rate of change was observed in the exhaust gas temperature of **Figure 9.8(c)**. Furthermore, **Tables 9.3-9.4** show that the time interval and air flow flowrate during HR-2 were smaller with the reverse-flow process.

These differences yielded higher energy efficiency for the reverse-flow process.

The one-directional CuO process with syngas fuel is shown in **Figure 9.9(a)**. In this case, the optimizer eliminated the HR-2 cycle completely, by finding a feasible set of cycle conditions that maximize the temperature uniformity during oxidation. This flat temperature profile for the exhaust stream, was described in detail in Han and Bollas [374] and is attributed to the slower and less exothermal kinetics in Cu oxidation. For the CLC with NiO and syngas (**Figure 9.9(c)**), a small HR-2 step was determined by the optimizer, to satisfy the requirements on the subsequent reduction cycle. The temperature of the reduction exhaust of **Figure 9.9(a)** initially decreased, because the residual heat from oxidation was being pushed out of the bed, and then increased, due to the exothermic reduction reactions between CuO and syngas. This heat front produced from the reduction reactions started leaving the reactor at the end of reduction and ultimately left the reactor after the purging step, shown in **Figure 9.9(a)**. Smaller temperature fluctuations are shown in **Figure 9.9(c)** during reduction, because of the lower bed temperatures at the start of reduction and the low exothermicity of the NiO reduction reactions by syngas.

The performance of the syngas-fed CLC with reverse-flow is shown in **Figures 9.9(b)** and **9.9Figure 9.9(d)**. Similar to **Figure 9.9(a)**, the reverse-flow equivalent (**Figure 9.9(b)**) was able to discharge all of the heat removal gas to a downstream gas turbine. An advantage of operating in the reverse-flow mode was the higher air flow rate during HR-1, as shown in **Tables 9.3-9.4**. Moreover, reverse-flow operation of the fixed bed reactor with NiO enabled a slight increase in the duration of HR-1, with the same air flow rate. The gas temperature during HR-1 presented in **Figure 9.9(d)** has smaller deviations from the *TIT* set-point, as compared to the temperature profile of **Figure 9.9(c)**. This was due to the more uniform temperature rise during oxidation, as a consequence of reversing the gas flow during reduction. In summary, **Figures 9.8-9.9** show that the reactor performance during oxidation and heat removal was positively influenced from reverse-flow operation during reduction and higher energy efficiency was feasible.

9.6.3. Comparison of system performance between the reverse-flow and one-directional reactor configurations

The overall system performance was quantified in terms of heat removal efficiency (defined in Eq.(9.1)), the standard deviation of the exhaust gas temperature during HR-1, σ_{HR}, and the fraction of time the process is in HR-1, χ_{HR}, defined by the following:

$$\sigma_{HR} = \sigma\{T_{HR,out}(t)\}, \tag{9.3}$$

$$\chi_{HR} = \tau_{HR-1} / \tau_{cycle}. \tag{9.4}$$

The performance coefficients for all of the case studies investigated are summarized in **Table 9.5**. With one-directional flow, the maximum η_{HR} was for the CLC with NiO oxygen carrier and CH_4 fuel at the *TIT* set-point of 1100°C. This was in part due to high *TIT* set-point, forcing the oxidation step to operate at higher temperatures, producing a higher enthalpy gas to the gas turbine. CLC with CuO at a *TIT* set-point of 1100°C is not feasible because the melting point of Cu is 1085°C. A second reason for the high efficiency of the NiO-CH_4 system is that it had a short reduction interval (**Table 9.3**), minimizing the extent of lower heat utilization of the reduction exhaust. For similar reasons, CLC with CuO oxygen carrier and syngas fuel had the lowest calculated η_{HR} among the one-directional flow reactors. As shown in **Table 9.5**, χ_{HR} was in the range of 0.43-0.59 for all of the one-directional flow case studies. The standard deviation of the exhaust gas temperature during HR-1 was less than 26°C for the processes with one-directional flow.

The energy efficiency was significantly increased when CLC was carried out in a reverse-flow process. As shown in **Table 9.5**, for any oxygen carrier, fuel type, and *TIT* set-point, the reverse-flow process had a higher η_{HR} than the equivalent one-directional case. The most significant improvement in η_{HR} was reported for the CLC with the CuO oxygen carrier and syngas fuel (up to ~30%). NiO-based processes were improved by ~10% with reverse-flow. Nonetheless, this was still a substantial change, given that the comparison between the one-directional and reverse-flow reactors was done at their individual optimal (maximum efficiency) operating conditions. For most of the case studies of **Table 9.5**, χ_{HR} was higher in

the reverse-flow process. To maximize η_{HR}, the optimizer could increase the flow rate of air during HR-1, as well as increase τ_{HR-1}. A higher flow rate of air was not reflected in χ_{HR} so it was possible for χ_{HR} to decrease, even though η_{HR} increased. Lastly, the standard deviation of $T_{HR,out}(t)$ was generally higher with the reverse-flow process. This can be construed as the consequence of sending more heat to the gas turbine. The maximum temperature fluctuation of the heat removal step was constrained by the dynamic problem to not exceed 50°C of the *TIT* set-point, so the deviation of temperature from its set point was not a problem. In summary, the results of **Table 9.5** illustrate that the reverse-flow reactor configuration was superior to its fixed bed reactor design equivalent. Dynamic optimization is well-suited for process analysis and comparison of the optimal process conditions and efficiencies feasible in each reactor configuration.

Table 9.5: Summary of the fixed bed reactor performance under one-directional (1D) flow and reverse-flow (RF) for the CLC with NiO and CuO oxygen carriers and CH_4 and syngas fuels.

	NiO with CH_4				**CuO with CH_4**			
Flow direction	**1D**		**RF**		**1D**		**RF**	
TIT set-point (°C)	1100	1000	1100	1000	1000	900	1000	900
η_{HR}	0.729	0.703	0.782	0.774	0.668	0.683	0.767	0.780
χ_{HR}	0.433	0.491	0.446	0.462	0.512	0.529	0.535	0.545
σ_{HR} (°C)	25.6	23.0	29.7	22.0	23.6	24.9	23.1	26.4
	NiO with syngas				**CuO with syngas**			
Flow direction	**1D**		**RF**		**1D**		**RF**	
TIT set-point (°C)	1100	1000	1100	1000	1000	900	1000	900
η_{HR}	0.640	0.685	0.729	0.761	0.555	0.695	0.727	0.736
χ_{HR}	0.459	0.481	0.454	0.492	0.455	0.592	0.525	0.633
σ_{HR} (°C)	26.0	24.7	31.9	23.8	13.0	14.8	21.2	13.0

9.7. Conclusions

The use of a reverse-flow reactor was explored as a process intensification option to improve the energy efficiency of chemical-looping combustion systems integrated into a combined cycle power plant. Periodic flow reversal of the fuel was shown to enhance the contact between the fuel and oxygen carrier, improve reactor bed temperature and conversion uniformity, and suppress carbon deposition. We addressed the operational challenges of the batch fixed bed CLC reactor using a model-based approach, focused on optimizing the cycle strategy for maximum process efficiency. We compared the optimal reverse-flow process against its optimized counterpart of CLC of methane and syngas fuels with Cu- and Ni-based oxygen carriers. This analysis showed that operating a fixed bed CLC reactor in the reverse-flow mode can be effective in increasing the power generation efficiency of a downstream gas turbine cycle. This fixed bed design avoids the issue of attrition and gas-solid separation typically found in circulating fluidized bed units. Furthermore, the simplicity of this process makes it easily applicable to existing bench-scale units without considerably complicated equipment.

Chapter 10 A NOVEL SIMULATED MOVING BED PROCESS FOR CHEMICAL-LOOPING COMBUSTION

A simulated moving bed process is explored for chemical-looping combustion (CLC). Countercurrent movement of gases and solids is simulated by continuously moving the feed point along the axial direction of the reactor bed. Application of this novel reactor concept to CLC with NiO and CH_4 fuel shows an increase in CO_2 capture efficiency, bed utilization, and temperature uniformity, compared to a conventional fixed bed reactor.

10.1. Introduction

Simulated moving bed (SMB) chromatography has been gaining more attention since its emergence in the 1930s. Its applications include sugar, petrochemical, and pharmaceutical separations [455]. SMB chromatography has become one of the preferred techniques for the separation of the enantiomers of a chiral compound [456]. Several active pharmaceutical ingredients, including blockbuster drugs, are manufactured using the SMB technology.

The basic principle of the SMB technology is the simulated counter-current movement between the solid and the liquid phases. Due to different adsorptions affinities of the two feed components, the more retained one moves toward the extract outlet, while the other (less retained) moves toward the raffinate outlet. The SMB process overcomes the technical problems associated with a true moving bed, wherein it is necessary to move both the fluid and solid phases. Circulation of the solid phase was reported to cause technical problems, including mechanical erosion of the adsorbent (which leads to the formation of fines and high-pressure drops), equipment abrasion, and difficulty in maintaining plug flow for the solids [457]. In the SMB, the counter-current movement is created by dynamically shifting the inlet and outlet ports in the same direction of the fluid flow, without circulation of the solid phase.

For CLC applications, a moving bed process was proposed by Fan and Li [458] to fully convert the Fe_2O_3

to Fe/FeO during reduction with syngas. This is because the Fe-based oxygen carrier has multiple oxidation states and the extent of conversion can be limited by thermodynamic equilibrium. When a fluidized bed reactor is used as the Reducer, the partial pressure ratio of CO_2 to CO is expected to be high throughout the reactor. Therefore, Fe_2O_3 can only be reduced to Fe_3O_4. In contrast, when a counter-current moving bed reactor is used, the extent of conversion of Fe_2O_3 can be high because of a low partial pressure ratio of CO_2 to CO at the solids outlet, yielding a reduced product in the form of Fe/FeO. Thus, to achieve the same fuel conversion in a CLC Reducer, a smaller inventory Fe_2O_3 particles is needed in a moving bed reactor, as compared to a fluidized bed reactor. The counter-current moving bed reactor also enhances the steam to hydrogen conversion during the regeneration of the reduced Fe/FeO particles [107]. The disadvantages of the moving bed process are the technical problems attributed to the continuous circulation of solids and requirement of large particle sizes rendering the reaction rates diffusion-limited.

In this study, a simulated moving bed process is explored as a reactor option for gaseous CLC. The performance of the SMB is compared against an equivalently designed fixed bed process, utilizing the same oxygen carrier, fuel, and operating conditions. Two case studies are analyzed in the model-based analysis. In the first case study, the reduction step of CLC commences over an isothermal bed of fully oxidized oxygen carrier, to evaluate the transient profiles of the NiO conversion and gaseous selectivity in the SMB and fixed bed configurations. In the second case study, CLC is simulated for multiple cycles in both reactor configurations and the comparison is made over their cyclic steady states. The cyclic steady state refers to the condition when the bed concentration and temperature profiles are repeated for consecutive cycles.

10.2. Basis of comparison

A SMB reactor is modeled using multiple fixed bed reactors in the configuration shown in **Figure 10.1(a)**. In configuration “A”, the flow passes through reactor "1" →"2" →"3". When the flow configuration is switched to “B”, the flow pass is changed to "2"→"3"→"1". And during configuration

"C", the flow pass is "3"→"1"→"2". The flow configuration dynamically alternates between "A", "B", and "C" during the course of the CLC reduction and/or oxidations step. In the fixed bed configuration, the three reactors of **Figure 10.1(a)** are aligned in series, and the flow pass is fixed to "1" →"2" →"3".

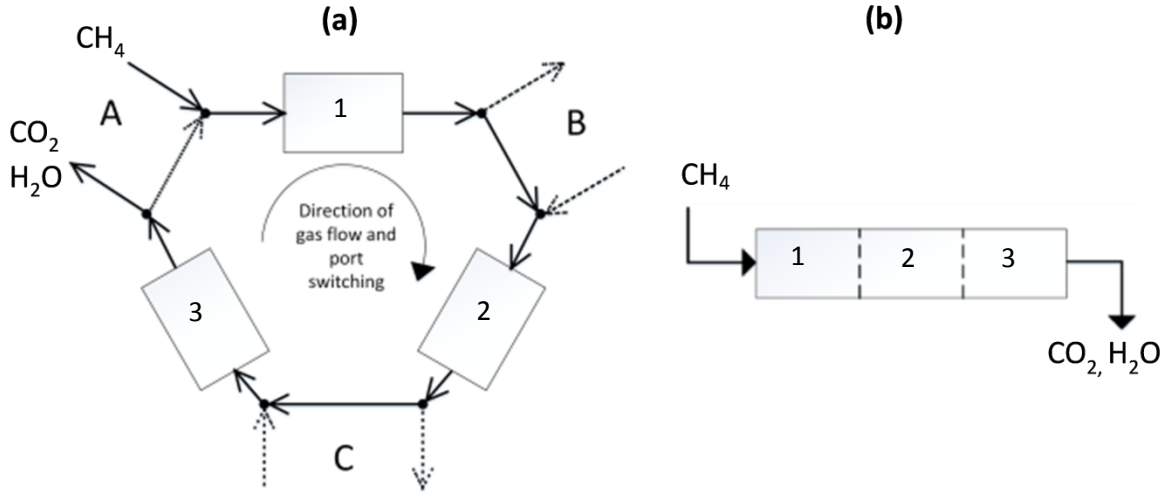

Figure 10.1: Reactor designs for CLC: (a) simulated moving bed and (b) fixed bed.

Table 10.1: Geometries and operating conditions of the SMB and fixed bed units.

Properties	*Simulated moving bed*	*Fixed bed*
NiO loading	18% NiO/$NiAl_2O_4$	18% NiO/$NiAl_2O_4$
Particle size	171 µm	171 µm
Bulk density	2200 kg/m3	2200 kg/m3
Solid loading	2.5 kg	2.5 kg
I.D.	60 mm	60 mm
Bed height	74.3 x3 mm	223 mm
Fuel gas flow rate	2.78E-04 m^3/s	2.78E-04 m^3/s
CH_4 composition	100% CH_4	100% CH_4

The dynamic 1D homogeneous model presented in Chapter 4 is used for the simulation of the SMB and fixed bed processes. This model incorporates the conservation balances of mass, energy, and momentum and was previously validated against literature-reported CLC data in bench-scale fixed bed units [193]. The reduction of NiO with CH_4 is simulated, using the published kinetics of Zhou et al. [119]. The second

column of **Table 10.1** lists the design of the fixed bed reactor. To simulate a SMB that is comparable to the fixed bed, the original fixed bed is divided into three units, by simplying shortening the bed length by a third. Thus, the SMB reactor in total has the same solids inventory, as the original fixed bed (**Table 10.1**).

10.3. Results and discussion

The performance of the simulated moving bed reactor was compared to its fixed bed counterpart in terms of CH_4 conversion, CO_2 capture efficiency, oxygen carrier conversion and selectivity to solid carbon. The reactor temperature profiles were also explored to identify potential advantages in heat utilization.

10.3.1. Case study I: Isothermal conditions

Implementation of the SMB process yields numerous benefits over its comparable fixed bed design with a negligible sacrifice to fuel conversion, shown in **Figure 10.2(a)**. First, the SMB achieves higher CO_2 selectivity at higher bed-averaged NiO conversions (**Figure 10.2(b)**). As the inlet and outlet ports were switched along the length of the reactor, the inlet feed was constantly introduced to fresh oxygen carrier particle, which promoted the conversion of CH_4 to CO_2 and suppressed the catalytic reactions that yielded partial oxidation products. As a result, a second benefit is the reduction in carbon deposition during the reduction cycle. A comparison of the SMB design to the fixed bed design is shown in **Figure 10.2(c)**. By recycling the combustion products (*i.e.*, CO_2 and H_2O) through the NiO-depleted regions of the reactor, any solid carbon formed previously could be gasified to CO and H_2.

Another advantage of the SMB process was the mitigation of cold spots inside the reactor, as shown in **Figure 10.3**. The reduction of NiO by CH_4 is generally endothermic, so the temperature of the bed decreases when fuel reacts with NiO. However in the SMB configuration, the reaction zone covers a larger reactor area, so the extent of the temperature fluctuations was reduced and circulation of hot gases within the reduced zones further warmed up the bed **Figure 10.3**.

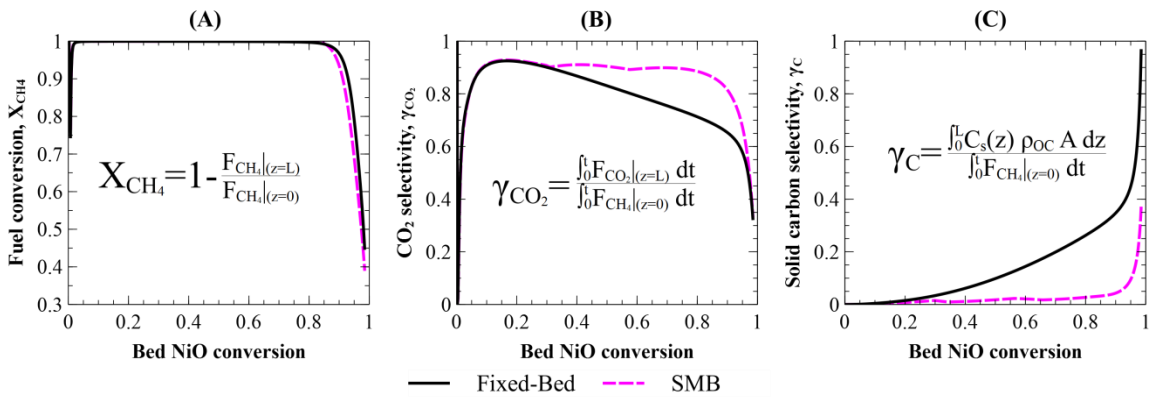

Figure 10.2: (a) fuel conversion, (b) CO_2 selectivity, and (c) solid carbon selectivity *vs*. bed NiO conversion for the fixed bed and SMB processes at an initial bed temperature of 900°C.

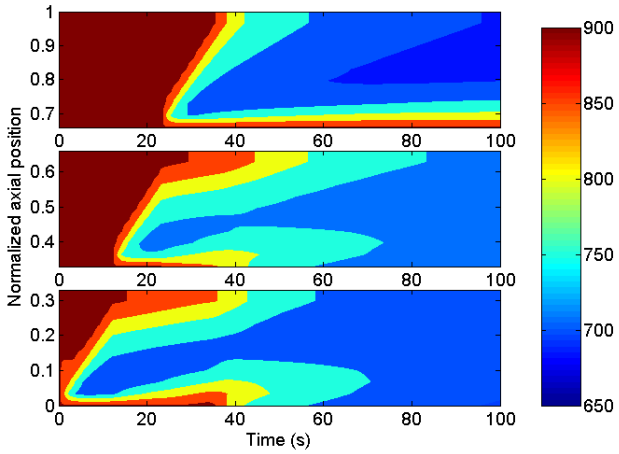

Figure 10.3: Transient temperature distributions (°C) for one CLC reduction step at an initial bed temperature of 900°C with the fixed bed and SMB processes.

10.3.2. Case study 2: Cyclic steady-state conditions

In the second case study, multiple reduction, purge, and oxidation cycles were simulated over the fixed bed and SMB designs. For this analysis, two versions of the fixed bed reactor was considered, maintaining the same reactor geometries listed in **Table 10.1**. The first version was the series configuration, which is the same as that modeleled in the first case study. The exit of the first reactor was taken as the inlet to the second, and the exit of the second reactor was the inlet to the third. The second

version was the parallel configuration, which assumes that three fixed beds are operating in parallel, each fed with a third of the total gas flow rate.

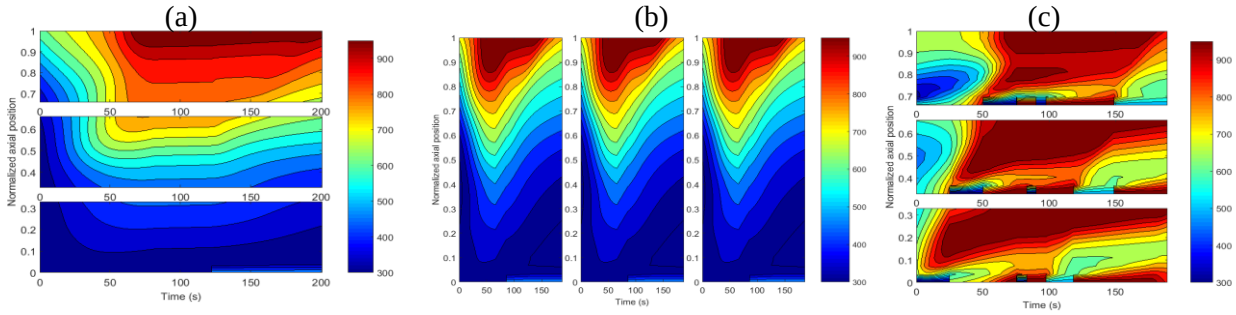

Figure 10.4: Internal temperature distribution inside (a) fixed bed reactor in series; (b) fixed bed in parallel; and (c) SMB reactor configuration.

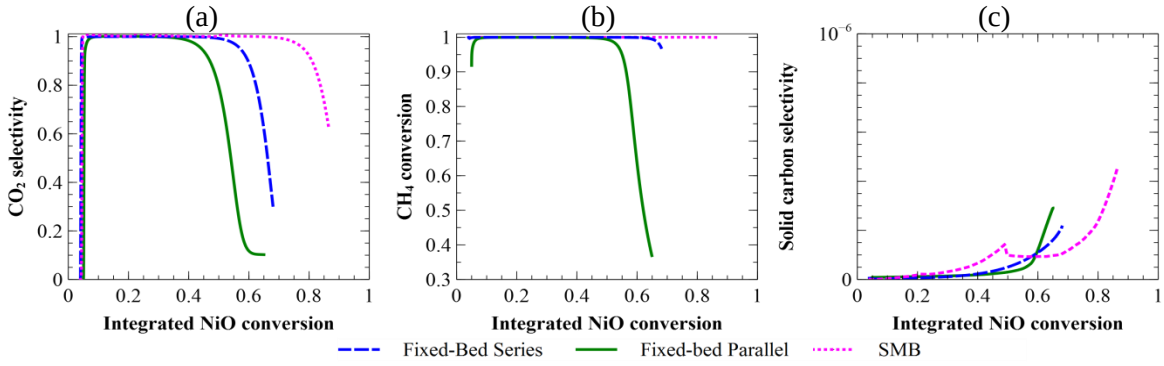

Figure 10.5: Exit gas concentration profiles of the (a) fixed bed reactor in series; (b) fixed bed in parallel; and (right) SMB reactor configuration.

Figure 10.4 presents the temperature distribution inside the reactors after reaching cyclic steady-state. As shown for both fixed bed configurations, an increase in temperature during oxidation can only be observed for the last reactor of **Figure 10.4(a)** and for the later portion of the reactor of **Figure 10.4(b)**. Due to the very low temperatures at the reactor inlet, there was not enough heat to drive the endothermic reduction reactions. As a result, ~1/3 of the total bed was rendered inactive in the CLC reactions. The bed

utilization was significantly improved with the SMB process of **Figure 10.4(c)**. Starting from oxidation, the temperature rise inside the reacor prevailed over a much larger area, which indicated that reduction was more favorable in the SMB design. By heating the bed uniformly, the reduction cycle was able to enjoy higher kinetics and greater bed conversion.

The gas and solid selectivities for the corresponding simulation results are shown in **Figure 10.5**. The fixed bed process in series has a better reduction performance than the fixed bed in parallel, indicated by the higher CO_2 selectivity and fuel conversion. This can be the result of the lack of optimality in reactor design for the reactors in parallel. With the SMB design, a high CO_2 selectivity can be sustained for longer NiO bed conversions. This was shown previously in Section 10.3.1. The SMB process was also able to partially gasify the deposited carbon in the reactor (**Figure 10.5(c)**). From the results of **Figures 10.2-10.5**, it is revealed that the SMB process delivers better CLC performance than the fixed bed reactor.

10.4. Conclusions

A simulated moving bed (SMB) reactor was proposed for CLC. This design avoids the issues of attrition and gas/solid separation, can accommodate a wide range of particle sizes, and be pressurized, just like the fixed bed design. A model-based analysis was carried out to analyze the performance of the SMB, in comparison with an equivalently designed fixed bed reactor. The SMB reactor was shown to have higher bed utilization and CO_2 capture efficiency than the fixed bed process. Thus, the simulated moved bed reactor design was shown to be promising option for CLC applications and future work is aimed at process design and optimization studies of the novel reactor design.

Chapter 11 CONCLUSIONS AND RECOMMENDATIONS

11.1. Concluding remarks

Chemical-looping technologies offer the potential to lower the cost of CO_2 capture for thermal power plants. This purpose of this thesis was to apply process engineering methodologies to accelerate the deployment of chemical-looping combustion (CLC) technologies. The key steps in this dissertation were: (1) the development and validation of process models that capture the hydrodynamics and kinetics of CLC reactors through optimal experimental design, (2) dynamic optimization of CLC reactor configurations for seamless integration with a downstream power cycle, and (3) proposition of the reverse-flow and simulated moving bed reactor configurations as process intensification options for commercial CLC systems.

In Chapter 1, the motivation for Carbon Capture and Sequestration (CCS) technologies was discussed as a necessary measure to make significant reductions in anthropogenic CO_2 emissions. The conventional CO_2 capture methods, including pre-combustion, oxy-fuel combustion, and post-combustion technologies, are well-established but they are highly energy intensive and thus significantly reduce the thermal efficiency of the power plant. Chemical-looping combustion (CLC) has emerged as one of the most promising technologies to deliver low-cost CO_2 capture. Chapter 2 surveyed the main research topics on CLC, covering the areas of oxygen carrier development, candidate reactor designs, kinetics and reactor modeling, and process design and integration. Based on the current literature, synthetic Ni and Cu-based oxygen carriers are suitable for CLC due to their intrinsic fast reaction rates. However, large-scale application of these oxygen carriers in the widely recognized fluidized bed reactor configuration is not practical, as the plant economics would quickly become unfavorable due to particle attrition. Moreover, the CLC reactor system needs to withstand the high temperatures and pressures of the power plant, which is not feasible in the current fluidized bed reactor configurations. Combined cycle power plants are preferred due to their high plant efficiencies, low-cost, high flexibility, and fast start-up. At the present, research is on-going to design and simulate fluidized bed reactors capable of withstanding the operation

of combined cycles. An alternative reactor configuration is needed in the immediate future to fulfill the gap in integrating CLC with combined cycle power plants.

To accurately design power systems integrated with CLC and estimate efficiencies, high-fidelity process models are required. Chapters 3-6 were focused on the development of accurate process and kinetic models that are capable of simulating CLC experimental data. Chapter 3 details the experimental procedure to prepare oxygen carriers, test their reactivity in a bench-scale fixed bed reactor and thermo-gravimetric analyzer, and analyze their structural and textural properties using SEM, BET, and XRD. In Chapters 4-5, a heterogeneous reactor/particle model was developed and used to describe experimental data reported in the literature. It was shown that in ideal cases, where the particle size was sufficiently small and isothermal and plug flow conditions were met, a homogeneous reactor model was sufficient to characterize the observed trends in gas profiles. However, these models are limited in terms of their scope because they are not suitable for representing large-scale systems, which are typically non-isothermal, limited by intraparticle diffusion limitations, and exhibit strong axial or radial dispersion forces. The developed heterogeneous model was demonstrated to be more accurate than the homogeneous models in representing the experimental data in cases of large particle sizes, significant dispersion, and temperature non-uniformities. Thus, this heterogeneous model was used in later studies, to better capture the hydrodynamics inside the CLC reactor.

In Chapter 6, a model-based framework coupling structural identifiability analysis and optimal design of experiments was presented and applied to address the controversies and discrepancies existing in the CLC kinetics. Specifically, the reduction kinetics between NiO and CH_4 was analyzed, in which there exists 160 different combinations of kinetic models of various reaction networks, kinetic mechanisms, and solid-state reaction models. First, structural identifiability and model distinguishability analyses were used to reject model structures on the basis of poor statistical significance in their kinetic parameters and lack of distinguishability from different model structures. Four suitable models were systematically identified from the preliminary analysis, and then further evaluated by optimal experimental design

techniques. Optimal designs for model discrimination were proposed and executed to determine a true model structure for the reaction kinetics of the CH_4-NiO system. The kinetic parameters of the true model were estimated with statistical significance, from experiments aimed at reducing parameter uncertainty. The final model was demonstrated to have predictive capabilities outside of the design space from which its parameters were derived. The kinetics resulting from this work (Chapters 3-6) was validated and suitable for application in process design and optimization.

In Chapter 7, an optimization framework was formulated to guide the design and operation of large-scale CLC reactors for the integration into power plants. A high-pressure fixed bed reactor was selected as a case study of the approach, to optimally integrate batch processes for power generation applications. The objective was to maximize the potential of the CLC reactor to produce a high quality gas stream suitable for a downstream gas turbine, taking into account the constraints on the system performance during reduction and oxidation and the requirements imposed by the power plant. Through several cases, it was shown that the reactor operating with the optimal cycle configuration was able to reach higher energy efficiencies than the baseline design. The analysis was extended to consider a system of fixed bed reactors operated in parallel. It was found that through the combination of multiple reactors, the extent of stream fluctuations sent to the gas turbine was further reduced. However, fluctuations of the lower quality streams prevailed and this impact should be analyzed by dynamically simulating the power plant.

Novel reactor concepts for CLC were presented in Chapters 8-10. In Chapter 8, a reverse-flow reactor was proposed, as a method of improving the gas/solid contact in the fixed bed reactor. For the modeling of industrial-scale reactors, a dusty-gas model was presented, to capture the mass/heat transport phenomena in concentrated gas/solid flows. This concept was analyzed for the CLC reduction of NiO with CH_4 in Chapter 8. The performance of the reverse-flow reactor was shown to have superior bed conversion and temperature uniformity, higher CO_2 capture efficiency, and suppressed carbon deposition, compared to their equivalent one-directional fixed bed reactors (Chapter 8). In Chapter 9, dynamic optimization of the cycling procedure was carried out to maximize the efficiency of the reverse-flow

reactor. The results from the comparative analysis showed that it was feasible to increase the energy efficiency of the process, by implementing CLC in the reverse-flow mode. The benefits of the reverse-flow operation were reported for several cases of CLC of NiO and CuO oxygen carriers with methane and syngas feedstocks. In Chapter 10, a simulated moving bed reactor concept was proposed as a superior alternative to the fixed reactor configuration. The simulated moving bed reactor has the potential to overcome the axial conversion fronts of the fixed bed reactor, limiting the bed utilization in the CLC cycles. The results of the model-based analysis showed that the simulated moving bed reactor was able to deliver a superior CO_2 capture efficiency and better bed utilization, compared to an equivalently designed fixed bed reactor. Future work is needed to compare the energy efficiency of the simulated moving bed reactor with that of the reverse-flow reactor.

11.2. Recommendations

The conclusions drawn from this work clearly illustrate that chemical-looping combustion can prove to be a ground breaking technology for highly efficient power generation with CO_2 capture. However, alongside the promising features of CLC, there also exists a number of technological barriers that must be overcome before a CLC-power plant can be realized. The recommendations given in this section will help the CLC-community in optimizing the design and operation of CLC reactor systems and investigate the real efficiency penalty of CO_2 capture.

11.2.1. Optimal reactor scale-up

CLC systems should be designed to always provide a high fuel conversion to CO_2 efficiency, regardless of fluctuations in the gas feedstocks, process conditions, and oxygen carrier properties. Current methods of scaling up bench-scale reactors involve the use of simple scaling factors and “rules-of-thumb.” Model-based techniques are used in other fields, such as catalytic reforming, but not widely implemented in CLC applications. As an extension of previous work on optimal experimental design (Chapter 6), the following optimization problem is presented to minimize the sensitivity of the product conversion and selectivity to

changes in the process conditions. Simply, this problem seeks a reactor design that can provide high conversions of fuel to CO_2, under uncertainty in the system inputs:

$$\begin{aligned} &\boldsymbol{\varphi} = \arg\max_{\boldsymbol{\varphi}\in\boldsymbol{\Phi}} \left\{ \det\left[\mathbf{V}_{\zeta}(\boldsymbol{\zeta}, \boldsymbol{\varphi}) \right] \right\} \\ &s.t. \quad \mathbf{f}\left(\dot{\mathbf{x}}(t), \mathbf{x}(t), \mathbf{u}(t_0), \hat{\boldsymbol{\theta}}, t \right) = 0, \\ &\quad\;\; \hat{\mathbf{y}}(t) = \mathbf{h}\left(\mathbf{x}(t) \right), \\ &\quad\;\; \mathbf{u}_{\min} \le \mathbf{u}(t) \le \mathbf{u}_{\max} \qquad\qquad \forall t \in [0, \tau], \end{aligned} \tag{11.1}$$

where $\mathbf{V}_{\zeta}(\boldsymbol{\zeta}, \boldsymbol{\phi})$ is the inverse of the information matrix, composed of the dynamic sensitivities of the reactor efficiencies $\boldsymbol{\zeta}$ with respect to the reactor design $\boldsymbol{\phi}$. The objective function of Eq.(11.1) is essentially the opposite of the D-optimal design problem, which seeks a design that maximizes the observances of the model parameters. The solution of Eq.(11.1) is the CLC reactor design that is suggested for process design analysis. Constraints can be incorporated in Eq.(11.1) to force the system, for instance, to always operate at high CO_2 capture efficiencies or low pressure drops.

11.2.2. Comparative analysis of reactor options for CLC

It is necessary to estimate the investment cost and the operational costs for a power plant with CLC. Thus, an optimized CLC reactor configuration should be considered in the preliminary design of a CLC-based power plant. This thesis discussed two main reactor candidates for CLC, (a) fluidized bed and (b) fixed bed, and proposed two novel reactor concepts, (c) reverse-flow reactor and (d) simulated moving bed reactor. A comparison should be made between all of the reactor options. In this work, optimization problems were formulated and used for the comparison between the reverse-flow reactor and the conventional fixed bed reactor. In the future, similar optimization problems should be solved to compare the optimal process conditions and efficiencies feasible in each reactor configuration.

A generic optimization problem for the CLC reactor is written as:

$$\begin{aligned} &\max_{\boldsymbol{\varphi}\in\boldsymbol{\Phi}} \quad J \\ &s.t. \quad \mathbf{f}(\dot{\mathbf{x}}(t), \mathbf{x}(t), \mathbf{u}(t), \boldsymbol{\theta}) = 0, \\ &\quad\;\; \mathbf{g}(\dot{\mathbf{x}}(t), \mathbf{x}(t), \mathbf{u}(t), \boldsymbol{\theta}) \le 0, \end{aligned} \tag{11.2}$$

where J is the performance index to the maximized, $\mathbf{x}$ is the vector of state variables, $\mathbf{u}(t)$ is the vector of

control variables, **f** is the set of differential equations describing the system dynamics, **g** is the vector of path constraints, and $\boldsymbol{\varphi}$ is the vector of design variables to be optimized. Eq.(11.2) should be tailored to each reactor configuration, to reflect the degrees of freedom from the perspective of process control. For instance, $\boldsymbol{\varphi}$ for the fixed bed and reverse-flow systems contains the cycle strategy (gas streams, time intervals, switching frequency) and oxygen carrier loading. The simulated moving bed process will have additional degrees of freedom, such as variations in inlet/outlet ports and number of reactor beds. The design of the fluidized bed process is more complicated, because of the circulation of solids which needs to be included in $\boldsymbol{\varphi}$. To characterize the behavior of these processes, **f** for the fixed bed reactor is described in Chapter 8 and for the fluidized bed reactor in the work of Zhou et al. [424]. The performance index *J* can be written for dynamic (Eq.(11.3)) or steady-state (Eq.(11.4)) systems:

$$J' = \frac{\int_{t_0}^{\tau_{HR}} \left(\dot{m}_{out}(t) \cdot h_{out}(t)\right) dt}{\int_{t_0}^{\tau_{cycle}} \left(\dot{m}_{out}(t) \cdot h_{out}(t)\right) dt}, \tag{11.3}$$

$$J'' = \frac{\left(\dot{m}_{out} \cdot h_{out}\right)\Big|_{AR}}{\left(\dot{m}_{out} \cdot h_{out}\right)\Big|_{AR} + \left(\dot{m}_{out} \cdot h_{out}\right)\Big|_{FR}}. \tag{11.4}$$

The optimization problem presented in Eq.(11.2) with the objective of maximizing the process efficiency, quantified by either Eq.(11.3) or Eq.(11.4), can be used to design optimal CLC reactors. By solving these dynamic optimization problems, it will be feasible to compare the optimal efficiencies of the fixed bed, fluidized bed, reverse-flow, and simulated moving bed reactor options. This will guide the optimal design of the power plant with CLC.

11.2.3. Dynamic simulation and optimization of integrated CLC-power plant models

In this work, CLC was conceputalized to be integrated with combined cycle configurations. The scope of this work was mainly concerned with meeting the input temperature and pressure requreiments of the gas turbine, as boundary conditions. Therefore, the work does not include the entire systems level model. One step forward in this direction is to develop a power plant model and integrate the streams with the CLC

reactor network. There is a variety of combined cycle configurations that can be assessed, with several options for the gas turbine technology, intercooling method, steam cycle configuration, and reheat cycles. These cycle configurations should be optimized with respect to these key parameters to order to maximize plant efficiencies and CO_2 capture.

Furthermore, the dynamic behavior of CLC should be analyzed with respect to the power plant. Dynamic analysis for the CLC-combined cycles is necessary, as the CLC reactor system is batch-operated and the power plant as a whole must constantly meet a time-varying electricity demand. To achieve this, it requires a modeling plaftform that offers the ability to conduct dynamic simulations, which is provided in software packages such as gPROMS and Modelica. It must be assured that the fluctuations of the CLC reactor exhaust do not lead to runaway behavior and allow the power plant to operate within safety and process limits. With a dynamically changing power plant, it becomes feasible to utilize the model for real-time optimization, with the objective of maintaining a high electrical efficiency and high CO_2 capture. The recommended research activities will provide a framework for the quantification of the real cost for CO_2 capture, which can be later levarged to address the increasing challenges of fossil fuels use.

Chapter 12 APPENDIX

12.1. Physical properties

Typical NiO oxygen carriers used in CLC processes have void fraction of 0.3-0.5, particle size of 0.08-1.0 mm, and solid density of 1700-4000 kg/m^3 [157]. The pore tortuosity, if no data is available, can be assumed 3.0 for spherical catalysts [459]. The gas phase diffusivities in the mixture depend on the combined effect of molecular diffusion and Knudsen diffusion for the relevant range of pore sizes of microporous or mesoporous oxygen carrier particles, typically being 20-500 Å. Binary gas phase diffusivities for a wide range of temperatures and pressures applicable are estimated through published correlations detailed in **Tables 12.2-12.3**. For all other component pairs, the semi-empirical Fuller equation can be used [460]. Gas phase diffusion ($D_{m,i}$) can be approximated using [461]:

$$D_{m,i} = \frac{1-y_i}{\sum_{j\neq i} y_j / D_{ij}}\,. \tag{12.1}$$

The effective diffusivity ($D_{e,i}$) calculates the true diffusion path from the molecular diffusivity and Knudsen diffusivity ($D_{K,i}$), as follows:

$$\frac{1}{D_{e,i}} = \frac{\tau}{\varepsilon_b}\left(\frac{1}{D_{m,i}} + \frac{1}{D_{K,i}}\right). \tag{12.2}$$

Table 12.1: Binary gas phase diffusivities for component pairs [459].

Pair	***A***	***B***	***C***	***D***	***E***	***Eq***
H_2-CO	15.39E-3	1.548	0.316E8	-2.80	1067	1
H_2-CO_2	3.14E-5	1.75	-	11.7	-	2
CO-CO_2	0.577E-5	1.803	-	0	-	2
CO_2-H_2O	9.24E-5	1.5	-	307.9	-	2
H_2-CH_4	3.13E-5	1.765	-	0	-	2
Ar-H_2	23.5E-3	1.519	0.488e8	39.8	0	1
Ar-CH_4	0.784E-5	1.785	-	0	-	2
Ar-CO	0.904E-5	1.752	-	0	-	2
Ar-CO_2	1.74E-5	1.646	-	89.1	-	2
N_2-H_2O	0.187E-5	2.072	-	0	-	2

Note D_{12}=D_{21}. Parameters below are for these expressions: (1) $D_{ij} = \left(\frac{AT^B}{P}\right)\left[ln\left(\frac{C}{T}\right)\right]^{-2} exp\left(-\frac{D}{T}-\frac{E}{T^2}\right)$; (2) $D_{ij} = \left(\frac{AT^B}{P}\right)exp\left(-\frac{D}{T}\right)$. Note: T is in K, P is in atm., and D_{ij} is in cm^2/s.

Table 12.2: Binary gas diffusivities for component pairs [167,460]. Note $D_{12} = D_{21}$. Parameters below are for the expression $D_{ij} = \frac{AT+B}{P}$. Note: T is in K, P is in atm, and D_{ij} is in cm^2/s.

Pair	***A***	***B***
H_2-N_2	6.007E-3	-0.99311
CO-N_2	0	0.322
H_2-H_2O	0	0.927
CH_4-H_2O	0	0.361
H_2-Ar	9.625E-3	-2.287804
CH_4-CO_2	0	0.153

The gas phase heat capacity ($C_{p,f}$) is taken as the molar average of the gas component heat capacity ($C_{p,i}$), which is estimated using the DIPPR equation from Aspen Plus software [462] and shown in Table 12.3.

Table 12.3: Gas phase heat capacity constants for relevant species, corresponding to the equation $C_{p,i} = A + B\left(\frac{C}{Tsinh\left(C/T\right)^2}\right) + D\left(\frac{E}{Tsinh\left(E/T\right)^2}\right)$ [462]. Note: T is in K and $C_{p,i}$ is in J/kmol-K.

	A	***B***	***C***	***D***	***E***
CH_4	33298	79933	2086.9	41602	991.96
H_2	27617	9560	2466	3760	567.6
H_2O	33363	26790	2610.5	8896	1169
CO	29108	8773	3085.1	8455.3	1538.2
CO_2	29370	34540	1428	26400	588
Ar	20786	--	--	--	--
N_2	29105	8614.9	1701.6	103.47	909.79

The gas phase viscosity of species can be estimated from the DIPPR correlation used in Aspen Plus, shown in **Table 12.4**. The viscosity of the gas mixture is estimated by the Wilke method with Herning and Zipperer approximation [460]:

$$\mu = \sum_{i=1}^{NoComp} \frac{y_i \mu_i}{\sum_{j=1}^{NoComp} y_j \sqrt{M_j / M_i}}. \tag{12.3}$$

Table 12.4: Gas phase viscosity constants for selected species, corresponding to the equation $\mu_i = \frac{AT^B}{1 + C/T + D/T^2}$ [462]. Note: T is in K and μ is in N-s/m^2.

	A	***B***	***C***	***D***
CH_4	5.255E-07	0.59006	105.67	0
H_2	1.797E-07	0.685	-0.59	140
H_2O	1.710E-08	1.1146	0	0
CO	1.113E-06	0.5338	94.7	0
CO_2	2.148E-06	0.46	290	0
Ar	9.212E-07	0.60529	83.24	0
N_2	6.5592E-07	0.6081	54.714	0

The gas phase thermal conductivity of species is estimated with the DIPPR equation used in Aspen Plus [462], shown in

. The thermal conductivity of the mixture is calculated by the Wassiljew equation [460],

$$\lambda_m = \sum_{i=1}^{NoComp} \frac{y_i \lambda_i}{\sum_{j=1}^{NoComp} y_j A_{ij}}. \tag{12.4}$$

The binary interaction parameter (A_{ij}) can be found based on Mason and Sexena's formulation (Eqs.(12.5) –(12.7)), where the ratio of the translational thermal ($\lambda_{tr_i}/\lambda_{tr_j}$) conductivities needs to be calculated from the reduced temperatures (T_r) and reduced, inverse thermal conductivity (Γ) [460].

$$A_{ij} = \frac{\varepsilon\left[1 + \left(\lambda_{tr_i} / \lambda_{tr_j}\right)^{1/2} \left(M_i / M_j\right)^{1/4}\right]^2}{\left[8\left(1 + M_i / M_j\right)\right]^{1/2}}, \tag{12.5}$$

$$\frac{\lambda_{tr_i}}{\lambda_{tr_j}} = \frac{\Gamma_j \left[\exp\left(0.0464 T_{ri}\right) - \exp\left(-0.2412 T_{ri}\right)\right]}{\Gamma_i \left[\exp\left(0.0464 T_{rj}\right) - \exp\left(-0.2412 T_{rj}\right)\right]}, \tag{12.6}$$

$$\Gamma = 210 \left(\frac{T_c M^3}{P_c^4} \right)^{1/6}. \tag{12.7}$$

Table 12.5: Gas phase thermal conductivity constants for species, corresponding to the equation $\lambda = \frac{AT^B}{1 + C/T + D/T^2}$ [462]. Note: T is in K and is in W/(m-K).

	A	***B***	***C***	***D***
CH_4	8.398E-06	1.4268	-49.654	0
H_2	2.653E-03	0.7452	12	0
H_2O	6.204E-06	1.3973	0	0
CO	5.988E-04	0.6863	57.13	501.92
CO_2	3.69	-0.3838	964	1.86E+06
Ar	6.33E-04	0.6221	70	0
N_2	3.31E-04	0.7722	16.323	373.72

The thermal conductivity of the oxygen carrier is calculated from the volume fraction of the metal compounds in the particle (Eq.(12.8)), and thus varied with the conversion [156].

$$\lambda_s = \frac{1}{\sum \frac{f_{v,i}}{\lambda_{s,i}}}. \tag{12.8}$$

Table 12.6: Physical properties of solids [156]. Note: $Cp^a = Cp_0 + Cp_1 T + Cp_2 T^2$; C_p^b at T_{ref}=1223 K (expect for Cu based OC where T_{ref}=7073 K); NDPT=Normal decomposition point.

	Thermal conductivity	***Heat capacity, C_p^a (J/kg/K)***				***Solid density, $\rho_{s,i}$***	***Melting Temperature***
	(W/m/K)	C_{p0}	C_{p1}	C_{p2}	C_p^b	(kg/m3)	(K)
				--Active material--			
Co	40	636	-5.13E-01	5.03E-04	761	8860	1768
CoO	5	751	-1.06E-01	1.03E-04	775	6440	2078
Cu	350	382	7.46E-03	6.76E-05	460	8920	1358
CuO	6	430	4.26E-01	-1.53E-04	705	6400	NDPT=1397
Cu_2O							1516
Fe	30	433	1.45E-01	1.66E-06	613	6980	1809
FeO	5	623	2.72E-01	-6.62E-05	856	5700	1650
Fe_2O_3	5	860	2.96E-03	1.57E-05	887	5240	NDPT=1735
Fe_3O_4	6	2009	-1.77	6.70E-04	847	5180	1870
MnO	3	546	3.12E-01	-8.80E-05	796	5430	2115
Mn_2O_3	3	498	5.08E-01	-1.29E-04	926	4500	NDPT=1350
Mn_3O_4	3	490	4.90E-02	-1.28E-04	358	4840	1835
Ni	75	347	2.71E-01	-5.52E-05	596	8900	1726
NiO	13	790	-2.06E-01	1.43E-04	752	6670	2228
				--Inert--			
Al_2O_3 (γ)	7	843	5.40E-01	-1.61E-04	1263	3965	2290
MgO	8	1013	3.47E-01	-8.96E-05	1304	3580	3105
SiO_2	2	953	2.91E-01	-7.82E-05	1192	2260	1996
TiO_2 (rutile)	4	785	2.12E-01	-5.97E-05	955	4260	2130
ZrO_2	3	482	1.74E-01	-4.09E-05	634	5600	2950

12.2. Transport through cylindrical particle

Mass and energy balances for transport through a cylindrical particle are presented Eqs.(12.9)-(12.10).

$$\varepsilon_c \frac{\partial C_{c,i}}{\partial t} = D_{e,i}\left(\frac{\partial^2 C_{c,i}}{\partial r_c^2} + \frac{1}{r_c}\frac{\partial C_{c,i}}{\partial r_c} + \frac{\partial^2 C_{c,i}}{\partial z_c}\right) + \rho_p \sum R_i, \tag{12.9}$$

$$\left(\varepsilon_c C_{T,c} C_{p,c} + (1-\varepsilon_c)\rho_p C_{p,s}\right)\frac{\partial T_c}{\partial t} = \lambda_s\left(\frac{\partial^2 T_c}{\partial r_c^2} + \frac{1}{r_c}\frac{\partial T_c}{\partial r_c} + \frac{\partial^2 T_c}{\partial z_c^2}\right), \tag{12.10}$$

The boundary conditions using the cylindrical particles are:

$$-D_{e,i}\left.\frac{\partial C_{c,i}}{\partial r_c}\right|_{r_c=R_p} = k_{f,i}\left(C_{c,i}\big|_{r_c=R_c} - C_i\right), \tag{12.11}$$

$$\left.\frac{\partial C_{c,i}}{\partial r_c}\right|_{r_c=0} = 0, \tag{12.12}$$

$$-D_{e,i}\left.\frac{\partial C_{c,i}}{\partial z_c}\right|_{z_c=L_p} = k_{f,i}\left(C_{c,i}\big|_{z_c=L_p} - C_i\right), \tag{12.13}$$

$$-D_{e,i}\left.\frac{\partial C_{c,i}}{\partial z_c}\right|_{z_c=0} = k_{f,i}\left(C_{c,i}\big|_{z_c=0} - C_i\right), \tag{12.14}$$

$$-\lambda_s\left.\frac{\partial T_c}{\partial r_c}\right|_{r_c=R_p} = h_f\left(T_p\big|_{r_c=R_p} - T\right), \tag{12.15}$$

$$\left.\frac{\partial T_c}{\partial r_c}\right|_{r_c=0} = 0, \tag{12.16}$$

$$-\lambda_s\left.\frac{\partial T_c}{\partial z_c}\right|_{z_c=L_p} = h_f\left(T_p\big|_{z_c=L_p} - T\right), \tag{12.17}$$

$$\lambda_s\left.\frac{\partial T_c}{\partial z_c}\right|_{z_c=0} = h_f\left(T_c\big|_{z_c=0} - T\right). \tag{12.18}$$

These equations can be combined with the fluid phase heterogeneous model equations in either the one-dimensional or two-dimensional form.

Chapter 13 NOMENCLATURE

Abbreviations

AE	Avrami-Erofe'ev
CCPP	combined cycle power plant
CCS	carbon capture and storage
CC	combined cycle
CL	chemical-looping
CLC	chemical-looping combustion
CLR	chemica-looping reforming
DAEs	differential and algebraic equations
GT	gas turbine
HR-1	heat remoal to the gas turbine
HR-2	heat removal to the steam turbine
IGCC	integrated gasification combined cycle
MSC	modified shrinking core
MV	modified volumetric
NGCC	natural gas fired combined cycle
OC	oxygen carrier
OX	oxidation
PU	purge
RED	reduction

SC shrinking core

SGI structural global identifiability

SLI structural local identifiability

ST steam turbine

RS reaction scheme

TIT turbine inlet temperature

V volumetric

General Symbols

A_c cross-sectional area of the reactor tube [m^2]

A_{ij} binary interaction parameter

a empirical parameter for the α_{cat} expression

a_l characteristic length of particle (V_p/S_p)

a_0 initial specific surface area of the oxygen carrier [m^2/kg OC]

a_v external particle surface area per unit reactor volume [1/m]

b empirical parameter for the α_{cat} expression

C_i gas concentration of species *i* in fluid phase [mol/m^3]

$C_{c,i}$ concentration of gas species *i* in solid phase [mol/m_3]

C_i^{TGA} Concentration of gas species i in the main gas flow of the TGA setting [mol/m^3]

C_{Ni} Ni concentration [kg Ni/kg OC]

C_{NiO} NiO concentration [kg Ni/kg OC]

$C_{NiAl2O4}$ $NiAl_2O_4$ concentration [kg $NiAl_2O_4$/kg OC]

C'_{NiO} initial NiO concentration [kg Ni/kg OC]

$C_{p,f}$ heat capacity of fluid phase [J/mol/K]

$C_{p,i}$ heat capacity of the gas species [J/mol-K]

$C_{p,c}$ heat capacity of gas mixture in the solid phase [J/mol/K]

$C_{p,s}$ heat capacity of solid phase [J/mol/K]

C_T total gas concentration in fluid phase [mol/m^3]

$C_{T,c}$ Total gas concentration in solid phase [mol/m^3]

c empirical parameter for the α_{cat} expression

$D_{ax,i}$ axial dispersion coefficient of species *i* [m^2/s]

$D_{e,i}$ effective diffusion coefficient of species *i* [m^2/s]

D_{ij} binary gas phase diffusivities [m^2/s]

$D_{K,i}$ Knudsen diffusion coefficient of species i [m^2/s]

$D_{m,i}$ diffusion coefficient of component *i* in the mixture [m^2/s]

D_p particle diameter [m]

D_r diameter of reactor [m]

$D_{rad,i}$ radial dispersion coefficient of species i [m^2/s]

Ea_j activation energy of reaction j [J/mol]

F_i mole flow rate of species *i* [mol/s]

$F_{i,in}$ inlet flow rate of species *i* [mol/s]

f_{NiO} weight fraction of NiO over NiO plus $NiAl_2O_4$

Fr Froude number ($u^2/g/D$)

F_t total molar flow rate [mol/s]

$F_{v,i}$ volume fraction of solid phase i

g acceleration of gravity [m/s^2]

G mass flux of the gas phase [kg/m^2/s]

h height of sample in TGA crucible [m]

h enthalpy of gas [J/Kg]

h_{bed} packed-bed heat transfer coefficient [W/m^2-K]

h_f heat transfer coefficient between bulk fluid and solid phase [W/m^2/K]

h_w Wall heat transfer coefficient [W/m^2-K]

i gas phase species (CH_4, H_2, H_2O, CO, CO_2, Ar, N_2)

J Flux of gas species i through the OC [mol/s-m^2]

j chemical reaction

$k_{c,i}$ external mass transfer coefficient of species i [m/s]

$K_{i,,j}$ adsorption coefficient of gas i for reaction j [bar^{-1}]

K_j equilibrium constant for reaction j

k_j rate constant

$k_{j,0}$ pre-exponential factor of rate constant for catalytic reaction j [mol/kg/s]

$k_{j,0}$ pre-exponential factor of rate constant for OC reduction reaction j [m/s]

k_j^{Tref} reference rate constant for reaction j

L length of fixed bed [m]

L_p OC particle length [m]

M_i molar weight of species [g/mol]

$\dot{m}$ Mass flow rate of gas [kg/s]

N_{exp} number of experiments

N_{sp} number of samples

n_{sw} number of flow switches

N_u number of manipulated inputs

N_x number of state variables

N_y number of measured variables

N_φ number of design variables

N_θ number of model parameters

Nu Fluid to wall Nusselt number ($h_w D_p/\lambda_m$)

n Avrami-Erofe'ev exponent

P total pressure [bar]

P_c critical pressure [bar]

Pe_a axial Peclet number $(u_0 D_p/D_{ax})$

Pe_r radial Peclet number $(u_0 Dp/D_{rad})$

P_i partial pressure of species *i* [bar]

Pr Prandlt number $(C_{p,f}\,\mu_m/\lambda_m)$

R reaction

Re Reynolds number based on superficial velocity ($uD_p\rho/\mu$)

Re_i Reynolds number based on interstitial velocity $(u_i D_p \rho/\mu)$

Re_p particle Reynolds number

R_p radius of oxygen carrier [m]

Rg ideal gas law constant

r reactor radial element

r_c oxygen carrier radial element

r_{cat} rate of catalytic reaction [mol/g/s]

r^0_{cat} rate of catalytic reaction [mol/g/s] over a completely reduced oxygen carrier

r_{ij} correlation coefficient between parameters *i* and *j*

r_j reaction rate

Sc Schmidt number $(\mu/\rho/D_{m,i})$

S_{CO_2} CO_2 capture efficiency

S_g initial specific surface area of the oxygen carrier [cm^2/g OC]

Sh Sherwood number ($k_{c,i}D_p/D_{m,i}$)

T temperature of fluid phase [˚C]

T_c critical Temperature [°C]

$T_{HR,out}$ Temperature of exhaust gas during heat removal (HR-1)

T_{in} temperature in the inlet [°C]

T^{max} Maximum temperature [°C]

T_r reduced temperature

T_{ref} reference temperature (600°C for catalytic reactions, 700°C for NiO reduction reactions)

T_s solid temperature [˚C]

T_{sp} Temperature set-point [°C]

T_w wall temperature [˚C]

t time

t_i *i*-th element of time

U overall heat transfer coefficient [J/m^2/K/s]

u superficial velocity [m/s]

u_i Interstitial velocity [m/s]

u_i element i of the control vector

u_0 superficial velocity at the inlet [m/s]

V volume element

V_p volume of particle

X oxygen carrier conversion

X_{fuel} fuel conversion

X_{NiO} conversion of OC due to NiO reduction

$X_{NiAl2O4}$ conversion of OC due to $NiAl_2O_4$ reduction

X_{red} actual solid conversion of OC

x state variable

y measured output

y_i mole fraction of species i

$y_{i,feed}$ mole fraction of species i in the feed

$\hat{\square}$ estimated response

z length element

z_c OC axial element (cylindrical particle)

Greek Letters

α Temperature normalization factor

α_{cat} factor of catalytic activity

δ stagnant gas thickness [m]

Γ Reduced inverse thermal conductivity

ΔH heat of reaction [J/mol]

Δt_1 earliest allowable time interval to take sample

$\square\square_{\square}^{max}$ maximum allowable time interval between consecutive sampling points

$\square\square_{\square}^{min}$ minimum allowable time interval between consecutive sampling points

ε numerical constant, near unity

ε_b porosity of fixed bed

ε_c porosity of the OC

ζ Phase displacement

η efficiency

η_j effectiveness factor for reaction R_j, $\eta_j = \frac{3\int_0^{R_p} r_c^2 R_j dr_c}{R_p^3 R_j}$

θ_i i-th model parameter

$\theta_{i,max}$ upper bound on i-th model parameter

$\theta_{i,min}$ lower bound on i-th model parameter

σ_{ij} ij-th element of the inverse matrix of measurement errors, Σ_y

λ_{ax} axial heat dispersion coefficient [W/m/K]

λ_e^0 static contribution to effective thermal conductivity [W/m-K]

λ_i thermal conductivity of species i [W/m-K]

λ_{rad} radial heat dispersion coefficient [W/m-K]

λ_m thermal conductivity of the gas mixture [W/m-K]

λ_s thermal conductivity of the oxygen carrier [W/m-K]

$\lambda_{tr,i}$ translational thermal conductivity for species i

μ viscosity of the gas mixture [N-s/m^2]

ρ density of fluid phase [kg/m^3]

ρ_s density of oxygen carrier [kg/m^3]

σ_{HR} standard deviation of the exit gas temperature during HR-1

τ experiment duration

τ pore tortuosity

τ_{cycle} time interval for one complete redox cycle

τ_{HR-1} time interval for the HR-1 cycle

τ_i time intervals for the *i*-th CLC step

$\tau_i^{\max}$ upper bound for the time intervals for the *i*-th CLC step

$\tau_i^{\min}$ lower bound for the time intervals for the *i*-th CLC step

φ_i *i*-th element of the design vector

Φ_n Thiele modulus for n-order reaction

χ^2 chi-square statistic to test goodness of fit

χ_{HR} fraction of time the process is in HR-1

ω weight fraction of metal oxide content

ω^{max} upper bound for the metal oxide content

ω^{min} lower bound for the metal oxide content

Vectors and Matrices

f system of differential and algebraic equations

$\mathbf{H}_\theta$ information matrix $[N_\theta \times N_\theta]$

h selection function

M model structure

$\mathbf{Q}_r$ dynamic sensitivity matrix of the *r*-th response variable

$\mathbf{t}_{sp}$ vector of sampling points $[N_{sp}]$

U vector of control space

u vector time varying or constant control variables $[N_u]$

$\mathbf{u}_{max}$ upper bound on u $[N_u]$

$\mathbf{u}_{min}$ lower bound on u $[N_u]$

$\mathbf{V}_\theta$ variance-covariance matrix of model parameters $[N_\theta \times N_\theta]$

$\mathbf{W}_\theta$ weighting matrix to assess SGI $[N_\theta \times N_\theta]$

$\mathbf{W}_y$ weighting matrix to assess SGI $[N_y \times N_y]$

$\mathbf{V}_\theta$ variance-covariance matrix of model parameters $[N_\theta \times N_\theta]$

$\mathbf{x}$ vector of state variables [N_x]

$\dot{\square}$ vector of derivatives of state variables [N_x]

$\mathbf{y}_0$ vector of initial conditions [N_y]

$\mathbf{y}$ vector of measured variables [N_y]

$\widehat{\square}$ vector of estimated responses [N_y]

$\boldsymbol{\Theta}$ parameter space

$\boldsymbol{\theta}$ vector of true values of model parameters [N_θ]

$\widehat{\square}$ vector of estimated values of model parameters [N_θ]

$\boldsymbol{\theta}^0$ vector of initial guesses of model parameters [N_θ]

$\boldsymbol{\Sigma}_y$ measurement errors variance-covariance matrix [$N_y \times N_y$]

$\boldsymbol{\Sigma}_\theta$ prior variance-covariance matrix of model parameters [$N_\theta \times N_\theta$]

$\boldsymbol{\Phi}$ simplified design space

$\boldsymbol{\Phi}$’ generic design space

$\boldsymbol{\varphi}$ simplified design vector [N_φ]

$\boldsymbol{\varphi}'$ generic design vector [N_φ]

$\boldsymbol{\varphi}^0$ initial design vector [N_φ]

LIST OF PUBLICATIONS AND CONFERENCE PRESENTATIONS

PUBLICATIONS:

1. Han, L.; Bollas, G.M. Chemical-looping combustion in a reverse-flow fixed-bed reactor. *Energy* (2015), in review.
2. Han, L.; Bollas, G.M. Dynamic Optimization of Fixed Bed Chemical-Looping Processes. *Energy* (2015), in review.
3. Han, L.; Zhou, Z.; Bollas, G.M. Model-Based Analysis of Chemical-Looping Combustion Experiments. Part I: Structural Identifiability of Kinetic Models. *AIChE J. (*2015) in review
4. Han, L.; Zhou, Z.; Bollas, G.M. Model-Based Analysis of Chemical-Looping Combustion Experiments. Part II: Model-based Analysis of Chemical-Looping Combustion Experiments. Part II: Optimal Design of Reduction Experiments. *AIChE J.(* 2015) in review
5. Han, L.; Zhou, Z.; Bollas, G.M. Heterogeneous modeling of chemical-looping combustion. Part 2: Particle model. *Chem. Eng. Sci.* 113 (2014) 116-128.
6. Han, L.; Zhou, Z.; Bollas, G.M. Heterogeneous modeling of chemical-looping combustion. Part 1: Reactor model. *Chem. Eng. Sci.* 104 (2013) 233–249.
7. Nordness, O.; Han, L.; Zhou, Z., Bollas, G.M. Kinetic Study of High-Pressure Chemical-Looping Combustion (CLC) Experiments with Methane and Synthesis gas with Ni and Cu Oxygen Carriers. *Energy & Fuels* (2015) accepted.
8. Zhou, Z.; Han, L.; Bollas, G.M. Model-assisted analysis of fluidized bed chemical-looping reactors. *Chem. Eng. Sci.* 134 (2015) 619-631.
9. Zhou, Z.; Han, L.; Nordness, O.; Bollas, G.M. Continuous regime of chemical looping combustion (CLC) and chemical-looping with oxygen uncoupling (CLOU) reactivity of CuO oxygen carriers. *Appl. Catal. B Environ*. 166-167 (2015) 132-144.
10. Zhou, Z.; Han, L.; Bollas, G.M. Kinetics of NiO reduction by H_2 and Ni oxidation at conditions relevant to chemical-looping combustion and reforming. *I. J. Hydrogen Energy.* 39 (2014) 8535-8556.

11. Zhou, Z.; Han, L.; Bollas, G.M. Overview of Chemical-Looping Reduction in Fixed Bed and Fluidized Bed Reactors Focused on Oxygen Carrier Utilization and Reactor Efficiency. *Aerosol and Air Quality Res.* 14 (2014) 559-571.
12. Zhou, Z.; Han, L.; Bollas, G.M. Model-based analysis of bench-scale fixed-bed units for chemical-looping combustion. *Chem. Eng. J.* 233 (2013) 331–348.

CONFERENCE ORAL PRESENTATIONS:

1. Han, L.; Bollas, G.M. "A model-based framework for dynamic optimization in power generation systems." 11th IFAC Symposium on Dynamics and Control of Process Systems, including Biosystems (2016) Trondheim, Norway.
2. Palmer, K.A.; Hale, W.T.; Han, L.; Jacobson, C.A.; Bollas, G.M. "Method for Fault Identifiability through Aerospace Built-in Test Applications." 11th IFAC Symposium on Dynamics and Control of Process Systems, including Biosystems (2016) Trondheim, Norway.
3. Han, L.; Chen, C.; Bollas, G.M. "Optimization of Chemical-Looping Combustion Fixed-Bed Reactors in Natural Gas-Fired Combined Cycle Power Plants." Annual AIChE Meeting (2015) Salt Lake City, UT.
4. Han, L.; Chen, C.; Bollas, G.M. "Dynamic Simulation of a Natural Gas-Fired Combined Cycle Power Plant Integrated with Chemical-Looping Combustion." Annual AIChE Meeting (2015) Salt Lake City, UT.
5. Palmer, C.; Han, L.; Bollas, G.M. "Analysis of a Simulated Moving Bed Configuration for Chemical-Looping Combustion." Annual AIChE Meeting (2015) Salt Lake City, UT.
6. Magnusson, F.; Palmer, K.A.; Han, L.; Bollas, G.M. "Dynamic Parametric Sensitivity Optimization Using Simultaneous Discretization in JModelica.org." International Conference on Complex Systems Engineering (2015) Storrs, CT.

7. Chen, C.; Han, L.; Such, K.D.; Zhou, Z.; Bollas, G.M. "Dynamic simulation of chemical-looping systems integrated in power plants." 40th Int. Tech. Conference on Clean Coal and Fuel Systems (2015) Clearwater, FL.
8. Han, L.; Zhou, Z.; Bollas, G.M. "Model-Based Design of Experiments to Achieve Kinetic Validation for Chemical-Looping Systems." **Selected by AIChE Session Chair, Dr. Joris Thybaut (Universiteit Gent), as the "Best Presentation" in the session "Modeling and Analysis of Chemical Reactors II" of the 2014 AIChE Annual Meeting in Atlanta, GA.**
9. Zhou, Z.; Han, L.; Bollas, G.M. "Continuous Regime of CLC/CLOU Reactivity and Its Impact on the Dynamic Performance of Cu_xO_y/SiO_2 Oxygen Carriers." Annual AIChE Meeting (2014), Atlanta, GA.
10. Han, L.; Zhou, Z.; Bollas, G.M. "Parameter identifiability and optimal experimental design: Theory and application on the identification of reaction kinetics in chemical-looping combustion." Seminar at Lund University (2014), Lund, Sweden.
11. Han, L.; Zhou, Z.; Bollas, G.M. "Novel Reactor Concepts for Chemical-Looping Combustion." 4th International Conference on Chemical Looping (2014), Gothenburg, Sweden.
12. Han, L.; Zhou, Z.; Bollas, G.M. "Effect of Pore and Particle Size of Oxygen Carriers On Chemical-Looping Combustion and Reforming." Annual AIChE Meeting (2013), San Francisco, CA.
13. Han, L.; Zhou, Z.; Bollas, G.M. "Implementation of Optimal Experimental Design in Chemical-Looping Experimentation." Annual AIChE Meeting (2013), San Francisco, CA.
14. Zhou, Z.; Han, L.; Bollas, G.M. "An Overview of Chemical-Looping Reduction in Fixed-Bed and Fluidized Bed Reactors Focused On Oxygen Carrier Utilization and Reactor Efficiency." Annual AIChE Meeting (2013), San Francisco, CA.
15. Han, L. "CO_2 capture and chemical-looping breakthroughs." Universitas 21 Graduate Energy Conference (2013), Dublin, Ireland.
16. Han, L.; Zhou, Z.; Bollas, G.M. "Optimal Experimental Design of Fixed-Bed Chemical-Looping Combustion Systems." Annual ACS Meeting (2013), New Orleans, LA.

17. Han, L.; Zhou, Z.; Bollas, G.M. "Dynamic 2D Heterogeneous Model for Chemical-Looping Combustion in Fixed-bed Reactors." AIChE Annual Meeting (2012), Pittsburgh PA.

CONFERENCE POSTER PRESENTATIONS:

1. Such, K.D.; Chen, C.; Han, L.; Bollas, G.M. "Dynamic Simulation of a Combined Cycle Power Plant Integrated with Chemical-looing Combustion." Annual AIChE Meeting (2015), Salt Lake City, UT. **Recipient of the 2nd place award at the Student Poster Sessions of the 2015 AIChE Annual Meeting.**
2. Palmer, C.; Han, L.; Bollas, G.M. "Reactor Design and Analysis of a Simulated Moving Bed Reactor for Chemical-Looping Combustion" Annual AIChE Meeting (2014), Atlanta, GA. **Recipient of the 3rd place award at the Student Poster Session of the 2014 AIChE Annual Meeting.**
3. Han, L.; Zhou, Z.; Bollas, G.M. "Model-based design of experiments to achieve kinetic validation for chemical-looping systems." PSE Advanced Modeling Forum (2014), New York, NY.
4. Han, L.; Fischer, A.; Bollas, G.M. "Optimal Experimental Design of Chemical-Looping Combustion of Syngas in Fixed-Bed Reactors." AIChE Annual Meeting (2012), Pittsburgh PA.
5. Han, L.; Zhou, Z.; Du. S.; Bollas, G.M. "Biomass Chemical Looping with Oxygen Uncoupling." Chemical Engineering Approaches to Challenges in Energy and Biomedicine (2012), organized by New York Academy of Sciences, NY, NY.
6. Han, L.; Parnas, R.; Phelan, F. "Multi-Phase Reaction Modeling of Biodiesel Production using Cahn-Hilliard Approach." Universitas 21 Undergraduate Research Conference (2010), Melbourne, Australia

COPYRIGHT

REFERENCES

[1] B. Metz, O.R. Davidson, P.R. Bosch, R. Dave, L.A. Meyer, IPCC, 2007: Climate Change 2007: Mitigation. Contribution of Working Group III to the Fourth Assessment Report of the Intergovernmental Panel on Climate Change, Cambridge Univ. Press, Cambridge, U. K., 2007.

[2] T.A. Boden, G. Marland, R.J. Andres, Global, Regional, and National Fossil-Fuel CO2 Emissions, Oak Ridge, TN, 2010.

[3] P. Trans, R. Keeling, Trends in Atmospheric Carbon Dioxide, n.d. www.esrl.noaa.gov/gmd/ccgg/trends/.

[4] IPCC, IPCC Special Report on Carbon Dioxide Capture and Storage, Cambridge University Press, Cambridge, UK, 2005.

[5] International Energy Agency: Energy Technology Perspectives, 2012. http://www.iea.org/etp/publications/etp2012/.

[6] M. Zaman, J.H. Lee, Carbon capture from stationary power generation sources: A review of the current status of the technologies, Korean J. Chem. Eng. 30 (2013) 1497–1526.

[7] M.E. Boot-Handford, J.C. Abanades, E.J. Anthony, M.J. Blunt, S. Brandani, N. Mac Dowell, et al., Carbon capture and storage update, Energy Environ. Sci. 7 (2014) 130.

[8] H.J. Herzog, What future for carbon capture and sequestration?, Environ. Sci. Technol. 35 (2001).

[9] L. Fan, L. Zeng, W. Wang, S. Luo, Chemical looping processes for CO_2 capture and carbonaceous fuel conversion – prospect and opportunity, Energy Environ. Sci. 5 (2012) 7254.

[10] P. Markewitz, W. Kuckshinrichs, W. Leitner, J. Linssen, P. Zapp, R. Bongartz, et al., Worldwide innovations in the development of carbon capture technologies and the utilization of CO_2, Energy Environ. Sci. 5 (2012) 7281.

[11] S. Sivalingam, CO_2 separation by calcium looping from full and partial fuel oxidation processes, Technische Universität München, 2013.

[12] R. Naqvi, Analysis of Natural Gas-Fired Power Cycles with Chemical Looping Combustion for CO_2 Capture, Norwegian University of Science and Technology, 2006.

[13] M.B. Toftegaard, J. Brix, P.A. Jensen, P. Glarborg, A.D. Jensen, Oxy-fuel combustion of solid fuels, Prog. Energy Combust. Sci. 36 (2010) 581–625.

[14] J. Davison, Performance and costs of power plants with capture and storage of CO_2, Energy. 32 (2007) 1163–1176.

[15] P. Folger, Carbon Capture: A Technology Assessment, 2010.

[16] E.S. Rubin, H. Mantripragada, A. Marks, P. Versteeg, J. Kitchin, The outlook for improved carbon capture technology, Prog. Energy Combust. Sci. 38 (2012) 630–671.

[17] K. Damen, M. Van Troost, A. Faaij, W. Turkenburg, A comparison of electricity and hydrogen production systems with CO2 capture and storage. Part A: Review and selection of promising conversion and capture technologies, Prog. Energy Combust. Sci. 32 (2006) 215–246.

[18] P.H.M. Feron, C. A. Hendriks, CO_2 capture process principles and costs, Oil Gas Sci. Technol. 60 (2005) 451–459.

[19] B.J.P. Buhre, L.K. Elliott, C.D. Sheng, R.P. Gupta, T.F. Wall, Oxy-fuel combustion technology for coal-fired power generation, Prog. Energy Combust. Sci. 31 (2005) 283–307.

[20] T. DC, B. SM., Carbon dioxide capture for storage in deep geologic formationse-results from the CO_2 capture project, Vol 1-2, Elsevier, Oxkford, Uk, 2005.

[21] H.R. Kerr, Capture and separation technologies gaps and priority research needs, Carbon Dioxide Capture Storage Deep Geol. Form. - Results from CO_2 Capture Proj. 1 (2005) 655–660.

[22] C. Ekström, F. Schwendig, O. Biede, F. Franco, G. Haupt, G. de Koeijer, et al., Techno-Economic Evaluations and Benchmarking of Pre-combustion CO2 Capture and Oxy-fuel Processes Developed in the European ENCAP Project, Energy Procedia. 1 (2009) 4233–4240.

[23] J. Adanez, A. Abad, F. Garcia-Labiano, P. Gayan, L.F. De Diego, Progress in chemical-looping

combustion and reforming technologies, Prog. Energy Combust. Sci. 38 (2012) 215–282.
[24] J.D. Figueroa, T. Fout, S. Plasynski, H. McIlvried, R.D. Srivastava, Advances in CO_2 capture technology-The U.S. Department of Energy's Carbon Sequestration Program, Int. J. Greenh. Gas Control. 2 (2008) 9–20.
[25] H.J. Richter, K.F. Knoche, Reversibility of Combustion Processes, ACS Symp. Ser. Vol. 235. (1983) 71–85.
[26] M. Ishida, D. Zheng, T. Akehata, Evaluation of a chemical-looping-combustion power-generation system by graphic exergy analysis, Energy. 12 (1987) 147–154.
[27] I. Adánez-Rubio, P. Gayán, A. Abad, F. García-Labiano, L.F. De Diego, J. Adánez, CO2 capture in coal combustion by chemical-looping with oxygen uncoupling (CLOU) with a Cu-based oxygen-carrier, Proc. 5th Int Conf Clean Coal Technol. (2011).
[28] J. Wolf, CO_2 Mitigation in Advanced Power Cycles - Chemical Looping Combustion and Steam-Based Gasification, KTH-Royal Institute of Technology, 2004.
[29] M.M. Hossain, H.I. de Lasa, Chemical-looping combustion (CLC) for inherent CO_2 separations-a review, Chem. Eng. Sci. 63 (2008) 4433–4451.
[30] A. Lyngfelt, Oxygen carriers for chemical looping combustion -4000 h of operational experience, Oil Gas Sci. Technol. – Rev. IFP Energies Nouv. 66 (2011) 161–172.
[31] S. Nasr, K.P. Plucknett, Kinetics of Iron Ore Reduction by Methane for Chemical Looping Combustion, Energy & Fuels. 28 (2014) 1387–1395.
[32] A. Abad, J. Adánez, A. Cuadrat, F. García-Labiano, P. Gayán, L.F. de Diego, Kinetics of redox reactions of ilmenite for chemical-looping combustion, Chem. Eng. Sci. 66 (2011) 689–702.
[33] T. Mattisson, A. Lyngfelt, Applications of chemical-looping combustion with capture of CO_2, Second Nord. Minisymp. Carbon Dioxide Capture Storage. (2001) 46–51.
[34] E. Jerndal, T. Mattisson, A. Lyngfelt, Thermal Analysis of Chemical-Looping Combustion, Chem. Eng. Res. Des. 84 (2006) 795–806.
[35] Q. Zafar, A. Abad, T. Mattisson, B. Gevert, Reaction kinetics of freeze-granulated NiO/MgAl2O4 oxygen carrier particles for chemical-looping combustion, Energy & Fuels. 21 (2007) 610–618.
[36] M. Rydén, M. Johansson, A. Lyngfelt, T. Mattisson, NiO supported on Mg–ZrO2 as oxygen carrier for chemical-looping combustion and chemical-looping reforming, Energy Environ. Sci. 2 (2009) 970.
[37] E. Jerndal, T. Mattisson, I. Thijs, F. Snijkers, A. Lyngfelt, NiO particles with Ca and Mg based additives produced by spray- drying as oxygen carriers for chemical-looping combustion, Energy Procedia. 1 (2009) 479–486.
[38] T. Mattisson, E. Jerndal, C. Linderholm, A. Lyngfelt, Reactivity of a spray-dried $NiO/NiAl_2O_4$ oxygen carrier for chemical-looping combustion, Chem. Eng. Sci. 66 (2011) 4636–4644.
[39] E. Jerndal, T. Mattisson, I. Thijs, F. Snijkers, A. Lyngfelt, Investigation of $NiO/NiAl_2O_4$ oxygen carriers for chemical-looping combustion produced by spray-drying, Int. J. Greenh. Gas Control. 4 (2010) 23–35.
[40] C. Dueso, A. Abad, F. García-Labiano, L.F. De Diego, P. Gayán, J. Adánez, et al., Reactivity of a NiO/Al_2O_3 oxygen carrier prepared by impregnation for chemical-looping combustion, Fuel. 89 (2010) 3399–3409.
[41] P. Gayán, C. Dueso, A. Abad, J. Adanez, L.F. de Diego, F. García-Labiano, NiO/Al_2O_3 oxygen carriers for chemical-looping combustion prepared by impregnation and deposition–precipitation methods, Fuel. 88 (2009) 1016–1023.
[42] F. García-Labiano, L.F. de Diego, J. Adánez, A. Abad, P. Gayán, Reduction and Oxidation Kinetics of a Copper-Based Oxygen Carrier Prepared by Impregnation for Chemical-Looping Combustion, Ind. Eng. Chem. Res. 43 (2004) 8168–8177.
[43] M. Minnermann, B. Neumann, V. Zielasek, M. Bäumer, Alumina-promoted cobalt and iron xerogels as catalyst for the Fischer–Tropsch synthesis, Catal. Sci. Technol. 3 (2013) 3256.
[44] R. Villa, C. Cristiani, G. Groppi, L. Lietti, P. Forzatti, U. Cornaro, et al., Ni based mixed oxide materials for CH_4 oxidation under redox cycle conditions, J. Mol. Catal. A Chem. 204-205 (2003)

637–646.
[45] P. Gayán, I. Adánez-rubio, A. Abad, L.F. De Diego, F. García-labiano, J. Adánez, et al., Development of Cu-based oxygen carriers for Chemical-Looping with Oxygen Uncoupling (CLOU) process, Fuel. in press (2012) 226–238.
[46] C. Linderholm, A. Abad, T. Mattisson, A. Lyngfelt, 160h of chemical-looping combustion in a 10kW reactor system with a NiO-based oxygen carrier, Int. J. Greenh. Gas Control. 2 (2008) 520–530.
[47] M. Ishida, H. Jin, T. Okamoto, A Fundamental Study of a New Kind of Medium Material for Chemical-Looping Combustion, Energy & Fuels. 10 (1996) 958–963.
[48] M. Johansson, Screening of oxygen-carrier particles based on iron-, manganese-, cupper- and nickel oxides for use in chemical looping technologies, Screen. Oxyg. Part. Based Iron-, Manganese-, Copper-and Nickel Oxides Use Chem. Technol. (2007).
[49] J. Adánez, F. García-Labiano, L.F. de Diego, P. Gayán, J. Celaya, A. Abad, Nickel-copper oxygen carriers to reach zero CO and H_2 emissions in chemical-looping combustion, Ind. Eng. Chem. Res. 45 (2006) 2617–2625.
[50] M. Johansson, T. Mattisson, A. Lyngfelt, Creating a synergy effect by using mixed oxides of iron- and nickel oxides in the combustion of methane in a chemical-looping combustion reactor, Energy & Fuels. 20 (2006) 2399–2407.
[51] H. Jin, T. Okamoto, M. Ishida, Development of a novel chemical-looping combustion: Synthesis of a looping material with a double metal oxide of CoO-NiO, Energy & Fuels. 12 (1998) 1272–1277.
[52] M.M. Hossain, H.I. De Lasa, Reactivity and stability of Co-Ni/Al_2O_3 oxygen carrier in multicycle CLC, AIChE J. 53 (2007) 1817–1829.
[53] M.M. Hossain, K.E. Sedor, H.I. de Lasa, Co–Ni/Al_2O_3 oxygen carrier for fluidized bed chemical-looping combustion: Desorption kinetics and metal-support interaction, Chem. Eng. Sci. 62 (2007) 5464–5472.
[54] Y. Matsumura, T. Nakamori, Steam reforming of methane over nickel catalysts at low reaction temperature, Appl. Catal. A Gen. 258 (2004) 107–114.
[55] A.C.S.C. Teixeira, R. Giudici, Deactivation of steam reforming catalysts by sintering: experiments and simulation, Chem. Eng. Sci. 54 (1999) 3609–3618.
[56] P. Cho, T. Mattisson, A. Lyngfelt, Carbon formation on nickel and iron oxide-containing oxygen carriers for chemical-looping combustion, Ind. Eng. Chem. Res. 44 (2005) 668–676.
[57] J. Adánez, L.F. de Diego, F. García-Labiano, P. Gayán, A. Abad, J.M. Palacios, Selection of Oxygen Carriers for Chemical-Looping Combustion, Energy & Fuels. 18 (2004) 371–377.
[58] I. Iliuta, R. Tahoces, G.S. Patience, S. Rifflart, F. Luck, Chemical-looping combustion process: Kinetics and mathematical modeling, AIChE J. 56 (2010) 1063–1079.
[59] M. Ishida, H. Jin, A novel chemical-looping combustor without NOx formation, Ind. Eng. Chem. Res. 5885 (1996) 2469–2472.
[60] H. Jin, T. Okamoto, M. Ishida, Development of a novel chemical-looping combustion: Synthesis of a solid looping material of NiO/$NiAl_2O_4$, Ind. Eng. Chem. Res. 38 (1999) 126–132.
[61] H. Jin, M. Ishida, Novel gas turbine cycle with hydrogen-fueled chemical-looping combustion, Int. J. Hydrogen Energy. 25 (2000) 1209–1215.
[62] H. Jin, M. Ishida, Reactivity study on a novel hydrogen fueled chemical-looping combustion, Int. J. Hydrogen Energy. 26 (2001) 889–894.
[63] T. Mattisson, A. Jardnas, A. Lyngfelt, Reactivity of Some Metal Oxides Supported on Alumina with Alternating Methane and Oxygen-Application for Chemical-Looping Combustion, Energy Fuels. 17 (2003) 643–651.
[64] S.R. Son, S.D. Kim, Chemical-looping combustion with NiO and Fe_2O_3 in a thermobalance and circulating fluidized bed reactor with double loops, in: Ind. Eng. Chem. Res., 2006: pp. 2689–2696.
[65] F. García-Labiano, J. Adánez, L.F. de Diego, P. Gayán, A. Abad, Effect of Pressure on the

Behavior of Copper-, Iron-, and Nickel-Based Oxygen Carriers for Chemical-Looping Combustion, Energy & Fuels. 20 (2006) 26–33.
[66] P. Cho, T. Mattisson, A. Lyngfelt, Comparison of iron-, nickel-, copper- and manganese-based oxygen carriers for chemical-looping combustion, Fuel. 83 (2004) 1215–1225.
[67] P. Cho, T. Mattisson, A. Lyngfelt, Defluidization conditions for a fluidized bed of iron oxide-, nickel oxide-, and manganese oxide-containing oxygen carriers for chemical-looping combustion, Ind. Eng. Chem. Res. 45 (2006) 968–977.
[68] K.E. Sedor, M.M. Hossain, H.I. de Lasa, Reactivity and stability of Ni/Al_2O_3 oxygen carrier for chemical-looping combustion (CLC), Chem. Eng. Sci. 63 (2008) 2994–3007.
[69] K.E. Sedor, M.M. Hossain, H.I. de Lasa, Reduction kinetics of a fluidizable nickel–alumina oxygen carrier for chemical-looping combustion, Can. J. Chem. Eng. 86 (2008) 323–334.
[70] R. Villa, C. Cristiani, G. Groppi, L. Lietti, P. Forzatti, U. Cornaro, et al., Ni based mixed oxide materials for CH4 oxidation under redox cycle conditions, J. Mol. Catal. A Chem. 204-205 (2003) 637–646.
[71] M. Johansson, T. Mattisson, A. Lyngfelt, Use of $NiO/NiAl_2O_4$ Particles in a 10 kW Chemical-Looping Combustor, (2006) 5911–5919.
[72] L.F. de Diego, M. Ortiz, F. García-Labiano, J. Adánez, A. Abad, P. Gayán, Hydrogen production by chemical-looping reforming in a circulating fluidized bed reactor using Ni-based oxygen carriers, J. Power Sources. 192 (2009) 27–34.
[73] T. Mattisson, M. Johansson, A. Lyngfelt, The use of NiO as an oxygen carrier in chemical-looping combustion, Fuel. 85 (2006) 736–747.
[74] A. Abad, T. Mattisson, A. Lyngfelt, M. Rydén, Chemical-looping combustion in a 300 W continuously operating reactor system using a manganese-based oxygen carrier, Fuel. 85 (2006) 1174–1185.
[75] H.-J. Ryu, D.-H. Bae, G.-T. Jin, Effect of temperature on reduction reactivity of oxygen carrier particles in a fixed bed chemical-looping combustor, Korean J. Chem. Eng. 20 (2003) 960–966.
[76] M. Ishida, M. Yamamoto, T. Ohba, Experimental results of chemical-looping combustion with $NiO/NiAl_2O_4$ particle circulation at 1200 °C, Energy Convers. Manag. 43 (2002) 1469–1478.
[77] M. Rydén, A. Lyngfelt, T. Mattisson, Synthesis gas generation by chemical-looping reforming in a continuously operating laboratory reactor, Fuel. 85 (2006) 1631–1641.
[78] E. Jerndal, T. Mattisson, A. Lyngfelt, Investigation of Different $NiO/NiAl_2O_4$ Particles as Oxygen Carriers for Chemical-Looping Combustion, Energy & Fuels. 23 (2009) 665–676.
[79] P. Gayán, L.F. de Diego, F. García-Labiano, J. Adánez, A. Abad, C. Dueso, Effect of support on reactivity and selectivity of Ni-based oxygen carriers for chemical-looping combustion, Fuel. 87 (2008) 2641–2650.
[80] A. Shulman, C. Linderholm, T. Mattisson, A. Lyngfelt, High reactivity and mechanical durability of $NiO/NiAl_2O_4$ and $NiO/NiAl_2O_4/MgAl_2O_4$ oxygen carrier particles used for more than 1000 h in a 10 kW CLC reactor, Ind. Eng. Chem. Res. 48 (2009) 7400–7405.
[81] M.M. Hossain, H.I. de Lasa, Chemical-looping combustion (CLC) for inherent separations—a review, Chem. Eng. Sci. 63 (2008) 4433–4451.
[82] L.F. De Diego, F. García-Labiano, J. Adánez, P. Gayán, A. Abad, B.M. Corbella, et al., Development of Cu-based oxygen carriers for chemical-looping combustion, Fuel. 83 (2004) 1749–1757.
[83] Y. Cao, B. Casenas, W.-P. Pan, Investigation of chemical looping combustion by solid fuels. 2. Redox reaction kinetics and product characterization with coal, biomass, and solid waste as solid fuels and CuO as an oxygen carrier, Energy & Fuels. 20 (2006) 1845–1854.
[84] J. Ada, L.F. De Diego, F. Garcı, P. Gaya, A. Abad, M.L. Casta, Selection of Oxygen Carriers for Chemical-Looping Combustion, (2004) 371–377.
[85] J. Adánez, F. García-Labiano, L.F. De Diego, P. Gayán, J. Celaya, A. Abad, Nickel-copper oxygen carriers to reach zero CO and H_2 emissions in chemical-looping combustion, in: Ind. Eng. Chem. Res., 2006: pp. 2617–2625.

[86] B.M. Corbella, L.F. de Diego, F. García-Labiano, J. Adánez, J.M. Palacios, Performance in a fixed-bed reactor of titania-supported nickel oxide as oxygen carriers for the chemical-looping combustion of methane in multicycle tests, Ind. Eng. Chem. Res. 45 (2006) 157–165.
[87] B.M. Corbella, L.F. De Diego, F. García-Labiano, J. Adánez, J.M. Palaciost, J.M. Palacios, Characterization study and five-cycle tests in a fixed-bed reactor of titania-supported nickel oxide as oxygen carriers for the chemical-looping combustion of methane, Environ. Sci. Technol. 39 (2005) 5796–5803.
[88] L.F. de Diego, P. Gayán, F. García-Labiano, J. Celaya, A. Abad, J. Adánez, Impregnated CuO/Al_2O_3 oxygen carriers for chemical-looping combustion: Avoiding fluidized bed agglomeration, Energy and Fuels. 19 (2005) 1850–1856.
[89] F. García-Labiano, J. Adánez, L.F. de Diego, P. Gayán, A. Abad, Effect of pressure on the behavior of copper-, iron-, and nickel-based oxygen carriers for chemical-looping combustion, Energy and Fuels. 20 (2006) 26–33.
[90] S.Y. Chuang, J.S. Dennis, A.N. Hayhurst, S.A. Scott, Development and performance of Cu-based oxygen carriers for chemical-looping combustion, Combust. Flame. 154 (2008) 109–121.
[91] B.M. Corbella, L.F. de Diego, F. Garcia-Labiano, J. Adánez, J.M. Palacios, Characterization and Performance in a Multicycle Test in a Fixed-Bed Reactor of Silica-Supported Copper Oxide as Oxygen Carrier for Chemical-Looping Combustion of Methane, Energy & Fuels. 20 (2006) 148–154.
[92] Q. Zafar, T. Mattisson, B. Gevert, Integrated hydrogen and power production with CO_2 capture using chemical-looping reforming-redox reactivity of particles of CuO, Mn_2O_3, NiO, and Fe_2O_3 using SiO_2 as a support, Ind. Eng. Chem. Res. 44 (2005) 3485–3496.
[93] Q. Zafar, T. Mattisson, B. Gevert, Redox Investigation of Some Oxides of Transition-State Metals Ni , Cu , Fe , and Mn Supported on SiO_2 and $MgAl_2O_4$, Energy & Fuels. 20 (2006) 34–44.
[94] S.R. Son, K.S. Go, S.D. Kim, Thermogravimetric Analysis of Copper Oxide for Chemical-Looping Hydrogen Generation, Ind. Eng. Chem. Res. 48 (2009) 380–387.
[95] A. Tong, S. Bayham, M. V. Kathe, L. Zeng, S. Luo, L.-S. Fan, Iron-based syngas chemical looping process and coal-direct chemical looping process development at Ohio State University, Appl. Energy. 113 (2014) 1836–1845.
[96] S. Noorman, M. van Sint Annaland, Packed Bed Reactor Technology for Chemical-Looping Combustion, Ind. Eng. Chem. Res. 46 (2007) 4212–4220.
[97] I.M. Dahl, E. Bakken, Y. Larring, A.I. Spjelkavik, S.F. Håkonsen, R. Blom, On the development of novel reactor concepts for chemical looping combustion, Energy Procedia. 1 (2009) 1513–1519.
[98] Z. Zhao, T. Chen, A.F. Ghoniem, Rotary Bed Reactor for Chemical-looping Combustion with Carbon Capture. Part II: Base Case and Sensitivity Analysis, Energy & Fuels. 27 (2013) 344-359.
[99] Z. Zhao, T. Chen, A.F. Ghoniem, Rotary Bed Reactor for Chemical-Looping Combustion with Carbon Capture. Part 1: Reactor Design and Model Development, Energy & Fuels. 27 (2013) 327–343.
[100] A. Lyngfelt, B. Leckner, T. Mattisson, A fluidized-bed combustion process with inherent CO_2 separation; application of chemical-looping combustion, Chem. Eng. Sci. 56 (2001) 3101–3113.
[101] B. Kronberger, E. Johansson, G. Löffer, T. Mattisson, A. Lyngfelt, H. Hofbauer, A two-compartment fluidized bed reactor for CO_2 capture by chemical-looping combustion, Chem. Eng. Technol. 27 (2004) 1318–1326.
[102] B. Kronberger, A. Lyngfelt, G. Löffler, H. Hofbauer, Design and Fluid Dynamic Analysis of a Bench-Scale Combustion System with CO_2 Separation−Chemical-Looping Combustion, Ind. Eng. Chem. Res. 44 (2005) 546–556.
[103] P. Kolbitsch, T. Pröll, J. Bolhar-Nordenkampf, H. Hofbauer, J. Bolhàr-Nordenkampf, H. Hofbauer, et al., Design of a Chemical Looping Combustor using a Dual Circulating Fluidized Bed (DCFB) Reactor System, Chem. Eng. Technol. 32 (2009) 398–403.
[104] A. Lyngfelt, H. Thunman, Chemical-looping combustion: Design construction and 100 h of operational experience of a 10 kW prototype, in: D. Thomas (Ed.), Carbon Dioxide Capture

Storage Deep Geol. Form. from CO_2 Capture Proj. Vol. 1-Capture Sep. Carbon Dioxide from Combust., Elsevier, London, UK, 2004.
[105] H. Ryu, G. Jin, C. Yi, Demonstration of inherent CO_2 separation and no NO_x emission in a 50kW chemical-looping combustor: continuous reduction and oxidation experiment, in: Proc. 7th Int. Conf. Greenh. Gas Control Technol., Vancouver, 2004.
[106] F. Li, L.-S. Fan, Clean coal conversion processes – progress and challenges, Energy Environ. Sci. 1 (2008) 248-267.
[107] F. Li, L. Zeng, L.G. Velazquez-vargas, Z. Yoscovits, L. Fan, Syngas Chemical Looping Gasification Process : Bench-Scale Studies and Reactor Simulations, AIChE J. 56 (2010).
[108] H.P. Hamers, F. Gallucci, P.D. Cobden, E. Kimball, M. Van Sint Annaland, A novel reactor configuration for packed bed chemical-looping combustion of syngas, Int. J. Greenh. Gas Control. 16 (2013) 1–12.
[109] V. Spallina, F. Gallucci, M.C. Romano, P. Chiesa, G. Lozza, M. Van Sint Annaland, Investigation of heat management for CLC of syngas in packed bed reactors, Chem. Eng. J. 225 (2013) 174–191.
[110] V. Spallina, P. Chiesa, E. Martelli, F. Gallucci, M.C. Romano, G. Lozza, et al., Reactor design and operation strategies for a large-scale packed-bed CLC power plant with coal syngas, Int. J. Greenh. Gas Control. 36 (2015) 34–50.
[111] V. Spallina, M.C.C. Romano, P. Chiesa, F. Gallucci, M. van Sint Annaland, G. Lozza, Integration of coal gasification and packed bed CLC for high efficiency and near-zero emission power generation, Int. J. Greenh. Gas Control. 27 (2014) 28–41.
[112] S.F. Håkonsen, C.A. Grande, R. Blom, Rotating bed reactor for CLC: Bed characteristics dependencies on internal gas mixing, Appl. Energy. 113 (2014) 1952–1957.
[113] S.F. Håkonsen, R. Blom, Chemical looping combustion in a rotating bed reactor--finding optimal process conditions for prototype reactor., Environ. Sci. Technol. 45 (2011) 9619–26.
[114] C. Dueso, M. Ortiz, A. Abad, F. García-Labiano, L.F. De Diego, P. Gayán, et al., Reduction and oxidation kinetics of nickel-based oxygen-carriers for chemical-looping combustion and chemical-looping reforming, Chem. Eng. J. 188 (2012) 142–154.
[115] A. Abad, F. García-Labiano, L.F. de Diego, P. Gayán, J. Adánez, Reduction kinetics of Cu-, Ni-, and Fe-based oxygen carriers using syngas ($CO + H_2$) for chemical-looping combustion, Energy & Fuels. 21 (2007) 1843–1853.
[116] A. Cabello, P. Gayán, F. García-Labiano, L.F. de Diego, A. Abad, M.T. Izquierdo, et al., Relevance of the catalytic activity on the performance of a $NiO/CaAl_2O_4$ oxygen carrier in a CLC process, Appl. Catal. B Environ. 147 (2014) 980–987.
[117] H. Rashidi, H. Ale Ebrahim, B. Dabir, Application of random pore model for synthesis gas production by nickel oxide reduction with methane, Energy Convers. Manag. 74 (2013) 249–260.
[118] M. Ortiz, L.F. De Diego, A. Abad, F. García-Labiano, P. Gayán, J. Adánez, Catalytic Activity of Ni-Based Oxygen-Carriers for Steam Methane Reforming in Chemical-Looping Processes, Energy & Fuels. 26 (2012) 791–800.
[119] Z. Zhou, L. Han, G.M. Bollas, Model-based analysis of bench-scale fixed-bed units for chemical-looping combustion, Chem. Eng. J. 233 (2013) 331–348.
[120] H.J. Jun, M.-J. Park, S.-C. Baek, J.W. Bae, K.-S. Ha, K.-W. Jun, Kinetics modeling for the mixed reforming of methane over $Ni-CeO_2/MgAl_2O_4$ catalyst, J. Nat. Gas Chem. 20 (2011) 9–17.
[121] M. Johansson, T. Mattisson, A. Lyngfelt, A. Abad, Using continuous and pulse experiments to compare two promising nickel-based oxygen carriers for use in chemical-looping technologies, Fuel. 87 (2008) 988–1001.
[122] A. Abad, J. Adánez, F. García-Labiano, L.F. De Diego, P. Gayán, P. Kolbitsch, et al., CLC Modeling the fuel reactor at fast fluidization - Conversion of CH_4 using a NiO-based oxygen carrier in a 120 kW_{th} unit, in: Proc. 1st Int Conf Chem. Looping. Lyon, Fr., 2010.
[123] A. Abad, J. Adánez, F. García-Labiano, L.F. de Diego, P. Gayán, Modeling of the chemical-looping combustion of methane using a Cu-based oxygen-carrier, Combust. Flame. 157 (2010)

602–615.
[124] F.-X. Chiron, G.S. Patience, S. Rifflart, Kinetic mechanism derived through dosing reactants over NiO, Ni and Ni-C, Proc. 1st Int Conf Chem. Looping. (2010).
[125] T. Mattisson, M. Johansson, A. Lyngfelt, The use of NiO as an oxygen carrier in chemical-looping combustion, Fuel. 85 (2006) 736–747.
[126] T. Mendiara, J.M. Johansen, R. Utrilla, A.D. Jensen, P. Glarborg, Evaluation of different oxygen carriers for biomass tar reforming (II): Carbon deposition in experiments with methane and other gases, Fuel. 90 (2011) 1370–1382.
[127] M.K. Chandel, A. Hoteit, A. Delebarre, Experimental investigation of some metal oxides for chemical looping combustion in a fluidized bed reactor, Fuel. 88 (2009) 898–908.
[128] L. Han, Z. Zhou, G.M. Bollas, Heterogeneous modeling of chemical-looping combustion. Part 2: Particle model, Chem. Eng. Sci. 113 (2014) 116–128.
[129] J. Szekely, C.I. Lin, H.Y. Sohn, A structural model for gas-solid reactions with a moving boundary-V an experimental study of the reduction of porous nickel-oxide pellets with hydrogen, Chem. Eng. Sci. 28 (1973) 1975–1989.
[130] M.M. Hossain, M.R. Quddus, H.I. de Lasa, Reduction Kinetics of La Modified NiO/La-γAl_2O_3 Oxygen Carrier for Chemical-Looping Combustion, Ind. Eng. Chem. Res. 49 (2010) 11009–11017.
[131] M.M. Hossain, H.I. De Lasa, Reactivity and stability of Co-Ni/Al2O3 oxygen carrier in multicycle CLC, AIChE J. 53 (2007) 1817–1829.
[132] Z. Zhou, L. Han, G.M. Bollas, Kinetics of NiO reduction by H_2 and Ni oxidation at conditions relevant to chemical-looping combustion and reforming, Int. J. Hydrogen Energy. 39 (2014) 8535–8556.
[133] K. Mahalatkar, J. Kuhlman, E.D. Huckaby, T. O'Brien, CFD simulation of a chemical-looping fuel reactor utilizing solid fuel, Chem. Eng. Sci. 66 (2011) 3617–3627.
[134] J. Jung, I.K. Gamwo, Multiphase CFD-based models for chemical looping combustion process: Fuel reactor modeling, Powder Technol. 183 (2008) 401–409.
[135] Z. Deng, R. Xiao, B. Jin, Q. Song, Numerical simulation of chemical looping combustion process with $CaSO_4$ oxygen carrier, Int. J. Greenh. Gas Control. 3 (2009) 368–375.
[136] W. Shuai, Y. Yunchao, L. Huilin, X. Pengfei, S. Liyan, Computational Fluid Dynamic Simulation Based Cluster Structures-Dependent Drag Coefficient Model in Dual Circulating Fluidized Beds of Chemical Looping Combustion, Ind. Eng. Chem. Res. 51 (2012) 1396–1412.
[137] M. Xu, N. Ellis, C.J. Lim, H.-J. Ryu, Mapping of the operating conditions for an interconnected fluidized bed reactor for CO2 separation by chemical looping combustion, Chem. Eng. Technol. 32 (2009) 404–409.
[138] W. Shuai, L. Guodong, L. Huilin, C. Juhui, H.H. Yurong, W. Jiaxing, Fluid dynamic simulation in a chemical looping combustion with two interconnected fluidized beds, Fuel Process. Technol. 92 (2010) 385–393.
[139] M.M.M. Yazdanpanah, A. Forret, T. Gauthier, A. Delebarre, Modeling of CH_4 combustion with $NiO/NiAl_2O_4$ in a 10kWth CLC pilot plant, Appl. Energy. 113 (2014) 1933–1944.
[140] T.A. Brown, J.S. Dennis, S.A. Scott, J.F. Davidson, A.N. Hayhurst, Gasification and chemical-looping combustion of a lignite char in a fluidized bed of iron oxide, Energy & Fuels. 24 (2010) 3034–3048.
[141] Z. Zhou, L. Han, G.M. Bollas, Model-assisted analysis of fluidized bed chemical-looping reactors, Chem. Eng. Sci. 134 (2015) 619–631.
[142] Z. Zhou, L. Han, O. Nordness, G.M. Bollas, Continuous regime of chemical looping combustion (CLC) and chemical-looping with oxygen uncoupling (CLOU) reactivity of CuO oxygen carriers, Appl. Catal. B Environ. 166-167 (2015) 132–144.
[143] J. Wolf, M. Anheden, J. Yan, Comparison of nickel- and iron-based oxygen carriers in chemical looping combustion for CO_2 capture in power generation, Fuel. 84 (2005) 993–1006.
[144] S. Consonni, G. Lozza, G. Pelliccia, S. Rossini, F. Saviano, Chemical-Looping Combustion for

Combined Cycles With CO_2 Capture, J. Eng. Gas Turbines Power. 128 (2006) 525.
[145] R. Naqvi, O. Bolland, Multi-stage chemical looping combustion (CLC) for combined cycles with CO_2 capture, Int. J. Greenh. Gas Control. 1 (2007) 19–30.
[146] S. Consonni, G. Lozza, G. Pelliccia, S. Rossini, F. Saviano, Chemical-looping combustion for combined cycles with CO_2 capture, J. Eng. Gas Turbines Power. 128 (2006) 525–534.
[147] G. Lozza, P. Chiesa, M. Romano, P. Savoldelli, Three Reactors Chemical Looping Combustion for High Efficiency Electricity Generation With CO2 Capture From Natural Gas, in: ASME Turbo Expo 2006 Power Land, Sea, Air, Barcelona, Spain, 2006: pp. 77–87.
[148] P. Chiesa, G. Lozza, A. Malandrino, M. Romano, V. Piccolo, Three-reactors chemical looping process for hydrogen production, Int. J. Hydrogen Energy. 33 (2008) 2233–2245.
[149] B. Erlach, M. Schmidt, G. Tsatsaronis, Comparison of carbon capture IGCC with pre-combustion decarbonisation and with chemical-looping combustion, Energy. 36 (2011) 3804–3815.
[150] S. Rezvani, Y. Huang, D. McIlveen-Wright, N. Hewitt, J.D. Mondol, Comparative assessment of coal fired IGCC systems with CO_2 capture using physical absorption, membrane reactors and chemical looping, Fuel. 88 (2009) 2463–2472.
[151] V. Spallina, M.C. Romano, P. Chiesa, G. Lozza, Integration of Coal Gasification and Packed Bed CLC process for High Efficiency and Near-zero Emission Power Generation, Energy Procedia. 37 (2013) 662–670.
[152] M. Sorgenfrei, G. Tsatsaronis, Design and evaluation of an IGCC power plant using iron-based syngas chemical-looping (SCL) combustion, Appl. Energy. 113 (2014) 1958–1964.
[153] A.H. Sahir, J.S. Lighty, H.Y. Sohn, Kinetics of Copper Oxidation in the Air Reactor of a Chemical Looping Combustion System using the Law of Additive Reaction Times, Ind. Eng. Chem. Res. 50 (2011) 13330–13339.
[154] S. Noorman, F. Gallucci, M. Van Sint Annaland, J.A.M. Kuipers, A theoretical investigation of CLC in packed beds. Part 1: Particle model, Chem. Eng. J. 167 (2011) 297–307.
[155] S. Noorman, F. Gallucci, M.van Sint Annaland, J.A.M. Kuipers, A theoretical investigation of CLC in packed beds. Part 2: Reactor model, Chem. Eng. J. 167 (2011) 369–376.
[156] F. García-Labiano, L.F. De Diego, J. Adánez, A. Abad, P. Gayán, Temperature variations in the oxygen carrier particles during their reduction and oxidation in a chemical-looping combustion system, Chem. Eng. Sci. 60 (2005) 851–862.
[157] A. Lyngfelt, B. Leckner, T. Mattisson, A fluidized-bed combustion process with inherent CO_2 separation; application of chemical-looping combustion, Chem. Eng. Sci. 56 (2001) 3101–3113.
[158] Z. Ilsen Önsan, A.K. Avci, Reactor Design for Fuel Processing, 2011. In: Fuel Cells: Technologies for Fuel Processing, 451-516.
[159] K.B. Bischoff, O. Levenspiel, Fluid dispersion—generalization and comparison of mathematical models—II comparison of models, Chem. Eng. Sci. 17 (1962) 257–264.
[160] J.O. Wilkes, Fluid mechanics for chemical engineers, 1999.
[161] E.A. Foumeny, M.A. Chowdhury, C. McGreavy, J.A.A. Castro, Estimation of Dispersion Coefficients in Packed Beds, Chem. Eng. Techology. 15 (1992) 161–181.
[162] M.E. Davis, R.J. Davis, Fundamentals of Chemical Reaction Engineering, 2003.
[163] S. Yagi, D. Kunii, N. Wakao, Studies on axial effective thermal conductivities in packed beds, AIChE J. 6 (1960) 543–546.
[164] S. Yagi, N. Wakao, Heat and mass transfer from wall to fluid in packed beds, AIChE J. 5 (1959) 79–85.
[165] N. Wako, S. Kaguei, T. Funazkri, Effect of fluid dispersion coefficients on particle-to-fluid heat transfer coefficients in packed beds: Correlation of nusselt numbers, Chem. Eng. Sci. 34 (1979) 325–336.
[166] P.E. Peters, R.S. Schiffino, P. Harriott, Heat transfer in packed-tube reactors, Ind. Eng. Chem. Res. 27 (1988) 226–233.
[167] C.N. Scatterfield, Mass Transfer in Heterogeneous Catalysis, 2nd ed., 1981.
[168] A.S. Pushnov, Calculation of average bed porosity, Chem. Pet. Eng. 42 (2006) 14–17.

[169] H.S. Fogler, Elements of chemical reaction engineering, 4th ed., 2005.
[170] Process Systems Enterprise Limited, gPROMS, (2015).
[171] H. Jin, M. Ishida, Reactivity Study on Natural-Gas-Fueled Chemical-Looping Combustion by a Fixed-Bed Reactor, Ind. Eng. Chem. Res. 41 (2002) 4004–4007.
[172] M. Rydén, A. Lyngfelt, T. Mattisson, D. Chen, A. Holmen, E. Bjørgum, Novel oxygen-carrier materials for chemical-looping combustion and chemical-looping reforming; $La_xSr_{1-x}Fe_yCo_{1-y}O_{3-\delta}$ perovskites and mixed-metal oxides of NiO, Fe_2O_3 and Mn_3O_4, Int. J. Greenh. Gas Control. 2 (2008) 21–36.
[173] L.-S. Fan, Chemical Looping Systems for Fossil Energy Conversions, 2011.
[174] H.A. Jakobsen, Fixed Bed Reactors, 2011.
[175] M. Johansson, T. Mattisson, A. Lyngfelt, Comparison of oxygen carriers for chemical-looping combustion, Therm. Sci. 10 (2006) 93–107.
[176] M. Johansson, T. Mattisson, M. Rydén, A. Lyngfelt, Carbon Capture via Chemical-Looping Combustion and Reforming Chemical-Looping Combustion, in: Int. Semin. Carbon Sequestration Clim. Chang., Rio de Janeiro, 2006.
[177] A.M. Diskin, R.H. Cunningham, R.M. Ormerod, The oxidative chemistry of methane over supported nickel catalysts, Catal. Today. 46 (1998) 147–154.
[178] H. Roh, K. Jun, W. Dong, S. Park, Y. Joe, Partial Oxidation of Methane over Ni/θ-Al2O3 Catalysts, Chem. Lett. (2001) 3–4.
[179] Y. Lu, J. Xue, C. Yu, Y. Liu, S. Shen, Mechanistic investigations on the partial oxidation of methane to synthesis gas over a nickel-on-alumina catalyst, Appl. Catal. A Gen. 174 (1998) 121–128.
[180] V.A. Tsipouriari, Z. Zhang, X.E. Verykios, Catalytic Partial Oxidation of Methane to Synthesis Gas over Ni-Based Catalysts: 1. Catalyst Performance Characteristics, J. Catal. 291 (1998) 283–291.
[181] Y. Zhang, G. Xiong, S. Sheng, W. Yang, Deactivation studies over $NiO/\gamma\text{-}Al_2O_3$ catalysts for partial oxidation of methane to syngas, Catal. Today. 63 (2000) 517–522.
[182] K. Schulze, W. Makowski, R. Chyzy, Nickel doped hydrotalcites as catalyst precursors for the partial oxidation of light paraffins, Appl. Clay Sci. 18 (2001) 59–69.
[183] J.I. Villacampa, C. Royo, E. Romeo, J.A. Montoya, P. Del Angel, a. Monzón, Catalytic decomposition of methane over Ni-Al2O3 coprecipitated catalysts, Appl. Catal. A Gen. 252 (2003) 363–383.
[184] T. Mattisson, M. Johansson, E. Jerndal, A. Lyngfelt, The reaction of $NiO/NiAl_2O_4$ particles with alternating methane and oxygen, Can. J. Chem. Eng. 86 (2008) 756–767.
[185] C. Linderholm, T. Mattisson, A. Lyngfelt, Long-term integrity testing of spray-dried particles in a 10-kW chemical-looping combustor using natural gas as fuel, Fuel. 88 (2009) 2083–2096.
[186] J.-I. Baek, J.-W. Kim, J.B. Lee, T.H. Eom, J. Ryu, C.K. Ryu, et al., Effects of support on the performance of NiO-Based oxygen carriers , Eff. Du Support Sur Les Performances Matériaux Transp. D'oxygène à Base D'oxyde Nickel. 66 (2011) 223–234.
[187] C. Dueso, A. Abad, F. García-Labiano, L.F. de Diego, P. Gayán, J. Adánez, et al., Reactivity of a NiO/Al_2O_3 oxygen carrier prepared by impregnation for chemical-looping combustion, Fuel. 89 (2010) 3399–3409.
[188] P. Ollero, a. Serrera, R. Arjona, S. Alcantarilla, Diffusional effects in TGA gasification experiments for kinetic determination q, Fuel. 81 (2002) 1989–2000.
[189] T. a. a. Utigard, M. Wu, G. Plascencia, T. Marin, Reduction kinetics of Goro nickel oxide using hydrogen, Chem. Eng. Sci. 60 (2005) 2061–2068.
[190] R. Chatterjee, S. Banerjee, S. Banerjee, D. Ghosh, Reduction of Nickel Oxide Powder and Pellet by Hydrogen, Trans. Indian Inst. Met. 65 (2012) 265–273.
[191] N.L. Galinsky, Y. Huang, A. Shafiefarhood, F. Li, Iron Oxide with Facilitated O 2– Transport for Facile Fuel Oxidation and CO_2 Capture in a Chemical Looping Scheme, ACS Sustain. Chem. Eng. 1 (2013) 364–373.

[192] A. Gómez-Barea, P. Ollero, R. Arjona, Reaction-diffusion model of TGA gasification experiments for estimating diffusional effects, Fuel. 84 (2005) 1695–1704.
[193] L. Han, Z. Zhou, G.M. Bollas, Heterogeneous modeling of chemical-looping combustion. Part 1: Reactor model, Chem. Eng. Sci. 104 (2013) 233–249.
[194] R.B. Bird, W.E. Stewart, E.N. Lightfoot, Transport Phenomena, 2nd ed., John Wiley & Sons, Inc., 2007.
[195] G. Pantoleontos, E.S. Kikkinides, M.C. Georgiadis, A heterogeneous dynamic model for the simulation and optimisation of the steam methane reforming reactor, Int. J. Hydrogen Energy. (2012) 1–13.
[196] E. Johansson, T. Mattisson, A. Lyngfelt, H. Thunman, Combustion of syngas and natural gas in a 300 W chemical-looping combustor, Chem. Eng. Res. Des. 84 (2006) 819–827.
[197] J. Adánez, C. Dueso, L.F. De Diego, F. García-Labiano, P. Gayán, A. Abad, Methane combustion in a 500 Wth chemical-looping combustion system using an impregnated ni-based oxygen carrier, Energy and Fuels. 23 (2009) 130–142.
[198] L.F. de Diego, M. Ortiz, J. Adánez, F. García-Labiano, A. Abad, P. Gayán, Synthesis gas generation by chemical-looping reforming in a batch fluidized bed reactor using Ni-based oxygen carriers, Chem. Eng. J. 144 (2008) 289–298.
[199] J. Adanez, F. García-Labiano, L.F. de Diego, P. Gayán, J. Celaya, A. Abad, Characterization of oxygen carriers for chemical-looping combustion, 7th Int. Conf. Greenh. Gas Technol. 18 (2004) 9.
[200] T. Mattisson, M. Johansson, A. Lyngfelt, Multicycle reduction and oxidation of different types of iron oxide particles-application to chemical-looping combustion, Energy & Fuels. 18 (2004) 628–637.
[201] L.F. de Diego, F. García-Labiano, J. Adánez, P. Gayán, A. Abad, B.M. Corbella, et al., Development of Cu-based oxygen carriers for chemical-looping combustion, Fuel. 83 (2004) 1749–1757.
[202] E. Jerndal, T. Mattisson, A. Lyngfelt, Investigation of Different $NiO/NiAl_2O_4$ Particles as Oxygen Carriers for Chemical-Looping Combustion, Energy & Fuels. 94 (2009) 665–676.
[203] A. Shulman, C. Linderholm, T. Mattisson, A. Lyngfelt, High Reactivity and Mechanical Durability of $NiO/NiAl_2O_4$ and $NiO/NiAl_2O_4/MgAl_2O_4$ Oxygen Carrier Particles Used for more than 1000 h in a 10 kW CLC Reactor, Ind. Eng. Chem. Res. 48 (2009) 7400–7405.
[204] A. Fossdal, E. Bakken, B.A. Øye, C. Schøning, I. Kaus, T. Mokkelbost, et al., Study of inexpensive oxygen carriers for chemical looping combustion, Int. J. Greenh. Gas Control. 5 (2011) 483–488.
[205] S. Zhang, C. Saha, Y. Yang, S. Bhattacharya, R. Xiao, Use of Fe_2O_3-Containing Industrial Wastes As the Oxygen Carrier for Chemical-Looping Combustion of Coal: Effects of Pressure and Cycles, Energy & Fuels. 25 (2011) 4357–4366.
[206] H. Gu, L. Shen, J. Xiao, S. Zhang, T. Song, Chemical Looping Combustion of Biomass/Coal with Natural Iron Ore as Oxygen Carrier in a Continuous Reactor, Energy & Fuels. 25 (2011) 446–455.
[207] H. Leion, T. Mattisson, A. Lyngfelt, Use of Ores and Industrial Products As Oxygen Carriers in Chemical-Looping Combustion, Energy & Fuels. 23 (2009) 2307–2315.
[208] T. Pröll, K. Mayer, J. Bolhàr-Nordenkampf, P. Kolbitsch, T. Mattisson, A. Lyngfelt, et al., Natural minerals as oxygen carriers for chemical looping combustion in a dual circulating fluidized bed system, Energy Procedia. 1 (2009) 27–34.
[209] M. Schwaab, L.P. Lemos, J.C. Pinto, Optimum reference temperature for reparameterization of the Arrhenius equation. Part 2: Problems involving multiple reparameterizations, Chem. Eng. Sci. 63 (2008) 2895–2906.
[210] H. Leion, A. Lyngfelt, M. Johansson, E. Jerndal, T. Mattisson, The use of ilmenite as an oxygen carrier in chemical-looping combustion, Chem. Eng. Res. Des. 86 (2008) 1017–1026.
[211] H. Leion, E. Jerndal, B.-M. Steenari, S. Hermansson, M. Israelsson, E. Jansson, et al., Solid fuels in chemical-looping combustion using oxide scale and unprocessed iron ore as oxygen carriers,

Fuel. 88 (2009) 1945–1954.
[212] M.M. Yazdanpanah, A. Forret, T. Gauthier, A. Delebarre, Modeling of CH_4 combustion with $NiO/NiAl_2O_4$ in a $10kW_{th}$ CLC pilot plant, Appl. Energy. 113 (2014) 1933–1944.
[213] A. Cabello, P. Gayán, F. García-Labiano, L.F. de Diego, A. Abad, M.T. Izquierdo, et al., Relevance of the catalytic activity on the performance of a $NiO/CaAl_2O_4$ oxygen carrier in a CLC process, Appl. Catal. B Environ. 147 (2014) 980–987.
[214] M.M. Hossain, H.I. de Lasa, Reduction and oxidation kinetics of Co-Ni/Al_2O_3 oxygen carrier involved in a chemical-looping combustion cycles, Chem. Eng. Sci. 65 (2010) 98–106.
[215] H.-J. Ryu, D.-H. Bae, K.-H. Han, S.-Y. Lee, G.-T. Jin, J.-H. Choi, Oxidation and reduction characteristics of oxygen carrier particles and reaction kinetics by unreacted core model, Korean J. Chem. Eng. 18 (2001) 831–837.
[216] M. Ortiz, A. Abad, L.F. De Diego, F. García-Labiano, P. Gayán, J. Adánez, Optimization of hydrogen production by Chemical-Looping auto-thermal Reforming working with Ni-based oxygen-carriers, Int. J. Hydrogen Energy. 36 (2011) 9663–9672.
[217] A. Abad, J. Adánez, F. García-Labiano, L.F. de Diego, P. Gayán, J. Celaya, Mapping of the range of operational conditions for Cu-, Fe-, and Ni-based oxygen carriers in chemical-looping combustion, Chem. Eng. Sci. 62 (2007) 533–549.
[218] M.R. Rahimpour, M. Hesami, M. Saidi, A. Jahanmiri, M. Farniaei, M. Abbasi, Methane Steam Reforming Thermally Coupled with Fuel Combustion: Application of Chemical Looping Concept as a Novel Technology, Energy & Fuels. 27 (2013) 2351–2362.
[219] J. Xu, G.F. Froment, Methane steam reforming, methanation and water-gas shift: I. Intrinsic kinetics, AIChE J. 35 (1989) 88–96.
[220] K. Hou, R. Hughes, The kinetics of methane steam reforming over a Ni/α-Al_2O catalyst, Chem. Eng. J. 82 (2001) 311–328.
[221] J. Klose, M. Baerns, Kinetics of the methanation of carbon monoxide on an alumina-supported nickel catalyst, J. Catal. 85 (1984) 105–116.
[222] R.W. Atherton, R.B. Schainker, E.R. Ducot, On the statistical sensitivity analysis of models for chemical kinetics, AIChE J. 21 (1975) 441–448.
[223] P. Heidebrecht, K. Sundmacher, L.T. Biegler, Optimal design of nonlinear temperature programmed reduction experiments, AIChE J. 57 (2011) 2888–2901.
[224] Z.R. Lazic, Design of Experiments in Chemical Engineering: A Practical Guide, Wiley-VCH, Weinheim, Germany, 2004.
[225] G.E.P. Box, N.R. Draper, Empirical Model-Building and Response Surfaces, 1st ed., Wiley, New York, 1987.
[226] G.E.P. Box, J.S. Hunter, W.G. Hunter, Statistics for Experimenters: An Introduction to Design, Data Analysis, and Model Building, Wiley, New York, 1978.
[227] A.C. Atkinson, A.N. Donev, Optimum Experimental Designs, Oxford University Press, New York, 1992.
[228] G. Vicente, a Coteron, M. Martinez, J. Aracil, Application of the factorial design of experiments and response surface methodology to optimize biodiesel production, Ind. Crops Prod. 8 (1998) 29–35.
[229] M.A. Dias, C.A. Rosa, V.L.R. Linardi, R.A. Conte, H.F. de Castro, H.F. De Castro, Application of factorial design to study of heavy metals biosorption by waste biomass from beverage distillery., Appl. Biochem. Biotechnol. 91-93 (2001) 413–422.
[230] J. Chen, K. Wang, Sequential Experimental Design Strategy for Optimal Batch Profiles Using Hybrid Function Approximations, Ind. Eng. Chem. Res. 43 (2004) 5260–5274.
[231] I. a M. Swinnen, K. Bernaerts, K. Gysemans, J.F. Van Impe, Quantifying microbial lag phenomena due to a sudden rise in temperature: a systematic macroscopic study., Int. J. Food Microbiol. 100 (2005) 85–96.
[232] G. Franceschini, S. Macchietto, Model-based design of experiments for parameter precision: State of the art, Chem. Eng. Sci. 63 (2008) 4846–4872.

[233] G.F. Froment, L.H. Hosten, Catalytic kinetics: Modelling, in: J.R. Anderson, M. Boudart (Eds.), Catal. Sci. Technol., Springer-Verlag, 1981.
[234] G.E.P. Box, W.G. Hunter, The Experimental Study of Physical Mechanisms, Technometrics. 7 (1965) 23–42.
[235] N.R. Draper, W.G. Hunter, The use of prior distributions in the design of experiments for parameter estimation in non-linear situations: multiresponse case., Biometrika. 54 (1967) 662–665.
[236] N.R. Draper, W.G. Hunter, Design of Experiments for Parameter Estimation in Multiresponse Situations, Biometrika. 53 (1966) 525–533.
[237] W.G. Hunter, W.J. Hill, T.L. Henson, Designing experiments for precise estimation of all or some of the constants in a mechanistic model, Can. J. Chem. Eng. 47 (1969) 76–80.
[238] R.K. Mehra, Optimal Input Signals for Parameter Estimation in Dynamic Systems-Survey and New Results, IEEE Trans. Automat. Contr. 19 (1974) 753–768.
[239] R.W. Shirt, T.J. Harris, D.W. Bacon, Experimental Design Considerations for Dynamic Systems, Ind. Eng. Chem. Res. 33 (1994) 2656–2667.
[240] D. Espie, S. Macchietto, The optimal design of dynamic experiments, AIChE J. 35 (1989) 223–229.
[241] S.P. Asprey, S. Macchietto, Statistical tools for optimal dynamic model building, Comput. Chem. Eng. 24 (2000) 1261–1267.
[242] L. Benabbas, S.P. Asprey, S. Macchietto, Curvature-based methods for designing optimally informative experiments in multiresponse nonlinear dynamic situations, Ind. Eng. Chem. Res. 44 (2005) 7120–7131.
[243] F. Galvanin, M. Barolo, S. Macchietto, F. Bezzo, Optimal Design of Clinical Tests for the Identification of Physiological Models of Type 1 Diabetes Mellitus, Ind. Eng. Chem. Res. 48 (2009) 1989–2002.
[244] A. Munack, Optimal Feeding Strategy for Identification of Monod-Type Models by Fed-Batch Experiments, in: N.M. Fish, R.I. Fox, N.F. Thornhill (Eds.), Comput. Appl. Ferment. Technol. Model. Control Biotechnol. Process., Springer Netherlands, 1989: pp. 195–204.
[245] P.A. Vanrolleghem, M. van Daele, D. Dochain, Practical identifiability of a biokinetic model of activated sludge respiration, Water Res. 29 (1995) 2561–2570.
[246] A. Holmberg, On the practical identifiability of microbial growth models incorporating Michaelis-Menten type nonlinearities, Math. Biosci. 62 (1982) 23–43.
[247] F.R. Sidoli, A. Mantalaris, S.P. Asprey, Toward global parametric estimability of a large-scale kinetic single-cell model for mammalian cell cultures, Ind. Eng. Chem. Res. 44 (2005) 868–878.
[248] F. Galvanin, A. Boschiero, M. Barolo, F. Bezzo, Model-Based Design of Experiments in the Presence of Continuous Measurement Systems, Ind. Eng. Chem. Res. 50 (2011) 2167–2175.
[249] G. Franceschini, S. Macchietto, Novel Anticorrelation Criteria for Model-Based Experiment Design: Theory and Formulations, AIChE J. 54 (2008) 1009–1024.
[250] M. Brendel, W. Marquardt, Experimental design for the identification of hybrid reaction models from transient data, Chem. Eng. J. 141 (2008) 264–277.
[251] M.D. Hoang, T. Barz, V.A. Merchan, L.T. Biegler, H. Arellano-Garcia, Simultaneous solution approach to model-based experimental design, AIChE J. 59 (2013) 4169–4183.
[252] B.H. Chen, S.P. Asprey, On the Design of Optimally Informative Dynamic Experiments for Model Discrimination in Multiresponse Nonlinear Situations, Ind. Eng. Chem. Res. 42 (2003) 1379–1390.
[253] M. Rodriguez-Fernandez, P. Mendes, J.R. Banga, A hybrid approach for efficient and robust parameter estimation in biochemical pathways., Biosystems. 83 (2006) 248–265.
[254] S. Žaković, B. Rustem, S.P. Asprey, A parallel algorithm for semi-infinite programming, Comput. Stat. Data Anal. 44 (2003) 377–390.
[255] T. Barz, H. Arellano-Garcia, G. Wozny, Handling Uncertainty in Model-Based Optimal Experimental Design, Ind. Eng. Chem. Res. 49 (2010) 5702–5713.

[256] J.A. Francesconi, M.C. Mussati, P.A. Aguirre, Analysis of design variables for water-gas-shift reactors by model-based optimization, J. Power Sources. 173 (2007) 467–477.
[257] C. Michalik, T. Schmidt, M. Zavrel, M. Ansorge-Schumacher, A. Spiess, W. Marquardt, Application of the incremental identification method to the formate oxidation using formate dehydrogenase, Chem. Eng. Sci. 62 (2007) 5592–5597.
[258] A. Vikhansky, Numerical analysis of the global identifiability of reaction–diffusion systems, Comput. Chem. Eng. 35 (2011) 1978–1982.
[259] A. Yang, E. Martin, G. Montague, J. Morris, Optimal experimental design for the precision of a subset of model parameters in process development, in: W. Markquardt, C. Pantelides (Eds.), 16th Eur. Symp. Comput. Aided Process Eng. 9th Int. Symp. Process Syst. Eng., Elsevier B.V., 2006: pp. 563–568.
[260] A.C. Atkinson, B. Bogacka, D- and Ds-Optimum Compound Designs for the Order of a Chemical Determining Reaction, Technometrics. 39 (1997) 347–356.
[261] G. Franceschini, S. Macchietto, Anti-Correlation Approach to Model-Based Experiment Design: Application to a Biodiesel Production Process, Ind. Eng. Chem. Res. 47 (2008) 2331–2348.
[262] G. Franceschini, S. Macchietto, Validation of a Model for Biodiesel Production through Model-Based Experiment Design, Ind. Eng. Chem. Res. 46 (2007) 220–232. doi:10.1021/ie060758c.
[263] C. Han, K. Chaloner, Bayesian Experimental Design for Nonlinear Mixed-Effects Models with Application to HIV Dynamics, Biometrics. 60 (2004) 25–33.
[264] P. Vajjah, S.B. Duffull, A generalisation of T-optimality for discriminating between competing models with an application to pharmacokinetic studies., Pharm. Stat. 11 (2012) 503–510.
[265] M. Zavrel, C. Michalik, T. Schwendt, T. Schmidt, M. Ansorge-Schumacher, C. Janzen, et al., Systematic determination of intrinsic reaction parameters in enzyme immobilizates, Chem. Eng. Sci. 65 (2010) 2491–2499.
[266] F. Galvanin, S. Macchietto, F. Bezzo, V. Pado, V. Marzolo, Model-Based Design of Parallel Experiments, Ind. Eng. Chem. Res. 46 (2007) 871–882.
[267] L. Zivanović, A. Licanski, M. Zecević, B. Jocić, M. Kostić, Application of experimental design in optimization of solid phase extraction of mycophenolic acid and mycophenolic acid glucuronide from human urine and plasma and SPE-RP-HPLC method validation., J. Pharm. Biomed. Anal. 47 (2008) 575–585.
[268] M. Brendel, D. Bonvin, W. Marquardt, Incremental identification of kinetic models for homogeneous reaction systems, Chem. Eng. Sci. 61 (2006) 5404–5420.
[269] M.P. Saccomani, S. Audoly, L. D'Angiò, Parameter identifiability of nonlinear systems: the role of initial conditions, Automatica. 39 (2003) 619–632.
[270] O.-T. Chis, J.R. Banga, E. Balsa-Canto, Structural Identifiability of Systems Biology Models: A Critical Comparison of Methods, PLoS One. 6 (2011) e27755.
[271] H. Miao, X. Xia, A.S. Perelson, H. Wu, On Identifiability of Nonlinear Ode Models and Applications in Viral Dynamics, SIAM Rev. Soc. Ind. Appl. Math. 53 (2011) 3–39.
[272] L. Ljung, T. Glad, On Global Identifiability for Arbitrary Model Parametrizations, Automatica. 30 (1994) 265–276.
[273] A. Saltelli, M. Ratto, S. Tarantola, F. Campolongo, Sensitivity analysis for chemical models, Chem. Rev. 105 (2005) 2811–2827.
[274] J. Guedj, R. Thiébaut, D. Commenges, Practical identifiability of HIV dynamics models., Bull. Math. Biol. 69 (2007) 2493–2513.
[275] L. Denis-Vidal, G. Joly-blanchard, An Easy to Check Criterion for (Un)identifiability of Uncontrolled Systems and Its Applications, IEEE Trans. Autom. Control Autom. Control. 45 (2000) 768–771.
[276] L. Denis-Vidal, G. Joly-Blanchard, C. Noiret, Some effective approaches to check the identifiability of uncontrolled nonlinear systems, Math. Comput. Simul. 57 (2001) 35–44.
[277] E. Walter, I. Braems, L. Jaulin, M. Kieffer, Guaranteed Numerical Computation as an Alternative to Computer Algebra for Testing Models for Identifiability, in: R. Alt, A. Frommer, R.B. Keafott,

W. Luther (Eds.), Numer. Softw. with Result Verif., Springer Berlin Heidelberg, Dagstuhl Castle, 2004: pp. 124–131.
[278] H. Pohjanpalo, System identifiability based on the power series expansion of the solution, Math. Biosci. 41 (1978) 21–33.
[279] E. Walter, Y. Lecourtier, Global approaches to identifiability testing for linear and nonlinear state space models, Math. Comput. Simul. 24 (1982) 472–482.
[280] M.J. Chappell, K.R. Godfrey, Structural identifiability of the parameters of a nonlinear batch reactor model, Math. Biosci. 108 (1992) 241–251.
[281] S. Vajda, K.R. Godfrey, H. Rabitz, Similarity transformation approach to identifiability analysis of nonlinear compartmental models, Math. Biosci. 93 (1989) 217–248.
[282] G. Margaria, E. Riccomagno, M.J. Chappell, H.P. Wynn, Differential algebra methods for the study of the structural identifiability of rational function state-space models in the biosciences, Math. Biosci. 174 (2001) 1–26.
[283] X. Xia, C.H. Moog, Identifiability of Nonlinear Systems With Application to HIV/AIDS Models, IEEE Trans. Automat. Contr. 48 (2003) 330–336.
[284] B.H. Chen, S. Bermingham, A.H. Neumann, H.J.M. Kramer, S.P. Asprey, On the Design of Optimally Informative Experiments for Dynamic Crystallization Process Modeling, Ind. Eng. Chem. Res. 43 (2004) 4889–4902.
[285] A. Raue, C. Kreutz, T. Maiwald, J. Bachmann, M. Schilling, U. Klingmüller, et al., Structural and practical identifiability analysis of partially observed dynamical models by exploiting the profile likelihood., Bioinformatics. 25 (2009) 1923–1929.
[286] J. Karlsson, M. Anguelova, An Efficient Method for Structural Identifiability Analysis of Large Dynamic Systems, in: 16th IFAC Symp. Syst. Identif., Brussels, Belgium, 2012: pp. 941–946.
[287] F. Galvanin, C.C. Ballan, M. Barolo, F. Bezzo, A general model-based design of experiments approach to achieve practical identifiability of pharmacokinetic and pharmacodynamic models., J. Pharmacokinet. Pharmacodyn. 40 (2013) 451–467.
[288] M. Rodriguez-Fernandez, J.A. Egea, J.R. Banga, Novel metaheuristic for parameter estimation in nonlinear dynamic biological systems., BMC Bioinformatics. 7 (2006) 483.
[289] T.J. Rothenberg, Identification in Parametric Models, Econometrica. 39 (1971) 577–591.
[290] R. Mehra, Optimal input signals for parameter estimation in dynamic systems--Survey and new results, IEEE Trans. Automat. Contr. 19 (1974).
[291] D.E. Zak, G.E. Gonye, J.S. Schwaber, F.J. Doyle III, Importance of Input Perturbations and Stochastic Gene Expression in the Reverse Engineering of Genetic Regulatory Networks: Insights From an Identifiability Analysis of an In Silico Network, Genome Res. 13 (2003) 2396–2405.
[292] A.J. Jacquez, P. Greif, Numerical Parameter Identifiability and Estimability: Integrating Identifiability, Estimability, and Optimal Sampling Design, Math. Biosci. 77 (1985) 201–227.
[293] C. Cobelli, J.J. DiStefano, Parameter and structural identifiability concepts and ambiguities: a critical review and analysis., Am. J. Physiol. 239 (1980) R7–R24.
[294] G.E. Box, K.B. Wilson, On the Experimental Attainment of Optimum Conditions, J. R. Stat. Soc. Ser. B. 13 (1951) 1–45.
[295] F.R. Sidoli, A. Mantalaris, S.P. Asprey, Modelling of Mammalian cells and cell culture processes., Cytotechnology. 44 (2004) 27–46.
[296] W.G. Hunter, A.M. Reiner, Designs for discriminating between two rival models, Technometrics. 7 (1965) 307–323.
[297] A.C. Atkinson, V. V Fedorov, Optimal design: Experiments for discriminating between several models, Biometrika. 62 (1975) 289–303.
[298] A.C. Atkinson, V.V. Fedorov, The Design of Experiments for Discriminating Between two Rival Models, Biometrika. 62 (1975) 57–70.
[299] S.M. Stigler, Optimal Experimental Design for Polynomial Regression, J. Am. Stat. Assoc. 66 (1971) 311–318.
[300] D. Uciński, B. Bogacka, T-optimum designs for discrimination between two multiresponse

dynamic models, J. R. Stat. Soc. B. 67 (2005) 3–18.
[301] H. Dette, V.B. Melas, P. Shpilev, Robust T-optimal discriminating designs, Ann. Stat. 41 (2013) 1693–1715.
[302] H. Dette, V.B. Melas, P. Shpilev, T-OPTIMAL DESIGNS FOR DISCRIMINATION BETWEEN TWO POLYNOMIAL MODELS, Ann. Stat. 40 (2012) 188–205.
[303] C. Tommasi, J. López-Fidalgo, Bayesian optimum designs for discriminating between models with any distribution, Comput. Stat. Data Anal. 54 (2010) 143–150.
[304] T.H. Waterhouse, J. a Eccleston, S.B. Duffull, Optimal design criteria for discrimination and estimation in nonlinear models., J. Biopharm. Stat. 19 (2009) 386–402.
[305] R. King, S.P. Brooks, Bayesian model discrimination for multiple strata capture-recapture data, Biometrika. 89 (2002) 785–806.
[306] W.E. Stewart, Y. Shon, G.E.P. Box, Discrimination and goodness of fit of multiresponse mechanistic models, AIChE J. 44 (1998) 1404–1412.
[307] G.E.P. Box, W.J. Hill, Discrimination Among Mechanistic Models, Technometrics. 9 (1967) 57–71.
[308] K. Chaloner, I. Verdinelli, Bayesian Experimental Design: A Review, Stat. Sci. 10 (1995) 273–304.
[309] D.J. Pritchard, D.W. Bacon, Statistical assessment of chemical kinetic models, Chem. Eng. Sci. 30 (1975) 567–574.
[310] G. Buzzi-Ferraris, P. Forzatti, A new sequential experimental design procedure for discriminating among rival models, Chem. Eng. Sci. 38 (1983) 225–232.
[311] G. Buzzi-Ferraris, Planning of experiments and kinetic analysis, Catal. Today. 52 (1999) 125–132.
[312] W.W. Hines, D.C. Montgomery, Probability and Statistics in Engineering, 4th ed., Wiley, New York, 2003.
[313] A.C. Atkinson, Posterior probabilities for choosing a regression model, Biometrika. 65 (1978) 39–48.
[314] F.J. Dumez, L.H. Hosten, G.F. Froment, The Use of Sequential Discrimination in the Kinetic Study of 1 -Butene Dehydrogenation, Ind. Eng. Chem. Fundam. 16 (1977) 298–301.
[315] M.J. Cooney, K.A. McDonald, Optimal dynamic experiments for bioreactor model discrimination, Appl. Microbiol. Biotechnol. 43 (1995) 826–837.
[316] G. Buzzi Ferraris, P. Forzatti, G. Emig, H. Hofmann, Sequential experimental design for model discrimination in the case of multiple responses, Chem. Eng. Sci. 39 (1984) 81–85.
[317] E. Walter, L. Pronzato, Qualitative and quantitative experiment design for phenomenological models—A survey, Automatica. 26 (1990) 195–213.
[318] A.C. Atkinson, A.N. Donev, Optimum experimental designs, Clarendon Press, 1992.
[319] D.L. Ma, R.D. Braatz, Robust identification and control of batch processes, Comput. Chem. Eng. 27 (2003) 1175–1184.
[320] E. Van Derlinden, K. Bernaerts, J.F. Van Impe, Simultaneous versus sequential optimal experiment design for the identification of multi-parameter microbial growth kinetics as a function of temperature, J. Theor. Biol. 264 (2010) 347–355.
[321] L.M. Cunha, F.A.R. Oliveira, Optimal experimental design for estimating the kinetic parameters of processes described by the first-order Arrhenius model under linearly increasing temperature profiles, J. Food Eng. 46 (2000) 53–60.
[322] A. Flores-Sánchez, A. Flores-Tlacuahuac, L.L. Pedraza-Segura, Model-Based Experimental Design to Estimate Kinetic Parameters of the Enzymatic Hydrolysis of Lignocellulose, Ind. Eng. Chem. Res. 52 (2013) 4834–4850.
[323] J.C. Pinto, M.W. Lobão, J.L. Monteiro, Sequential experimental design for parameter estimation: a different approach, Chem. Eng. Sci. 45 (1990) 883–892.
[324] Z. Zhou, L. Han, G.M. Bollas, Overview of Chemical-Looping Reduction in Fixed Bed and Fluidized Bed Reactors Focused on Oxygen Carrier Utilization and Reactor Efficiency, Aerosol

Air Qual. Res. 14 (2014) 559–571.
[325] J. Solsvik, H.A. Jakobsen, Impacts on the reactor performance of intra-particle multicomponent mass diffusion limitations: Knudsen diffusion, Energy Procedia. 26 (2012) 116–124.
[326] J. Solsvik, H. a. Jakobsen, Modeling of multicomponent mass diffusion in porous spherical pellets: Application to steam methane reforming and methanol synthesis, Chem. Eng. Sci. 66 (2011) 1986–2000.
[327] J. Solsvik, S. Tangen, H.A. Jakobsen, On the Consistent Modeling of Porous Catalyst Pellets: Mass and Molar Formulations, Ind. Eng. Chem. Res. 51 (2012) 8222–8236.
[328] M. Schwaab, J.C. Pinto, Optimum reference temperature for reparameterization of the Arrhenius equation. Part 1: Problems involving one kinetic constant, Chem. Eng. Sci. 62 (2007) 2750–2764.
[329] D.J. Pritchard, D.W. Bacon, Prospects for reducing correlations among parameter estimates in kinetic models, Chem. Eng. Sci. 33 (1978) 1539–1543.
[330] A. Cuesta, A. Martínez-Alonso, J.M.D. Tascón, Correlation between Arrhenius Kinetic Parameters in the Reaction of Different Carbon Materials with Oxygen, Energy & Fuels. 7 (1993) 1141–1145.
[331] D.M. Espie, S. Macchietto, Nonlinear transformations for parameter estimation, Ind. Eng. Chem. Res. 27 (1988) 2175–2179.
[332] D.G. Watts, Estimating parameters in nonlinear rate equations, Can. J. Chem. Eng. 72 (1994) 701–710.
[333] L. Han, Z. Zhou, G.M. Bollas, Model-based Analysis of Chemical-Looping Combustion Experiments. Part I: Structural Identifiability of Kinetic Models, AIChE J. (2015) (In Review).
[334] A.K. Avetisov, J.R. Rostrup-Nielsen, V.L. Kuchaev, J.-H. Bak Hansen, A.G. Zyskin, E.N. Shapatina, Steady-state kinetics and mechanism of methane reforming with steam and carbon dioxide over Ni catalyst, J. Mol. Catal. A Chem. 315 (2010) 155–162.
[335] J. Rostrup-Nielsen, L.J. Christiansen, Concepts in Syngas Manufacture (Catalytic Science), 1st ed., Imperial College Press, 2011.
[336] J.R. Rostrup-Nielsen, Steam reforming, in: J.R. Anderson, M. Boudart (Eds.), Catal. Sci. Technol., Springer-Verlag, Berlin, 1984: pp. 1–117.
[337] J. Rostrup-Nielsen, Reaction Kinetics and Industrial Catalysis, in: R.W. Joyner, R.A. van Santen (Eds.), Elem. React. Steps Heterog. Catal., Kluwer Academic Publishers, Dordrecht, 1993: pp. 441–461.
[338] A. Franco, A. Franco, C. Casarosa, C. Casarosa, On some perspectives for increasing the efficiency of combined cycle power plants, Appl. Therm. Eng. 22 (2002) 1501–1518.
[339] T. Heppenstall, Advanced gas turbine cycles for power generation: a critical review, Appl. Therm. Eng. 18 (1998) 837–846.
[340] Sargent & Lundy, New Coal-fired Power Plant Performance and Cost Estimates, 2009.
[341] M.C. Woods, P.J. Capicotto, J.L. Haslbeck, N.J. Kuehn, M. Matuszewski, L.L. Pinkerton, et al., Cost and Performance Baseline for Fossil Energy Plants. Volume 1: Bituminous Coal and Natural Gas to Electricity, DOE/NETL, 2013.
[342] T.A. Adams II, P.I. Barton, High-efficiency power production from natural gas with carbon capture, J. Power Sources. 195 (2010) 1971–1983.
[343] P. Chiesa, S. Consonni, Natural Gas Fired Combined Cycles With Low CO_2 Emissions, J. Eng. Gas Turbines Power. 122 (2000) 429.
[344] Y.S. Kim, J.J. Lee, T.S. Kim, J.L. Sohn, Y.J. Joo, Performance analysis of a syngas-fed gas turbine considering the operating limitations of its components, Appl. Energy. 87 (2010) 1602–1611.
[345] C. Descamps, C. Bouallou, M. Kanniche, Efficiency of an Integrated Gasification Combined Cycle (IGCC) power plant including CO_2 removal, Energy. 33 (2008) 874–881.
[346] Rolf Bachmann, H. Nielsen, J. Warner, R. Kehlofer, Combined-Cycle Gas & Steam Turbine Power Plants, 3rd ed., PennWell, Tulsa, Oklahoma, 2009.

[347] C. Linderholm, A. Abad, T. Mattisson, A. Lyngfelt, 160 h of chemical-looping combustion in a 10 kW reactor system with a NiO-based oxygen carrier, Int. J. Greenh. Gas Control. 2 (2008) 520–530.
[348] J. Adánez, P. Gayán, J. Celaya, L.F. De Diego, F. García-Labiano, A. Abad, Chemical looping combustion in a 10 kW_{th} prototype using a CuO/Al_2O_3 oxygen carrier: Effect of operating conditions on methane combustion, Ind. Eng. Chem. Res. 45 (2006) 6075–6080.
[349] E. Johansson, T. Mattisson, A. Lyngfelt, H. Thunman, A 300W laboratory reactor system for chemical-looping combustion with particle circulation, Fuel. 85 (2006) 1428–1438.
[350] A. Abad, T. Mattisson, A. Lyngfelt, M. Johansson, The use of iron oxide as oxygen carrier in a chemical-looping reactor, Fuel. 86 (2007) 1021–1035.
[351] R. Xiao, Q. Song, M. Song, Z. Lu, S. Zhang, L. Shen, Pressurized chemical-looping combustion of coal with an iron ore-based oxygen carrier, Combust. Flame. 157 (2010) 1140–1153.
[352] R. Xiao, Q. Song, S. Zhang, W. Zheng, Y. Yang, Pressurized chemical-looping combustion of chinese bituminous coal: Cyclic performance and characterization of iron ore-based oxygen carrier, Energy & Fuels. 24 (2010) 1449–1463.
[353] A. Bischi, Ø. Langørgen, I. Saanum, J. Bakken, M. Seljeskog, M. Bysveen, et al., Design study of a 150kWth double loop circulating fluidized bed reactor system for chemical looping combustion with focus on industrial applicability and pressurization, Int. J. Greenh. Gas Control. 5 (2010) 467–474.
[354] J.R. Fernández, J.C. Abanades, Conceptual design of a Ni-based chemical looping combustion process using fixed-beds, Appl. Energy. 135 (2014) 309–319.
[355] D.R. Clarke, M. Oechsner, N.P. Padture, Thermal-barrier coatings for more efficient gas-turbine engines, MRS Bull. 37 (2012) 891–898.
[356] H.P. Hamers, M.C. Romano, V. Spallina, P. Chiesa, F. Gallucci, M.V.S. Annaland, Comparison on process efficiency for CLC of syngas operated in packed bed and fluidized bed reactors, Int. J. Greenh. Gas Control. 28 (2014) 65–78.
[357] S. Noorman, F. Gallucci, M.M. van Sint Annaland, J.A.M. Kuipers, A theoretical investigation of CLC in packed beds. Part 2: Reactor model, Chem. Eng. J. 167 (2011) 369–376.
[358] V. Spallina, F. Gallucci, M.C.C. Romano, P. Chiesa, G. Lozza, M. Van Sint Annaland, Investigation of heat management for CLC of syngas in packed bed reactors, Chem. Eng. J. 225 (2013) 174–191.
[359] I. Martínez, M.C. Romano, J.R. Fernández, P. Chiesa, R. Murillo, J.C. Abanades, Process design of a hydrogen production plant from natural gas with CO_2 capture based on a novel Ca/Cu chemical loop, Appl. Energy. 114 (2014) 192–208.
[360] J.R. Fernández, J.M. Alarcón, Chemical looping combustion process in fixed-bed reactors using ilmenite as oxygen carrier: Conceptual design and operation strategy, Chem. Eng. J. 264 (2015) 797–806.
[361] A. Tică, H. Guéguen, D. Dumur, D. Faille, F. Davelaar, Design of a combined cycle power plant model for optimization, Appl. Energy. 98 (2012) 256–265.
[362] F. He, Z. Li, P. Liu, L. Ma, E.N. Pistikopoulos, Operation window and part-load performance study of a syngas fired gas turbine, Appl. Energy. 89 (2012) 133–141.
[363] Y.S. Kim, S.K. Park, J.J. Lee, D.W. Kang, T.S. Kim, Analysis of the impact of gas turbine modifications in integrated gasification combined cycle power plants, Energy. 55 (2013) 977–986.
[364] J.R. Fernandez, J.C. Abanades, R. Murillo, Modeling of Cu oxidation in an adiabatic fixed-bed reactor with N_2 recycling, Appl. Energy. 113 (2014) 1945–1951.
[365] B. Sathyaseelan, I. Baskaran, K. Sivakumar, Phase Transition Behavior of Nanocrystalline Al_2O_3 Powders, Soft Nanosci. Lett. 3 (2013) 69–74.
[366] C. Iloeje, Z. Zhao, A.F. Ghoniem, Analysis of thermally coupled chemical looping combustion-based power plants with carbon capture, Int. J. Greenh. Gas Control. 35 (2015) 56–70.
[367] A. Lawal, M. Wang, P. Stephenson, O. Obi, Demonstrating full-scale post-combustion CO_2 capture for coal-fired power plants through dynamic modelling and simulation, Fuel. 101 (2012)

115–128.
[368] L. Han, Z. Zhou, G.M. Bollas, Model-based Analysis of Chemical-Looping Combustion Experiments. Part II: Optimal Design of Reduction Experiments, AIChE J. (2015) (In Review).
[369] O. Nordness, L. Han, Z. Zhou, G.M. Bollas, Kinetic Study of High-Pressure Chemical-Looping Combustion (CLC) Experiments with Methane and Synthesis gas with Ni and Cu Oxygen Carriers, Energy & Fuels. Accepted (2015).
[370] W.J. Fischer, P. Nag, H-class High Performance Siemens Gas Turbine SGT-8000H series, in: Power-Gen Int., Las Vegas, NV, 2011.
[371] A. Foust, Siemens SGT6-5000F Gas Turbine - An Evolutionary Approach, in: Electr. Power Conf. Exhib., New Orleans, LA, 2014.
[372] F.J. Brooks, GE Gas Turbine Performance Characteristics, Schenectady, NY, 2000.
[373] J.R. Johnston, Performance and Relability Improvements for Heavy-Duty Gas Turbines, Schenectady, NY, 2000.
[374] L. Han, G.M. Bollas, Dynamic Optimization of Fixed Bed Chemical-Looping Processes, Energy. (2015) (In review).
[375] A. Lyngfelt, M. Johansson, T. Mattisson, Chemical-Looping Combustion-Status of Development, in: 9th Int. Conf. Circ. Fluid. Beds, Hamburg, Germany, 2008.
[376] J. Wolf, J. Yan, Parametric study of chemical looping combustion for tri-generation of hydrogen, heat, and electrical power with CO_2 capture, Int. J. Energy Res. 29 (2005) 739–753.
[377] M. Ishida, M. Yamamoto, T. Ohba, Experimental results of chemical-looping combustion with $NiO/NiAl_2O_4$ particle circulation at 1200 ° C, Energy Convers. 43 (2002) 1469–1478.
[378] E. Jerndal, T. Mattisson, A. Lyngfelt, Investigation of Different $NiO/NiAl_2O_4$ Particles as Oxygen Carriers for Chemical-Looping Combustion, Energy & Fuels. 23 (2009) 665–676.
[379] K.E. Sedor, M.M. Hossain, H.I. de Lasa, Reactivity and stability of Ni/Al_2O_3 oxygen carrier for chemical-looping combustion (CLC), Chem. Eng. Sci. 63 (2008) 2994–3007.
[380] M. Johansson, T. Mattisson, A. Lyngfelt, Use of $NiO/NiAl_2O_4$ Particles in a 10 kW Chemical-Looping Combustor, Ind. Eng. Chem. Res. 45 (2006) 5911–5919.
[381] H.-. J. Ryu, G. Jin, C. Yi, Demonstration of inherent CO_2 separation and no NOx emission in a 50kW chemical-looping combustor: Continuous reduction and oxidation experiment, in: Conf. Greenh. Gas Control Technol., Vancouver, Canada, 2004.
[382] M. Rydén, A. Lyngfelt, T. Mattisson, Chemical-looping combustion and chemical-looping reforming in a circulating fluidized-bed reactor using Ni-based oxygen carriers, Energy and Fuels. 22 (2008) 2585–2597.
[383] J. Adánez, P. Gayán, J. Celaya, L.F. de Diego, F. Garcia-Labiano, A. Abad, Chemical Looping Combustion in a 10 kW th Prototype Using a CuO/Al_2O_3 Oxygen Carrier: Effect of Operating Conditions on Methane Combustion, Ind. Eng. Chem. Res. 45 (2006) 6075–6080.
[384] D. Sridhar, A. Tong, H. Kim, L. Zeng, F. Li, L. Fan, Syngas Chemical Looping Process: Design and Construction of a 25 kW_{th} Subpilot Unit, Energy & Fuels. 26 (2012) 2292−2302.
[385] A. Tong, D. Sridhar, Z. Sun, H.R. Kim, L. Zeng, F. Wang, et al., Continuous high purity hydrogen generation from a syngas chemical looping 25kWth sub-pilot unit with 100% carbon capture, Fuel. 103 (2013) 495–505.
[386] Q. Zhou, L. Zeng, L. Fan, Syngas Chemical Looping Process: Dynamic Modeling of a Moving-Bed Reducer, AIChE J. 59 (2013) 3432–3443.
[387] S.F. Håkonsen, R. Blom, Chemical looping combustion in a rotating bed reactor - Finding optimal process conditions for prototype reactor, Environ. Sci. Technol. 45 (2011) 9619–9626.
[388] R.K. Shah, T. Skiepko, Influence of leakage distribution on the thermal performance of a rotary regenerator, Appl. Therm. Eng. 19 (1999) 685–705.
[389] Y.S. Matros, Prospects of use of unsteady-processes in catalytic reactors, JVKhO Im. D. I. Mendeleeva [Journal All-Union Chem. Soc. 22 (1977) 576–580.
[390] Y.S. Matros, G.A. Bunimovich, Reverse-Flow Operation in Fixed Bed Catalytic Reactors, Catal. Rev. 38 (1996) 1–68.

[391] G. Kolios, J. Frauhammer, G. Eigenberger, Autothermal fixed-bed reactor concepts, Chem. Eng. Sci. 55 (2000) 5945–5967.
[392] F. Larachi, P.L. Mills, M.P. Duduković, Multiphase catalytic reactors: a perspective on current knowledge and future trends, Catal. Rev. Sci. Eng. 44 (2002) 123–246.
[393] Y.S. Matros, Catalytic processes under unsteady state conditions, Elsvier, 1988.
[394] M.P. Dudukovic, Frontiers in reactor engineering., Science. 325 (2009) 698–701.
[395] M.S. Kulkarni, M.P. Duduković, A bidirectional fixed-bed reactor for coupling of exothermic and endothermic reactions, AIChE J. 42 (1996) 2897–2910.
[396] G. Kolios, G. Eigenberger, Styrene synthesis in a reverse-flow reactor, Chem. Eng. Sci. 54 (1999) 2637–2646.
[397] M.S. Kulkarni, M.P. Dudukovic, Periodic Operation of Asymmetric Bidirectional Fixed-Bed Reactors with Temperature Limitations, Ind. Eng. Chem. Res. 37 (1998) 770–781.
[398] M.S. Kulkarni, M.P. Duduković, A robust algorithm for fixed-bed reactors with steep moving temperature and reaction fronts, Chem. Eng. Sci. 51 (1996) 571–585.
[399] M.S. Kulkarni, M.P. Dudukovic, Dynamics of gas phase and solid phase reactions in fixed bed reactors, Chem. Eng. Sci. 51 (1996) 3083–3088.
[400] B. Glöckler, G. Kolios, C. Tellaeche, U. Nieken, A Heat-Integrated Reverse-Flow Reactor Concept for Endothermic High-Temperature Syntheses. Part I: Fundamentals - Short-Cut Theory and Experimental Verification of a Traveling Endothermic Reaction Zone, Chem. Eng. Technol. 32 (2009) 1339–1347.
[401] M.V.S. Annaland, H.A.R. Scholts, J.A.M. Kuipers, W.P.M. Van Swaaij, A novel reverse flow reactor coupling endothermic and exothermic reactions Part II : Sequential reactor configurations for reversible endothermic reactions, Chem. Eng. Sci. 57 (2002) 855–872.
[402] Y.S. Matros, G.A. Bunnimovich, G.K. Boreskov, Unsteady-State Performance of Sulphur Dixodie Oxidation in Production of Sulphuric Acid, Front. Chem. React. Eng. 2 (1984) 386–397.
[403] G.A. Bunimovich, G.K. Boreskov, Y.S. Matros, A.A. Ivanov, Catalytic Processes Carried Out Under Non-Steady-State Conditions: Switching the Direction for the Feed of the Reaction Mixture to the Catalyst Bed. Experimental Results, Kinet. Catal. 23 (1982) 402–406.
[404] G.A. Bunimovich, N. V. Vernikovskaya, V.O. Strots, B.S. Balzhinimaev, Y.S. Matros, SO2 oxidation in a reverse-flow reactor: Influence of a vanadium catalyst dynamic properties, Chem. Eng. Sci. 50 (1995) 565–580.
[405] R.F. Blanks, T.S. Wittrig, D.A. Peterson, Bidirectional adiabatic synthesis gas generator, Chem. Eng. Sci. 45 (1990) 2407–2413.
[406] A.M. De Groote, G.F. Froment, T. Kobylinski, Synthesis gas production from natural gas in a fixed bed reactor with reversed flow, Can. J. Chem. Eng. 74 (1996) 735–742.
[407] R. Hong, X. Li, H. Li, W. Yuan, Modeling and simulation of SO_2 oxidation in a fixed-bed reactor with periodic flow reversal, Catal. Today. 38 (1997) 47–58.
[408] W. De Xiao, H. Wang, W.K. Yuan, An SO_2 converter with flow reversal and interstage heat removal: From laboratory to industry, Chem. Eng. Sci. 54 (1999) 1307–1311.
[409] K.M. Vanden Bussche, S.N. Neophytides, I.A. Zolotarskii, G.F. Froment, Modelling and simulation of the reversed flow operation of a fixed-bed reactor for methanol synthesis, Chem. Eng. Sci. 48 (1993) 3335–3345.
[410] G. Eigenberger, U. Niecken, Catalytic Combustion with Periodic Flow Reversal, Chem. Eng. Sci. 43 (1988) 2109–2155.
[411] C. Sapundzhiev, J. Chaouki, C. Guy, D. Klvana, Catalytic combustion of natural gas in a fixed bed reactor with flow reversal, Chem. Eng. Commun. 125 (1993) 171–186.
[412] J. Chaouki, C. Sapundzhiev, D. Kusohorsky, D. Klvana, Combustion of Methane in a Cyclic Catalytic Reactor, Ind. Eng. Chem. Res. 33 (1994) 2957–2963.
[413] B. van de Beld, R.A. Borman, O.R. Derkx, B.A.A. van Woezik, K.R. Westerterp, Removal of Volatile Organic Compounds from Polluted Air in a Reverse Flow Reactor: An Experimental Study, Ind. Eng. Chem. Res. 33 (1994) 2946–2956.

[414] L. van de Beld, K.R. Westerterp, Air purification in a reverse-flow reactor: Model simulations vs. experiments, AIChE J. 42 (1996) 1139–1148.
[415] L. van de Beld, K.R. Westerterp, Operation of a Catalytic Reverse Flow Reactor for the Purification of Air Contaiminated with Volatile Organic Compounds, Can. J. Chem. Eng. 75 (1997) 975–983.
[416] H. Ziifle, T. Turek, Catalytic combustion in a reactor with periodic flow reversal . Part 1. Experimental results, Chem. Eng. Process. 36 (1997) 327–340.
[417] H. Ziifle, T. Turek, Catalytic combustion in a reactor with periodic flow reversal. Part 2. Steady-state reactor model, Chem. Eng. Process. 36 (1997) 341–352.
[418] J.L. Nijdam, C.W.M. Van Der Geld, A comparison of hybrid and numerical techniques to model heat transfer in reverse flow reactors, Appl. Therm. Eng. 19 (1999) 1045–1070.
[419] J.L. Nijdam, C.W.M. van der Geld, Experiments with a large-scale reverse flow reactor, Chem. Eng. Sci. 52 (1997) 2729–2741.
[420] M. Cittadini, M. Vanni, A. a. Barresi, G. Baldi, Simplified procedure for design of catalytic combustors with periodic flow reversal, Chem. Eng. Process. Process Intensif. 40 (2001) 255–262.
[421] S. Salomons, R.E. Hayes, M. Poirier, H. Sapoundjiev, Modelling a reverse flow reactor for the catalytic combustion of fugitive methane emissions, Comput. Chem. Eng. 28 (2004) 1599–1610.
[422] A. Kushwaha, M. Poirier, H. Sapoundjiev, R.E. Hayes, Effect of reactor internal properties on the performance of a flow reversal catalytic reactor for methane combustion, Chem. Eng. Sci. 59 (2004) 4081–4093.
[423] R.Q. Ferreira, C.A. Costa, S. Masetti, Reverse-flow reactor for a selective oxidation process, Chem. Eng. Sci. 54 (1999) 4615–4627.
[424] Z. Zhou, L. Han, G.M. Bollas, Model-assisted analysis of fluidized bed chemical-looping reactors, Chem. Eng. Sci. 134 (2015) 619–631.
[425] O. V. Kiselev, Y.S. Matros, Intrinsic Energy Removal in the Heat Front Moving in Catalyst Bed, Fiz. Goreniia I Vzryva [Combust. Explos. Shock Waves]. 23 (1987) 167–174.
[426] O. V. Kiselev, Y.S. Matros, N.A. Chumakova, Phenomenon of Heat Front Propagation in Catalyst Bed, in: Y.S. Matros (Ed.), Propag. Heat Waves Heterog. Media [in Russ., Nauka, Novosibirsk, 1988: pp. 145–202.
[427] A. Gawdzik, L. Rakowski, Dynamic properties of the adiabatic tubular reactor with switch flow, Chem. Eng. Sci. 43 (1988) 3023–3030.
[428] K. Gosiewski, R. Sztaba, Simplified design of reverse flow nonstationary reactor for low reactant concentration, in: Unsteady State Process. Catal., VNU Science Press, Utrecht-Tokyo, 1990: pp. 629–635.
[429] J. Řeháček, M. Kubíček, M. Marek, Modelling of a tubular catalytic reactor with flow reversal, Chem. Eng. Sci. 47 (1992) 2897–2902.
[430] J.D. Snyder, B. Subramaniam, Numerical simulation of a periodic flow reversal reactor for sulfur dioxide oxidation, Chem. Eng. Sci. 48 (1993) 4051–4064.
[431] M.V.S. Annaland, R.C. Nijssen, A novel reverse flow reactor coupling endothermic and exothermic reactions: an experimental study, Chem. Eng. Sci. 57 (2002) 4967–4985.
[432] M. van Sint Annaland, H.A.R. Scholts, J.A.M. Kuipers, W.P.M. van Swaaij, A novel reverse flow reactor coupling endothermic and exothermic reactions. Part I: comparison of reactor configurations for irreversible endothermic reactions, Chem. Eng. Sci. 57 (2002) 833–854.
[433] Y.W. Budhi, Reverse Flow Reactor Operation for Control of Catalyst Surface Coverage, Ridderprint Offsetdrukkerij B.V., Eindhoven, the Netherlands, 2005.
[434] K.R. Rout, M. Hillestad, H. a. Jakobsen, A numerical study of pellet model consistency with respect to molar and mass average velocities, pressure gradients and porosity models for methanol synthesis process: Effects of flux models on reactor performance, Chem. Eng. Res. Des. 91 (2013) 296–317.
[435] P.S.E. GPROMS, gPROMS, (2014).

[436] Z. Zhou, L. Han, G.M. Bollas, Overview of chemical-looping reduction in fixed-bed and fluidized-bed reactors focused on oxygen carrier utilization and reactor efficiency, Aerosol Air Qual. Res. 14 (2014) 559-571.
[437] J. Adánez, C. Dueso, L.F. de Diego, F. García-Labiano, P. Gayan, A. Abad, Effect of Fuel Gas Composition in Chemical-Looping Combustion with Ni-Based Oxygen Carriers. 2. Fate of Light Hydrocarbons, Ind. Eng. Chem. Res. 48 (2009) 2509–2518.
[438] M. Zlokarnik, Scale-Up in Chemical Engineering, Wiley-VCH Verlag GmbH & Co. KGaA, 2002.
[439] L.R. Glicksman, Scaling relationships for fluidized beds, Chem. Eng. Sci. 43 (1988) 1419–1421.
[440] G. Donati, R. Paludetto, Scale up of chemical reactors, Catal. Today. 34 (1997) 483–533.
[441] E.B. Nauman, Chemical Reactor Design, Optimization, and Scaleup, McGraw-Hill, 2002.
[442] W. Kim, C. Yun, K.T. Jung, S. Park, S.H. Kim, Computer-aided scale-up of a packed-bed tubular reactor, Comput. Chem. Eng. 39 (2012) 96–104.
[443] T.A. Adams II, P.I. Barton, A dynamic two-dimensional heterogeneous model for water gas shift reactors, Int. J. Hydrogen Energy. 34 (2009) 8877–8891.
[444] W. Xiang, S. Wang, T. Di, Investigation of Gasification Chemical Looping Combustion Combined Cycle Performance, Energy & Fuels. 22 (2008) 961–966.
[445] F. Petrakopoulou, G. Tsatsaronis, T. Morosuk, Conventional Exergetic and Exergoeconomic Analyses of a Power Plant with Chemical Looping Combustion for CO_2 Capture, Int. J. Thermodyn. 13 (2010) 77–86.
[446] B. Hassan, T. Shamim, Effect of oxygen carriers on performance of power plants with chemical looping combustion, Procedia Eng. 56 (2013) 407–412.
[447] O. Brandvoll, O. Bolland, Inherent CO_2 Capture Using Chemical Looping Combustion in a Natural Gas Fired Power Cycle, J. Eng. Gas Turbines Power. 126 (2004) 316.
[448] R. Sharma, M.K. Chandel, A. Delebarre, B. Alappat, 200-MW chemical looping combustion based thermal power plant for clean power generation, Int. J. Energy Res. 37 (2013) 49–58.
[449] H.M. Kvamsdal, K. Jordal, O. Bolland, A quantitative comparison of gas turbine cycles with CO_2 capture, Energy. 32 (2007) 10–24.
[450] M. Anheden, G. Svedberg, Chemical-looping combustion in combination with integrated coal gasification-a way to avoid CO_2 emission from coal fired power plants without a significant decrease in net power efficiency, in: IECEC 96. Proc. 31st Intersoc. Energy Convers. Eng. Conf., IEEE, 1997: pp. 2045–2050.
[451] C. Dueso, F. García-Labiano, J. Adánez, L.F. de Diego, P. Gayán, A. Abad, Syngas combustion in a chemical-looping combustion system using an impregnated Ni-based oxygen carrier, Fuel. 88 (2009) 2357–2364.
[452] M. Ishida, H. Jin, Chemical-looping combustion power generation plant system, Chem. Combust. Power Gener. Plant Syst. (1995).
[453] R. Xiao, L. Chen, C. Saha, S. Zhang, S. Bhattacharya, Pressurized chemical-looping combustion of coal using an iron ore as oxygen carrier in a pilot-scale unit, Int. J. Greenh. Gas Control. 10 (2012) 363–373.
[454] L. Han, G.M. Bollas, Chemical-looping combustion in a reverse-flow fixed bed reactor, Energy. (in review (2015).
[455] Y. Kawajiri, L.T. Biegler, Optimization strategies for simulated moving bed and powerfeed processes, AIChE J. 52 (2006) 1343–1350.
[456] A. Rajendran, G. Paredes, M. Mazzotti, Simulated moving bed chromatography for the separation of enantiomers, J. Chromatogr. A. 1216 (2009) 709–738.
[457] P.S. Gomes, A.E. Rodrigues, Simulated moving bed chromatography: From concept to proof-of-concept, Chem. Eng. Technol. 35 (2012) 17–34.
[458] L.-S. Fan, F. Li, Chemical looping technology and its fossil energy conversion applications, Ind. Eng. Chem. Res. 49 (2010) 10200–10211.
[459] T.R. Marrero, E.A. Mason, Gaseous diffusion constants, J. Phys. Chem. Ref. Data. 1 (1972) 1–

118.
[460] B.E. Poling, J.M. Prausnitz, J.P. O'Connel, The properties of liquids and gases, 2000.
[461] R.H. Perry, D.W. Green, Perry's chemical engineer's handbook, 7th ed., 1997.
[462] Aspen, Aspen technology: physcial property system, (2007).